Manipulating Light at Micro- and Nano-Scale:
Enable Photonic Structures Toward Real-World Applications

by

Chengang Ji

A dissertation submitted in partial fulfillment
of the requirements for the degree of
Doctor of Philosophy
(Electrical Engineering)
in the University of Michigan
2019

Doctoral Committee:

        Professor L. Jay Guo, Chair
        Professor Nicholas A. Kotov
        Associate Professor Pei-Cheng Ku
        Assistant Professor Becky L. Peterson

Chengang Ji

jichg@umich.edu

ORCID iD: 0000-0002-6658-9853

This dissertation is lovingly dedicated to my parents and the whole family, whose constant love and support have sustained me through all the hard times in my life.

ACKNOWLEDGEMENTS

First of all, I would like to sincerely express my appreciation to my Ph.D. advisor, Prof. L. Jay Guo, for bringing me into a fantastic research world and offering invaluable advice throughout my whole Ph.D. study. He has leaded me out of the confusion and helped me adapt to the new environment and regain the confidence when I came to the States. Influenced by his strong passion for research and rigorous attitude, I have acquired independent problem-solving and logical-thinking skills, which prepared me well for more critical challenges in the future. He has always been very generous and encouraged me to explore different ideas. I really appreciate the precious opportunities provided by him to commercialize our technologies, allowing my own research to be extended into real-world applications, which is like a dream come true for me. In addition, he has always been so patient to help me grow up by sharing his life experience, teaching me how to handle negative emotions, and guiding me the right way to get along with people. There are so many valuable memories worth being cherished during the Ph.D. life and it is definitely the most important five years for me that will benefit my whole life.

I would like to express my deep gratitude to my doctoral committee members, Prof. Nicholas A. Kotov, Prof. Pei-Cheng Ku, and Professor Becky L. Peterson, for their insightful suggestions and guidance on my dissertation and research. I have learnt so much from them about the semiconductor fundamentals, various fabrication techniques, and the efficient way of scientific

writing and presentation, which have laid the solid foundations for my Ph.D. study, via taking their courses.

I would like to thank all my colleagues and friends in Guo group and at the University of Michigan. Without their help and accompany, I could have not completed my Ph.D. work and my life here would have lost its meaning. First, I would like to express my sincere gratitude to my mentors, Prof. Kyu-Tae Lee and Dr. Cheng Zhang, for kindly teaching me the optical design and fabrication skills. Their patience and great guidance played a critical role in stimulating my strong interest in research. I would express my sincere gratitude to Dr. Jing Zhou and Dr. Chenying Yang for their helpful guidance in the topics of plasmonics and structural colors. I am thankful to Prof. Xinliang Chen for the fruitful discussions on multi-functional colored solar cells. I would like to thank Prof. Stephen Forrest, Dr. Yongxi Li, Mr. Yue Qu, and Ms. Xinjing Huang for the collaborations on highly-efficient transparent solar cells. I appreciate Prof. Stephen Maldonado and Mr. Saurabh Acharya for their great assistance in the fabrication of solution-processed color filters. I would like to acknowledge the collaboration with Mr. Heyan Wang on characterizations of the electromagnetic shielding performance of ultrathin silver films and the great help from Mr. Junan Chen with measurements of the flat solar concentrator. I am thankful to former lab-mates and visiting scholars, Dr. Xi Chen, Dr. Qiaochu Li, Mr. Zeyu Lei, Prof. Dong Liu (my cousin), Mr. Shengping Liu, Mr. Hao Xiong, Mr. Yeonjoon Cheong, Mr. Darwin Cordovilla, Dr. Dewei Zhao, Dr. Jae Yong Lee, Dr. Ashwin Panday, Dr. Long Chen, Dr. Taehwa Lee, Dr. Taehee Jang, Dr. Jinhwan Lee, Dr. Qingyu Huang, Dr. Qingjiang Yu, Prof. Xudi Wang, Dr. Hui Xia, Prof. Wei Luo, Ms. Jin Yuan, Ms. Ci Song, Dr. Lei Wan, Mr. Cong Chen, Prof. Ting Xu, Prof. Hui Joon Park, Dr. Haofei Shi, and Dr. Peng Zhu. I would express my gratitude to all the current group members and visiting scholars, Mr. Sangeon Lee, Mr. Qingyu Cui, Mr. Sunghyun Nam, Mr. Suneel Joglekar,

TABLE OF CONTENTS

LIST OF TABLES

LIST OF FIGURES

under ambient light, validating the angular-robust colors desired for decorative applications. The scale bars are 1 cm.

Figure 6.2.1 (a) A schematic diagram of the proposed broadband visible absorber with improved viewing angle employing multi-cavity resonances in ultrathin highly absorbing materials. (b) Simulated absorption spectra obtained from metal-semiconductor-metal (MSM) and semiconductor-metal-semiconductor-metal (SMSM) configurations. It is obvious that the absorption spectrum is greatly broadened by introducing an additional resonance for SMSM stacks as compared to the MSM structure.

Figure 6.2.2 Influence of (a) – (b) metals and (c) – (d) semiconductors on absorption spectra. A broad and high absorption property can be attained employing lossy metals, such as Au, Cu, and Al as shown in Figure 6.2.2 (a), however, the absorber structure with Ag metallic mirrors shows the highest absorption in a-Si layers among all the cases exhibited in Figure 6.2.2 (b), which is critical to achieve high efficiency PV devices. This is because a higher absorption only in the photoactive semiconductor layer is required for high performance PV cells. The bandwidth of the optical absorption can be broadened by using low band gap semiconductors, such as silicon-germanium (SiGe) and germanium (Ge), as depicted in (c) and (d). We note that it is difficult to observe the multi-cavity resonance phenomena in the Ge-based absorber structure due to its very large absorption coefficient at visible frequencies, yielding a very broad resonance. We should also note that an V_{oc} gets lower with the low band gap semiconductor materials although the broad absorption bandwidth, which corresponds to the high J_{sc}, could be obtained. The specific structures are [12 nm a-Si/30 nm Ag/24 nm a-Si/80 nm Ag], [10 nm a-Si/40 nm Au/20 nm a-Si/80 nm Au], [10 nm a-Si/45 nm Cu/20 nm a-Si/80 nm Cu], and [17 nm a-Si/15 nm Al/35 nm a-Si/80 nm Al] in

ABSTRACT

Recent advances in fabrication and processing methods have spurred many breakthroughs in the field of nano- and micro-structures that provide novel ways of manipulating light interaction in a well controllable manner, thereby enabling various innovative applications. In this dissertation, new photonic design concepts and materials featuring high performance and long-term stability are investigated for bridging the gap between the research and the real-world applications.

Firstly, angle-insensitive and high-purity structural color filters based on one-dimensional layered structures that are suitable for mass-production are studied. Various scenarios including reducing the layer number and depositing the whole device via an all-solution process have been proposed to simplify the fabrication, thereby lowering the manufacturing cost. The proposed structures offer significant advantages over existing colorant-based filters in terms of high efficiency, slim dimension, and being free from photobleaching. They have been successfully adapted into practical applications including decorative paints, visibly-opaque but near-infrared-transmitting camouflage coatings, and highly-efficient colored photovoltaics. As a special color, 'black' has been studied separately based on ultrabroadband absorbers that are achieved by simultaneously exciting multiple absorption resonances. It can significantly enhance the efficiency of energy harvesting and conversion in various applications. In addition, optical designs are incorporated into vehicle interiors, opening up a new path to the extensive use of optics in automobiles: Anti-

glare colored dashboard with the potential for high-resolution dashboard displays are demonstrated with micro-scale lenticular lenses; Invisible vehicle pillars for safe driving are realized with compact optical cloaks using different optical components, including polarizers and mirrors. The next part is the research into a cost-effective and easy-to-fabricate method for flexible transparent electrodes employing ultrathin (thickness <10 nm), ultra-smooth (roughness <1 nm), and low-loss copper-doped silver. This novel silver alloy requires only room-temperature deposition and presents outstanding optical and electrical properties, mechanical flexibility, and environmental stability, which are greatly desired in potential high-performance flexible optoelectronic devices. Lastly, other optical structures inspired by methods employed in above researches that have impactful applications, including retro-reflective particles that can be embedded in transparent glasses for light detection and ranging and omnidirectional planar solar concentrators based on curved micro-reflectors, are briefly discussed. All the strategies and methodologies proposed here could bring optical researches out of the labs and open up more opportunities for further advancement.

Chapter 1

Introduction

1.1 Background

The advent of various advanced micro- and nano-patterning technologies, which significantly boost the manufacturing throughput and yield, opens up possibilities for wide applications of optical and optoelectronic devices. This Ph.D. thesis describes some representative optical structures that are suitable for mass-production and their corresponding practical applications, aiming to intensify the impacts of lab researches by extending them into real-world applications.

Nanostructures exploiting either photonic or plasmonic resonances provide new optical properties and enable unique optical devices with desired functionalities [1-8]. Such novel characteristics offer great potentials for a wide variety of research fields such as near-field probes with ultrahigh resolutions for sensing and imaging, optical trapping at the nanoscale with extraordinary precision, tight light confinement to deep subwavelength volumes via plasmonic lenses, and steering light beyond the diffraction limit. One emerging area that attracts much attention in recent years is the ability of designed nanostructures to generate distinctive colors employing optical resonant properties, often referred as structural colors. In contrast with the traditional approach of using different organic dyes or inorganic pigments to create colors, different structural colors can be

created by using the same materials (*e.g.*, metal and dielectric) but simply changing the geometry and dimension of the structures. Vivid structural colors can be observed in nature, *e.g.*, Morpho butterfly wings, peacock feathers, fruits, beetles, and opals, arise from optical interference effects in multilayer structures [9-14]. Both transmissive or reflective colors have been realized by various means, offering distinct advantages such as high stability, high reproducibility, easy manufacturability, high spatial resolution, and slim dimension, over existing color filters that made of organic dyes or pigments to absorb a spectral portion in the visible wavelength range for the color generation. One-dimensional (1D) structural colors that provide a wide variety of color selections and cost-effective scaling-up methods are well explored here. All the designs exhibit both high brightness and wide-angle independent appearance and can be extended into several applications with well-controlled fabrication cost, including vehicle paints, camouflage coatings, and highly-efficient colored solar cells, etc [15-20].

Black can be considered as a special color, which can be created with nanostructured absorbers featuring highly-efficient and broadband absorption, or with overlapped absorption bands to cover the entire visible range. Broadband absorbers contrast the aforementioned color filters whose function is to produce a relatively sharp resonance to filter a narrow spectral range of visible light. Much effort was aimed at achieving "Perfect absorption", which can benefit various applications such as photovoltaics (PVs), solar-thermal harvesting, photodetectors, thermal emitters, and bolometers, owing to their exceptional absorption characteristics with unique functionalities for energy harvesting and conversion [3, 21-40]. Special attention has been paid to broadband absorbers achieved via exciting multiple resonances simultaneously, which span a wide wavelength range for high absorption performance, in this dissertation based on multi-layered structures [41, 42]. Considering that our proposed structures already involve active materials such

2

as amorphous silicon (a-Si) and germanium (Ge), they can be potentially adapted into PVs after inserting efficient hole and electron transport layers. The facile configurations enable the designs to be mass-produced by roll-to-roll (R2R) deposition method and applied in large areas.

Accommodation of various advanced technologies into automobiles are highly desired in the industry with the target at future smart and autonomous cars. It has revoked the whole automotive market and opened up more possibilities for optics as well, considering the large demands of sensor and display technologies in cars. Applying structural colors as vehicle paints discussed above is one example that has been thoroughly investigated. All current vehicle dashboards are black in order to prevent any veiling glare that interferes safe driving. We reported on a novel design of surface that can impart color to the dashboard and does not cause veiling glare to the driver [43]. This is made possible by covering a substrate with alternating absorber/colored stripes with specially designed lenticular lens arrays, where reflected light rays are controlled out of the veiling glare range while at the same time create visual colors to drivers. As an experimental demonstration, a large-scale sample is fabricated by imprinting method. The presented approach provides a new application of lenticular lenses and can be potentially applied to embellish vehicles' interiors. Due to the small pitches (~50 µm) of lenses, the proposed method can even be extended for dashboard displays with high resolutions if replacing those passive colored stripes beneath with active devices, such as light emitting diodes (LEDs). In addition to colored dashboard surfaces, invisible vehicle pillars, which possess image projection capabilities at the same time, have been realized utilizing broadband optical cloaks that can conceal a large object in the full visible region [44]. Our devices consist of commercially available optical components such as polarizers and mirrors, and therefore, provides a significant further step towards practical application scenarios such as transparent devices and see-through displays.

Transparent electrodes are another widely investigated topic in optics due to the huge demands in almost all optoelectronic devices, including LEDs, PVs, touchscreens, smart windows, etc [45-51]. Currently, the dominantly used transparent conductors are conductive oxides such as indium tin oxide (ITO). However, their intrinsic issues, such as poor mechanical flexibility, low abundance, and incompatibility with polymeric substrates, significantly hinder their wide applications in emerging devices which require not only high transparency and conductivity but also excellent flexibility [52-54]. To overcome these challenges, new transparent electrodes have been developed including carbon-based materials, patterned metal grids, metallic nanowire networks, etc [55-59]. However, all of these alternatives are still limited to some extent in real applications. We report on a highly-transparent and stable transparent electrode of excellent flexibility based on a new copper (Cu)-doped silver (Ag), which is achieved by introducing a very small amount of Cu during the Ag sputtering deposition [60]. This metallic film is ultrathin (~6.5 nm thick), ultra-smooth (roughness <1 nm), and of low loss, which can significantly enhance the electrode transparency. In addition, it maintains the high conductivity of Ag itself and only requires the room-temperature deposition method, thus providing new platforms for various applications that are impossible with traditional methods. Its applications in transparent radio frequency (RF) shielding is demonstrated as an example [61]. The present approach has resolved the problems faced by existing flexible transparent electrodes and may have the potential to replace traditional ITO counterparts, thus facilitating high-performance flexible displays and optoelectronic devices.

Other practical applications including designs of retroreflective particles that can be embedded in transparent glasses for light detection and ranging (LIDAR) [62] and omnidirectional planar solar concentrators (PSCs) [63] based on curved micro-reflectors for more efficient harvesting of solar energy, both of which are strong demands conforming to nowadays the fast developments of

technologies for artificial intelligence [64-66] and renewable energy [67-69], are also briefly discussed as an extension of the well-developed ray-tracing technologies discussed above.

1.2 Thesis Outline

Chapter 2 describes new schemes for polarization-independent reflective structural colors that exhibit high purity and luminance over a wide angular range up to $\pm 60°$ from both directions. In this chapter, we will first present structural colors generated with 1D photonic crystals (PCs). Due to the high refractive index materials involved in the design, high reflection intensity and angular-insensitivity can be easily achieved with only 7 layers. Then we further simplify the design and successfully reduce the layer number to 5 while maintaining the high color purity assisted by induced transmission, which is greatly advantageous for lowering manufacturing cost.

Chapter 3 discusses a facile and low-cost method for structural colors via all-solution processes. A multilayered structure consisting of thick gold (Au) on the bottom, a cuprous oxide (Cu_2O) film sandwiched in the middle, and an ultrathin Au layer on the top are subsequently deposited on a Si substrate using electroplating, forming an asymmetric metal-dielectric-metal (MDM) optical cavity. Different colors can be achieved by simply tuning the thickness of the middle dielectric layer. Due to the high refractive index of Cu_2O, the generated colors are invariant to incident angles. Unlike structural colored realized by vacuum depositions, this method can be applied to surfaces of any shapes and large scales with a much lower manufacturing cost, which can potentially extend structural colors into more applications at an affordable cost.

Chapter 4 presents an angular robust colored solar cell of high efficiency by simply integrating a crystal silicon (c-Si) solar panel with passive color filters atop. We will first investigate the reasons behind the various optical properties, including distinctive colored reflection, broadband transmission, and wide-angle performance, of the passive filters, which consist of only 5 layers. Then, we adapt the passive devices, which include a semiconductor layer in the middle, into active solar cells, thereby further enhancing the efficiency of the whole solar cell system. This facile method with significantly reduced layers compared to 1D PCs simultaneously overcomes the angle-sensitivity and low-efficiency issues of typical colored solar cells, therefore presenting great potential for various applications.

Chapter 5 discusses a new scheme for visibly-opaque but near-infrared-transmitting filters involving 7 layers based on 1D PCs, with capabilities in reaching nearly 100% transmission efficiency in the near-infrared (NIR) region. Different decorative reflection colors can be created by adding additional three layers while maintaining the NIR transmission performance. In addition, our proposed structural colors show great angular insensitivity up to ±60° for both transverse electric (TE) and transverse magnetic (TM) polarizations, which are highly desired in various fields.

Chapter 6 presents two different schemes for angle- and polarization-independent ultrathin broadband absorbers based on multi-cavity resonances in highly absorbing media. We will discuss the design principles fundamentally and detailed optical performance will also be evaluated. Both proposed structures based on 1D layered configurations provide simple and cost-effective means

for realizing highly efficient device at large scale and can be potentially adjusted into high efficiency PV cells.

Chapter 7 demonstrates a colored dashboard surface without veiling glare by laminating an alternating absorber/colored stripe substrate underneath a lenticular lens array with specific dimensions. We will discuss the design principles of lenticular lens arrays that can avoid the veiling glare but create visual colors to drivers. Feasible methods for large-scale fabrications and device performance evaluation will also be provided.

Chapter 8 reports a multi-functional cloaking device that can hind a large object in the full visible region and have the image display capabilities at the same time employing wire grid polarizers and mirrors. The cloaking is realized via one polarization and the image projection is made possible using the other orthogonal polarization. The described method provides great simplicity and feasibility for real applications as compared to other solutions including either complicated metamaterials or active display devices.

Chapter 9 reports on a highly-transparent and stable electrode of excellent flexibility based on a dielectric-metal-dielectric (DMD) configuration with a new Cu-doped Ag sandwiched in the middle. This metallic film is ultrathin, ultra-smooth, and of low loss, which is critical in achieving high transmission. It maintains the high conductivity of silver itself and only requires the room-temperature deposition method. In addition, the ultrathin silver is well protected from degradation under high temperature and humidity employing suitable dielectrics, which simultaneously

improve the broadband transmission of the tri-layer stack. Applications of DMD-based transparent electrodes in shielding electromagnetic interference (EMI) are demonstrated illustrating its potential to replace traditional ITO counterparts for high-performance flexible optoelectronics.

Chapter 10 discusses extended applications based on ray-tracing methods including retroreflective particles that enable LIDAR sensors to detect transparent objects and omnidirectional flat solar concentrators for efficient energy harvesting. The retroreflective particles based on a core-shell configuration focus paraxial and non-paraxial rays simultaneously at a small spot on the back reflective coating, which subsequently retro-reflects the incoming light back. The planar concentrator is achieved by collapsing the concave cylindrical surface of a conventional bulk focusing mirror into micron segments. The detailed designs and evaluated performance will be discussed.

Chapter 11 summarizes the main findings discussed in this thesis and lists out future directions.

Chapter 2

Angular- and Polarization-Independent, High-Purity Reflective Structural Colors Based on 1D Layered Structures for Vehicle Paint Applications

2.1 Introduction

Color filters have played a vital role in various areas, including colored displays, LEDs, image sensors, optical detections, and high-chroma pigments [70-79]. Existing color filters employ either chemical colorant pigments or organic dyes to create colors by selectively absorbing a portion of visible light. However, their absorptive nature causes luminous intensity of the resulting colors to be significantly reduced. Besides, the traditional color filters suffer from a short life time due to their susceptibility to environmental factors such as moisture, high temperature, and constant ultraviolet (UV) exposure [80]. To address these difficulties, structural colors, where certain wavelength components in the visible spectrum physically interact with nanostructured materials to produce vivid reflective or transmissive colors, have been proposed as alternatives. Various colors can be generated without changing materials but just simply adjusting the structural dimensions, such as a period, a height, and a duty cycle, of the subwavelength patterns, which

9

selectively transmit or reflect visible light via coupling incident light into Fabry-Pérot (F-P) resonance, guided-mode resonance (GMR), or surface plasmon polariton (SPP) [72, 81-101]. In addition to easy tunability, the structural colors feature high durability, easy scalability, high efficiency, high resolution, slim dimension, and non-photobleaching. However, both the plasmonic and the photonic resonances vary with an angle and a polarization state of incident light due to the momentum matching condition, thereby affecting their color appearance, which are undesired in many applications. To resolve such undesired angle-sensitive characteristics, various approaches that either exploit a localized resonance or a phase compensation mechanism have been demonstrated [77-79, 102-107]. However, these proposed designs are difficult to be scaled to large areas. Besides, the 1D grating structures utilized in previously works typically response to only one polarization [82, 98, 102]. Furthermore, an extension of many reflective color filter designs in the previous reports to a bifacial color generation from both illumination directions has remained highly challenging, which is required for producing pigment flakes in color paint [70, 108-111]. Unless all the aforementioned issues are addressed, it is extremely difficult to replace the conventional dyes with structural colors.

In this chapter, we present new schemes that exhibit angular- and polarization-independent, high-purity reflective colors based on simple 1D layered configurations. A design utilizing 1D PCs is firstly discussed in Section 2.2 [15] and a simpler structure with fewer layers employing higher-order resonances is presented in Section 2.3 [16]. The off-resonance reflection of these designs is perfectly suppressed, leading to great color purity with high luminous intensity. In addition, both scenarios adopt a symmetric design resulting into the same reflection color from both the top and bottom illumination sides, which enable these films to be used as pigment flakes in paint [112].

The strategies described in this study involve one deposition run, which provides a significant step towards large-area applications in various areas.

2.2 Reflective Colors Employing 1D Photonic Crystals

A schematic diagram of the proposed wide-angle and polarization-independent structural color that is composed of an alternating sequence of silicon nitride (Si_3N_4) and amorphous silicon (a-Si) is shown in Figure 2.2.1 (a). Both Si_3N_4 and a-Si are deposited by a plasma-enhanced chemical vapor deposition (PECVD). Even though our strategy can be used to produce various colors, our focus primarily lies on creating the red colors with high purity and angle-insensitivity, which remains largely challenging because of the following two facts: (1) a longer cavity thickness to form a resonance at a longer wavelength range is required, yielding a sensitivity to the angle of incidence and (2) higher-order resonances in a short wavelength regime appear, causing the color purity to be influenced [113]. The center wavelength (λ_c) of a photonic stopband is located at 800 nm. To achieve strong constructive reflection interferences at λ_c, the thickness of each layer is set as a quarter wavelength ($d_{1,2} = \lambda_c /4n_{1,2}$), *i.e.*, 100 nm for Si_3N_4 ($n_1 = 2$) and 50 nm for a-Si ($n_2 = 4$). The bandwidth ($\Delta\left(\frac{\lambda_c}{\lambda}\right) = \frac{4}{\pi}\sin^{-1}\left(\frac{n_2 - n_1}{n_2 + n_1}\right)$) of the photonic stopband of our designed structure is 350 nm that allows the reflected light below ~600 nm to be lower whereas generating strong reflection at longer wavelengths beyond ~600 nm. The reflections from 400 nm to 600 nm, however, are not much suppressed showing ~33% of average reflections due to a high index contrast at the air/a-Si interface as shown by the blue solid line in Figure 2.2.1 (b). The numerical simulation is carried out to further mitigate the reflections in particular at shorter wavelengths. In Figure 2.2.1 (c), the calculated reflections as functions of the refractive index of a 50 nm anti-

reflection (AR) layer at 400, 500, and 600 nm are exhibited. It clearly shows that the reflection

below 600 nm is significantly suppressed (<1.3%) when *n* (the real part of the refractive index)

and *k* (the imaginary part of the refractive index) are equal to 1.98 and 0.14, respectively.

Experimentally, Si_3N_4 is selected as the AR layer as its refractive index is fairly close to the optimal

value, and it can be processed in the same deposition run without breaking the chamber and will

not add additional materials in the fabrication, where the latter is highly desired in reducing

manufacturing cost. Other colors (*e.g.*, blue and green) can be simply achieved by adjusting the

thickness of each layer as summarized in Figure 2.2.2 and Table 2.2.1.
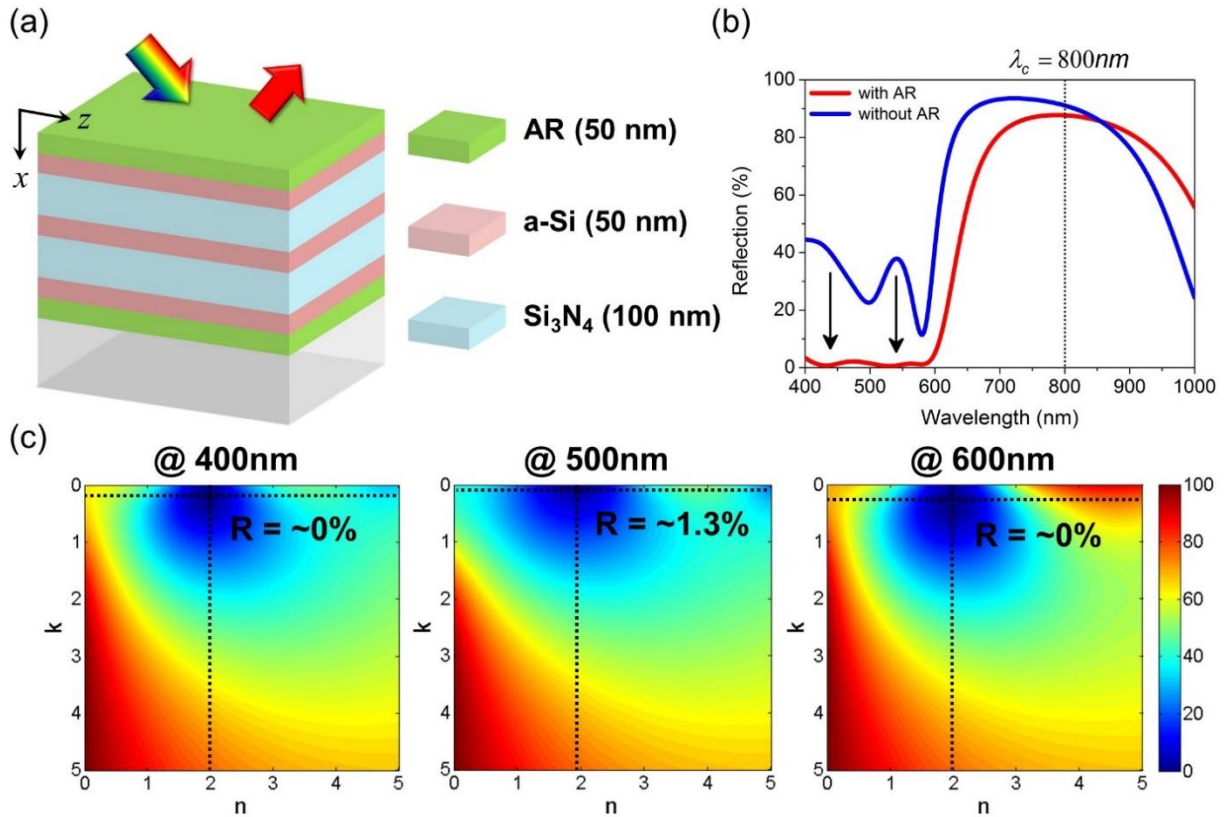
Figure 2.2.1 (a) Schematic of the proposed PC-based structural color. (b) Calculated reflection with (red solid line) and without (blue solid line) an AR coating. It is apparent that reflection below 600 nm gets greatly suppressed with the AR layer. (c) Calculated reflection dependent on the refractive index of the 50nm thick AR layer at 400, 500, and 600 nm, respectively. The color scale represents the reflection intensity.
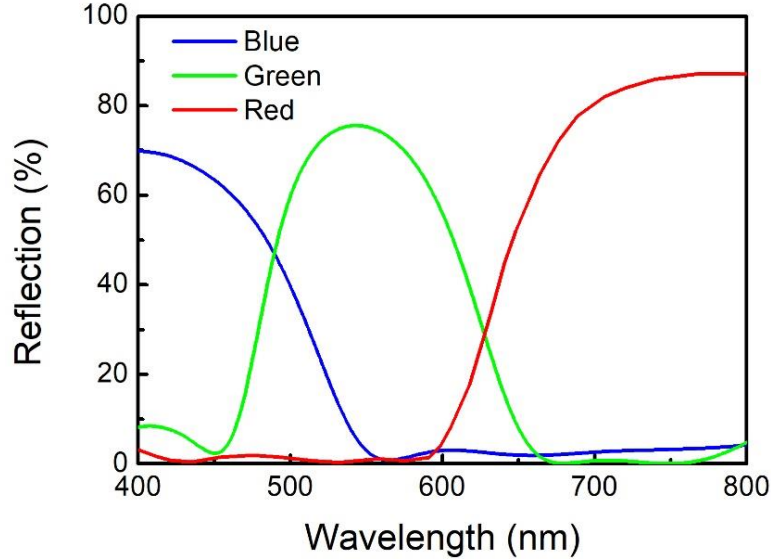
Figure 2.2.2 Calculated reflection spectra of red, green, and blue (RGB) colors based on different structure configurations.

Table 2.2.1 A summary of structure configurations for various colors.

	Si_3N_4	a-Si	Si_3N_4	a-Si	Si_3N_4	a-Si	Si_3N_4
Blue	120 nm	12 nm	75 nm	12 nm	75 nm	12 nm	120 nm
Green	150 nm	30 nm	25 nm	40 nm	130 nm	5 nm	150 nm
Red	50 nm	50 nm	100 nm	50 nm	100 nm	50 nm	50 nm

We investigate the effects of the AR coating with an optical admittance diagram, which provides an effective way to visually represent the optical surface admittance of the multi-layered structure [114, 115]. The optical admittance ($Y = \sqrt{\varepsilon / \mu}$) is the inverse of the impedance with ε and μ being the permittivity and permeability, respectively, and is equal to material complex refractive index due to the negligible magnetic effects at optical frequencies. At normal incidence, the reflection coefficient of a surface can be related to optical admittance via

$$r = \frac{Y_0 - Y}{Y_0 + Y}, \tag{2.2.1}$$

13

where Y_0 and Y are the optical admittance of the incident medium and the structure surface, respectively. With $r = |r|e^{i\varphi} = \alpha + i\beta$ where $\varphi = \frac{2\pi n}{\lambda} d \cos(\theta_{inc})$, d is the layer thickness, and θ_{inc} is the incident angle and $Y = x + iy$, Equation 2.2.1 can be written as

$$|r|e^{i\varphi} = \frac{Y_0 - x - iy}{Y_0 + x + iy} . \tag{2.2.2}$$

Multiplying each side of Equation 2.2.2 with its complex conjugate leads to

$$x^2 + y^2 - 2Y_0 \left(\frac{1 + r^2}{1 - r^2} \right) x + Y_0^2 = 0 . \tag{2.2.3}$$

The admittance locus described by Equation 2.2.3 is a circle for transparent dielectrics and perfect electric conductors, and a spiral for absorbing materials such as semiconductors and real metals [116]. Figure 2.2.3 (a) and (b) present the optical admittance diagrams of the proposed structures without and with the top AR coating, respectively, at three discrete wavelengths (400, 500, and 600 nm). The admittance of the structure starts with the substrate and rotates on the circular or spiral trajectory as the thickness increases. The distance (indicated by the black solid line in the plot) between the termination admittance point of the layered structure and the admittance of air (1, 0) determines the reflection intensity by

$$R = \left(\frac{Y_0 - Y_1}{Y_0 + Y_1} \right) \left(\frac{Y_0 - Y_1}{Y_0 + Y_1} \right)^* \tag{2.2.4}$$

where Y_0 and Y_1 refer to the air admittance and the termination admittance point of the structure, respectively. The termination admittance points at 400, 500, and 600 nm are calculated as (0.95, 0.38), (1.35, -0.34), and (1.03, 0.04), respectively, after adding the AR layer. All of them are much closer to air compared to the structure without the AR coating, which are (4.85, -1.66), (3.24, -0.05), and (2.03, -1.02) for 400, 500, and 600 nm, respectively. As a result, the reflection below 600 nm is well suppressed <5% at all wavelengths, generating the final high-purity red reflection. The simulations are performed based on transfer matrix method with the refractive indices of

materials measured by a spectroscopic ellipsometer (M-2000, J. A. Woollam Co.), which are given

in Figure 2.2.4.
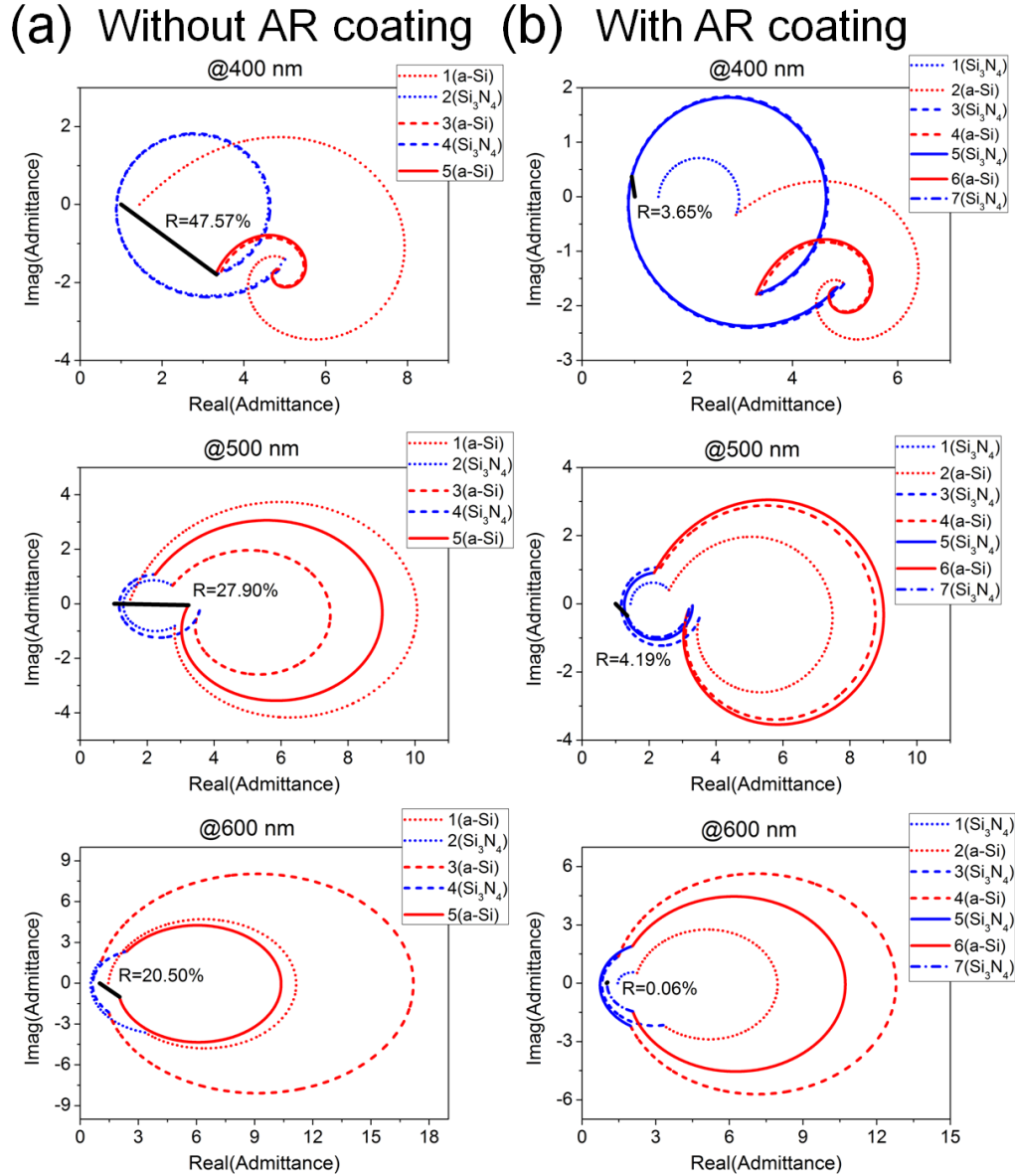
Figure 2.2.3 Optical admittance diagrams of the proposed structural color (a) without and (b) with the AR coating at three discrete wavelengths below 600 nm. It is clear that the reflection, which is indicated by the distance between the final admittance point and the air, is greatly suppressed with the AR layers.
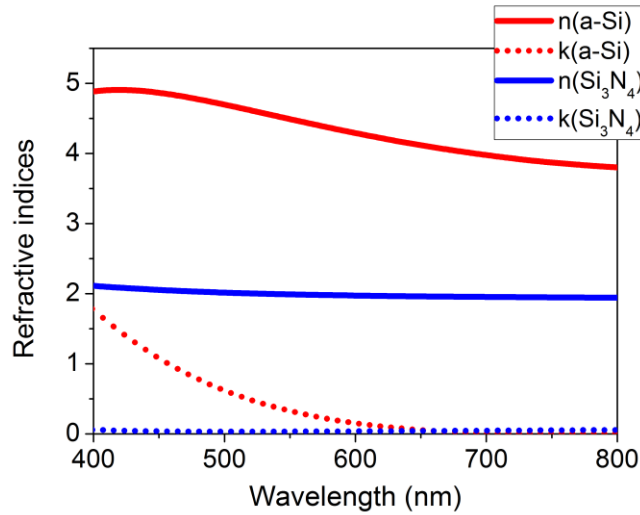
Figure 2.2.4 Measured refractive indices of Si_3N_4 and a-Si.

To verify the design, the measured reflection and transmission (blue curves) of the fabricated structure are provided in Figure 2.2.5 (a), which show great consistency with calculated spectra. The calculated spectra are obtained via the transfer matrix method with the measured refractive indices of Si_3N_4 and a-Si. The reflection spectra at normal incidence are obtained with a thin-film measurement instrument (F20, Filmetrics) and the transmission is measured using a spectroscopic ellipsometer (M-2000, J. A. Woollam). The slight discrepancy between the simulated and measured results can be credited to the thickness and refractive index variation during the deposition process. The strong reflection beyond 600 nm and the negligible noise at shorter wavelength regions (*i.e.*, 400-600 nm) clearly indicate the high-purity red reflective color. It should be noted that the brightness of the generated structural color possessing a peak reflection intensity of ~96% is much improved as compared to traditional dye-based colors, which typically provide luminous intensity of ~50%. The purity of the red color is further evaluated on the CIE 1931 chromaticity diagram as displayed in Figure 2.2.5 (b). Both calculated (0.655, 0.294) and measured

(0.656, 0.321) colors are very close the standard red (0.64, 0.33) used in the liquid crystal display (LCD) devices, which is indicated by the crossing point of two black solid lines.
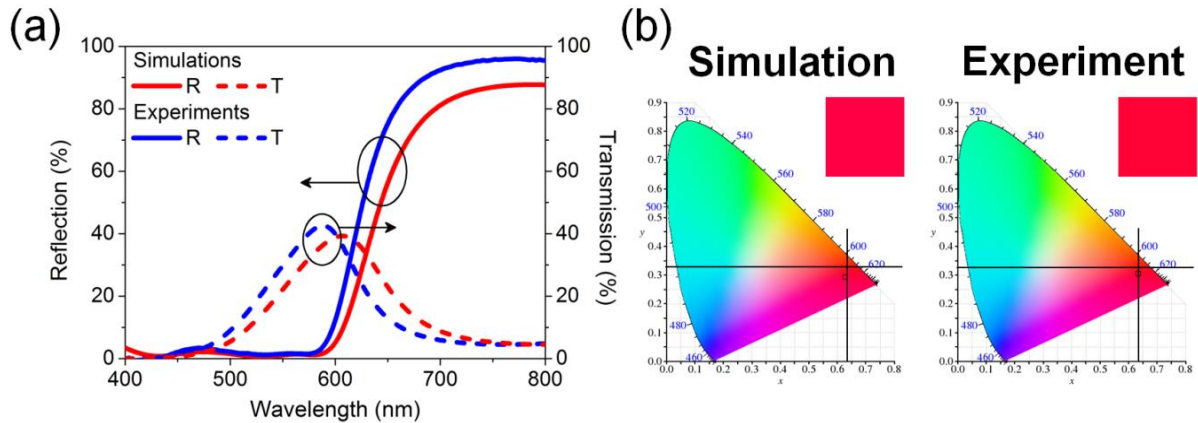
Figure 2.2.5 (a) Calculated (red curves) and measured (blue curves) spectra of the designed structural colors at normal incidence. (b) Evaluated color purity based on both the simulated and measured reflection spectra on the CIE 1931 chromaticity diagram. The crossing point of the two black lines denote the stand red coordinate (0.64, 0.33) used in the LCD devices.

Lastly, the dependence of the colored appearance on the incident angle and polarization is investigated in Figure 2.2.6 (a) – (d). The measured angle resolved reflection for both TE and TM polarizations indicates the great angular- and polarization-insensitive performance with the flat dispersion curves, which can be attributed to the high refractive indices of the materials involved in the proposed design and is in good consistency with the simulated results. The simulation data are calculated with the transfer matrix method and the angular behavior of the fabricated devices from 45° to 80° is measured with a spectroscopic ellipsometer (M-2000, J. A. Woollam). As high reflection at long wavelengths and suppressed reflection below 600 nm are maintained at oblique incidence for both polarizations, a distinctive red color of the fabricated sample is expected to be observed at all angles under ambient light illumination as presented in Figure 2.2.6 (e). It should be noted that the optical photographs are taken with a black background which can absorb the transmitted light and avoid the interference with reflective appearance of the device. In addition, the distinctive red color can also be observed from the backside of the device due to the symmetric

17

configuration of the design. Such bi-directional, angle- and polarization-invariant, and high-purity

properties are highly desired in various applications such as pigment flakes.
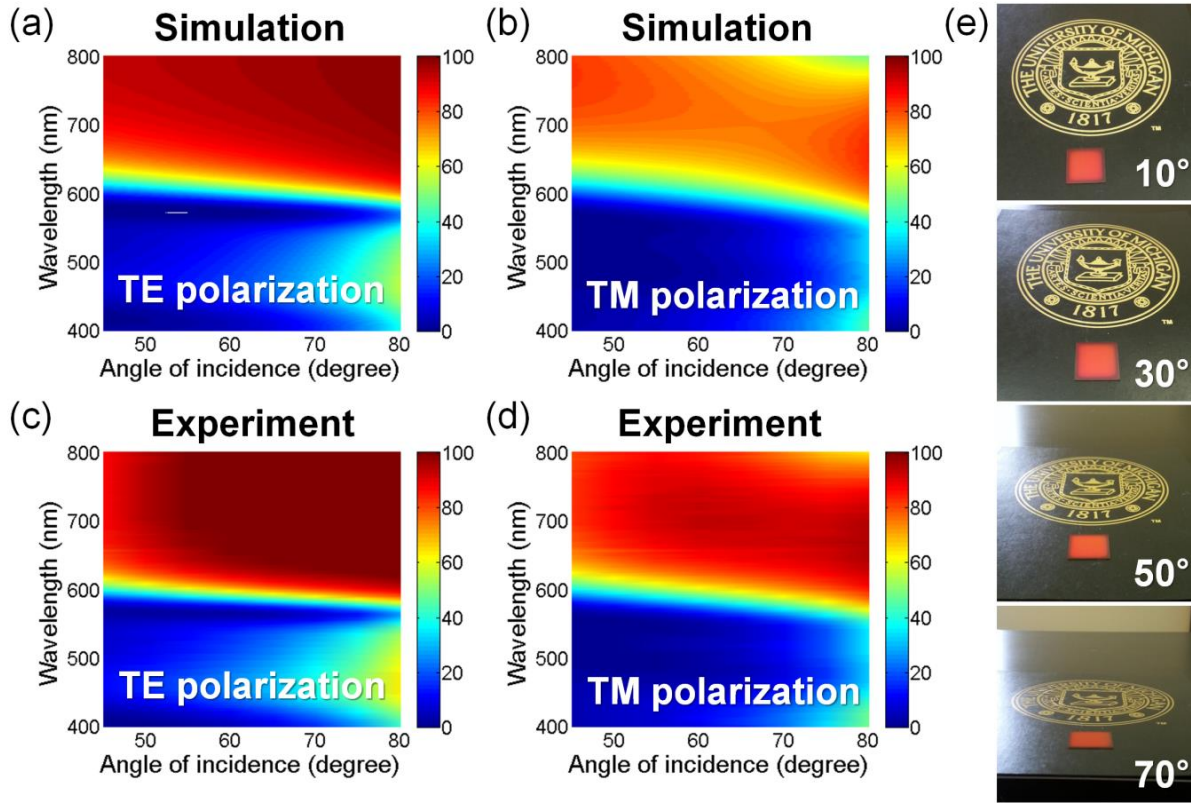
Figure 2.2.6 (a) – (b) Calculated angle-resolved reflection of the designed structural red for TE and TM polarizations. (c) – (d) Corresponding measured angular performance for both polarizations. (e) Optical photographs of the fabricated red device with a black background at different observing angles under the ambient light illumination.

2.3 Reflective Colors Based on Higher-Order Resonances (A Simpler Design)

Considering the significant influence of the layer number on the manufacturing cost, simpler structural

designs with reduced layers are still demanded to further lower the manufacturing cost, which is a decisive

factor affecting in the feasibility for the mass-production [15, 105]. In this section, we demonstrate a penta-

layer structure that can produce wide-angle, polarization-insensitive, and high-purity reflective colors

viewed from both sides of the structure. The designed structure presents a high-purity performance that

arises from a steep reflection exploiting the higher-order cavity resonance and suppressed sideband

reflections with a top AR layer and a symmetric transmission-inducing stacks beneath. Due to the high index materials utilized in the device structure, angle-invariant appearance can be maintained up to ±60° for TE and TM polarizations from both illumination directions, which enables color pigment applications. The simple design approach can be easily realized using a single deposition step, which holds the potential for various applications, including color displays and optical decorations at low cost over large areas.
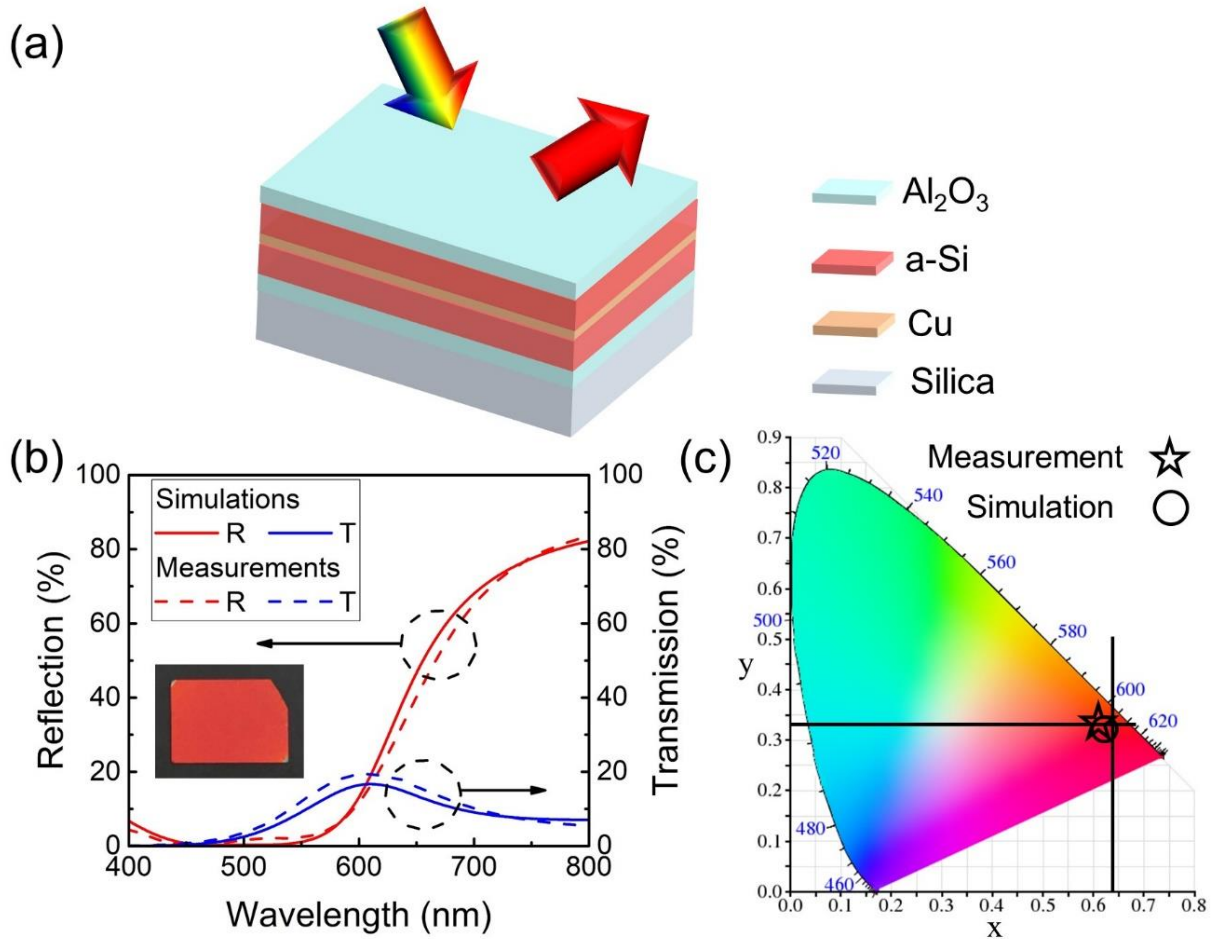
Figure 2.3.1 (a) A schematic diagram of a proposed symmetric structure for high-purity reflection colors. (b) Calculated (solid lines) and measured (dashed lines) reflection (red) and transmission (blue) spectra of the proposed device at normal incidence. The inset shows a photograph of a fabricated sample on a black paper, which presents a bright and pure red reflective color. (c) An illustration of color coordinates calculated from the reflection spectra in Figure 2.3.1(b) on the CIE 1931 chromaticity diagram. The crossing point of the two black lines represent the standard red coordinate (0.64, 0.33) utilized in LCDs.

Figure 2.3.1(a) depicts a schematic view of the proposed structural color filter consisting of five thin-film layers in a symmetric configuration on a silica substrate, which can create angle-

insensitive and polarization-independent reflective colors from both directions. A 30 nm thick copper (Cu) is sandwiched by two stacks of alternating alumina (Al_2O_3)/a-Si layers with the thicknesses of Al_2O_3 and a-Si being 65 and 95 nm, respectively. All materials are deposited on a silica substrate using a sputtering system (Lab 18, Kurt J. Lesker Company). Cu is selected as a metallic layer owing to its abundance (*i.e.*, low cost) and its intrinsic absorption characteristics at the short wavelengths, the latter of which is preferred for highly-saturated red color generation. A higher-order cavity resonance is generated inside a thick a-Si layer, which provides a sufficient absorption and enables a steeper reflection. Al_2O_3 functions as an effective AR layer to further suppress the unwanted reflections. Both a-Si and Al_2O_3 contribute critically to the final high-purity reflection. Detailed analysis of the functions of Al_2O_3 and a-Si layers will be discussed in the following paragraphs. It is worthwhile noting that green and blue colors can also be achieved with the proposed structure by simply adjusting the thickness of each layer while the reflection intensity may be lower due to the material absorption in the short wavelength range (as shown in Figure 2.3.2). Figure 2.3.1 (b) provides calculated reflection and transmission spectra (solid lines) of the designed structure at normal incidence, presenting a good agreement with measured profiles (dashed lines). The reflection below 600nm is greatly suppressed and a peak reflection over 80% is achieved at the long wavelength, both of which are responsible for producing the high-purity red color as presented in an inset image of Figure 2.3.1 (b). It should be noted that the fabricated device in the inset of Figure 2.3.1 (b) is placed on a black paper to avoid the interference of the transmitted light. Color coordinates are evaluated from the calculated and the measured reflection under the standard Illuminant D65 and described on the CIE 1931 chromaticity diagram (*i.e.*, the 2° standard observer) in Figure 2.3.1 (c). As can be seen from the figure, the color coordinates of both the simulated (0.62, 0.32) and the measured (0.61, 0.34) results are very close to the standard

red (0.64, 0.33) utilized in LCDs. All the simulations are performed based on transfer matrix method with refractive indices of materials measured using the spectroscopic ellipsometer, which are presented in Figure 2.3.3.
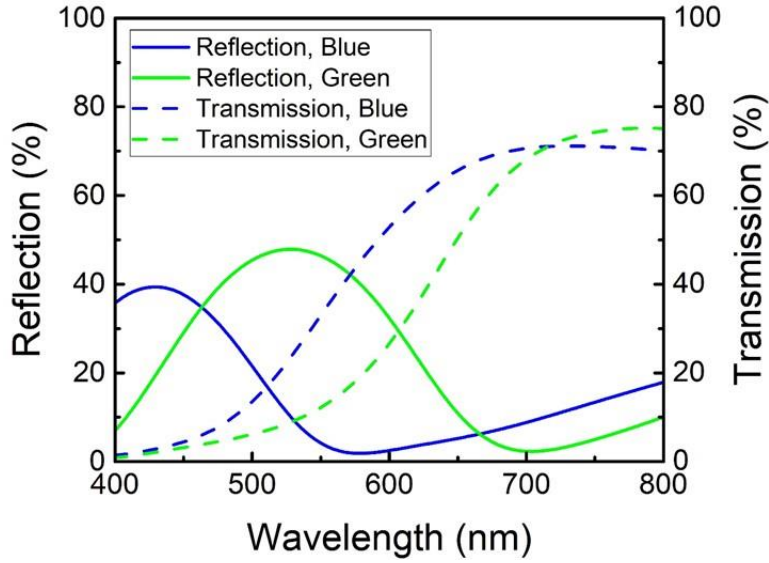
Figure 2.3.2 Simulated reflection and transmission spectra for green and blue colored devices. The configurations are designed as 'Silica substrate/130 nm Al_2O_3/40 nm a-Si/15nm Cu/40 nm a-Si/130 nm Al_2O_3' for the blue color and 'Silica substrate/160 nm Al_2O_3/55 nm a-Si/15nm Cu/55 nm a-Si/160 nm Al_2O_3' for the green color.
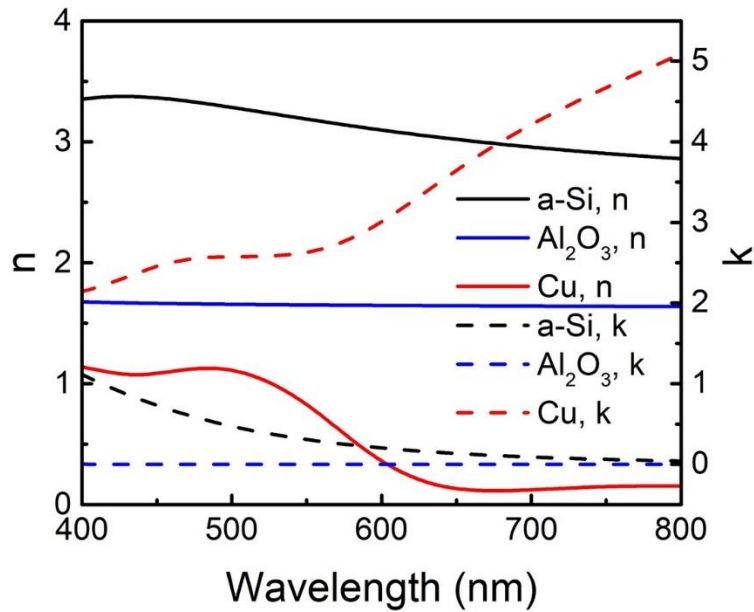
Figure 2.3.3 Refractive indices of Al_2O_3, a-Si, and Cu measured using a spectroscopic ellipsometer (M-2000, J. A. Woollam).

21

When adding the 95 nm thick a-Si on top of the Cu layer, the reflection below 600 nm, especially between 500 and 600 nm, gets significantly reduced (blue dotted curve) by exciting an absorption resonance inside the lossy a-Si as shown with the red dashed curve in Figure 2.3.4 (a). However, due to the large index contrast between a-Si and the incident medium (*i.e.*, air), a considerable amount of reflection still exists within the short wavelength range. The additional 65 nm thick Al_2O_3 is added on top of a-Si and functions as an effective AR layer to further suppress the remaining sideband reflection. This is achieved by ensuring near-perfect impedance match with air spanning from 400 to 600 nm (*i.e.*, the whole blue and green color range) as shown with the black solid curve in the plot. The absorption behavior inside the a-Si layer and the AR effects of Al_2O_3, which co-function to suppress the undesired reflection for the highly-pure color appearance, can be clearly explained by performing the phase analysis for these two layers. Both the absorption and AR resonances occur when the net phase shift, which includes two reflection phases at both the top and bottom interfaces and the propagation phase accumulated within the layer, equals to a multiple of 2π. As presented in Figure 2.3.4 (b), a 1st order absorption resonance is excited at 550 nm inside the top a-Si (the intersection point of the black dashed line and the blue dashed curve, *i.e.*, the resonance #1) and multiple AR resonances are created at 450, 505, and 590 nm within the Al_2O_3 layer (the intersection points of the black dashed line and the red solid curve, *i.e.*, the resonances #2, #3, and #4) to reduce the broadband reflection outside the red color range. The same phase analysis can be applied to the symmetric a-Si and Al_2O_3 stacks underneath the Cu layer. It is found out that the additional resonances inside the bottom two layers further improve the color purity to some extent by suppressing the short wavelength reflection with induced transmission as shown in Figure 2.3.5. Following the basic design principle of a F-P cavity, a thick (95 nm) a-Si layer is utilized here to achieve a sharper reflection spectrum by exciting a higher

order resonance, which is desired for a pure color generation [117]. As presented in Figure 2.3.4 (c), the reflection spectrum of the structure employing the 1st order absorption resonance (the black solid curve) shows a much steeper slope than that of the design exciting only the fundamental absorption resonance (*i.e.*, the zero-order resonance). It should be noted that the thickness of the a-Si in the structure corresponding to the zero-order resonance at ~550 nm is 8.1 nm and the order of the absorption resonance is confirmed by calculating the net phase shift inside the a-Si layer, which is equal to 0 as presented in Figure 2.3.4 (d). On the other hand, the thick a-Si layer absorbs more short-wavelength light below 600 nm compared to the thin a-Si structure, thereby generating the final pure reflection color, which is illustrated by the absorption spectra in Figure 2.3.4 (c).
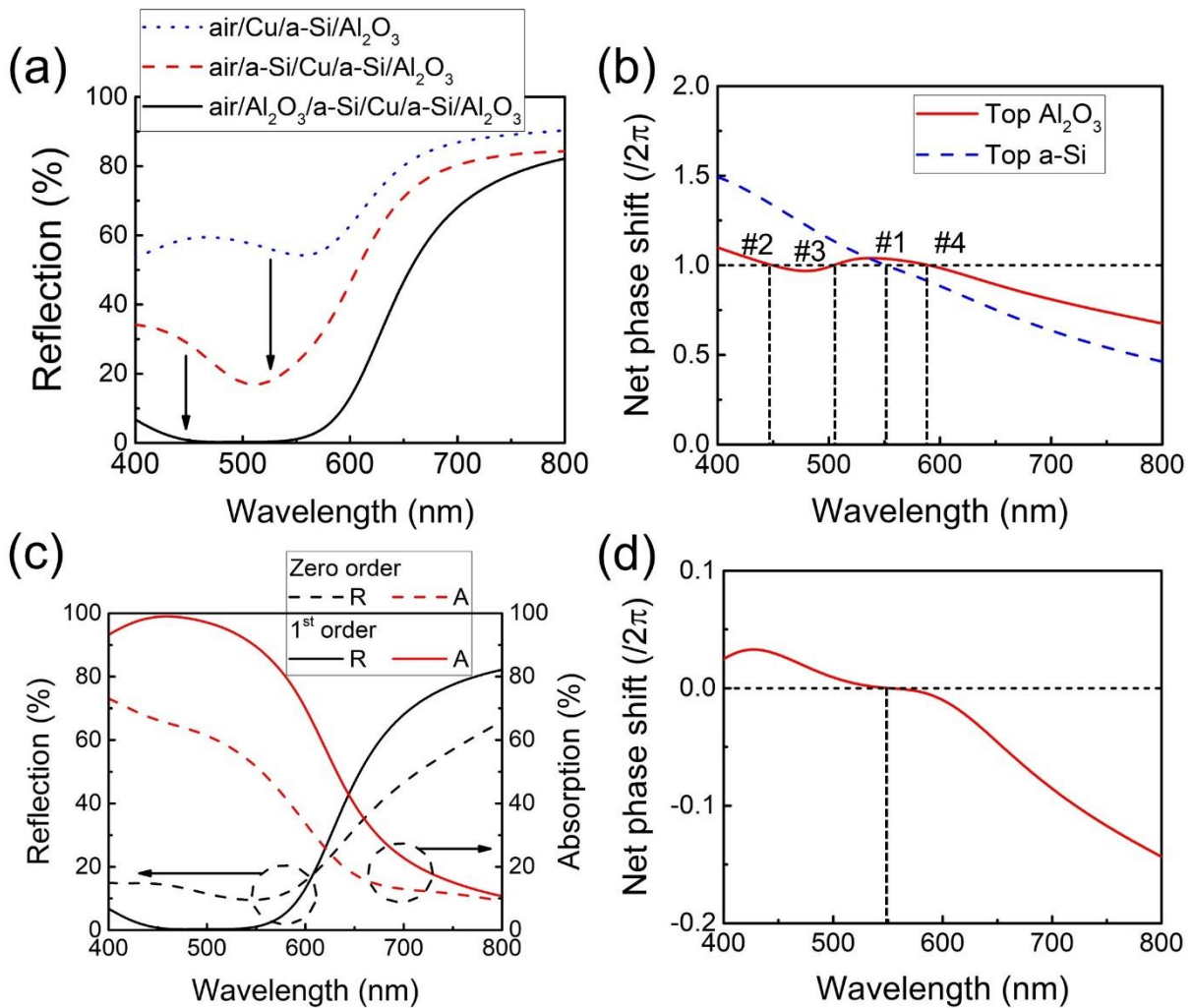
Figure 2.3.4 (a) Calculated reflection spectra of the structures without top a-Si and Al_2O_3 layers (blue), with top a-Si only (red), and with both a-Si and Al_2O_3 atop (black), showing the effect of a-Si and Al_2O_3 layers on how to suppress the reflection in the short wavelength regime to create a high-color-purity red color. (b) Phase analysis of top a-Si and Al_2O_3 layers. Both the absorption resonance inside a-Si and the AR resonances within Al_2O_3 occur when the net phase shift is equal to a multiple of 2π. (c) Calculated reflection and absorption spectra of the structures based on the higher-order (1st order) and fundamental (zero order) absorption resonances. (d) Phase analysis of the thin a-Si layer in the structure generating the zero-order absorption resonance at ~550 nm inside the a-Si. The thickness of the a-Si is 8.1 nm. The absorption resonance is denoted as the zero order as the net phase shift is equal to 0.
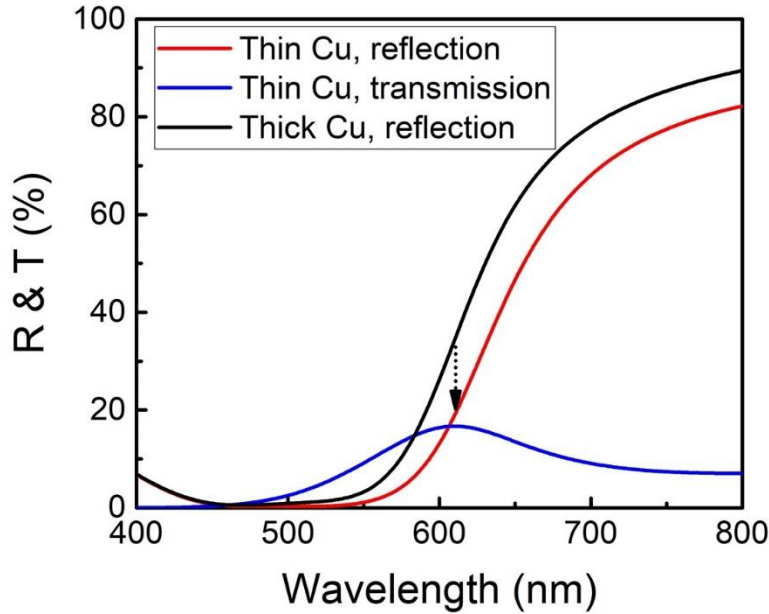
Figure 2.3.5 Reflection and transmission spectra of the structures employing 30 nm thin Cu with symmetric a-Si/Al_2O_3 stacks beneath and 100 nm thick Cu, where the thick metal in the latter case blocks any transmission. The a-Si/Al_2O_3 layers further enhance the red purity to some extent by pushing the reflection spectrum towards longer wavelengths with the induced transmission within the short wavelength range.

The AR function of the Al_2O_3 layers can be validated by studying an optical admittance ($Y = \sqrt{\varepsilon / \mu}$) of the structure (as provided in Figure 2.3.6).). It is clear that the reflection within the short wavelength range (@400, 500, and 600 nm) is effectively suppressed after adding the Al_2O_3 AR layers, which is represented with black solid lines in the plots with AR layers compared to those without AR coatings, thereby enhancing the reflection color purity.
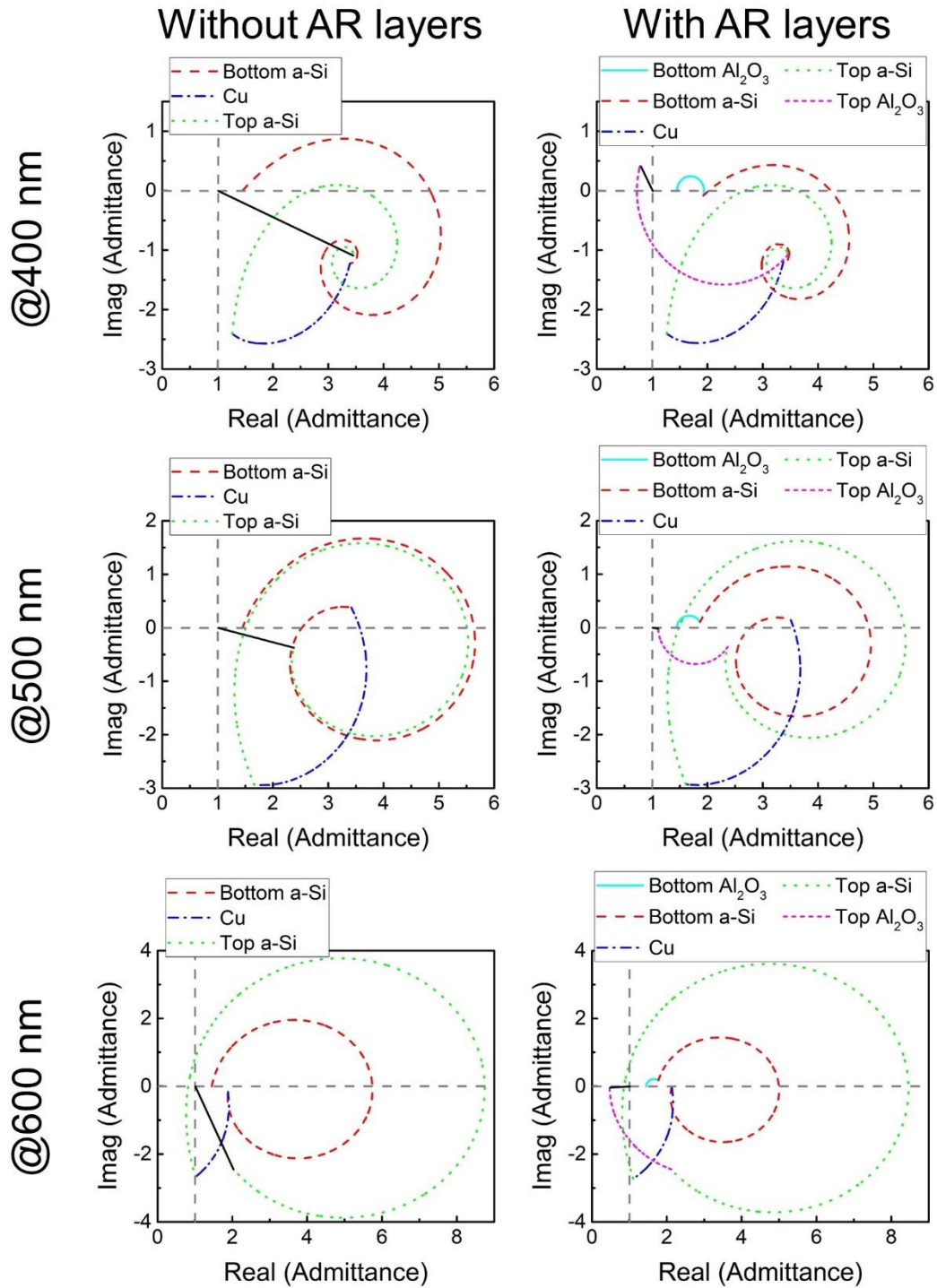
Figure 2.3.6 Admittance diagrams of the structures without (left) and with (right) the AR layers at 400 (the 1st row), 500 (the 2nd row), and 600 nm (the 3rd row). A black solid line between a termination point and air (1, 0) represents how high reflection is at normal incidence.

Figure 2.3.7 (a) and (b) provide calculated angle-resolved reflection spectra for TE and TM polarizations, which are in excellent agreement with measured results using the spectroscopic ellipsometer as exhibited in Figure 2.3.7 (c) and (d), showing flat dispersion curves. Such angle- and polarization-insensitive characteristics are attributed to the constituent material with high refractive index, which is highly desired in diverse applications [15, 105]. The color change with the incident angle up to 60° is displayed on the CIE 1931 chromaticity diagram in Figure 2.3.7 (e). The closely-located color coordinates at different incident angles further prove the excellent angle-robust performance. Figure 2.3.7 (f) presents photographs of the fabricated sample taken at different observing angles on a black background to prevent the reflection, showing a negligible color variation even at large angles.
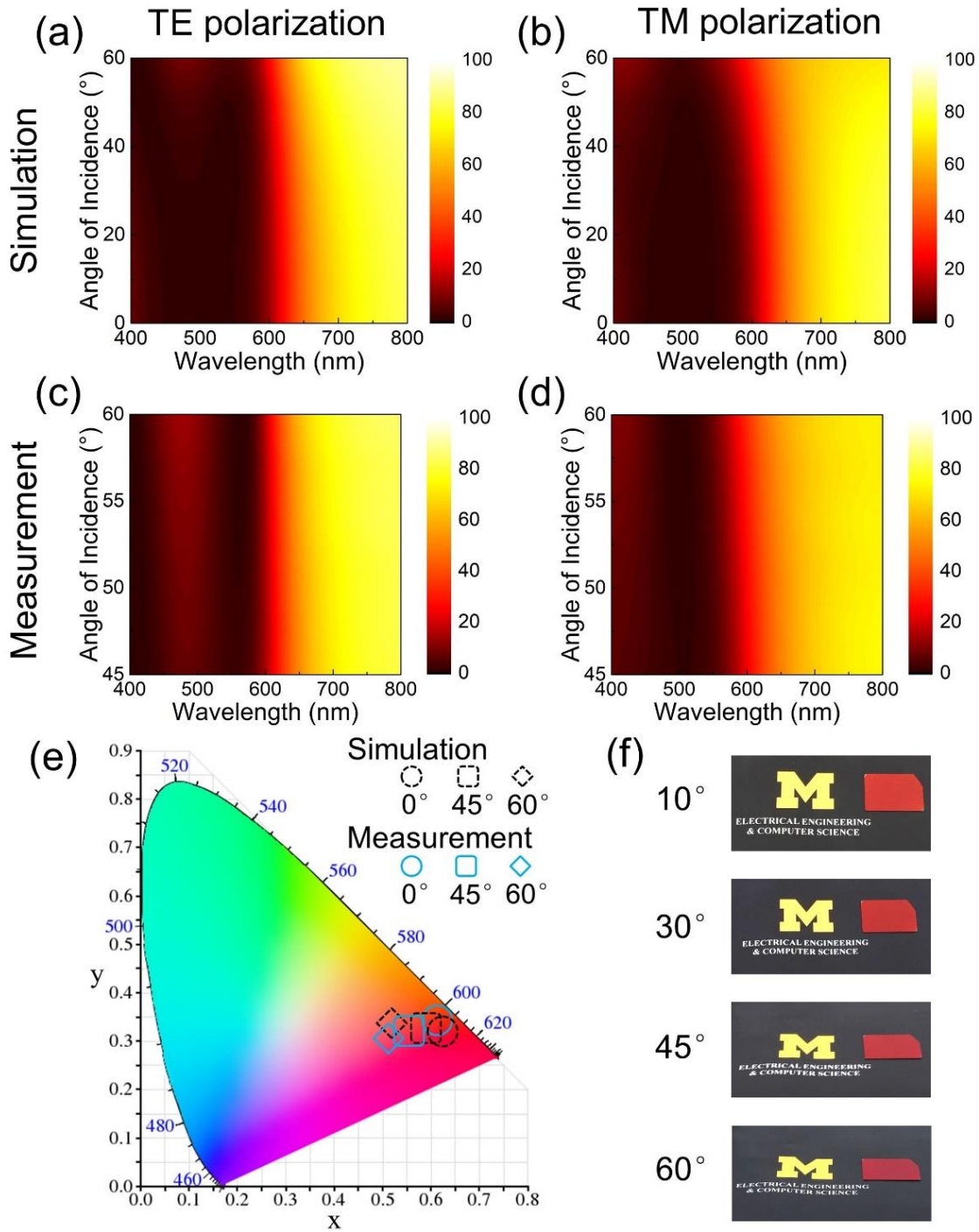
Figure 2.3.7 (a) and (b) Simulated angle-resolved reflection spectra under TE and TM polarizations. (c) and (d) Measured angular dependences corresponding to those in (a) and (b). (e) Visualization of color change with the incident angle on the CIE 1931 chromaticity diagram. Color coordinates at different incident angles are calculated from the reflection spectra of unpolarized light under Illuminant D65. (f) Optical images of the fabricated red color filter taken with the ambient light at different oblique angles of incidence. The distinctive red color is preserved at non-normal angles up to ±60°.

2.4 Conclusion

In summary, novel approaches have been demonstrated for the distinctive reflection color generation based on 1D layered structures. By adopting a symmetric configuration and high refractive index materials, the whole stacks display excellent angle-invariant performance with bi-directional functionality, both of which are highly pursued in color pigments. Only deposition method is involved for the device fabrication, thus opening up new possibilities for mass production employing R2R deposition tools at lower cost over large areas. Toyota Research Institute of North America (TRINA), with whom we collaborated on the red color filters, has applied their design of structural blue colors for the next generation vehicle paints [118].

Chapter 3

Facile Solution Processing of Angular-Insensitive Structural Colors

3.1 Introduction

Although the layered configurations for the structural colors described above are feasible for mass production compared to other previously-reported designs involving complicated nano-patterns, the high manufacturing cost is still an obstacle that will hinder their wide applications in decorative paints. A large portion of the cost comes from the expensive vacuum systems as well as the fees required for the equipment maintenance and electricity consumption.

In this chapter, we present a vacuum-free approach for structural colors via electroplating. The design is based on a tri-layer asymmetric MDM configuration, where both the top thin and the bottom thick metals are fixed, and the thickness of the sandwiched dielectric can be adjusted for different color generation. Similar to those designs proposed in the previous chapter, the generated reflective colors here are also insensitive to incident angles due to the high refractive index of the middle layer (Cu_2O). To the best of our knowledge, this is the first demonstration of multilayered

29

structure colors achieved via an all-solution process, which may lead to more applications of structural colors with easier fabrications and lower manufacturing costs.

3.2 Design Principle and Results

Figure 3.2.1 (a) shows a schematic of the solution-processed structure color with Au/Cu$_2$O/Au three layers subsequently deposited on a Si (111) substrate with a 0.5° miscut angle. Both of the crystalline orientation and the small miscut of the Si wafer is preferably select to guarantee the high smoothness of the whole stack, which will be discussed in detail in the following descriptions. The thickness of the middle Cu$_2$O is adjusted for cyan (70 nm), magenta (45 nm), and yellow (20 nm) colors by exciting absorption resonances at different positions, and the bottom and top Au layers are fixed as 40 and 15 nm, respectively. Essentially, this method proposed in this work is applicable to different conductive surfaces regardless of their smoothness and shapes. Measured reflection spectra (dashed curves) of CMY devices are provided in Figure 3.2.1 (b), which are in great consistency with simulated results (solid curves). The insets are the photographs of fabricated devices, showing distinct CMY colors as designed. The simulation is performed based on the transfer matrix method with the refractive indices (provided in Figure 3.2.2) and thicknesses of Au and Cu$_2$O layers characterized using a spectroscopic ellipsometer (M-2000, J. A. Woollam).
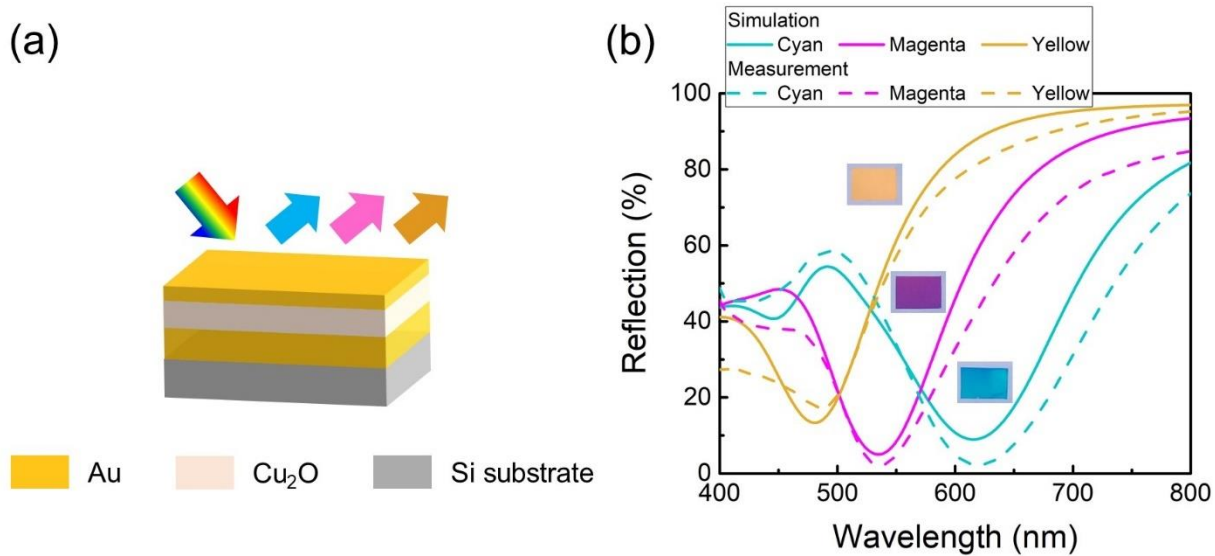
Figure 3.2.1 (a) A schematic diagram of the structural color deposited by electroplating on a Si substrate. (b) Measured and calculated reflection spectra of CMY colored devices, showing great consistency with each other. Insets are photographs of fabricated CMY samples. The size of each sample is 1.5 cm × 1.0 cm.
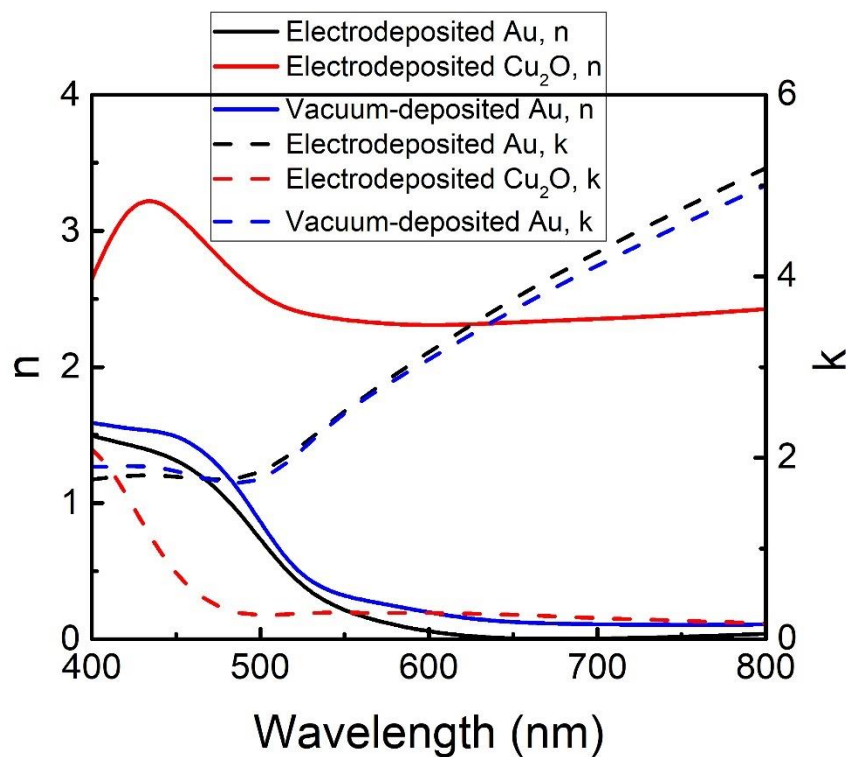
Figure 3.2.2 Refractive indices of electrodeposited Au and Cu_2O, and thermally evaporated Au measured with the ellipsometer.

Using the magenta colored device as an example, the cross-section scanning electron microscopy (SEM) in Figure 3.2.3 (a) verifies the thickness of each layer, which is very close to the design presented in Figure 3.2.1 (b). Both the thickness variation during deposition and the surface roughness of electrodeposited films lead to the slight discrepancy between the measurement and simulation as depicted in Figure 3.2.1 (b). Figure 3.2.3 (b) gives out the net phase shifts within the Cu_2O layer of all three devices, clearly indicating the absorption resonances (@458 nm for yellow, @531 nm for magenta, and @618 nm for cyan where the net phase shift is equal to 2π) that selectively absorb light in the visible range for the reflective color generation.
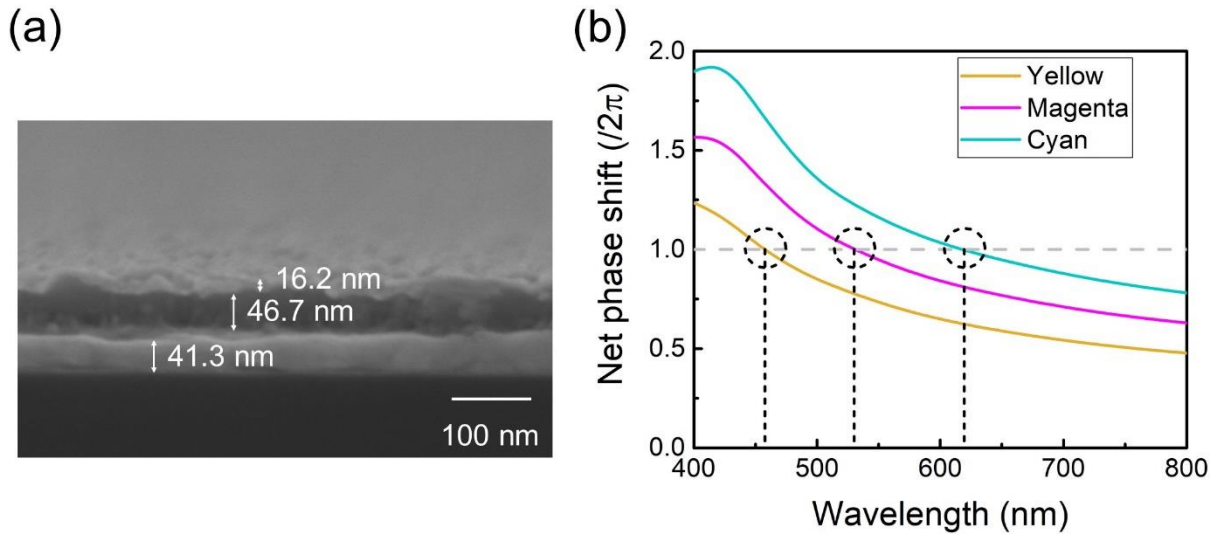
Figure 3.2.3 (a) Cross-section SEM image of the magenta colored devices, verifying the thickness of each layer. (b) Net phase shift analysis of CMY colored devices. Absorption resonances that result in the reflection valleys for the color generation occur when the net phase shift is equal to 2π.

The electrodeposition of the metal and dielectric layers of the MDM stack were performed using a standard three-electrode electrochemical cell as shown in Figure 3.2.4 (a). For Au deposition, a stock solution of 0.1 mM chloroauric acid ($HAuCl_4$), 1 mM potassium chloride (KCl), and 100 mM potassium sulfate (K_2SO_4) was prepared in DI water. For the electrodeposition solution, a portion of this stock solution was separated and 1 mM H_2SO_4 was added to it to adjust the pH to

~3. Computer controlled potentiostat (CHI760C, CH Instruments) was used for the electrodeposition. A platinum mesh and a silver chloride (AgCl)-coated Ag wire immersed in saturated KCl and sealed behind a glass frit were employed as the counter and reference electrodes, respectively. Ohmic contact to the Si wafer was made by applying eutectic gallium indium (GaIn) to the tip of the wafer and clipping the working electrode of the potentiostat to this region. The Si substrate was prepolarized by applying a potential of $E = -1.9$ V versus Ag/AgCl and was then immersed into the solution in the beaker. This prepolarization step is necessary to avoid electroless plating of Au and the formation of a native oxide layer on Si that could prevent epitaxial Au growth. From cyclic voltammograms performed using Si substrates in the aqueous solution, it is seen that Au electrodeposition occurs in the potential range of $-2 < E < -1$ V versus Ag/AgCl and the deposition rate is fairly constant in this voltage range. An electrodeposition potential of $E = -1.9$ V versus Ag/AgCl gives the best results for this solution since the hydrogen evolution reaction (HER) is enhanced at these potentials, which plays a very important role in enhancing the Au/Au mobility and maintaining layer-by-layer 2D growth of the Au film [119, 120]. The growths performed for 50 minutes at 35 °C and a stir rate of 200 rpm yielded uniform 50 nm thick Au films. The electrodeposition rate can be increased by increasing the concentration of the precursor in solution while adjusting for the pH. Figure 3.2.4 (b) shows atomic force microscopy (AFM) measurements of electrodeposited Au on a Si (111) substrate. The electrodeposited Au is ultra-smooth with a root-mean-square (RMS) roughness of only ~1.4 nm and the characterized refractive index is very similar to that of thermally evaporated Au as compared in Figure 3.2.2, both of which indicate the high quality of the electrodeposited thin Au films.

Although electrodeposition of materials generally results in conformal coatings, the electrodeposited films are generally rougher than those deposited using vacuum systems, unless

appropriate care is taken. Since all three layers are electrodeposited, the roughness is expected to gradually increase from the bottom to the top film. Epitaxial growth of ultra-smooth Au is achieved on the bottom to reduce the roughness of the subsequent dielectric and metal layers and thus, the overall device roughness by using degenerately doped n-type Si (111) substrates, which guarantee both vertically directional growth and small coincidence site lattice mismatch between Au and Si atoms [121, 122]. In addition to the Si (111) orientation, the staircase structures of substrates with a small (0.5°) miscut also contribute to the electrodeposition of smooth Au thin films by functioning as numerous nucleation sites [119]. The wafer substrates were degreased by sequentially sonicating for 5 minutes each in acetone, methanol, isopropyl alcohol, and water, and then dried under a nitrogen (N_2) gas stream. The following protocol was followed to create a hydrogen (H)-terminated Si surface: the native oxide was etched by immersing the substrates in 5% hydrofluoric acid (HF) for 30 seconds and the substrates were soaked in DI water at 95 °C for 20 minutes to create a fresh silicon oxide (SiO_x) passivating layer. The Si substrates were then etched in 5% HF for 30 seconds and buffered HF for 30 seconds to create the H-terminated Si surface. The samples were immediately cleaned in deionized (DI) water and dried under a N_2 stream for the electrodeposition.

Cu_2O was electrodeposited from alkaline Cu(II)-citrate solutions [123]. An aqueous solution of 0.4 M copper(II) sulfate pentahydrate ($CuSO_4 \cdot 5H_2O$) and 1.6 M citric acid was prepared and sodium hydroxide (NaOH) was slowly added to this solution to raise the pH to ~10.9. A platinum mesh counter electrode and a mercury sulphate reference electrode (MSE) were employed in the three-electrode cell. The Au-coated Si (111) substrates obtained above were used as the working electrode and immersed into the solution beaker without the prepolarization step. By controlling the cathodic current density, Cu_2O can be deposited through the following reactions [124]:

$$[Cu_2H_{-2}Cit_2]^{4-} + 2e^- + H_2O = Cu_2O + 2Cit^{3-}.$$
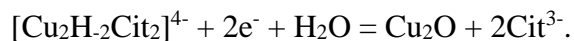
Electrodepositions performed with a cathodic current density of 0.05 to 0.1 mA/cm^2 at 50 °C and a stir rate of 200 rpm result in uniform Cu$_2$O electrodeposition (~0.05 – 0.1 nm/s). A potential of -0.6 to -0.85 V versus MSE was measured during the Cu$_2$O electrodeposition. Ellipsometry measurements were performed on these films to extract the refractive index (Figure 3.2.2). Cu$_2$O films of different thicknesses for the cyan, magenta, and yellow samples were deposited by altering the electrodeposition time and maintaining all other parameters constant. AFM measurements of Cu$_2$O on the previously electrodeposited Au is shown in Figure 3.2.4 (c). As expected, the RMS roughness (~45 nm Cu2O for the magenta color is used as an example) increases to 4.2 nm, but nonetheless these films are still smooth and possess a mirror-like appearance.
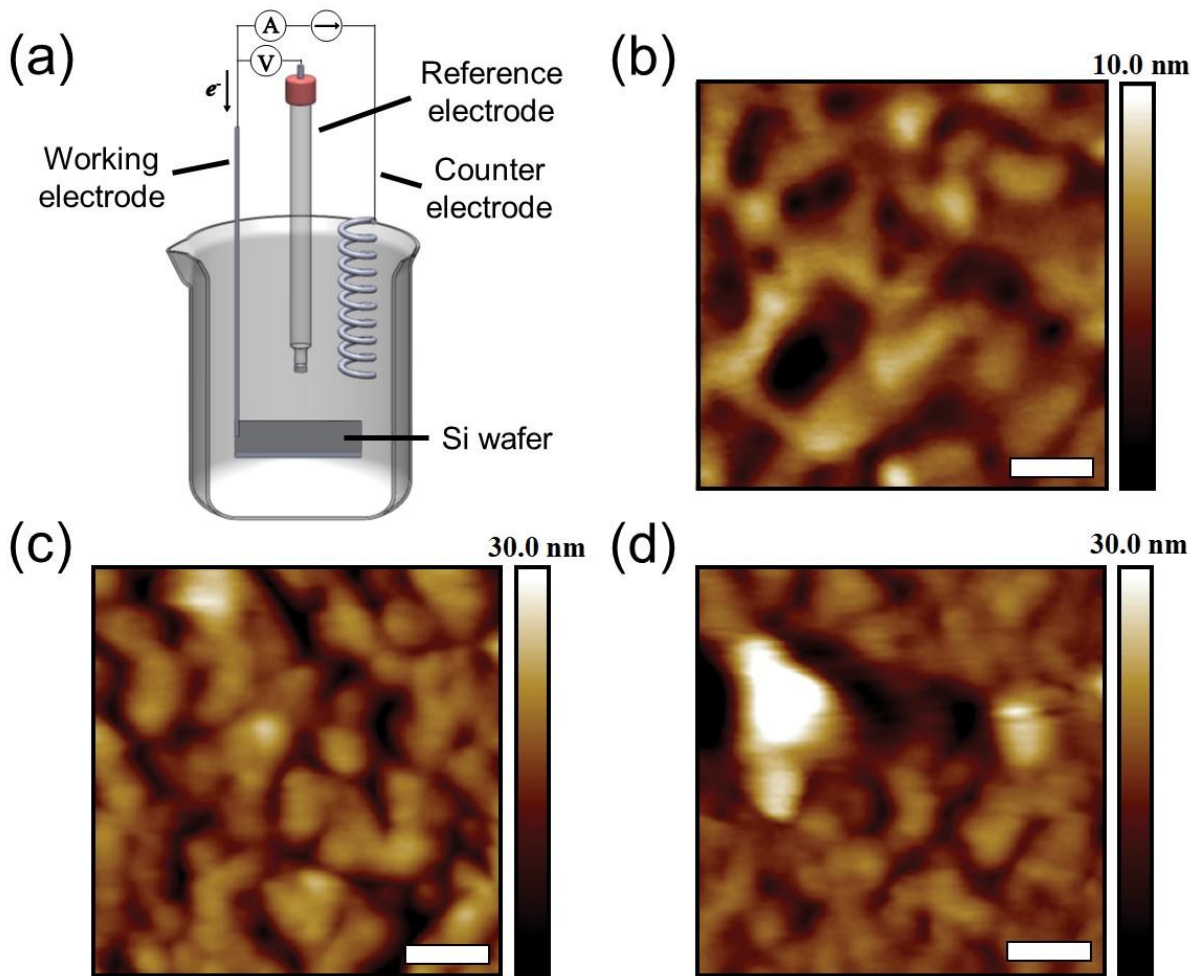
Figure 3.2.4 (a) A schematic diagram of the three-electrode electrochemical cell used for the electrodeposition of MDM structures. AFM measurements of (b) the bottom Au, (c) Cu_2O/Au, and (d) final Au/Cu_2O/Au on Si (111) substrates. The scale bars denote 100 nm.

Electrodeposition of the top metal layer of our tri-layer stack is the trickiest since we require it to be ultrathin (<20 nm) and ultra-smooth, while also ensuring that the electrodeposition conditions does not etch the underlying Cu_2O layer. The pH ~3 electrodeposition solution used for the bottom Au film is not a viable option since the Cu_2O film gets etched in the acidic solution. For this reason, a Au-precursor containing basic solution was used for electrodepositing the top Au layer. A portion of the stock solution prepared for the bottom Au electrodeposition was separated and its pH was adjusted to ~10 by addition of NaOH [120]. Similar to the pH ~3 solution used above, the cyclic

voltammetry of this solution indicates Au electrodeposition proceeds within a wide potential range of approximately $-2.5 < E < -1.1$ V versus MSE. Even though HER is suppressed using basic solutions as compared to acidic solutions for the potential range mentioned above, electrodeposition at $E = -2.2$ V versus MSE produces smoother films compared to electrodeposition at $E = -1.1$ V versus MSE due to increased HER at the higher cathodic potential. However, for our purposes, electrodepositions performed at $E = -2$ V versus MSE on Si substrates containing the Au/Cu$_2$O films resulted in peeling off the bi-layer films due to H$_2$ gas bubble formation. Thus, the top Au layer (~15 nm thick) was electrodeposited using the pH ~10 solution at $E = -1.1$ V versus MSE, 35 °C, and a stir rate of 200 rpm. The AFM of the MDM structure after the top metal electrodeposition is provided in Figure 3.2.4 (d). The top metal electrodeposition does not significantly increase the roughness of the tri-layer stack (RMS roughness ~5.3 nm) as compared to that of the bi-layer Cu$_2$O/Au stack on Si, although there are domains of increased 3D Au growth that appear as ~100 nm sized particles with a thickness of 30 nm in the AFM of the top Au layer. This is a direct consequence of the reduced electrodeposition potential, which consequently suppresses the HER.

Figure 3.2.5 (a) – (c) present the measured angle-resolved reflection spectra under unpolarized light, which are in great match with the calculated results displayed in Figure 3.2.5 (d) – (f). It is evident that the reflection valleys (*i.e.*, the absorption resonances) are almost invariant with respect to the incident angle up to 60°. This angular-insensitive performance is due to the high refractive index of the cavity material Cu$_2$O, which leads to a very small refracted angle into the structure. In Figure 3.2.5 (g), the photographs of the fabricated CMY samples taken at various angles under ambient light clearly validate the highly-desired angle-robust appearance.
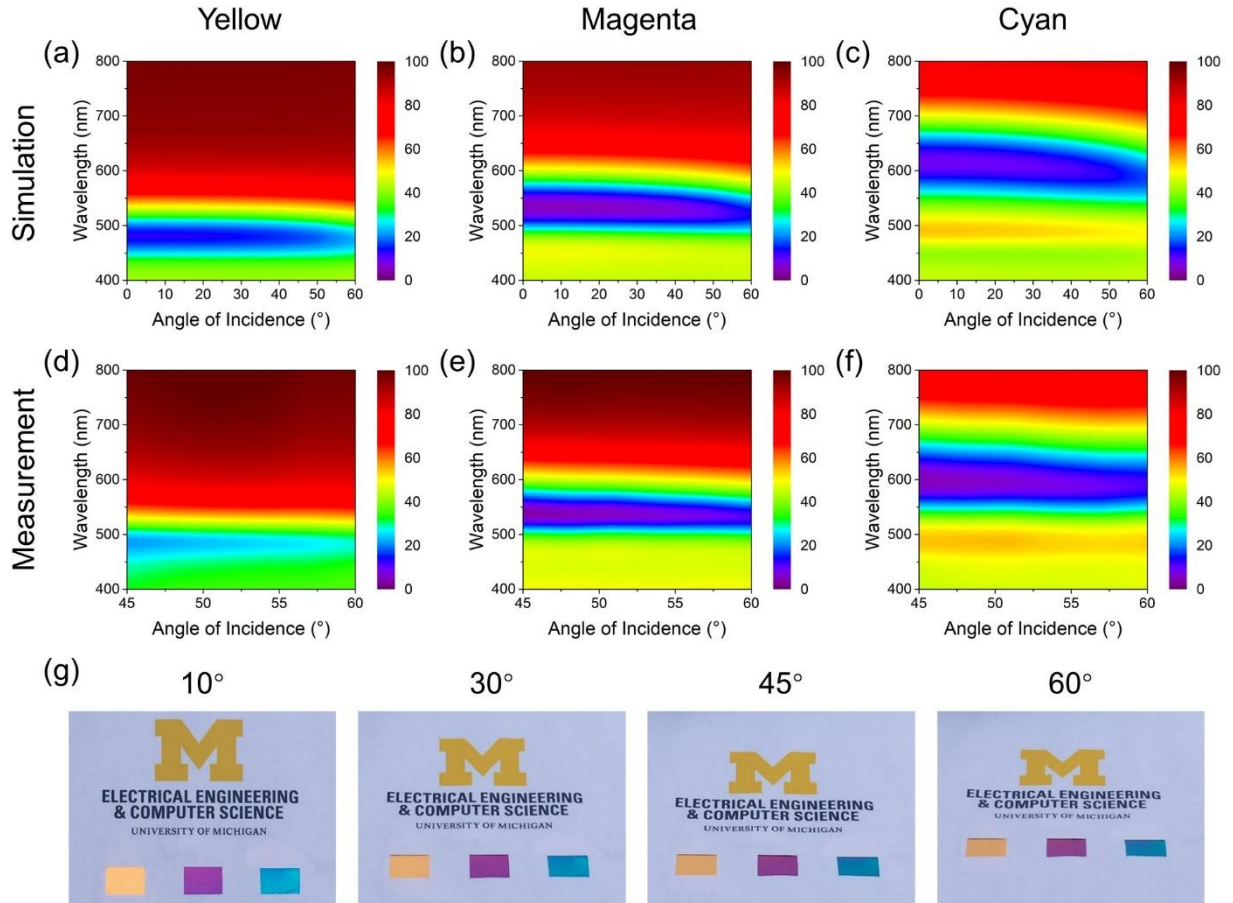
Figure 3.2.5 (a) – (c) Simulated angle-resolved reflection spectra of CMY colored structures under unpolarized light illumination. (d) – (f) Corresponding measured angle-resolved reflection of fabricated devices. (g) Photographs of fabricated CMY samples taken at various observation angles, showing the great angle-invariant performance. The sample size is 1.5 cm × 1.0 cm.

3.3 Conclusion

In summary, a novel and facile method for structural colors employing all-solution electroplating has been demonstrated. The structure is designed based on an asymmetric MDM F-P resonator. The thickness of the sandwiched dielectric layer can be tuned for generating various colors. Due to the high refractive index of the cavity material, stable colored appearance can be observed up to ±60°, which is highly-pursued in many decoration applications. Without using any vacuum deposition, the fabrication cost of large-scale device is expected to be greatly reduced, which enables more uses of structural colors at an affordable cost.

Chapter 4

Highly-Efficient and Angular-Robust Colored Solar Panels

4.1 Introduction

Special attention has been paid to only the reflection of the structures in above discussions for decoration applications. Transmission is ignored (wasted) by either being absorbed with lossy semiconductors or blocked with thick metals. Structural colors that present distinctive colored appearance and simultaneously transmit light within a certain wavelength range are also highly desired in a wide variety of applications. For instance, trans-reflective color filtering devices featuring narrowband reflective colors and broadband transmission spanning the whole solar spectrum can be used for decorating traditional solar panels while maintaining their high power conversion efficiency (PCE).

Decorative solar cells have received considerable interest over the past decades due to their potential applications in building integrated photovoltaics (BIPVs) and automobiles to exploit the otherwise wasted energy [125-129]. Traditional solar panels, which typically include a very thick semiconductor layer to efficiently absorb incident light, is unsuitable for decorating vehicle and

building exteriors due to their black and dull appearance [130, 131]. Therefore, there is a strong need to develop multifunctional PVs that can offer aesthetic features.

Various approaches, including dyed sensitized solar cells (DSSCs) and organic PVs (OPVs), have been utilized to create colored solar cells [132-142]. However, their color purity and tunability are heavily limited by available dyes and organic materials. Moreover, those organic devices have lifetime issues due to the material degradation especially after long-time exposure to moisture, oxygen and ultraviolet radiation. Recently, a scheme of integrating color filters with PV panels has been developed to simultaneously create colored appearance and electric power via spectrum-selective absorption [95, 97, 136, 137, 141, 143-145]. However, the color filters involved in those solar cells either based on F-P cavities or plasmonic resonances produce colors that will vary with viewing angles and incidence light polarizations, which are undesirable for the decorative applications. In addition, those nano-structured plasmonic colors are difficult to be scaled to practical large areas. To solve all the aforementioned issues, layered a-Si hybrid solar cells featuring angular and polarization insensitive colors have been proposed [109, 146, 147]. The non-iridescent colored appearance can be credited to the nontrivial reflection phase change at the a-Si/metal interface, which consequently compensates the propagation phase of light propagating through the ultrathin semiconductor layer (<30 nm) [108, 148, 149]. However, the PCE for the colored PV panel is significantly limited because only a small amount of light is absorbed. Most of the incident light gets reflected for generating subtractive colors generation (*i.e.*, cyan, magenta, and yellow (CMY) colors), which adversely affects both the electric performance and color purity. Creating narrowband RGB reflective colors while absorbing the remaining light spanning a broadband range is of vital importance in achieving pure and efficient colored solar cells [144, 150, 151].

In this chapter, we present a highly-efficient colored solar cell with high PCE employing a tandem configuration comprising a c-Si PV panel and a trans-reflective color filter atop [19]. Specifically, the blue device presents the highest PCE of ~13.9%, which corresponds to only ~3.9% decrease compared to initial c-Si panel, and the efficiencies of both green and red colored devices are also >10%. The color filtering device simply consisting of five layers exhibits a distinctive narrowband reflection (~60% reflection peak), where the high reflection is mainly attributed to the high-index a-Si semiconductor sandwiched between two stacks of transparent dielectrics. By avoiding using any reflective metals, the designed structures can transmit a large portion of solar spectrum onto the c-Si module beneath with a symmetric gradient index profile with respect to the middle a-Si layer, thereby achieving the overall high efficiency and final narrowband reflection by suppressing the undesired sideband reflection. In addition, the entire colored solar module presents a distinctive color with great angular insensitivity up to ±60° due to the high refractive indices of materials involved in the filter structure, which is highly pursued in decoration applications. This method providing great simplicity over traditional 1D PCs, which typically consist of tens of layers, can be readily applied for mass-production in the foreseeable future. Moreover, it is expected that the PCE can be further enhanced if adapting the passive filter into an active photovoltaic device by replacing the dielectrics with transparent electrodes and hole/electron transport layers, thus forming four-terminal PV devices [20]. Considering the overall high PCE and the simple implementation, the proposed approach could pave the way for various applications including innovative solar-harvesting coatings, solar buildings, and next-generation solar-powered cars.

4.2 Trans-reflective Filters with Broadband Transmission for Decorative Solar Cells

Figure 4.2.1 (a) shows a schematic diagram of the proposed highly-efficient colored solar cells, which integrate c-Si solar panels with decorative trans-reflective filters atop. The detailed configuration of the angle-invariant trans-reflective filter that can generate a distinctive reflection color as well as broadband high transmission is provided in the inset. As depicted in the plot, it consists of five layers on a silica substrate with a thin a-Si layer sandwiched between two stacks of transparent dielectrics (zinc selenide (ZnSe) / Si_3N_4) forming a symmetric graded index profile, which consequently results in remarkable transmission across the whole solar spectrum to be harvested by the c-Si PV beneath. As presented in Figure 4.2.1 (b), the high index of a-Si directly contributes to the final high reflection of designed colors with the peak reflections ~60% at different wavelengths, which is further elucidated in Figure 4.2.2 by comparing the reflection spectra of blue colored devices as an example employing materials of different refractive indices as the middle layer. Different reflection colors can be created by simply adjusting the thickness of each layer and the detailed configurations of the three colored devices are summarized in Table 4.2.1. It can be clearly observed that thicker films are required to generate reflection colors at longer wavelengths. As the a-Si refractive index decreases at longer wavelengths (as shown in Figure 4.2.3), the a-Si thickness employed in green and red colored devices are intentionally increased compared to the blue colored filter to maintain the high reflection intensity. The insets in Figure 4.2.1 (b) show the fabricated RGB colored samples on top of a c-Si solar panel under ambient illumination, exhibiting bright and distinctive colors at normal incidence. Figure 4.2.1(c) presents the efficient and broadband transmission spectra of all three devices and their high transparency can be clearly visualized with the inset photographs of fabricated samples. Both the reflection and transmission plots show the excellent consistency between the calculated and measured results, thus validating our design principles. All the calculations are performed based

on the transfer matrix method with the refractive indices of the materials characterized using a spectroscopic ellipsometer (M-2000, J. A. Woollam), which are provided in Figure 4.2.3 [152].
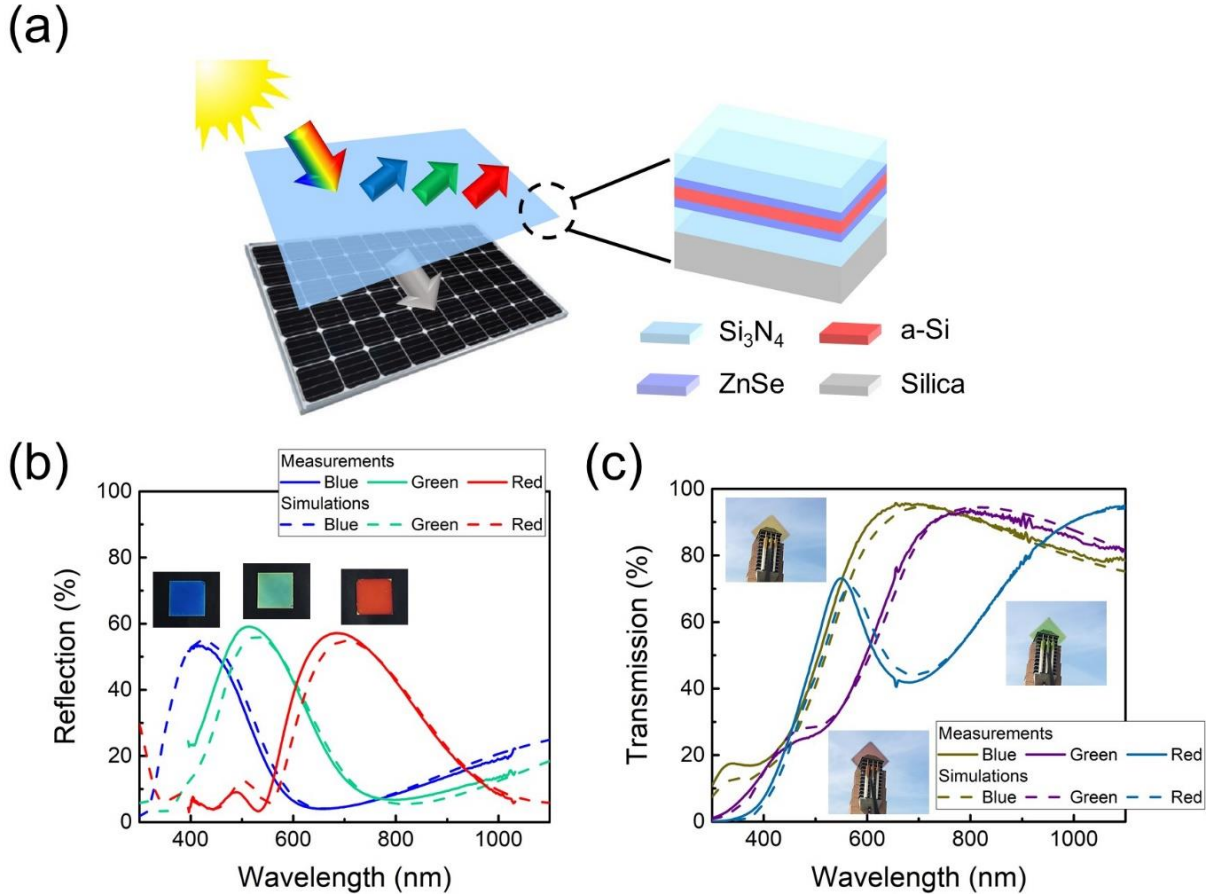
Figure 4.2.1 (a) The schematic diagram of the proposed highly-efficient colored solar cells. The angular-robust trans-reflective filter atop consists of 5 layers with the high index a-Si sandwiched between two stacks of dielectrics. (b) Simulated and measured reflection spectra of trans-reflective colored filters. Insets show the photographs of the fabricated RGB colored samples on top of a black c-Si solar panel. (c) Simulated and measured transmission spectra of trans-reflective colored filters. Inset photographs present the high transparency of fabricated trans-reflective samples.
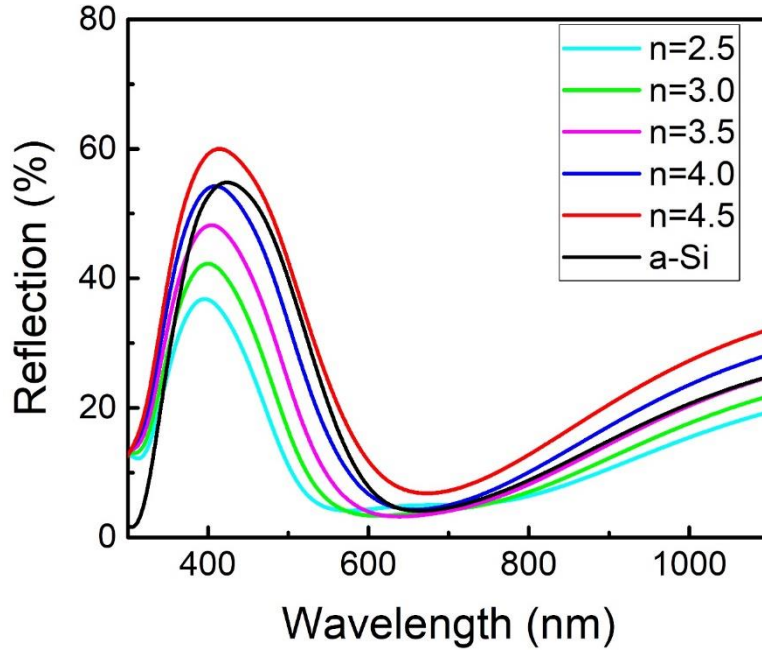
Figure 4.2.2 Reflection spectra of blue colored structures with the middle a-Si layer replaced by materials of different refractive indices. The thicknesses of all 5 layers remain the same in each case. We have ignored the dispersion of all those materials except a-Si ($n = 4.89 + i1.28$, peak intensity ~55% @424 nm). As can be seen from the plot, the peak reflection intensity remains in the blue color range and increases with the refractive index: ~37% @397 nm ($n = 2.5$), ~42% @400 nm ($n = 3.0$), 48% @404 nm ($n = 3.5$), 54% @409 nm ($n = 4.0$), 60% @414 nm ($n = 4.5$), thus validating that the high reflection is due to the high index of the middle layer as clarified in the main text. It is worthwhile noting that the structure employing a-Si as the middle layer does not present the highest reflection due to the material absorption at the short wavelengths although a-Si has the largest real part refractive index.

Table 4.2.1 Device configuration of reflective RGB colored filters.

Materials	Si₃N₄	ZnSe	a-Si	ZnSe	Si₃N₄
Blue (nm)	95	15	13	15	95
Green (nm)	110	20	25	20	110
Red (nm)	150	30	40	30	150
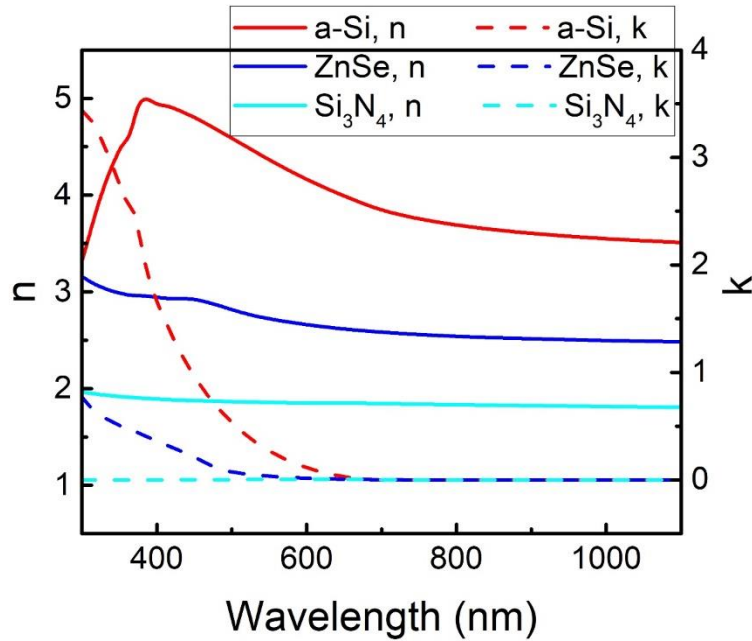
Figure 4.2.3 Measured refractive indices of a-Si, ZnSe, and Si₃N₄ using a spectroscopic ellipsometer (M-2000, J. A. Woollam).

Figure 4.2.4 presents the measured current density-voltage (*J-V*) characteristics of the colored solar panels, which are realized by integrating the passive filter with the c-Si panel beneath. Due to the largest amount of light transmission through the top filter harvested by the c-Si cell (as shown in Figure 4.2.1 (c)), the blue colored PV system shows a highest PCE of ~13.9% with a short circuit current density J_{sc} of ~30.3 mA/cm^2, an open circuit voltage V_{oc} of ~594.1 mV, and a fill factor (FF) of ~77.2%, which is only ~3.9% lower than the efficiency of the original c-Si solar cell without any color filter covering (J_{sc} ~38.0 mA/cm^2, V_{oc} ~604.7 mV, and FF ~77.5%, corresponding to a PCE of ~17.8%). Decent efficiencies have also been achieved for the green (PCE ~12.0%) and red (PCE ~10.1%) colored cells and the performance is summarized in Table 4.2.2 for comparison. The designed colored solar cells with great efficiency performance have effectively overcome the low efficiency limitations of typical colored PVs and open up a new path to the extensive use for a wide variety of applications. The detailed measurement method is provided in Figure 4.2.5. As discussed above, more transmitted light will be harvested by the

underneath c-Si solar cell if lowering the reflective color intensity employing a thinner a-Si layer in the middle, which is one effective approach to enhance the overall PCE of the colored solar module. In addition, the efficiency can be further improved if adding an index-match layer between the passive filter and the underneath c-Si cell to reduce the ~4.0% reflection from the back of the silica substrate or utilizing a more efficient solar panel beneath instead of the c-Si solar cell.
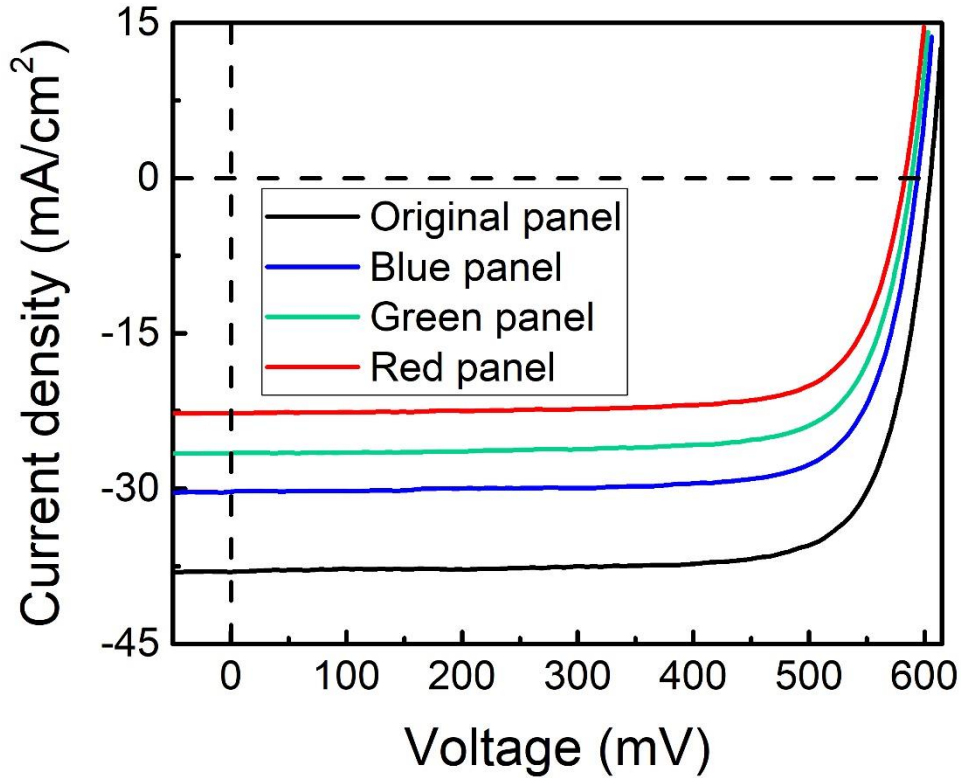
Figure 4.2.4 Measured current density-voltage (J–V) characteristics of the integrated colored solar panels under AM1.5 illumination (~100 mW/cm^2) compared to that of the original c-Si cell. The RGB colored devices exhibit efficiencies of ~10.1%, ~12.0%, and 13.9%, respectively, and the PCE of the original c-Si solar panel without any filter covering is ~17.8%.

Table 4.2.2 A summary of the electrical performance of colored solar panels in comparison with the original c-Si solar cell.

	J_{sc} (mA/cm^2)	V_{oc} (mV)	FF (%)	PCE (%)
Original panel	38.0	604.7	77.5	17.8
Blue panel	30.3	594.1	77.2	13.9
Green panel	26.5	588.7	76.8	12.0
Red panel	22.7	582.9	76.0	10.1
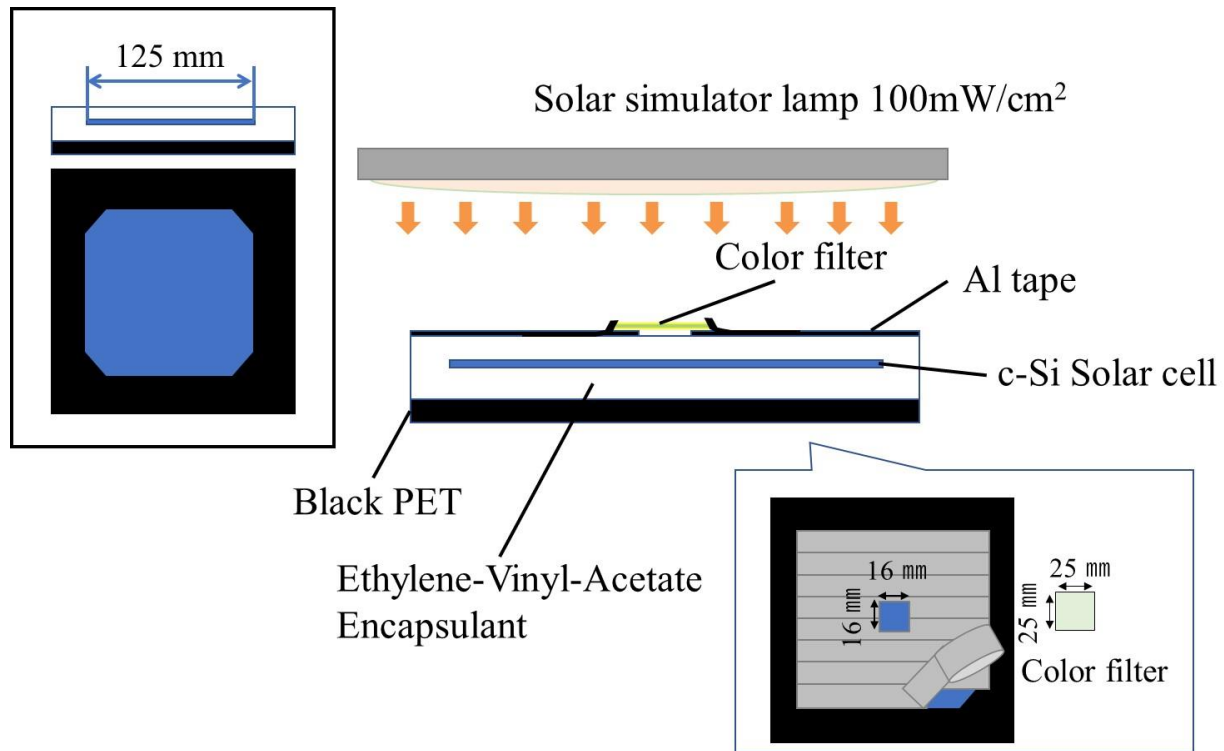
Figure 4.2.5 Setup for the current density-voltage (*J-V*) data acquisition of the integrated solar cells. Insets at the top left and bottom right present the dimensions of the c-Si solar panel and aluminum (Al) tape opening at the top surface, respectively. A commercial back contact c-Si solar panel (~125 mm × 125 mm square, Maxeon®, Sunpower Corporation) is covered using the Al foil with a 16 mm × 16 mm square opening at the center for the integration of the 25 mm × 25 mm square passive filters atop. Then the current density-voltage (*J-V*) performance of the integrated colored solar cell is recorded under the illumination of AM1.5 simulated sunlight (~100 mW/cm^2) by connecting MP-160 (EKO Instruments) to electrodes.

The calculated angle-resolved reflection spectra of designed RGB colored solar panels under unpolarized light illumination are described in Figure 4.2.6 (a) – (c), showing great consistency with the measurements in Figure 4.2.6 (d) – (f). The reflection peaks of all devices remain constant with respect to the viewing angles up to ±60° from both the simulation and measurement results, which clearly indicates the angular robust performance and is a direct result of the high indices of the materials (*i.e.*, a-Si, ZnSe, and Si$_3$N$_4$) involved in our designs. Considering that only the material deposition process is required, the proposed structure is an excellent candidate for the decorative PV applications with low manufacturing cost. The photographs of the fabricated samples against a black background under ambient light illumination in Figure 4.2.6 (g) show that

stable colors can be viewed at various angles, which further validates the angular invariant properties of our designs. Note that the black background is utilized to absorb the transmitted light, thus avoiding its interference with the reflection color.
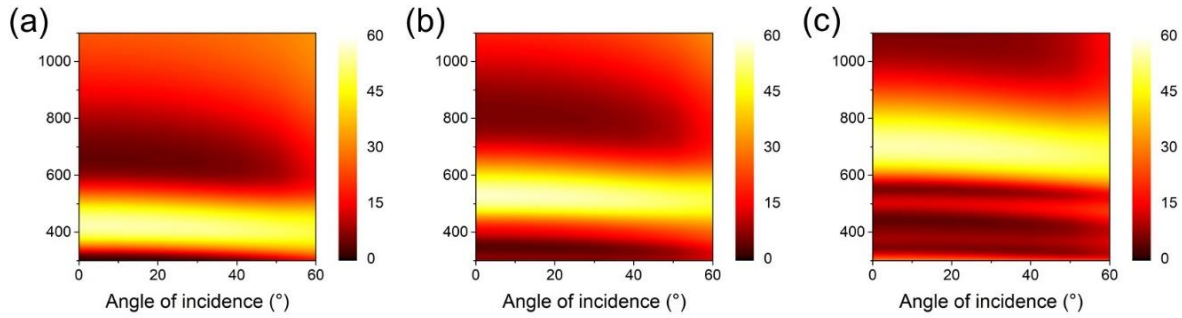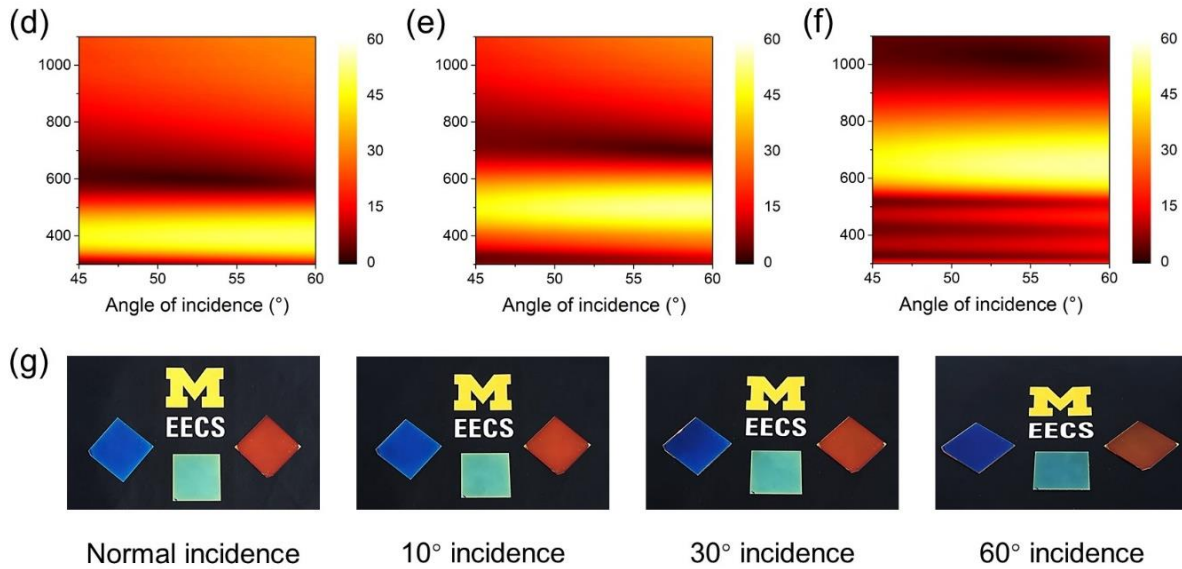
Figure 4.2.6 (a) ― (c) Calculated angle-resolved reflection for blue, green, and red colored solar panels. (d) – (f) Measured angular behaviors corresponding to those samples in (a) ― (c). (g) Photos of the fabricated RGB colored samples under ambient light illumination taken with a black background at four different viewing angles, showing that stable appearance can be maintained over a wide angular range for different colors.

The broadband transmission and colored appearance of the designed trans-reflective filters atop can be explained by multiple resonances at various wavelengths in those dielectric stacks. For simplicity, the blue colored device is used as an example for explanation in the following

discussions. The same working and design principles also apply to the other colored structures. In Figure 4.2.7 (a), the net phase shift is plotted for each dielectric layer. Transmission gets efficiently enhanced at those wavelengths where the net phase shift is equal to a multiple of 2π, *i.e.*, creating the F-P resonances to reduce the reflection, which consequently induces the transmission. Specifically, the reflection dip at ~300 nm results from the resonances inside all four dielectric layers, *i.e.*, resonances at 292 nm and 294 nm in the top and bottom Si_3N_4 layers, respectively, and resonances at 318 nm and 317 nm in the top and bottom ZnSe layers, respectively. Reflection at longer wavelengths are well suppressed with the broadband transmission owing to the multiple resonances at discrete wavelengths (resonances at 653 nm in the top Si_3N_4, at 663 nm in the top ZnSe, and at 754 nm in the bottom Si_3N_4). As a result, only light within the blue color range, where no transmission resonances are excited, gets effectively reflected, thereby generating the distinctive color appearance. The calculated electric filed distribution inside the structure as the function of wavelength is depicted in Figure 4.2.7 (b). The strong reflection within the short wavelength range spanning from 400 to 500 nm clearly indicates the blue color reflection of the designed structure.
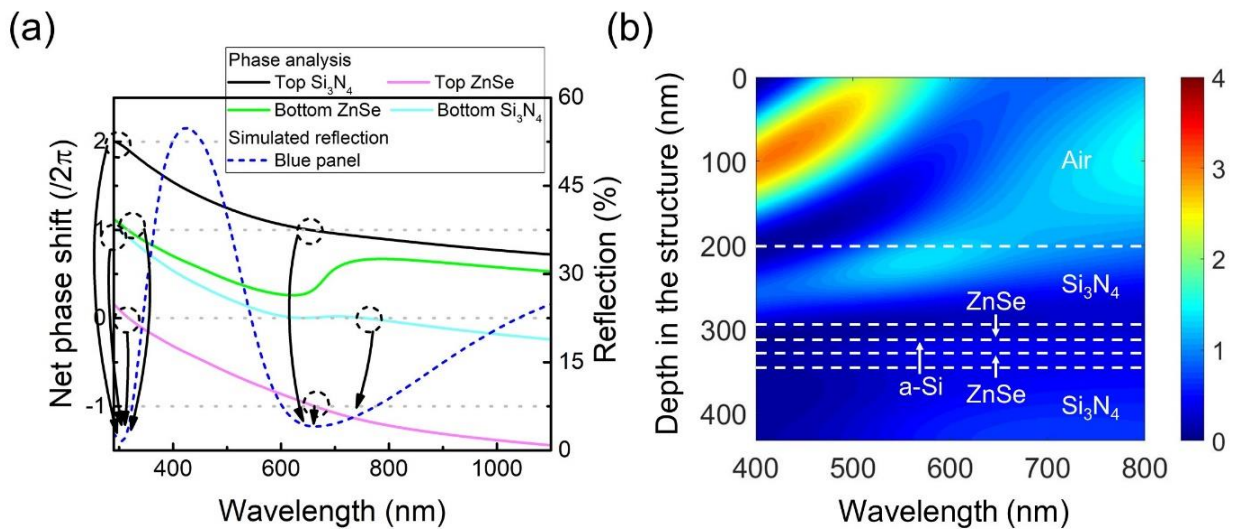
Figure 4.2.7 Calculated normalized net phase shift within each dielectric layer of the blue color device, indicating the positions of transmissive F-P resonances that results in the enhanced transmission. The resonances occur at the wavelength where the net phase shift is equal to a multiple of 2π. (b) Electric field distribution within the whole structure dependent on wavelengths. The strong reflection in the short wavelength range indicates the distinctive blue color reflection of the proposed device.

On the other hand, the high efficiency of the broadband transmission results from AR effects of the dielectric layers featuring a gradient index profile. This can be clearly validated by plotting the optical admittance diagram, which provides an effective way to visually represent the optical surface admittance of the multilayered structure [116]. Figure 4.2.8 plots the admittance diagram of the proposed blue colored structure at various wavelengths including 300 nm, 424 nm (the reflection peak), 600 nm, 800 nm, and 1000 nm, where the final admittance positions are (1.29, -0.08), (5.67, 2.37), (0.73, 0.30), (0.97, -0.49), and (1.31, -1.04), corresponding to reflections of around 1.76%, 54.70%, 5.35%, 5.82%, and 18.35%, respectively. The only strong reflection intensity within the blue wavelength range well explains the vivid-colored appearance and broadband high transmission. The same method can also be used to explain the distinctive color and high performance of green and red colored devices.
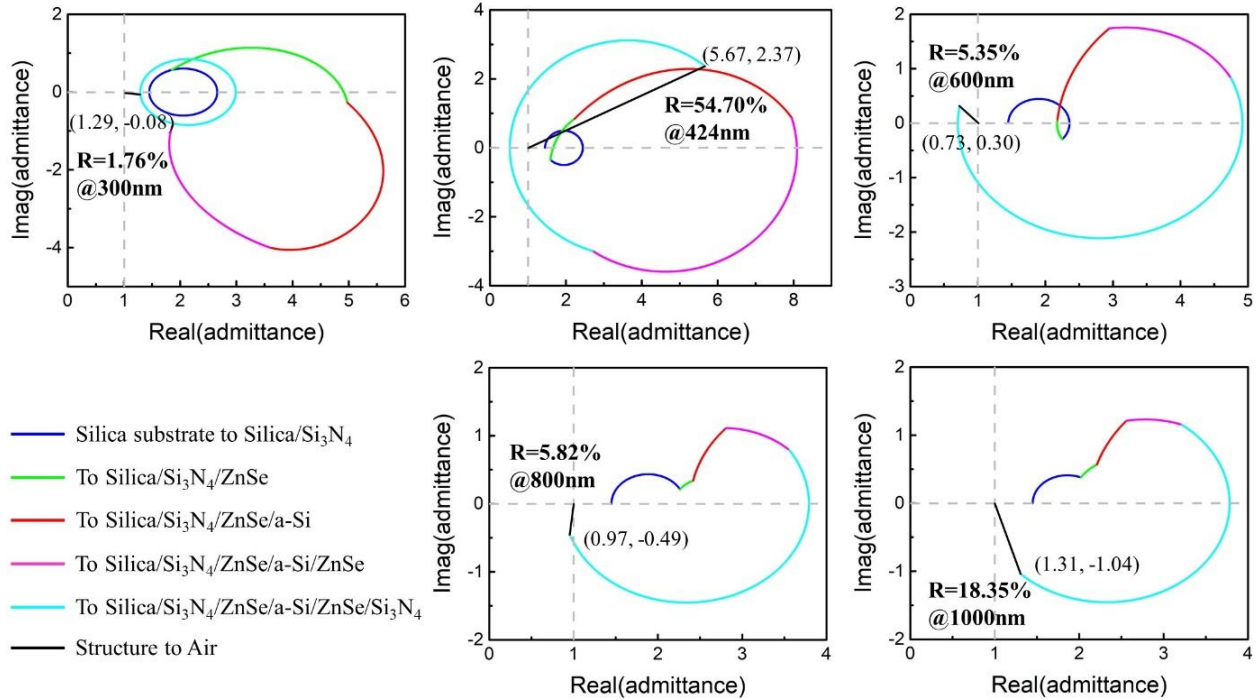
Figure 4.2.8 Optical admittance diagrams of the proposed blue filter at 300 nm, 424 nm (reflection peak), 600 nm, 800 nm, and 1000 nm wavelengths, respectively. The length of the black line connecting the termination admittance point of the structure and air provides a measure of the reflectance of the structure.

4.3 Trans-reflective PV Cells for Additional Efficiency Enhancement

As a-Si is a widely-used active material, above devices can be adapted in active solar cells after replacing ZnSe and Si_3N_4 with suitable hole/electron transport layers and transparent electrodes. Here, we used n- and p-SiO_x as electron and hole transport layers, respectively, considering their perfect band alignment with a-Si. Aluminum doped zinc oxide (AZO) and ITO are employed as anode and cathode, respectively, due to their transparency and compatibility with corresponding interfacial layers. Suitable thickness of each layer is selected for optimal electrical performance as shown in Figure 4.3.1 (a). A green colored solar cell is fabricated for demonstration as shown in Figure 4.3.1 (b) (patterned areas for electrical measurement). It maintains the broadband high transmission except at wavelengths that are used for color generation as presented in Figure 4.3.1 (c) and additional 2.80% PCE is acquired with only 11nm a-Si (Figure 4.3.1 (d)), which could

51

further enhance the efficiency of the whole tandem solar panel. Other colors (blue and red) can also be achieved by slightly tuning the thickness of each layer as shown by the simulated results in Figure 4.3.2. The detailed designs for all RGB colored a-Si solar cells are summarized in Table 4.3.1. It should be noted that we are working on optimizing the structural configuration to improve the optical performance of the designed active colored a-Si solar cells by getting rid of the oscillations in the spectra and enhancing the overall transmission.
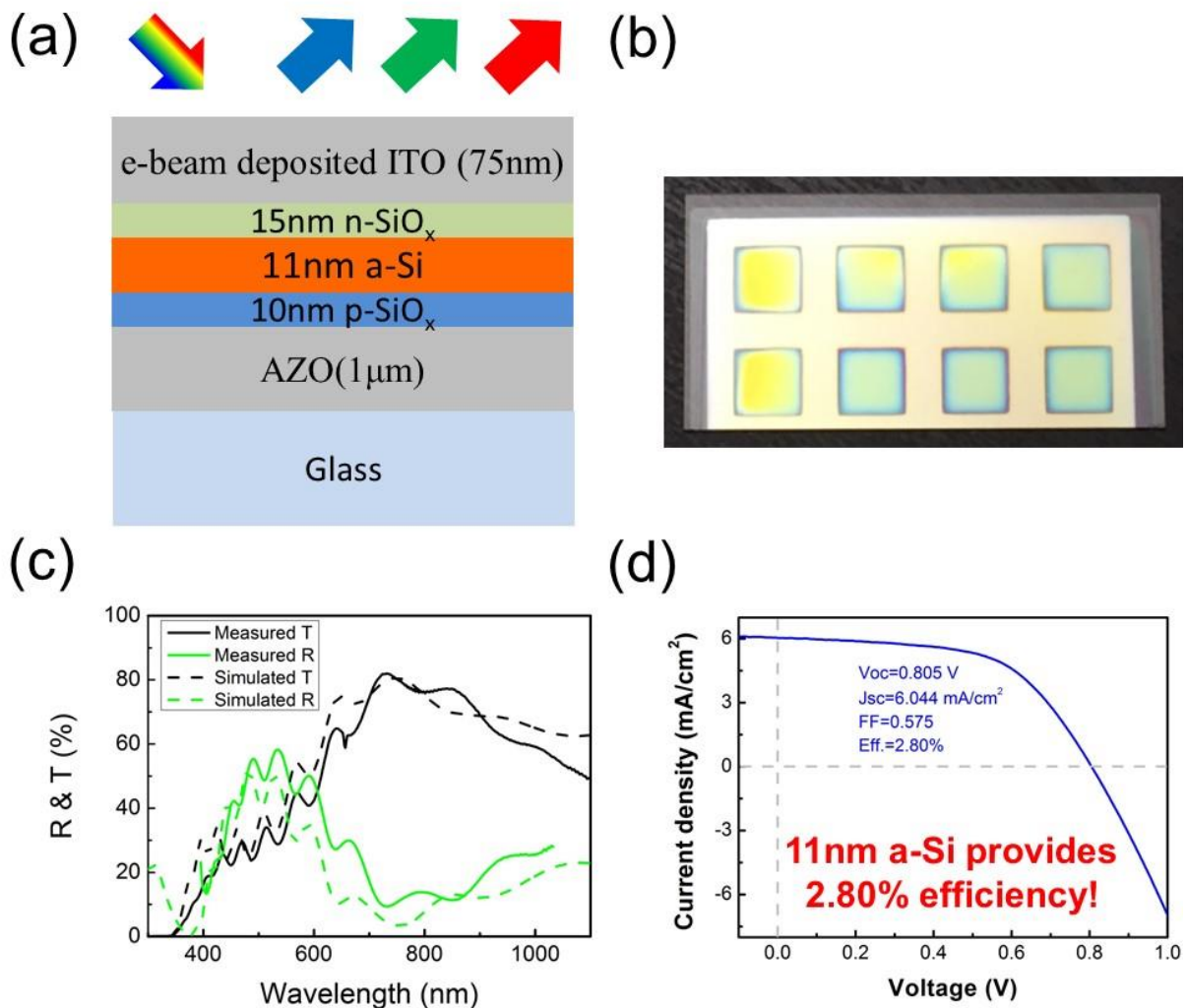
Figure 4.3.1 (a) The schematic diagram of colored a-Si solar cell adapted from passive filters. The thickness of each layer is listed out in the plot. (b) Green colored solar cell fabricated for demonstration. (c) Optical and (d) electrical performance of the fabricated device.
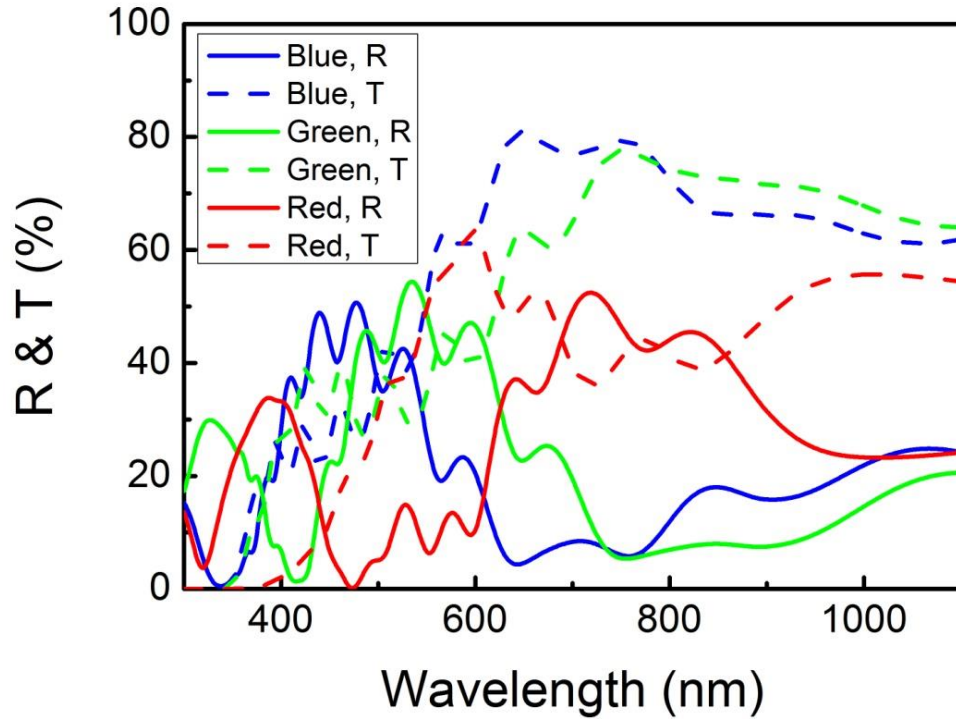
Figure 4.3.2 Simulated optical performance of designed a-Si solar cells of different RGB colors.

Table 4.3.1 Device configuration of reflective RGB colored filters.

Materials	AZO	p-SiO$_x$	a-Si	n-SiO$_x$	ITO
Blue (nm)	1000	19	10	19	105
Green (nm)	1000	19	13	19	135
Red (nm)	1000	19	55	19	170

4.4 Conclusion

In conclusion, we have demonstrated a new approach for high-performance colored solar cells by integrating a trans-reflective filter on the top of a c-Si solar panel. The filter design simply consists of 5 layers, where a lossy semiconductor of high refractive index is sandwiched between two stacks of dielectrics. A distinctive reflection color together with overall high transmission across the

whole solar spectrum, where the latter is subsequently harvested by the c-Si panel beneath and results in the final high PCE, has been generated utilizing the filter featuring a gradient index profile. Due to the high index materials involved in the filter module, the whole system presents high brightness and great angular invariant appearance up to ±60°. As the middle a-Si is a potential active layer, the efficiency of the proposed colored solar panel can be further enhanced if adapting the passive filter into an active solar cell by replacing the dielectrics with transparent electrodes and hole/electron transport layers. Considering that only deposition method is involved in the fabrication of the designed structure, the scheme described here featuring high PCE has overcome the limitations of typical colored solar cells and could open up new possibilities for various applications in the future.

Chapter 5

Decorative Near-Infrared Transmission Filters Featuring High-Efficiency and Angular-Insensitivity Employing 1D Photonic Crystals

5.1 Introduction

Visibly-opaque but near-infrared NIR-transmitting filters is another good example of application when taking use of both the reflection and transmission properties structural color filters. This type of filters has received considerable interest due to their irreplaceable roles in various applications including NIR spectroscopy, security imaging, optical detections, to name an important few [153-160]. In recent years, decorative NIR filters that exhibit aesthetic colors are also highly desired to both enhance the signal-to-noise ratio and hide the unappealing appearance of sensors (*e.g.*, proximity sensors, gesture sensors, and camera monitoring systems) integral to advanced technologies that are closely related to our daily life, such as vehicles, cell phones, etc. Organic dyes or pigments that can absorb ultraviolet UV and visible light but transmit NIR waves provide one option [161-163]. However, these organic materials suffer from short life-time problems due to their susceptibility to environmental factors such as moisture, high temperature and constant

UV exposure. Structural NIR-transmitting filters that are patterned at the subwavelength scale to excite either GMR or SPP have been demonstrated to address the aforementioned challenges [164-170]. The coupling of incident light into those resonances needs to be achieved with the subwavelength gratings, which require complicated fabrication procedures such as e-beam lithography and focused ion beam milling, rendering them difficult for large-area applications. Moreover, the resulting transmission spectra are highly sensitive to an angle of incidence due to the momentum matching condition, thereby dramatically limiting their potential for many applications. A more cost-effective and widely-adopted method to create NIR transmission while blocking the visible light is using 1D PCs, which are made of periodic layered structures consisting of alternating high and low index materials [116, 157, 171-175]. By locating the passband in the NIR range while the stopband in the visible, adjustable NIR transmission performance can be achieved by selecting different constituent materials and layer thicknesses. However, as the structures based on single-periodic stacks have very limited stopband bandwidth, stacking of different period units are typically required to produce overlapping multiple stopbands to broaden the stopband, in order to block all the visible light transmission. As a result, these PC-based filters typically involve tens or even hundreds of layers, which faces the manufacturing cost and yield issues.

In this work, we report a new approach for colored NIR transmission filters that blocks the visible light, with the option to create desired color reflection [18]. The design exploits 1D ternary PCs involving 7 layers. Simultaneously, taking the advantage of the absorptive property of the constituent semiconductor (*e.g.*, a-Si) in the visible range, various reflection colors, not limited to the one complementary to the transmissive spectrum, can be generated without affecting the transmission performance, which can be used for decoration applications and 'hide' objects behind

the filters. The proposed structural color exhibits ultrahigh transmission efficiency with the maximum close to 100% and angle invariant property up to ±60° regardless of the polarization state of incident light from both illumination directions due to the low loss and high refractive indices of the materials used, surpassing the performance of many previous works. An additional advantage of the proposed structural colors lies in their simplicity where only thin film deposition is required for the fabrication, thus enabling large-scale manufacturing for practical applications. The approach described in this work could open up many potential applications such as imaging sensors, optical measurement systems, and decorations.

5.2 Design Principle and Results

A schematic diagram of the proposed structure featuring angular- and polarization-independent NIR transmission is depicted in Figure 5.2.1 (a). It is targeted at high transmissive efficiency employing three stacks of '$H/2LH/2$' unit as an effective AR coating based on Herpin's equivalent index [116, 176]. Here, H and L denote the high and low refractive index materials with a quarter-wavelength thickness, separately (*i.e.*, $H = \lambda_c / 4n_H$ and $L = \lambda_c / 4n_L$). Selecting a central wavelength of the stopband as $\lambda_c = 550$ nm and a-Si ($n_H = 4.4 + i0.27$) and Si_3N_4 ($n_L = 1.9$) as H (~32 nm) and L (~72 nm) layers, respectively, the stopband bandwidth can be calculated from $\Delta(\lambda_c / \lambda) = (4 / \pi)\sin^{-1}[(n_H - n_L) / (n_H + n_L)]$ with the left and right band edge located at $\lambda_L = 430$ nm and $\lambda_R = 740$ nm, respectively (Figure 5.2.1 (b)) [116]. It should be noted that both H and $\Delta\lambda$ are approximated using the real part of refractive index of a-Si in the calculation considering its small but nonzero extinction efficiency [116]. It is easy to understand from the above equation that such a broad stopband is a direct consequence of the high index contrast between the high (a-Si) and low (Si_3N_4) index materials used in the design. Due to the wide range stopband together with the semiconductor

loss, visible incidence (wavelength <650 nm) is effectively blocked with only 7 layers as shown by the spectra in Figure 5.2.1 (b). As a result, the fabricated samples showing mirror-like bright reflection (inset at the bottom-left corner). As a comparison, the simulated reflection and transmission spectra of the 7-layered PC structure based on lower refractive index material combinations (*i.e.*, employing titanium dioxide (TiO_2) and silicon dioxide (SiO_2) as the high and low index materials, respectively), is given in Figure 5.2.2. It is obvious that its stopband bandwidth is much narrower and visible light can pass through the stacks even within the stopband range. The thickness of TiO_2/SiO_2 is designed so that the center wavelength of the stopband is located at the same position ($\lambda_c = 550$ nm). Due to the negligible absorption loss of both a-Si and Si_3N_4 materials beyond 700 nm, high transmission close to unity (99.88% @735 nm) can be achieved at normal incidence in NIR range as plotted in Figure 5.2.1 (b) showing excellent agreement between the calculated and measured results. Here, the simulations based on the transfer matrix method [152] with the refractive indices of materials calibrated using a spectroscopic ellipsometer (M-2000, J. A. Woollam) are performed, and the reflection and transmission spectra are measured by using the spectrophotometer (Cary 7000, Agilent). Both a-Si and Si_3N_4 are deposited with PECVD at 260 °C alternatively without breaking the vacuum chamber. We note that the measured transmission is slightly lower than the calculations and this can be attributed to the reflection at the interface between the air and the bottom of the fused silica substrate, which has not been considered in the simulations. Due to the symmetric configuration of the proposed structure, the stacks exhibit the same performance at both top and bottom illuminations, which can further extend our design into more applications, such as color pigments.
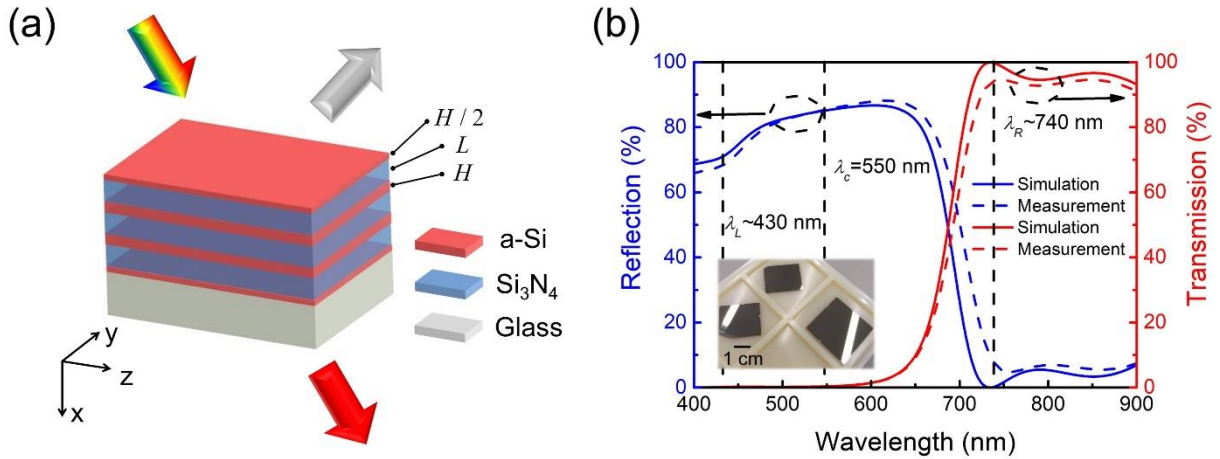
Figure 5.2.1 (a) A schematic diagram of the proposed transmissive structure color employing 1D ternary PCs. (b) Simulated and measured spectra of our design. Transmission below 650 nm is greatly suppressed due to both the broad stopband resulting from the high refractive index materials and slight loss of a-Si. The inset at the bottom-left corner is the fabricated samples, showing mirror-like reflection as the visible light is well blocked. The scale bar is 1 cm.
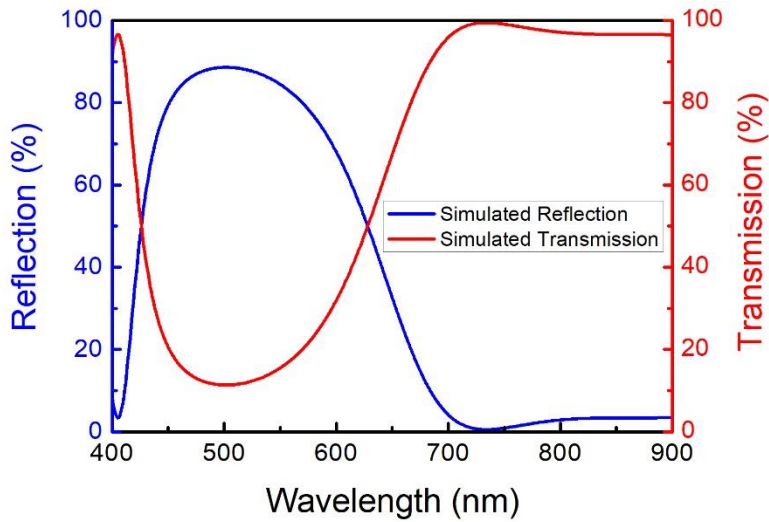
Figure 5.2.2 The simulated reflection and transmission spectra of the 7-layered PC structure employing TiO_2 as H layer and SiO_2 as L layer, respectively. It is clear that its stopband bandwidth is much narrower than that of the a-Si/Si_3N_4 stacks, and there is more visible light transmission.

For ternary PCs consisting of the '$H/2LH/2$' unit, the characteristic matrix of one period is

$$\overleftrightarrow{M} = \begin{pmatrix} M_{11} & M_{12} \\ M_{21} & M_{22} \end{pmatrix}$$

with

$$M_{11} = \cos 2k_{H,x} \cos k_{L,x} - \frac{1}{2}\left(\frac{k_{L,x}}{k_{H,x}} + \frac{k_{H,x}}{k_{L,x}}\right)\sin 2k_{H,x} \sin k_{L,x}$$

$$M_{12} = \frac{k_0 H/2}{ik_{H,x}}\left[\sin 2k_{H,x}\cos k_{L,x} + \frac{1}{2}\left(\frac{k_{L,x}}{k_{H,x}} + \frac{k_{H,x}}{k_{L,x}}\right)\cos 2k_{H,x}\sin k_{L,x} + \frac{1}{2}\left(\frac{k_{H,x}}{k_{L,x}} - \frac{k_{L,x}}{k_{H,x}}\right)\sin k_{L,x}\right]$$

$$M_{21} = -i\frac{k_{H,x}}{k_0 H/2}\left[\sin 2k_{H,x}\cos k_{L,x} + \frac{1}{2}\left(\frac{k_{L,x}}{k_{H,x}} + \frac{k_{H,x}}{k_{L,x}}\right)\cos 2k_{H,x}\sin k_{L,x} - \frac{1}{2}\left(\frac{k_{H,x}}{k_{L,x}} - \frac{k_{L,x}}{k_{H,x}}\right)\sin k_{L,x}\right]$$

$$M_{22} = M_{11}$$

for TE polarization, and

$$M_{11} = \cos 2k_{H,x} \cos k_{L,x} - \frac{1}{2}\left(\frac{n_H^2 k_{L,x}}{n_L^2 k_{H,x}} + \frac{n_L^2 k_{H,x}}{n_H^2 k_{L,x}}\right)\sin 2k_{H,x} \sin k_{L,x}$$

$$M_{12} = \frac{n_H^2 k_0 H}{2ik_{H,x}}\left[\sin 2k_{H,x}\cos k_{L,x} + \frac{1}{2}\left(\frac{n_H^2 k_{L,x}}{n_L^2 k_{H,x}} + \frac{n_L^2 k_{H,x}}{n_H^2 k_{L,x}}\right)\cos 2k_{H,x}\sin k_{L,x} + \frac{1}{2}\left(\frac{n_L^2 k_{H,x}}{n_H^2 k_{L,x}} - \frac{n_H^2 k_{L,x}}{n_L^2 k_{H,x}}\right)\sin k_{L,x}\right]$$

$$M_{21} = \frac{-2ik_{H,x}}{n_H^2 k_0 H}\left[\sin 2k_{H,x}\cos k_{L,x} + \frac{1}{2}\left(\frac{n_H^2 k_{L,x}}{n_L^2 k_{H,x}} + \frac{n_L^2 k_{H,x}}{n_H^2 k_{L,x}}\right)\cos 2k_{H,x}\sin k_{L,x} - \frac{1}{2}\left(\frac{n_L^2 k_{H,x}}{n_H^2 k_{L,x}} - \frac{n_H^2 k_{L,x}}{n_L^2 k_{H,x}}\right)\sin k_{L,x}\right]$$

$$M_{22} = M_{11}$$

for TM polarization [116, 177-179]. $k_{H,x} = k_0 n_H H \cos\theta_H / 2$ and $k_{L,x} = k_0 n_L L \cos\theta_L / 2$ are the wave vectors along the x direction for the waves propagating in the high and low refractive index layers, respectively, $k_0 = \omega\sqrt{\varepsilon_0\mu_0}$ is the free-space wave vector with ω as the frequency of incident light, and $\theta_{H(L)}$ is the corresponding propagation angle in each layer determined by the Snell's law. Based on the characteristic matrix, the projected band structure for both polarizations can be calculated from the Bloch wave number $K(\omega,\beta) = \cos^{-1}[(M_{11} + M_{22}) / 2] / \Lambda$ as depicted in Figure 5.2.3 (a) [15]. Here, $\Lambda = H + L$ is the period of the PCs, $\beta = k_0\sin\theta_0$ is the wave vector in the z direction remaining unchanged during propagation in different layers, and θ_0 is the incidence angle. The shaded region in the plot, which is obtained by setting $(M_{11} + M_{22}) / 2 < 1$, corresponds to the propagating Bloch modes, while the blank area represents the stopband calculated with $(M_{11} + M_{22}) / 2 > 1$ instead. Since all the modes in the free space must obey $\omega = c\sqrt{k_{x0}^2 + \beta^2}$, the entire blank

region above the line $\omega = c\beta$ refers to the modes that cannot directly propagate into the PCs from the surrounding air without additional coupling mechanism. Here, c is the speed of light in air and k_{x0} is the x direction wave vector in air. As highlighted in the figure, the wavelength range between the dashed lines going through the open and solid circles ($0.16 < \omega\Lambda / 2\pi c < 0.24$) corresponds to the omnidirectional stopband that will reflect incident light at all angles irrespective of polarizations and is calculated as from 430 nm to 650 nm in terms of wavelength unit. This broad stopband efficiently suppresses the transmission below 650 nm. It can be observed that this omnidirectional stopband is very close to the stopband at normal incidence (the range defined by the dashed lines going through the open circle and square) due to the flat band structure, which leads into the omnidirectional transmission performance with little dispersion at different incident angles. By comparison, the band structure of the PCs consisting of lower refractive index materials (*i.e.* utilizing TiO_2 and SiO_2 as H and L layers, respectively) is also plotted featuring a much steeper slope as presented in Figure 5.2.4, which indicates a significant blue shift of the pass band (or stopband) at large angles of incidence and will be discussed in detail in the next section. Therefore, it can be concluded that the flat band structure directly results from the high refractive indices of the constituent materials (*i.e.*, a-Si and Si_3N_4), allowing a small refracted angle into the structure according to Snell's law and exhibiting the great angular-insensitive property. In addition, the refractive indices of the materials are also a key factor affecting the stop bandwidth. As plotted in Figure 5.2.3 (b), the dependency of the omnidirectional stop bandwidth on the low refractive index material (n_L) and refractive index contrast (n_H / n_L) reveals that both large n_L and n_H / n_L are required to achieve a broad omnidirectional stopband.
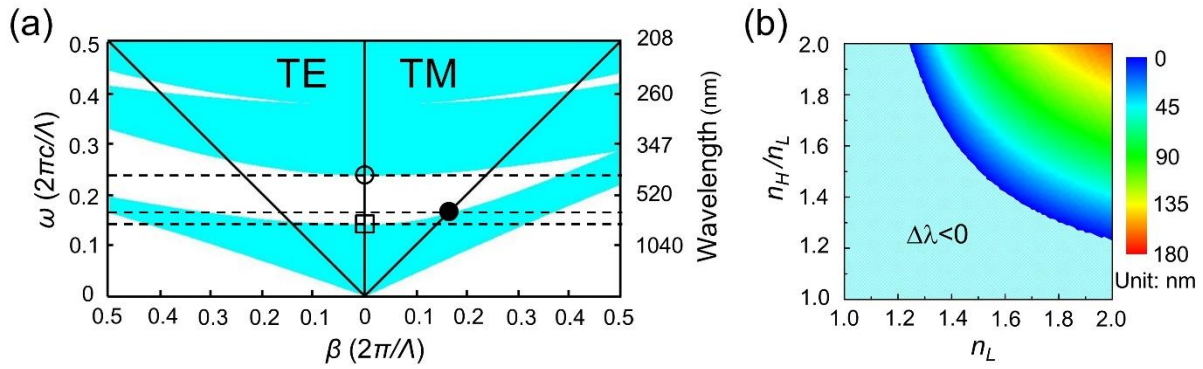
Figure 5.2.3 (a) The projected band structures for both TE and TM polarizations calculated from the characteristic matrix of the ternary PCs. (b) Dependency of the omnidirectional stopband of the ternary PCs on the constituent low refractive index material n_L and refractive index contrast n_H / n_L. The region where $\Delta\lambda < 0$ indicates that omnidirectional stopband does not exists in these cases, *i.e.*, no light will be blocked at all angles. The color scale represents the bandwidth of the omnidirectional stopband.
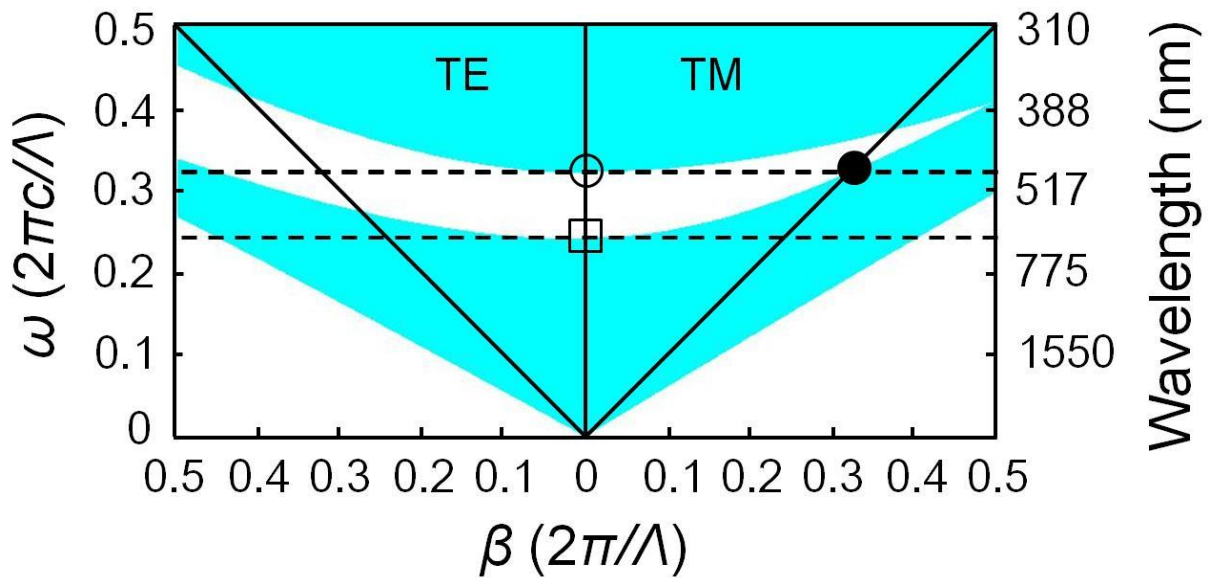
Figure 5.2.4 The projected band structure for the ternary PCs made up of TiO$_2$ as *H* layer and SiO$_2$ as *L* layer. The omnidirectional stopband shrinks close to zero for this combination of low refractive index materials (the wavelength range between the dashed lines going through the open and solid circles) and it is totally different from the stop bandwidth at normal incidence (the range between the dashed lines going through the open circle and square). This indicates the highly angular sensitive performance of the transmission spectra as shown in Figure 5.2.7.

It is typically challenging to generate wide-angle NIR transmission because the longer cavity thickness to create a resonance at a longer wavelength range is required, resulting in sensitivity to the angle of incidence. To investigate the angular performance of this transmissive-type PC

structure, the calculated and measured angle-resolved transmission spectra are illustrated in Figure 5.2.5 (a) – (d) for both TE and TM polarized light. Obviously, the transmission below 650 nm is effectively blocked at all angles, which is in good agreement with the prediction of Figure 5.2.3 (a). Due to the high refractive indices of the materials in the design as analyzed in the last section, angular insensitivity up to ±60° are observed regardless of polarizations as indicated by the flat dispersion curves in the plot. The simulation is carried out using transfer matrix method and the measured transmission spectra at different angles are obtained by the spectrophotometer (Cary 7000, Agilent) with angle resolved measurement accessory (UMA). Optical images of the fabricated samples at different observing angles under ambient light illumination are provided in Figure 5.2.5 (e), displaying stable mirror reflection appearance over a wide angular range. It further validates the angular insensitive performance of our designed structures and this outstanding characteristic is highly desired in decoration applications. The corresponding reflection spectra dependence on incidence angles are provided in Figure 5.2.6. For comparison, the simulated angular-dependent transmission spectra of the structure utilizing the lower refractive index materials based on TiO_2 and SiO_2, presenting a blue-shifted transmission profile and hence the degraded colors with increasing incident angles, which are well consistent with the prediction in Figure 5.2.4 and Fig. 5.2.3 (b), are provided in Figure 5.2.7. Hence, compared with the common TiO_2/SiO_2 film stack, the a-Si/Si_3N_4 stack can greatly improve the incident angular performance and dramatically decrease the split for two polarizations. For a wide variety of applications such as spectral analysis and imaging, the filter is desired to have a much sharper NIR transmission to exclude the severe effects caused by the unwanted light at short wavelengths. Thus, the influence of the number of '$H/2LH/2$' unit on the passband (stopband) sharpness is explored. Simulated reflection and transmission spectra for structures consisting of different numbers of stacks are

illustrated in Figure 5.2.8. By increasing the stacks, a steeper passband (stopband) that is close to the ideal case for the infinite stacks, which is presented by the band structure in Figure 5.2.3 (a), can be achieved. When the stack number reaches 7, the steepness of the spectra almost remains unchanged even if further increasing the number of stacks.
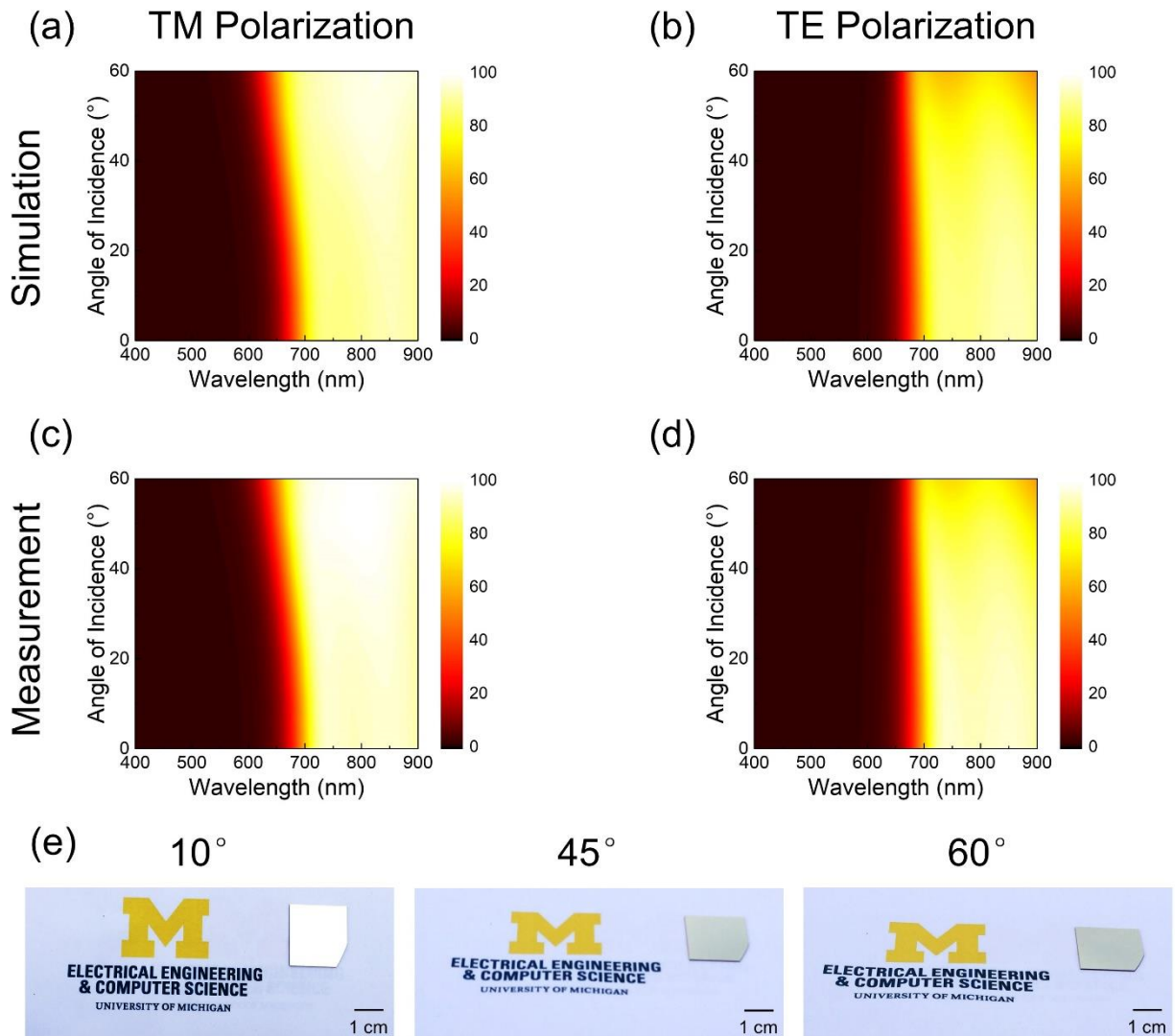
Figure 5.2.5 Simulated angle-resolved transmission spectra for (a) TM and (b) TE polarizations, respectively. Measured angle-resolved transmission spectra for (c) TM and (d) TE polarizations, respectively, showing great agreement with the calculated results in (a) and (b). (e) Optical photographs of fabricated samples at different observing angles under ambient light, showing robust mirror-like images over a wide angle range. The scale bars are 1 cm.
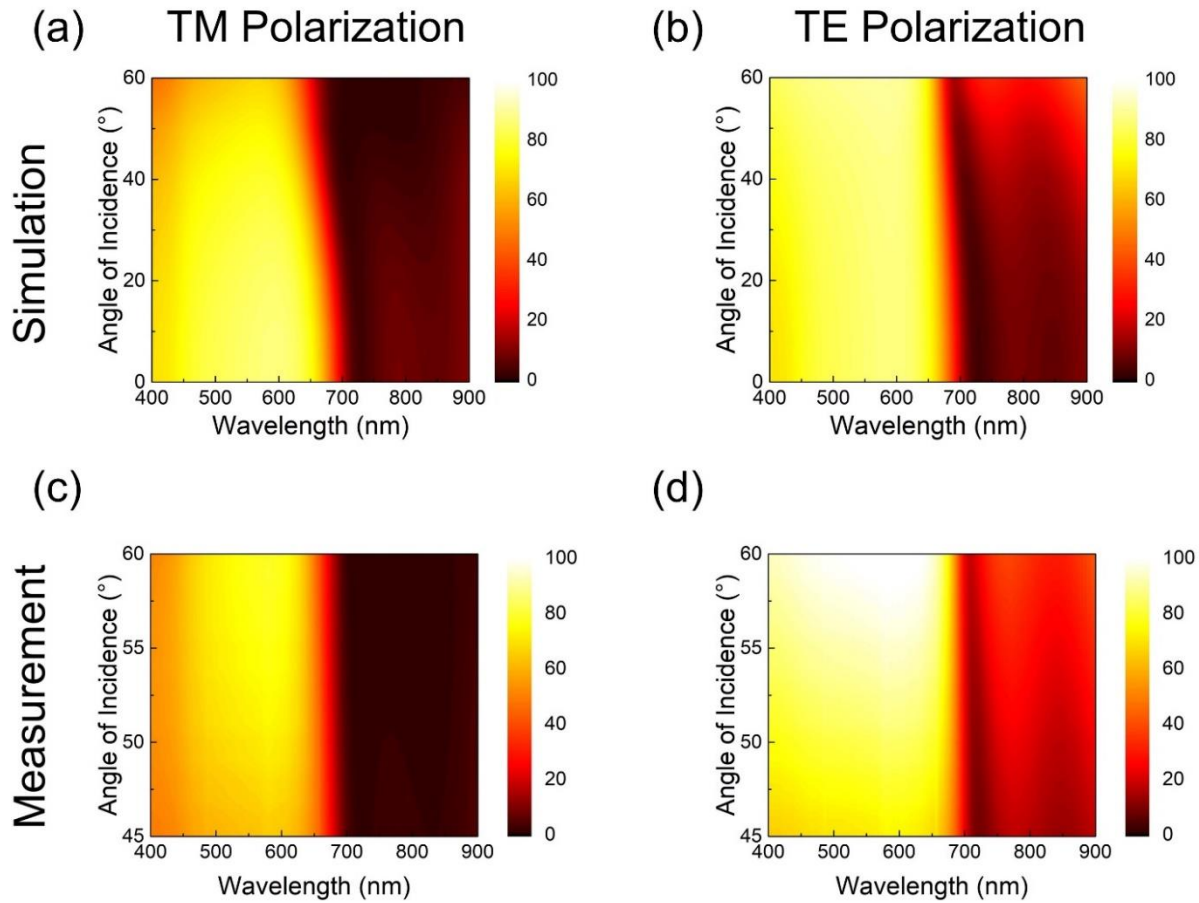
Figure 5.2.6 Simulated angle-resolved reflection spectra for (a) TM and (b) TE polarizations, respectively. Measured angle-resolved reflection spectra for (c) TM and (d) TE polarizations, respectively. The flat dispersion curves indicate the great angular-insensitive performance of fabricated samples.
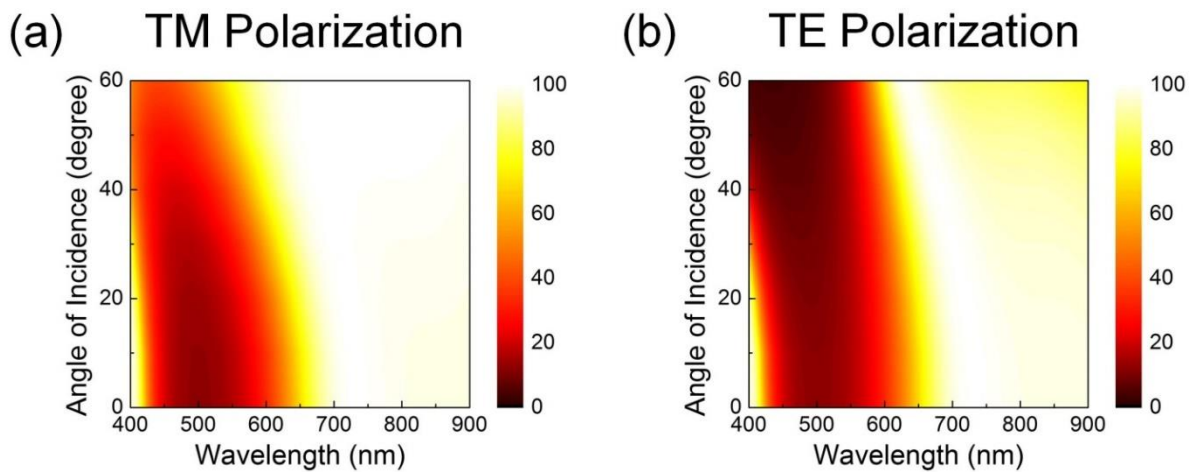
Figure 5.2.7 Simulated angular resolved transmission spectra for ternary PCs consisting of low index materials (*i.e.*, utilizing TiO_2 and SiO_2 as H and L layers, respectively) for (a) TM and (b) TE polarizations, respectively. Obvious blue shift of the transmission band can be observed at large incident angles. Here $H = 60$ nm and $L = 95$ nm by remaining the central wavelength of the stopband

unchanged as λ_c = 550 nm.
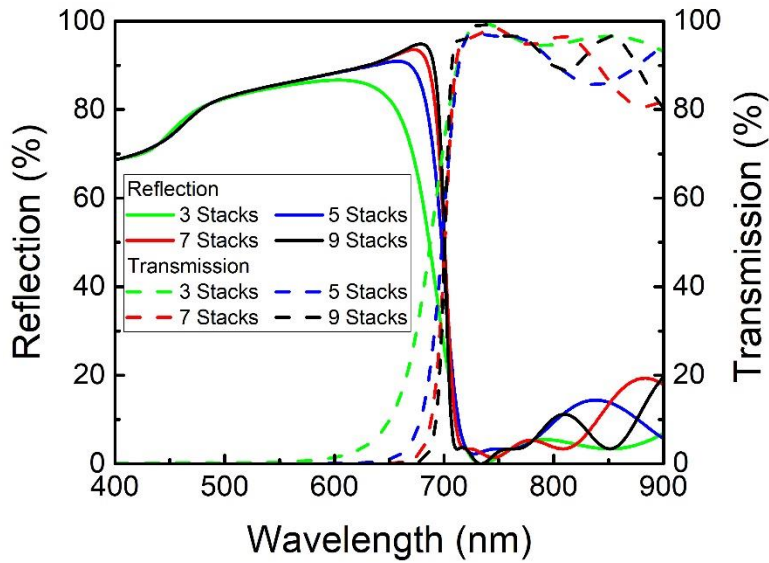
Figure 5.2.8 Investigation of the reflection and transmission spectra performance with different numbers of '*H*/2*LH*/2' stacks. The steepness of the spectra remains unchanged when the stack number reaches 7.

The structure discussed above with great angular-insensitive mirror-like reflection provides one option for decorative uses, *e.g.*, hiding the black holes of NIR sensors that are integral to vehicle cockpits and cell phones. In real applications, other colors in addition to the mirror-like appearance, which are impossible with traditional PCs employing transparent materials, are highly desired. To generate various decorative colors, additional three layers (thin Si_3N_4/a-Si/thick Si_3N_4) are incorporated on top of the proposed ternary PC structures as depicted in Figure 5.2.9 (a). Different CMY colors can be realized by simply adjusting the thicknesses of the added thin Si_3N_4 and a-Si layers while maintaining the high NIR transmission without changing the bottom PCs as plotted in Figure 5.2.9 (b) – (d), respectively. Insets in the figures provide the optical images of three colored devices at normal incidence. The slight discrepancy between the simulated and measured results are due to the thickness variation in the deposition process. The detailed structure configuration of each color is summarized in Table 5.2.1. The reflection spectra with sharp dips

correspond to distinctive colored appearance of CMY devices with their color coordinates described in the chromaticity diagram as shown in Figure 5.2.9 (e). As one potential application of these decorative NIR-transmitting filters is to hide the unappealing appearance of sensors used in vehicles and cell phones and these silicon-based NIR sensors typically work near 900 nm, the optical performance of our proposed devices is evaluated up to 900 nm. On the other hand, our structure can prove high transmission at even longer wavelengths (*e.g.*, 1.2µm, see Figure 5.2.10).
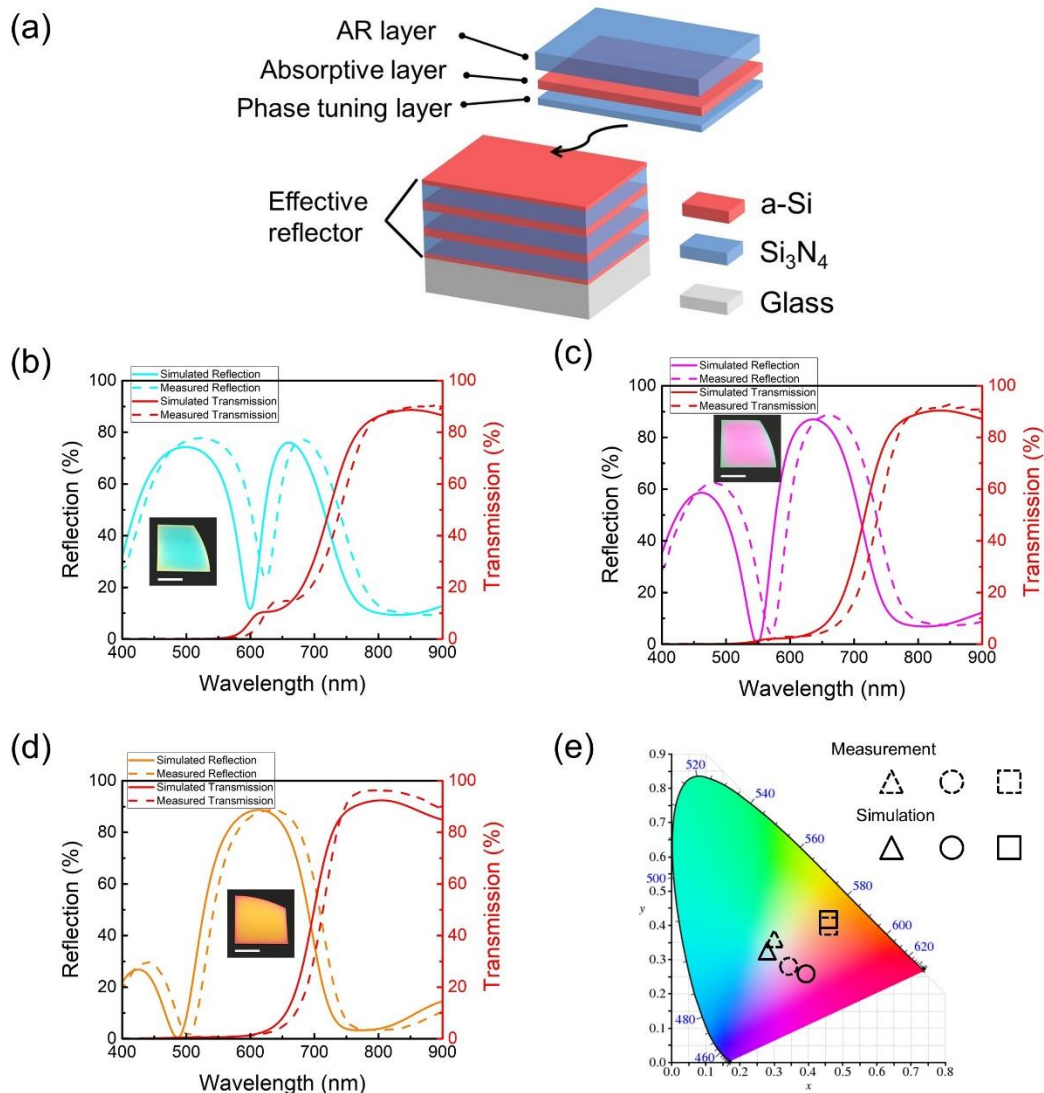
Figure 5.2.9 (a) A schematic diagram of new designs for decorative visibly-opaque but NIR-transmitting filters. (b) – (d) Simulated and measured optical performance of CMY colored NIR-transmitting filters. Insets show the optical images of fabricated devices on silica substrates. The scale bars are 1 cm. (e) Colored appearance of decorative NIR-transmitting devices evaluated on the CIE 1931 chromaticity diagram. The color coordinates calculated from the measured reflection spectra of CMY colors are (0.30, 0.36), (0.34, 0.28), and (0.46, 0.38), respectively, showing good match with the simulated results (cyan (0.28, 0.33), magenta (0.39, 0.26),

and yellow (0.46, 0.42)).

Table 5.2.1 Structural configurations of CMY colored decorative NIR-transmitting filters. The bottom effective reflectors in all designs employ the same 7-layer PC as presented in Figure 5.2.1(a).

	Thin Si_3N_4 (nm)	a-Si (nm)	Thick Si_3N_4 (nm)
Cyan	45	25	140
Magenta	30	20	140
Yellow	25	10	140
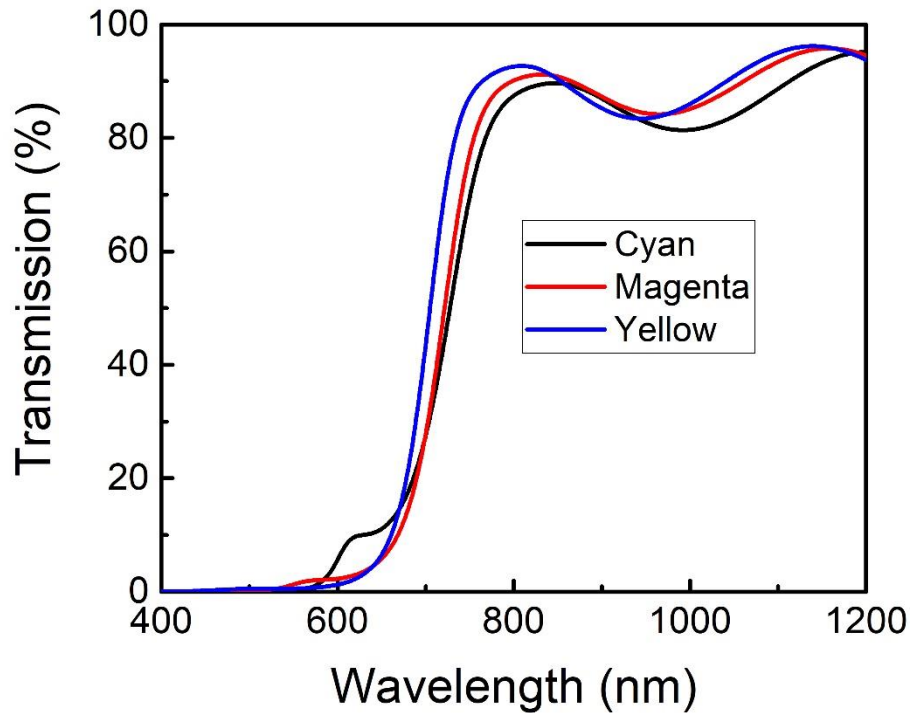
Figure 5.2.10 Transmission spectra of our proposed CMY colored devices within a broader wavelength range. High NIR transmission can be maintained to 1200 nm for all the structures, which indicates the possibility of our devices in more applications.

To better understand the mechanism of decorative visibly-opaque but NIR-transmitting structures, the yellow colored design is taken as an example to elucidate the function of each layer. Essentially, the new structure can be effectively simplified into an asymmetric F-P cavity by treating the bottom

68

PC stacks as a reflective mirror in the visible, which is illustrated in Figure 5.2.9 (a). The yellow color is created by suppressing the reflection in the blue color range (light with wavelength <500 nm, as shown by the reflection dip @~500 nm in Figure 5.2.9 (d)) while maintaining the high reflection intensity of light in the other portion in the visible. The suppression of blue light is due to the perfect absorption of a-Si layers, which can be seen from the near 100% absorption peak of the total absorption spectrum as depicted in Figure 5.2.11 (a). This guarantees the low detection noise in NIR sensor applications by blocking the visible transmission but allowing only NIR light to pass the stacks, which is impossible with traditional PC structures based on transparent materials. According to the absorption spectra of each a-Si layer, the absorption is mainly ascribed to the 1st (additionally added 10 nm a-Si) and 2nd a-Si (the top 16 nm a-Si of the bottom PC mirror stacks). By calculating the net phase shifts of the 1st and 2nd a-Si layers, it is interesting to find out that the added thin Si$_3$N$_4$ (25 nm) between the bottom PC mirror and the top 10 nm a-Si is an effective phase tuning layer that excites the absorption resonances in the blue color range within the absorptive a-Si layers, thereby generating the reflective yellow color [180, 181]. The absorption resonance occurs when the net phase shift is equal to a multiple of 2π. After adding the thin Si$_3$N$_4$ phase tuning layer, two closely positioned absorption resonances are excited within the 1st (#1 @493 nm) and 2nd (@504 nm) a-Si layers as shown in Figure 5.2.11 (b), which significantly enhances the short wavelength absorption and are well-consistent with the absorption peaks of the red and blue curves in Figure 5.2.11 (a). For comparison, the net phase shift of the top a-Si layer after removing the Si$_3$N$_4$ phase tuning layer (in this case the 1st and 2nd a-Si layers will become one single layer) is also plotted in the figure and no absorption resonance exists near 500 nm wavelength. The phase tuning function of the added Si$_3$N$_4$ can be further confirmed by the strong reflection dip of the designed yellow colored NIR-transmitting structure when compared to the

69

reflection spectrum of the stacks without the 25 nm Si_3N_4 layer as depicted in Figure 5.2.11 (c). On the other hand, the very top thick Si_3N_4 serves as an AR layer that maintains the high NIR transmission, which can be clearly observed when comparing the transmission spectra of the stacks with and without the top 140 nm Si_3N_4 in the Figure 5.2.11 (c). The AR resonance occurs @728 nm as illustrated by the black solid cure in Figure 5.2.11 (b), where the net phase shift of the top Si_3N_4 is equal to a multiple of 2π. Figure 5.2.11 (d) provides the calculated electric field distribution inside the yellow device as a function of wavelength. Confined electric field within the short wavelength range inside the 1st and 2nd a-Si layers (#1 and #2 solid circles) corresponds to strong absorption @~500 nm as the optical absorption is directly proportional to the electric field intensity (Absorption $= (1/2)c\varepsilon_0\alpha n|E(x)|^2$, where c is the speed of light, ε_0 is the permittivity of free space, n is the real part of the refractive index, and is $\alpha = 4\pi\kappa / \lambda$ is the absorption coefficient with κ being the imaginary part of the refractive index). Absorption resonances also exist inside the other a-Si layers but with much weaker intensities (white dashed circle #A), which are well consistent with the absorption spectra provided in Figure 5.2.11 (a). In addition, the strong AR resonance beyond 700 nm inside the top Si_3N_4 effectively induce the NIR transmission as seen from the propagating modes in the underneath layers (black dashed elliptical circle #B). All the information extracted from the electric field distribution plot agrees well with the predictions of Figure 5.2.11 (a) – (c), thus validating the phase tuning and AR functions of additionally added thin and thick Si_3N_4 layers, respectively.
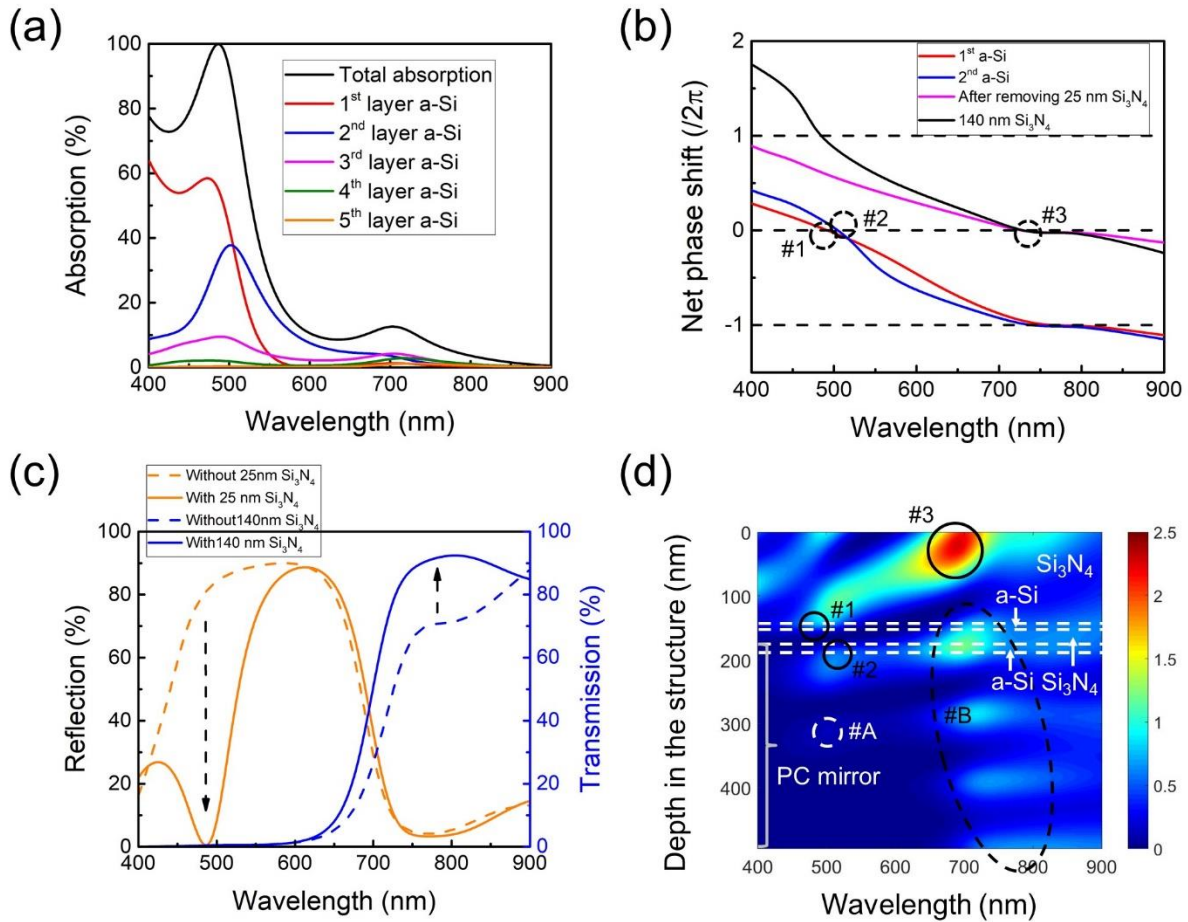
Figure 5.2.11 (a) Total absorption spectra and separate absorption in each a-Si layer. The absorption mainly occurs in the 1st and 2nd a-Si layers. (b) Calculated net phase shift analyzing the functions of the additionally added thin and thick Si_3N_4. (c) Spectra comparison of the stacks with and without thin (thick) Si_3N_4, clearly indicating the phase tuning (anti-reflection) function of the added Si_3N_4 layer. (d) Wavelength-dependent electric field distribution inside the whole structure. The strong field in the short wavelength range confined inside the 1st and 2nd a-Si layers directly results in the efficient absorption, thereby generating the decorative color. The additional added 140 nm Si_3N_4 atop effectively induces the strong NIR transmission by exciting AR resonances beyond 700 nm wavelength.

Similarly, due to the high refractive indices of both a-Si and Si_3N_4 employed in the designs, all the fabricated CMY colored devices present angular-insensitive performance that is highly-preferred in decorative applications. Figure 5.2.12 (a) – (c) provide the calculated angle-resolved reflection spectra of all three colors under unpolarized light illumination, which agree with the measured results presented in Figure 5.2.12 (d) – (f). The flat dispersion curves in both simulated and measured plots clearly indicate the excellent omnidirectional properties up to ±60°. Figure 5.2.12

71

(g) presents photographs of fabricated colored samples are taken at several observing directions, further validating the angle-robust decorative appearance.
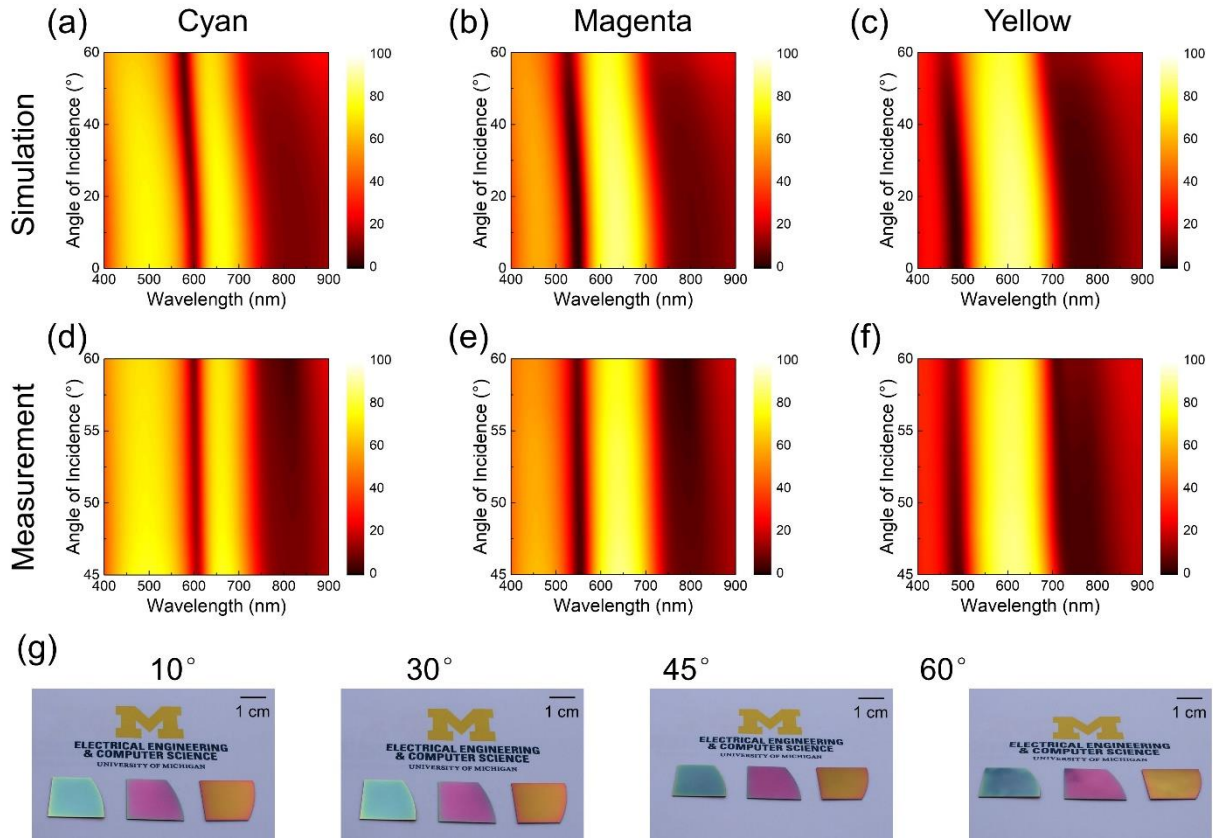
Figure 5.2.12 (a) – (c) Simulated angle-resolved reflection spectra for CMY colors under unpolarized light illumination. (d) – (f) The corresponding measured angle-resolved reflection spectra for three colored devices under unpolarized light illumination. The flat dispersion curves in both simulated and measured results indicated the great angular-insensitivity of our proposed structures. (e) Optical images of fabricated CMY colored samples at different observing angles under ambient light, validating the angular-robust colors desired for decorative applications. The scale bars are 1 cm.

5.3 Conclusion

In summary, we have experimentally demonstrated colored visibly-opaque but highly NIR-transmitting filters based on 1D ternary PCs. A wide variety of decorative reflection colors can be created without affecting the high NIR transmission performance, which is impossible with traditional PC structures based on transparent materials. Resulting from the high refractive index contrast between the materials employed in the design as well as the absorption loss of

72

semiconductors, the proposed NIR filter effectively blocks visible transmission with only 7 layers, which is far fewer than conventional schemes. It also exhibits great angle-robust performance up to ±60° irrespective of the polarization state of incident light at both top and back incidence due to the high refractive index of all the involved materials. With the fabrication simplicity where only the deposition step needs to be involved, the presented strategy offers an attractive route towards large-scale structural filters in a variety of applications such as imaging, displays, holography, and especially NIR-sensor decorations.

Chapter 6

Broadband and Wide-Angle Ultrathin Absorbers Based on Multi-Cavity Resonances

6.1 Introduction

In contrast to the aforementioned structural color filters where a sharp resonance with capabilities of filtering a narrow spectral range of visible light is highly desired for producing the colors with high purity, nanostructured 'perfect black', which can be regarded as a special color featuring highly-efficient and broadband absorption at the visible frequency, has also attracted substantial interest in different research fields.

In solar-thermal harvesting applications, broadband absorption covering most of the solar spectrum is in critical demand as one of the most important clean energies. For a compact imaging spectrometer based on multichannel filters, the perfect optical absorber is highly desired to prevent the crosstalk between the adjacent channels in the aerospace and semiconductor industries. In recent years, efficient optical absorption in the visible and NIR region, which can be potentially applied in fields of detecting, imaging, PVs, and so forth, have attracted enormous interests [182-201]. Among all the designs for the absorbers, broadband absorbers based on metamaterials and

transformation optics have been investigated widely and developed in many areas [190-199], whose absorptions are enhanced by the excitation of the surface plasmon resonance. Especially, the tapered structure consisting of alternating metallic and dielectric thin films is mostly discussed, which can be treated as a hyperbolic metamaterial (HMM) waveguide with varying width [197-199]. Zhou et al. theoretically verified that the broadband absorption of this structure constituted by these closely spaced resonances is formed between the top of the tapered stacks and the cutoff level in the waveguide [198]. As the shadow effect during the evaporation is subtly exploited to construct the tapered structure instead of the complicated process of focused ion beam milling, the time and cost of fabrication are significantly reduced. Liang et al. designed the broadest bandwidth of this structure, which covers a 1−14 μm region [199]. Apart from this tapered structure, Chen et al. proposed a broadband absorber of robust high absorption efficiency for the 900-1600 nm wavelength range by creating patterns of nanoparticles dispersed on a Au film spaced by a thin dielectric layer [202]. Bouchon et al. experimentally demonstrated that a patchwork of four metal−insulator−metal patches leads to an unpolarized wideband omnidirectional absorption constituted by corresponding absorption peaks [203].

However, all the broadband absorbers described above require either accurate controls or complicated procedures with multiple steps of nanolithography, reactive ion etching, e-beam lithography, or focused ion beam milling, severely limiting their practical applications especially in relatively large areas. Therefore, thin film devices have been pursued as an alternative approach [200, 204, 205]. The most common film stack in the previous studies is the MDM stack on a reflecting metal [200, 205]. The metal layer in the MDM stack is always selected from metals with strong optical absorption, such as chromium (Cr), titanium (Ti), and nickel (Ni), and the thickness of this layer is very thin, allowing multiple reflections within the structure and leading to strong

absorption. However, both the bandwidth and the absorption efficiency are still highly limited for NIR applications. Furthermore, the capability of absorbing a broad spectral range of light with high efficiency from any incident direction regardless of the polarization state of incident light, needed for numerous applications, remains significantly challenging.

In this chapter, we propose and experimentally demonstrate ultrathin (<500 nm) absorbers based on multi-cavity resonances in highly absorbing media using two different schemes. The first proposed visible absorber is capable of absorbing the light from 400 nm to 650 nm and comprises two stacks of a highly absorbing material and a metal showing 95.5% absorption at a resonance [41]. The second structure has a novel device configuration featuring a graded refractive index profile that allows the absorption of the device to be significantly enhanced (average absorption ∼98% from 400 nm to 2000 nm) by exploiting AR effects, while the ultrabroadband absorption characteristics are achieved by the designed tandem structure of three absorptive materials with resonances being strongly overlapped [42]. The absorption bandwidth can be further extended up to 3500 nm while maintaining the high absorption efficiency by inserting more semiconductor−metal stacks. Both devices exhibit high performance of the absorption that is insensitive to the angle of incidence as well as the polarization state of incident light. Besides of these features, only deposition method is involved to fabricate our designed absorber, thus providing a powerful scheme for achieving highly efficient device with relatively simple and cost-effective means for large scale that are distinctly different from those observed in the previous reports, involving expensive fabrication techniques such as e-beam lithography. Finally, we discuss the applicability of our proposed schemes to PV technologies for high efficiency PV cells. The strategies described here could have the potential for many applications, such as metamaterials, thermal emitters, and PV.

6.2 Broadband Visible Absorption by Stacking Multiple Cavities

A schematic view of the proposed visible absorber utilizing the multi-cavity resonance behaviors in ultrathin semiconductor layers featuring angle-insensitive and polarization independent broadband absorption property is depicted in Figure 6.2.1 (a). The device structure simply consists of two stacks of a metal and a semiconductor with its optimized thickness to achieve a broadband absorption characteristic with a high efficiency in the visible range. a-Si material is utilized as a highly absorbing medium due to its strong absorption property at visible frequencies, and Ag functions as a reflective mirror since it is highly reflective and has the lowest absorption loss among noble metals. Although the overall absorption could be even enhanced by employing lossy metals such as Al, Cu, and Cr, we aim at designing the structure with the improved absorption property only in the semiconductor layer, thus potentially extending the range of possible applications, including tandem PV systems. More detailed investigations on how the metal and the semiconductor layers affect the absorption behavior of the structure are given in Figure 6.2.2. In our absorber design, the thickness of a top metallic film is designed to be optically transparent (30 nm) so that it allows incident light to pass through a middle semiconductor layer to create an additional resonance at a different wavelength, thereby making the bandwidth broad, whereas a bottom metallic layer is 80 nm that is thick enough to prevent any transmitted light, thus validating the equation A = 1 − R, where A is the total absorption and R represents the reflection. In Figure 6.2.1 (b), a simulated absorption spectrum of the proposed four-layer device (red solid line) is described along with that of the three-layer device (blue solid line) without a top semiconductor film (*i.e.*, metal-semiconductor-metal (MSM)) for the comparison. As can be seen from the figure, our proposed device structure exhibits a much broad absorption performance with the higher efficiency (>95%), which arises from two distinctive resonances appearing at 490 nm and 575 nm,

while the MSM structure shows only one resonance peak with a lower absorption efficiency (61.5%) at 550 nm. Although the broadband absorption can also be achieved by a single thick a-Si layer, the charge recombination will be more dominant when the thick structure is applied for solar cells as the diffusion length of a-Si is only tens of nanometers. As a result, the final PCE will be greatly reduced. Based on this consideration, the thickness of a-Si solar cell is usually limited as <200 nm [109, 146, 206]. We note that the absorptions only in the semiconductor layers plotted by dotted lines are slightly lower than the overall absorptions of the device due to a small absorption loss of the Ag material. The simulated absorption spectra are calculated by the transfer matrix method with refractive indices of the Ag and a-Si measured by a spectroscopic ellipsometer (M-2000, J.A. Woollam), which are presented in Figure 6.2.3.

Figure 6.2.1 (a) A schematic diagram of the proposed broadband visible absorber with improved viewing angle employing multi-cavity resonances in ultrathin highly absorbing materials. (b) Simulated absorption spectra obtained from metal-semiconductor-metal (MSM) and semiconductor-metal-semiconductor-metal (SMSM) configurations. It is obvious that the absorption spectrum is greatly broadened by introducing an additional resonance for SMSM stacks as compared to the MSM structure.

Figure 6.2.2 Influence of (a) − (b) metals and (c) − (d) semiconductors on absorption spectra. A broad and high absorption property can be attained employing lossy metals, such as Au, Cu, and Al as shown in Figure 6.2.2 (a), however, the absorber structure with Ag metallic mirrors shows the highest absorption in a-Si layers among all the cases exhibited in Figure 6.2.2 (b), which is critical to achieve high efficiency PV devices. This is because a higher absorption only in the photoactive semiconductor layer is required for high performance PV cells. The bandwidth of the optical absorption can be broadened by using low band gap semiconductors, such as silicon-germanium (SiGe) and germanium (Ge), as depicted in (c) and (d). We note that it is difficult to observe the multi-cavity resonance phenomena in the Ge-based absorber structure due to its very large absorption coefficient at visible frequencies, yielding a very broad resonance. We should also note that an V_{oc} gets lower with the low band gap semiconductor materials although the broad absorption bandwidth, which corresponds to the high J_{sc}, could be obtained. The specific structures are [12 nm a-Si/30 nm Ag/24 nm a-Si/80 nm Ag], [10 nm a-Si/40 nm Au/20 nm a-Si/80 nm Au], [10 nm a-Si/45 nm Cu/20 nm a-Si/80 nm Cu], and [17 nm a-Si/15 nm Al/35 nm a-Si/80 nm Al] in (a) – (b), and [12 nm a-Si/30 nm Ag/24 nm a-Si/80 nm Ag], [12 nm SiGe/30 nm Ag/25 nm SiGe/80 nm Ag], [20 nm Ge/80 nm Ag] for (c) – (d).
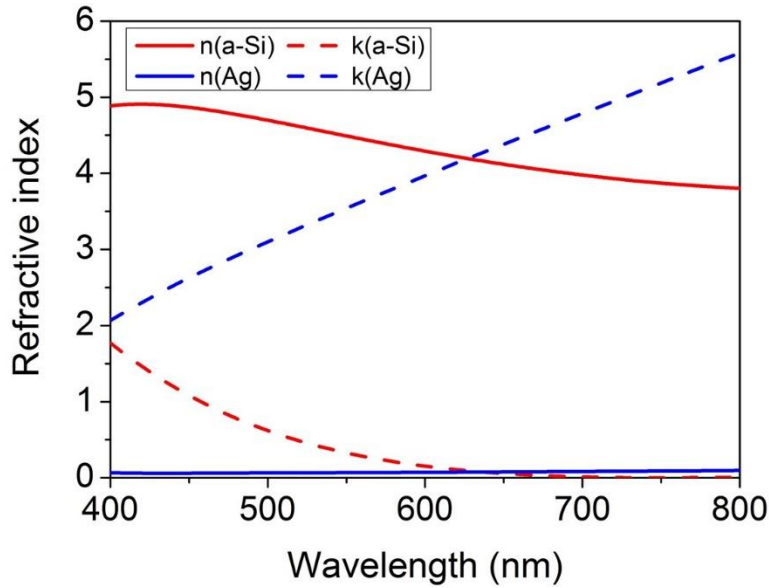
Figure 6.2.3 Refractive indices of thick Ag and a-Si (50 nm) materials, both of which are measured by a spectroscopic ellipsometer (M-2000, J. A. Woollam).

Figures 6.2.4 (a) and (b) show simulated and measured absorption spectra of the proposed absorber structure at normal incidence. The experimental reflectance is measured by using a film thickness measurement system (F20-EXR, Filmetrics) with a spectrometer and a white light source, and the absorption profile is then obtained from 1 – R relation and illustrated in Figure 6.2.4 (b) exhibiting great agreement with the simulated profile as shown in Figure 6.2.4 (a). As is seen from the figures, 95.5 (96.1) % and 94.3 (92.3) % of nearly perfect absorptions are achieved at 490 (493) nm and 575 (568) nm, respectively, from the simulation (experiment). The measured spectrum has a relatively broader profile than the simulated result, which is attributed to a non-even surface of actual films that induces the light scattering. In addition to the scattering, the refractive indices and the thicknesses in the experiment could be slightly different from those used in the simulation, causing a discrepancy between the measured and the simulated spectra. Noted that the resonance in the middle cavity (a-Si = 24 nm) is somewhat sharper than that of the top cavity (a-Si = 12 nm), which is attributed to strong reflections from both top and bottom metal-semiconductor interfaces

as compared with the reflection at air-semiconductor interface. A large absorption coefficient of the a-Si material at shorter wavelengths also contributes to the broad resonance at 490 nm. The Ag and the a-Si materials are deposited by a thermal evaporation and a PECVD, respectively. This suggests that the design principle discussed here could be easily scalable to large-area applications since it only involves the deposition without any patterning process.
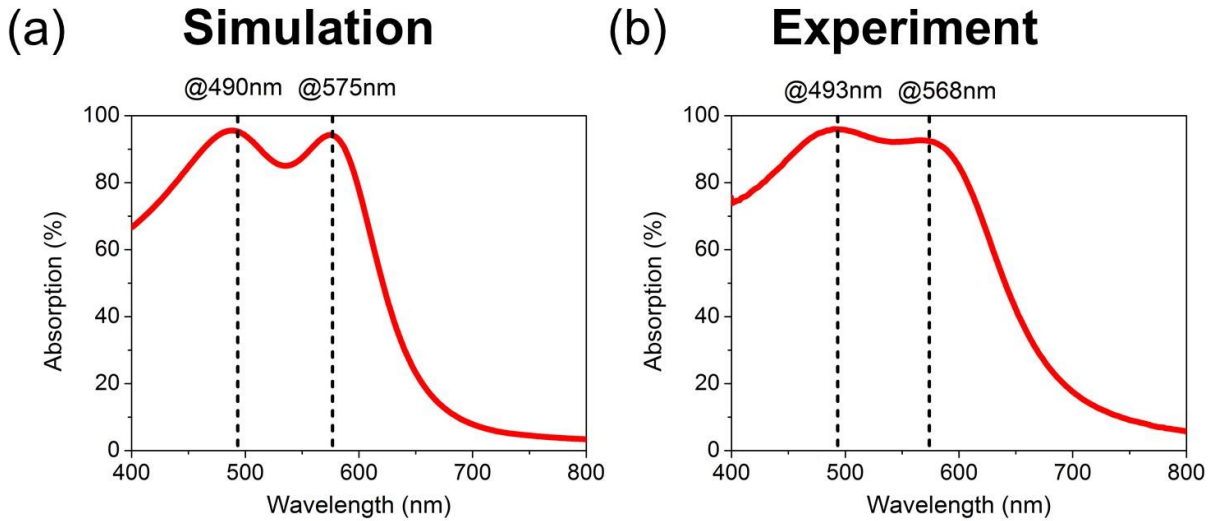
Figure 6.2.4 Simulated and measured absorption spectra of the proposed ultrathin broadband visible absorber at normal incident angle in (a) and (b), respectively, showing great agreement with each other. The broadband absorption profile arises from the multi-cavity resonances within the two a-Si layers.

To investigate the effect of the multiple resonances on the absorption spectra, the net phase shift is calculated as presented in Figure 6.2.5 (a). The propagation phase accumulation can be simply obtained with the equation $(2\pi / \lambda) \cdot 2nd\cos\theta$, where λ: the incident wavelength, n: real part of the refractive index, d: the thickness of semiconductor layer, and θ: the direction of wave propagation and is zero for the normal incidence, while the phase shift occurring upon the reflection from each surface can be calculated from the reflection coefficient for TE (TM) polarization, which is $r = \frac{r_{12} + r_{23}e^{2ik}}{1 + r_{12}r_{23}e^{2ik}}$ where $r_{ab} = \frac{n_a\cos(\theta_b) - n_b\cos(\theta_a)}{n_a\cos(\theta_b) + n_b\cos(\theta_a)}$ $(r_{ab} = \frac{n_a\cos(\theta_a) - n_b\cos(\theta_b)}{n_a\cos(\theta_a) + n_b\cos(\theta_b)})$ and $k = \left(\frac{2\pi}{\lambda}\right) n_2t_2\cos(\theta_2)$. It is noted that the net phase shift is divided by 2π, so it represents the number of cavity modes. The resonance

modes in the top a-Si cavity (blue line) appear at 496 nm (#1) and 591 nm (#3), where the net phase shift gets zero, indicating the fundamental resonance mode. Similarly, an additional absorption resonance is observed at 568 nm (#2) inside the middle a-Si cavity (red line). These resulting resonance wavelengths correspond well with the peak positions in the absorption spectrum shown in Figure 6.2.4. It is important to note that the relative sharp resonance at 575 nm could also be resulting from the overlapped resonance near that wavelength in each a-Si cavity (*i.e.*, top and middle cavities have the resonance at 591 and 568 nm, respectively). The calculated electric field distribution depicted in Figure 6.2.5 (b) further unveils the reason for the strong absorption at those resonances as the optical absorption is directly proportional to the electric field intensity (Absorption = $(1/2)c\varepsilon_0\alpha n|E(x)|^2$) [152]. It is obvious that the positions where the field intensity is highly concentrated in both the top and middle cavities, which correspond to strong absorptions, show great match with the resonance wavelengths in Figure 6.2.5 (a). Although it is shown that the electric field intensity at 496 nm (#1) is relatively lower than that at 591 nm (#3), the absorption performance at 496 nm could be still high due to the large absorption coefficient of the a-Si material at shorter wavelengths (*i.e.*, $4.71 + i0.65$ at 496 nm and $4.33 + i0.18$ at 591 nm). It is noted that even broader and higher absorption efficiency can be achieved by inserting a more number of stacks to create additional resonances at different wavelengths as shown in Figure 6.2.6.
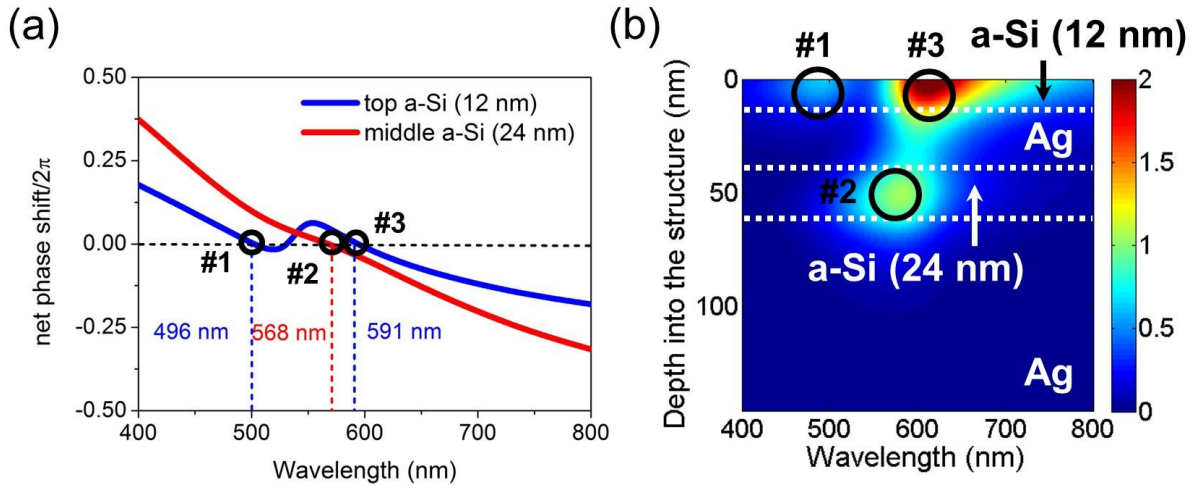
Figure 6.2.5 (a) The calculated net phase shift, which includes the two reflection phase shifts and the propagation phase shift, of both the top and middle a-Si layers as a function of the wavelength. The resonances occur at the wavelength where the net phase change is zero. (b) Electric field distribution within the whole structure at all wavelengths. The positions where the optical field is strongly concentrated and therefore the higher absorption is in good agreement with the positions of the multiple resonances in Figure 6.2.5 (a) as well as the absorption peaks shown in Figure 6.2.4.
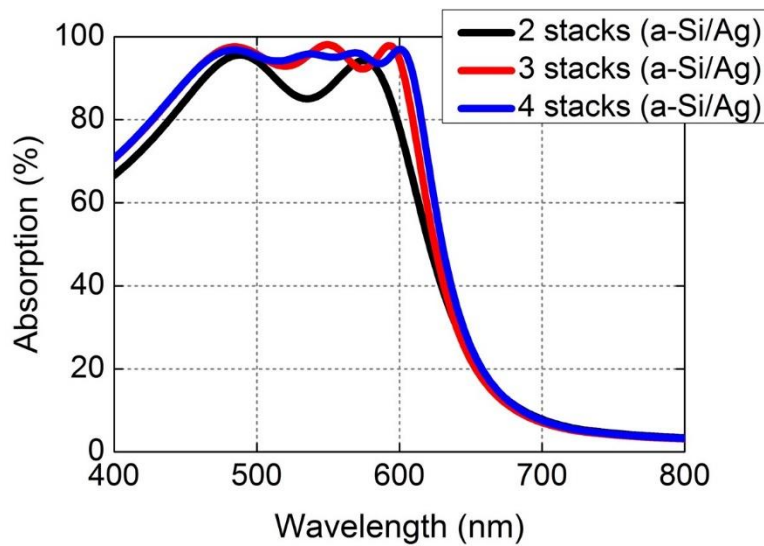
Figure 6.2.6 Calculated absorption spectra for a different number of a-Si/Ag stacks. The absorption efficiency can be improved with increased stack numbers by creating more resonances in other cavity systems. The specific structures are [12 nm a-Si/30 nm Ag/24 nm a-Si/80 nm Ag], [11 nm a-Si/32 nm Ag/25 nm a-Si/40 nm Ag/28 nm a-Si/80 nm Ag], and [11 nm a-Si/31 nm Ag/25 nm a-Si/36 nm Ag/27 nm a-Si/47 nm Ag/28 nm a-Si/80 nm Ag] for 2, 3, 4 stacks of a-Si/Ag, respectively.

Next, we examine the dependence of the absorption efficiency on the thickness change in the top

Ag and the top a-Si layers. In Figure 6.2.7 (a), a calculated 2D contour plot of the optical absorption

as a function of the top Ag film thickness and the wavelength is shown, given fixed thickness of

the top a-Si layer as 12 nm. The multiple resonances get shifted as the thickness of the top Ag layer varies, which is a direct consequence of varied reflection phase shifts at the interface between the top Ag film and the a-Si layer. When the top Ag becomes thinner, the resonances move farther apart and finally merge into a single resonance in the case that the Ag is so thin that the separation between the a-Si layers cannot be perceived by the propagating light. As the thickness of the top Ag film increases, the intensity of the reflected light gets higher, thus leading to a high Q-factor (*i.e.*, narrow bandwidth with high efficiency). Similarly, the influence of the top a-Si thickness on both the absorption efficiency and the bandwidth is also investigated with the top Ag fixed at 30 nm as shown in Figure 6.2.7 (b). The multiple resonances are separated when reducing the thickness of the top a-Si film as the resonance is created at shorter wavelengths with decreased cavity layer thickness. In contrast, with increased thickness of the top a-Si layer, the multiple absorption peaks get closer since the resonance inside the top a-Si film moves toward the longer wavelength range, where the resonance of the middle cavity exists as analyzed above. From this investigation, it is found that the optimal thicknesses for the top Ag and the top a-Si are 30 nm and 12 nm, respectively, in order to achieve the highest absorption performance.
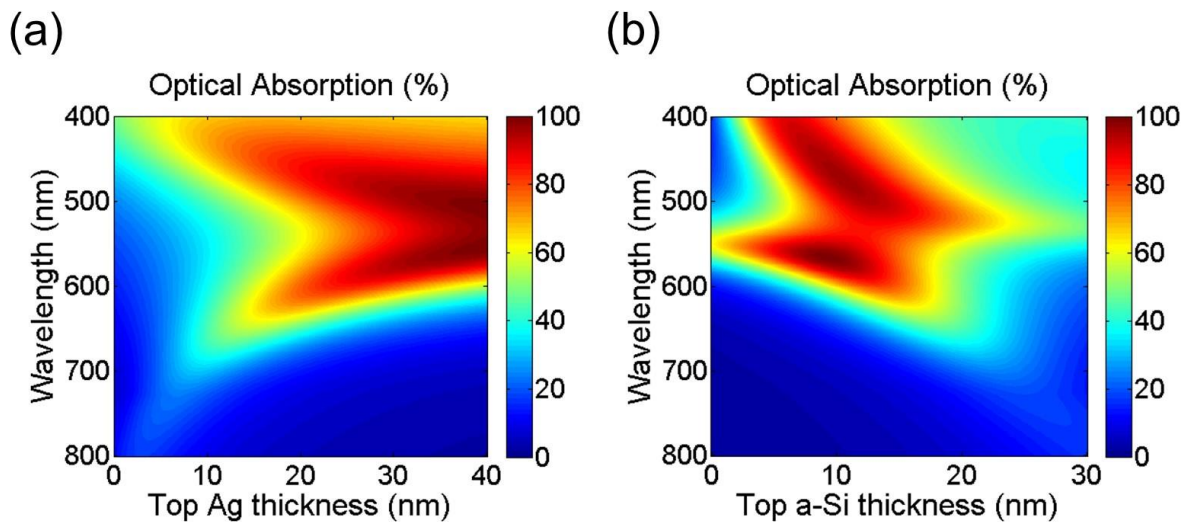
Figure 6.2.7 The dependence of the thickness of (a) the top Ag and (b) the top a-Si on the optical absorption characteristics. Both the absorption efficiency and the bandwidth vary with the top a-Si-Ag stack thickness and the highest absorption efficiency is achieved when the top Ag and the top a-Si layers are designed to be 30 nm and 12 nm, respectively.

Simulated and measured angular dependences for both TE and TM polarizations are shown in Figures 6.2.8 (a) – (d), respectively. The resulting angle resolved absorption spectra of the fabricated device are measured by the spectroscopic ellipsometer (M-2000, J.A. Woollam) at the angle of incidence ranging from 45° to 70° exhibiting good agreement with the simulation. A highly efficient absorption characteristic encompassing the wavelengths from 400 nm to 650 nm is accomplished over a wide range of incident angles up to ±70°. Note that the bandwidth of the optical absorption of our proposed absorber is limited to some extent as it is difficult for the a-Si material to capture wavelengths beyond 650 nm due to its band gap. We also note that the range of the absorption could be broader by utilizing either low band gap semiconductors or lossy metals. The angle insensitive performance could be explained by the fact that the phase shift accumulated during the propagation through the ultrathin a-Si layer is almost insignificant because the a-Si film thickness is much thinner than the wavelength of incident light [108, 109, 146, 148, 207-209]. Such an angle robust functionality is greatly crucial for a wide variety of applications, such as PV, photodetectors, and thermal emitters.
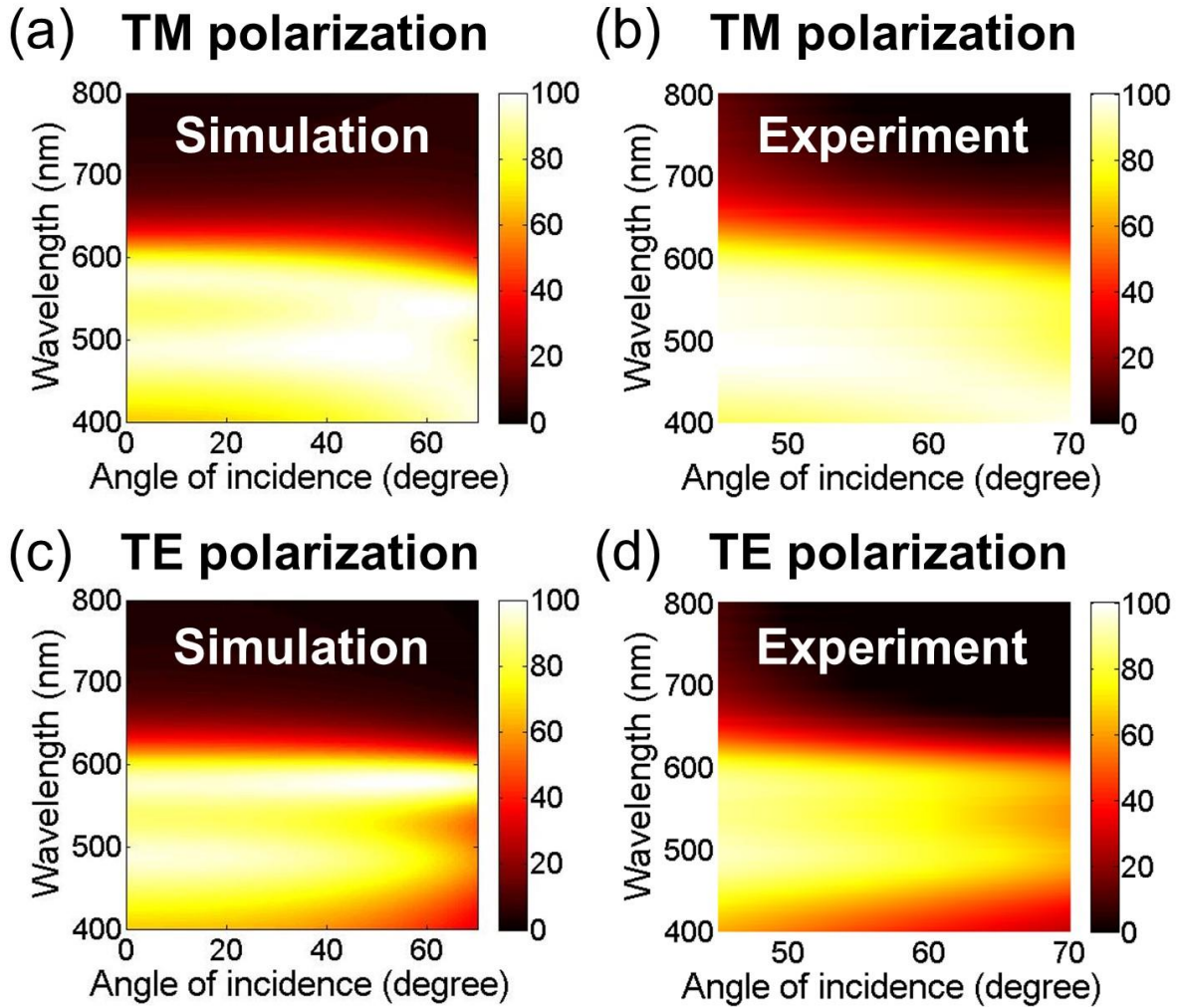
Figure 6.2.8 Simulated and measured angle resolved absorption spectra for (a), (b) TM and (c), (d) TE polarizations up to 70°. The angle insensitivity of the proposed broadband absorber is enabled by the negligible propagation phase accumulation within the ultrathin a-Si layers, showing a flat dispersion curve.

Finally, we explore the possibility of applying our strategy to tandem PV cells. Figure 6.2.9 (a) depicts the schematic diagram of the tandem-mimicking ultrathin a-Si PV that can be realized by placing our proposed broadband absorber structure onto the ITO-glass. It should be noted that efficient hole and electron transporting layers, such as vanadium pentoxide (V_2O_5) and indene-C60 bisadduct (ICBA), need to be inserted for this structure to operate as the PV device with a better band alignment as discussed in the previous works [109, 146]. In Figure 6.2.9 (b), simulated absorption spectra in top (black) and middle (red) a-Si photoactive layer are shown. When the

device is illuminated from the ITO-glass side, the top cell (#1, a-Si = 13 nm) mainly harvests the

shorter wavelengths (*i.e.*, blue ranges), while the middle cell (#2, a-Si = 31 nm) strongly absorbs

the green spectral regions, thereby spanning a broad range of visible wavelengths toward high PCE.

We note that the absorption beyond 650 nm is limited by the a-Si material. The calculated J_{sc}

values in each cell are found to be 5.62 mA/cm^2 (#1) and 5.64 mA/cm^2 (#2), respectively, using

the following equation:

$$J_{sc} = \int_{400 \text{ nm}}^{800 \text{ nm}} \frac{e\lambda}{hc} QE(\lambda) I_{AM1.5}(\lambda) d\lambda \, ,$$

where e, h, λ and c are elementary charge, Plank constant, wavelength, and speed of light,

respectively. $I_{AM1.5}(\lambda)$ is AM 1.5G solar radiation spectrum. We assume that $QE(\lambda)$ is equal to the

optical absorption spectrum in the photoactive layer (*i.e.*, internal quantum efficiency is 100%).

Since the photoactive layer whose thickness is much thinner than a carrier diffusion length of the

a-Si material is used in our design, 100% of internal quantum efficiency would be good

approximation due to a nearly negligible charge carrier recombination [109, 146]. Figure 6.2.9 (c)

exhibits the calculated absorption spectra in the photoactive layer of our proposed tandem PV cell

together with the single layer based PV device with the same active layer thickness (total a-Si =

44 nm). It is clear that the spectrum broadening mechanism with the multiple resonances allows

the absorption property of the tandem PV device to be significantly enhanced, which can result in

a PCE of 4.50%, more than twice higher than the PCE of the PV cell with the single photoactive

layer (2.12%). These PCE values are estimated with the assumed 64% FF and V_{oc} 0.60 V and 0.65

V, all of which were taken from our previous work [109].
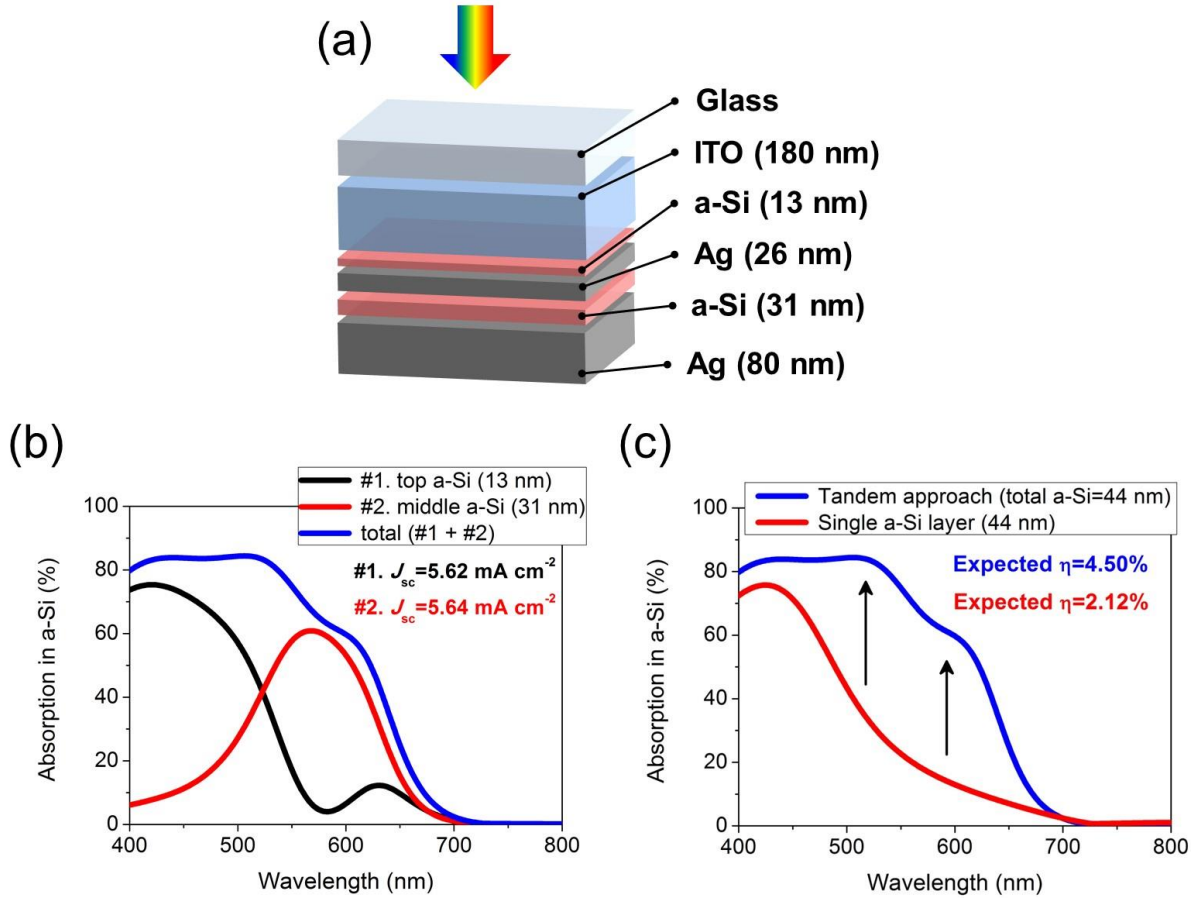
Figure 6.2.9 (a) A schematic representation of the proposed tandem-mimicking ultrathin a-Si PV device, which could be made on ITO-glass. (b) Simulated absorption spectra in both top (black) and middle (red) a-Si photoactive layers along with the calculated corresponding J_{sc} values. The top cell (#1), which has the thinner thickness than the middle cell (#2), primarily captures the shorter wavelengths of solar radiation, while #2 harvests the green portion of solar energy, thus being able to achieve the broadband absorptions for high efficiency. Note that it is difficult for the a-Si material to absorb the longer wavelengths beyond 650 nm due to its band gap. (c) Simulated absorption spectra in the photoactive layer of the tandem-mimicking a-Si PV cell and the single a-Si layer based PV, both of which have the same total photoactive layer thickness, clearly exhibiting that our proposed tandem approach can significantly boost the absorption in the photoactive layer, thereby leading to higher PCE. J_{sc} is calculated assuming that the internal quantum efficiency is 100 % and both FF and V_{oc} are taken from our previous work to estimate the efficiency.

6.3 Ultrabroadband Absorbers Employing Gradient-Index Multilayers

Due to the absorption capability of a-Si in the above design, the structure absorbs only a limited

portion of solar energy. We proposed another novel design that can efficiently harvest the whole

wavelength range of sun radiation (up to 2000 nm) with the average absorption ~98%.
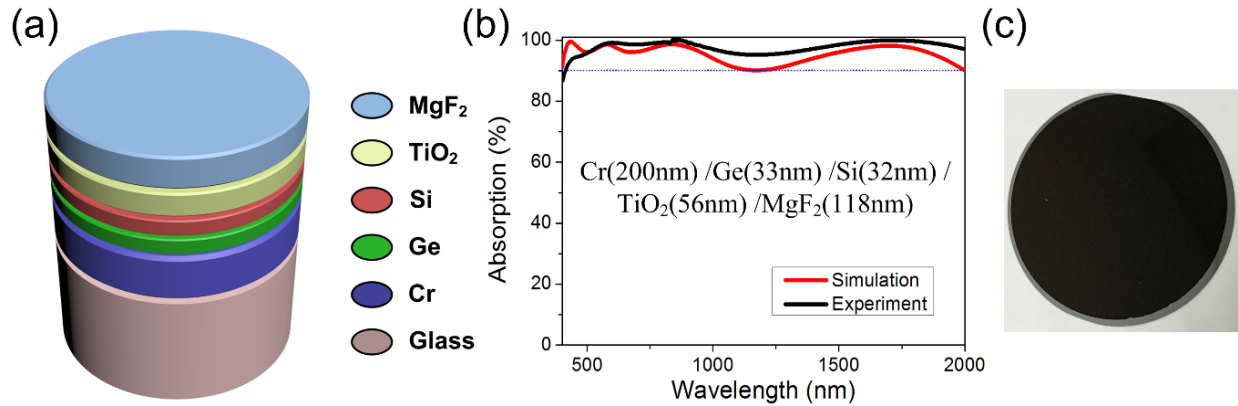
Figure 6.3.1 (a) The schematic diagram of the proposed efficient ultrabroadband absorber. (b) The simulated and the measured absorption of the proposed absorber targeted for 400-2000 nm range (Film stack 1). (c) A photograph of the fabricated absorber device under normal incidence.

Figure 6.3.1 (a) depicts a schematic diagram of the proposed ultrabroadband and omnidirectional absorber where four thin dielectrics and semiconductors are placed on top of an optically thick metallic substrate. Multiple resonances in each dielectric and semiconductor film at different wavelengths are established, and the overlap of these resonances enables broadband absorption up to 2 μm, which is much longer than the state-of-the-art solar thermal absorber [200, 201, 205], especially than that (400 nm to 1.4 μm) reported in ref. [200]. It should be noted that the bandwidth can be further widened by inserting more semiconductor−metal stacks, which will be discussed in the later section of this paper. To achieve highly efficient absorption characteristics over a broad range of wavelengths, an absorptive metal with a high refractive index and extinction coefficient is selected as the bottom metal layer. Although Cr is chosen for the demonstration in our work, other absorptive metals, such as Ti, iridium (Ir), tungsten (W), Ni, or their alloys can also be used (see Figure 6.3.2) to attain a similar property. Reflective metals, such as Ag, can also be utilized as the substrate if the absorption needs to be mostly confined within the semiconductor layers, which is required by PV applications (see Figure 6.3.3). Considering the absorption $A = 1 - R - T$ with R being the reflectance and T being the transmission, the bottom metallic film is designed

89

to be thick enough (>100 nm) to block any transmitted light so that a perfect absorption property is equal to a zero-reflection property in our system. Four dielectric and semiconductor layers, Ge, Si, TiO$_2$, and magnesium fluoride (MgF$_2$), are subsequently deposited on top of the metallic substrate to create a graded index profiled stack that produce the AR effect, while highly absorbing materials (*i.e.*, Si and Ge) are responsible for the strong absorption at shorter wavelengths. It is important to mention that other dielectric materials with a similar optical constant can be utilized to replace TiO$_2$ (*e.g.*, by hafnium dioxide (HfO$_2$) or tantalum pentoxide (Ta$_2$O$_5$)) and MgF$_2$ (*e.g.*, by SiO$_2$ or yttrium lithium fluoride (YLiF$_4$)), which is given in the Figure 6.3.4.
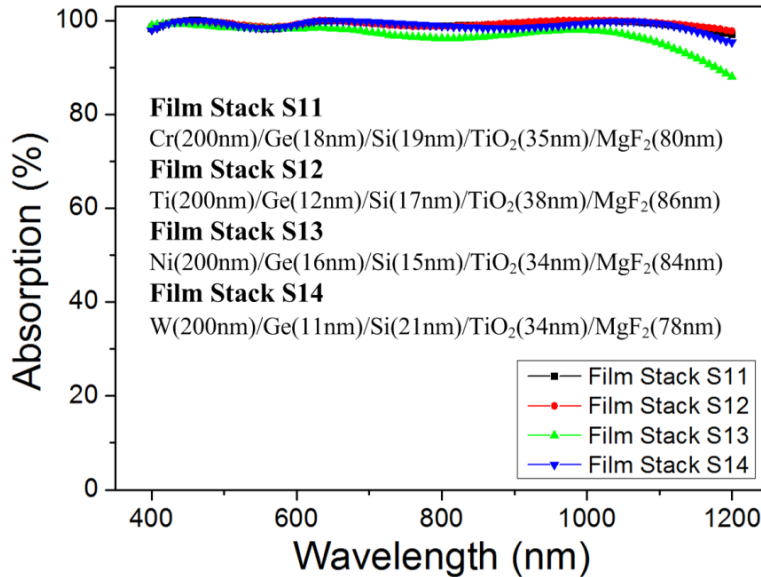
Figure 6.3.2 The absorption spectra of the 5-layer structure with various alternative metals. Similar high efficiency absorption can be achieved with different absorptive metals. The slight degradation of absorption spectra for Ni at long wavelengths is due to the weak index mismatch of the graded layers.
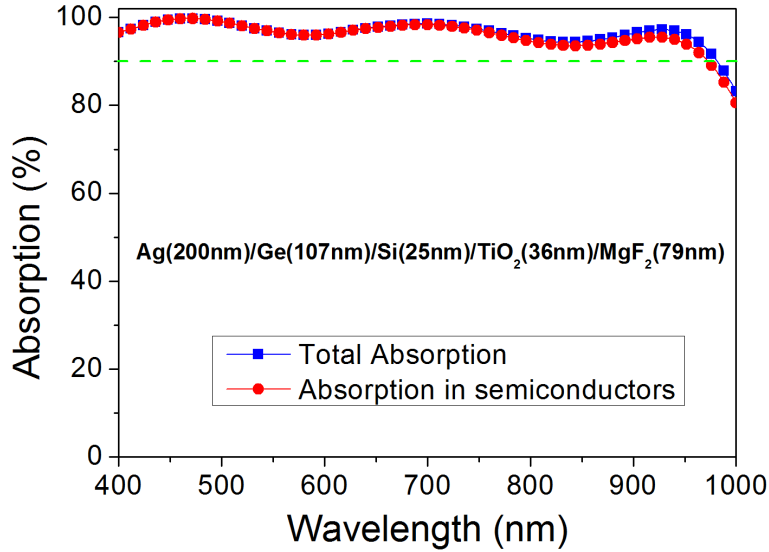
Figure 6.3.3 The absorption spectrum of the proposed structure with the bottom absorptive layer replaced by reflective metals, here Ag, which is potentially applied for the PV applications to make the absorption mostly confined within the semiconductor layers.
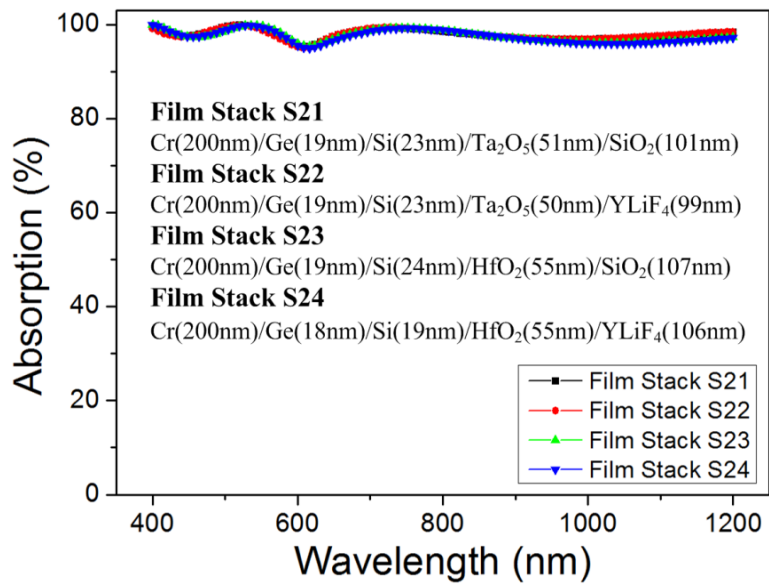
Figure 6.3.4 The absorption spectra of the 5-layer structure with different alternative materials of intermediate layers. Anti-reflection result, which is equal to the high absorption here without any transmission, can be achived as long as the refractive indices are graded from bottom to top, which provides more freedom for our designs.

For many solar-related applications, such as PV, thermoPV, solar-thermal energy conversion, and solar control glazing windows, achieving high-efficiency broadband absorption characteristics over the full solar spectrum, spanning from UV to NIR, is highly desired. Targeting at the best

91

absorption behavior over the broad wavelength ranges from 400 to 2000 nm, the required dimension parameters of the device structure are designed by the transfer matrix method. The thickness of each layer is found to be 118, 56, 32, and 33 nm for MgF_2, TiO_2, Si, and Ge layers on the thick Cr metallic substrate. In the device fabrication, the stack was successively deposited by e-beam evaporation with the substrate kept at 150 °C to obtain dense films. Figure 6.3.1 (b) shows the calculated and measured absorption spectra of our proposed device at normal incidence, showing great agreement with each other. The average absorption from the simulation and the experiment for wavelengths from 400 to 2000 nm is 95.37% and 97.76%, respectively, both of which show very high absorption efficiency. The slight discrepancy between the measured and calculated results is primarily due to the refractive index values for both Cr and Ge materials, which are sensitive to the preparation condition and quite different from the bulk data in the literature [210]. We should also note that our device design can be modified to apply to areas such as aerospace applications (*e.g.*, to eliminate stray light) and consumer electronics applications of visible-IR detections, all of which require the perfect absorption of wavelengths from 400 to 1200 nm. This can be easily enabled by slightly decreasing the thickness of each layer, which moves the resonances toward the shorter wavelength region (see Figure 6.3.5). Figure 6.3.1 (c) presents a photograph of the fabricated device taken at normal incidence, showing a totally black appearance due to the broadband absorption behavior.
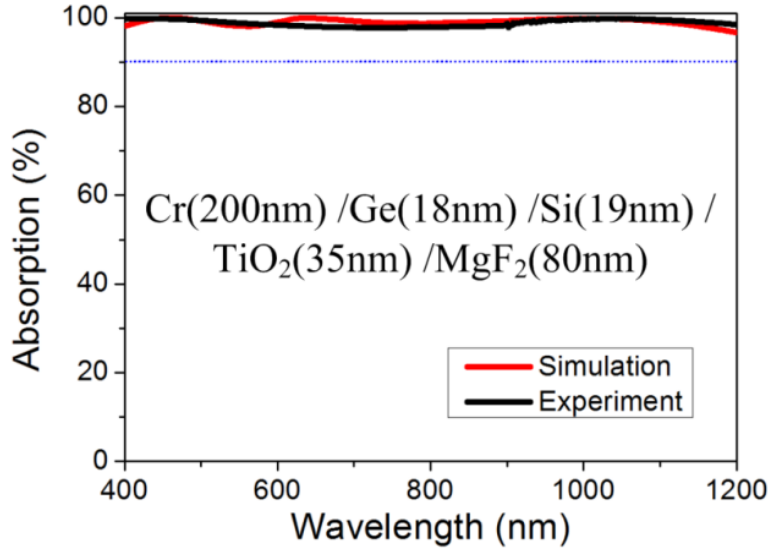
Figure 6.3.5 The simulated and measured absorption of the proposed absorber based on the 5-layer structure targeted for 400-1200 nm range. The calculated average absorption across 400-1200 nm region is up to 99.14% while the measured average absorption reaches 98.90%.

We also explored the angular dependence by both simulation and experiment. The calculated and measured angle-resolved absorption spectra under unpolarized light illumination are displayed in Figure 6.3.6 (a) and (b), obviously presenting a high angular tolerance feature up to 60° with little variation of the absorption efficiency. To clearly see the effect of the incidence angle beyond 60° on the absorption efficiency of our device, the average absorption efficiency for both the simulation and the experiment is plotted as a function of the incidence angle ranging from 0° to 70°, as shown in Figure 6.3.6 (c). It is clear that the average absorption of our design varies very little up to 40°, while the average absorption efficiency gradually decreases as the incidence angle (greater than 40°) increases further. It is shown that less than a 5% decrease of the average absorption can be kept up to 60°. The optical absorption efficiency is still higher than 80% even at a very large angle (70°). Figure 6.3.6 (d) exhibits optical images of the fabricated device taken under indoor ambient light illumination (unpolarized light) at three different angles up to 60°, clearly showing a black color with negligible reflection. Clearly, the absorber shows a robust

angular insensitivity property, which is attributed to the broad resonances. In addition, the designed absorber structure consists of two semiconductors with a high refractive index (*i.e.*, Ge and Si), which can lead to a very small angle of refraction into the structure by Snell's law ($n_1\sin\theta_1 = n_2\sin\theta_2$) at IR ranges [15, 211]. The strong resonance effects in ultrathin highly absorbing media (*i.e.*, Ge and Si) appearing at visible frequencies [148], where the phase cancellation effect between the propagation phase shifts through the ultrathin semiconductor films and the reflection phase from the metal film, contribute to the angle-invariant characteristics [108, 109].
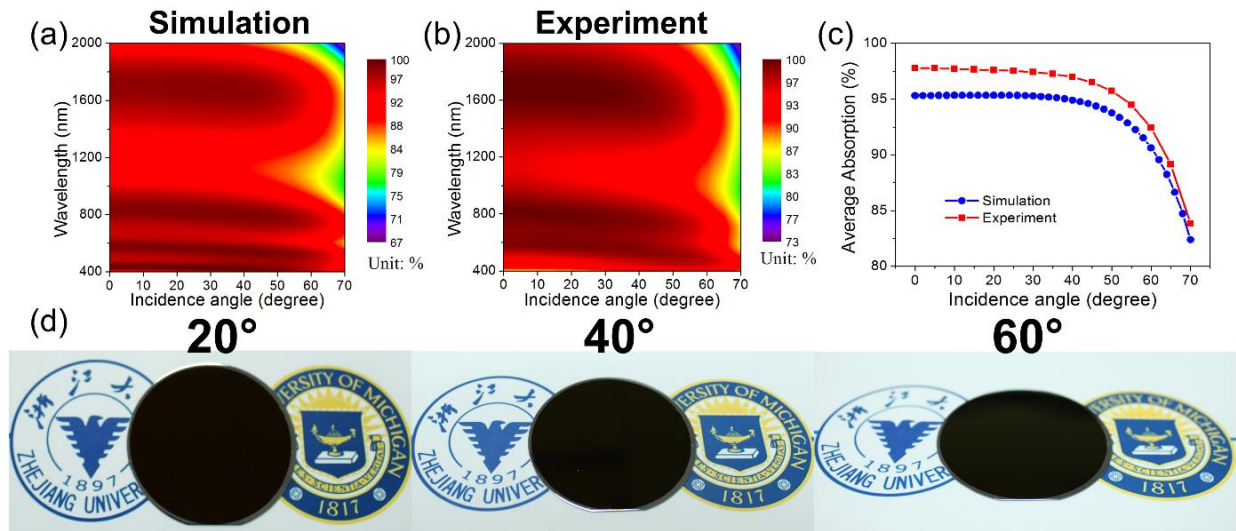
Figure 6.3.6 (a) The simulated incident angle resolved spectrum response of the ultrabroadband absorber. (b) The measured incident angle resolved spectrum response of the ultrabroadband absorber. (c) The simulated and measured average absorption of the proposed ultrabroadband absorber for Film stack 1 at different incident angles. (d) The optical images of the fabricated absorber taken with indoor ambient light at oblique incidence of 20°, 40°, 60°. The diameter of the fabricated device is 2 inches.

We also examine why our absorber structure exhibits highly efficient absorptions. As there is no transmitted light due to the thick metallic substrate, the high absorptions correspond to the low reflections, which can be studied by the optical admittance (inverse of the impedance) at different wavelengths [116]. Figure 6.3.7 shows the optical admittance locus of our absorber as the thicknesses of the different films increase. At long wavelengths, the Ge/Si/TiO$_2$/MgF$_2$ combination forms a typical graded index profile of broadband antireflection coatings for the Cr substrate,

94

where the Cr film has the largest refractive index ($n > 4$, $k > 5$) at 839, 1175, and 1710 nm. So, the overall admittance gradually turns small and is finally close to (1, 0), *i.e.*, the index of the incident medium, air. However, the refractive index of Ge is larger than Cr at short wavelengths of 434, 496, 580, and 686 nm. Thus, it is Ge/Cr, rather than the single Cr layer, that has the largest effective admittance, and the admittance of the whole structure is reduced gradually to 1 by Si/TiO$_2$/MgF$_2$ layers as AR coatings (ARCs). The graded index profile results in a smaller effective admittance so as to reduce the reflectance of the whole structure gradually. In Figure 6.3.7, the length of the black lines (*i.e.*, distance between the termination point and the air) provides a measure of the reflectance of the structure for some wavelengths and is very small for all cases, which is attributed to the graded refractive index profile producing the broadband AR effects. The reflectance of the stack at the corresponding wavelength is calculated by the Fresnel reflection formula and then inserted at the bottom-left corner of each plot in Figure 6.3.7.
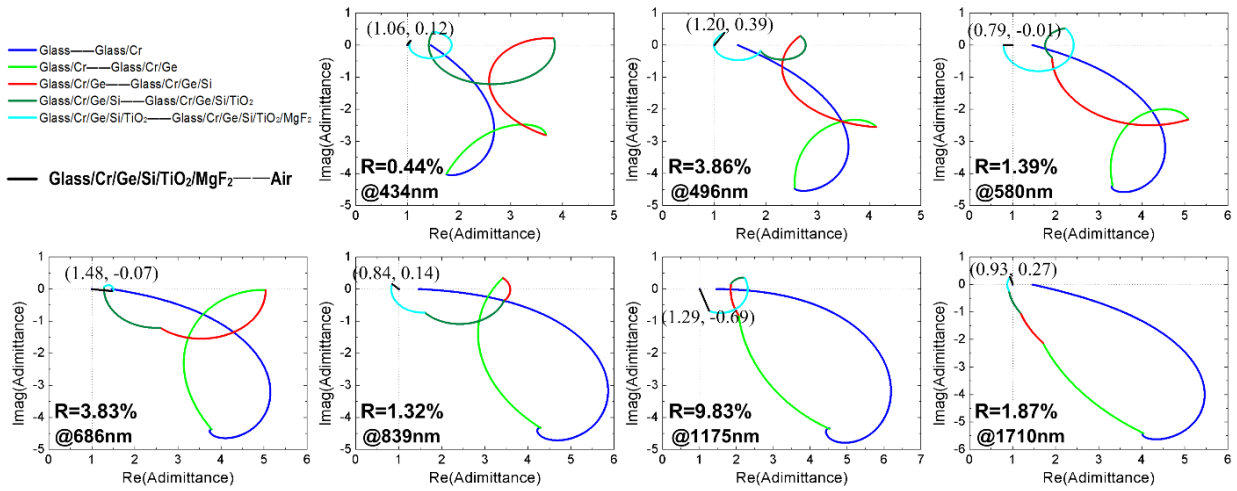
Figure 6.3.7 The optical admittance locus of the ultrabroadband absorber for Film stack 1 at each peak reflectance wavelengths and valley reflectance wavelengths. The length of the black line provides a measure of the reflectance of the structure. The reflectance marked in the figure is calculated by the Fresnel reflection formula with the acquired equivalent admittance.

The ultrabroadband absorption mechanisms are further investigated by studying the main absorptive layers at different wavelengths. A transition of absorption layers from Si to Cr when

moving to longer wavelengths is clearly identified. Since the upper TiO_2 layer and MgF_2 layers are lossless in the visible and NIR range, they do not contribute to the absorption but act as the graded index layers for the AR and assist in additional resonances. The absorption takes place in the three lower layers, Si, Ge, and Cr layers, particularly at shorter wavelengths. The absorption distribution profiles of the proposed structure at different wavelengths are shown in Figure 6.3.8. Intuitively, as the wavelength increases from the visible to the NIR, the main absorption layers change from Ge/Si layers, to a Ge layer, then to Cr/Ge layers, and eventually to a Cr layer only. This can be easily understood by examining the refractive indices of the layers at various wavelength ranges. From the refractive indices given in Figure 6.3.9, we can see that the extinction coefficient of Ge and Si is relatively large from 400 to 500 nm, which makes the Ge and Si layers the main absorption layers within a short wavelength range. As the wavelength increases, the extinction coefficient of Si decreases while that of Ge still remains high, which results in only the Ge layer contributing to the absorption. When the wavelength is longer than 750 nm, the extinction coefficient of Ge decreases while Cr becomes more absorptive with a higher extinction coefficient; thus, the main absorption layers turn to both the Cr layer and the Ge layer. When the wavelength further goes beyond 1200 nm, Ge becomes transparent; therefore, the absorption occurs only within the Cr layer. On the basis of results in Figure 6.3.8 together with those of Figure 6.3.7, each of the absorptive materials is responsible for the prefect absorption at specific wavelengths forming the overlapped absorption, whereas the various resonances within corresponding transparent layers on top of those lossy media help to enhance the absorption by increasing the transmission into the absorptive layers with graded indices.
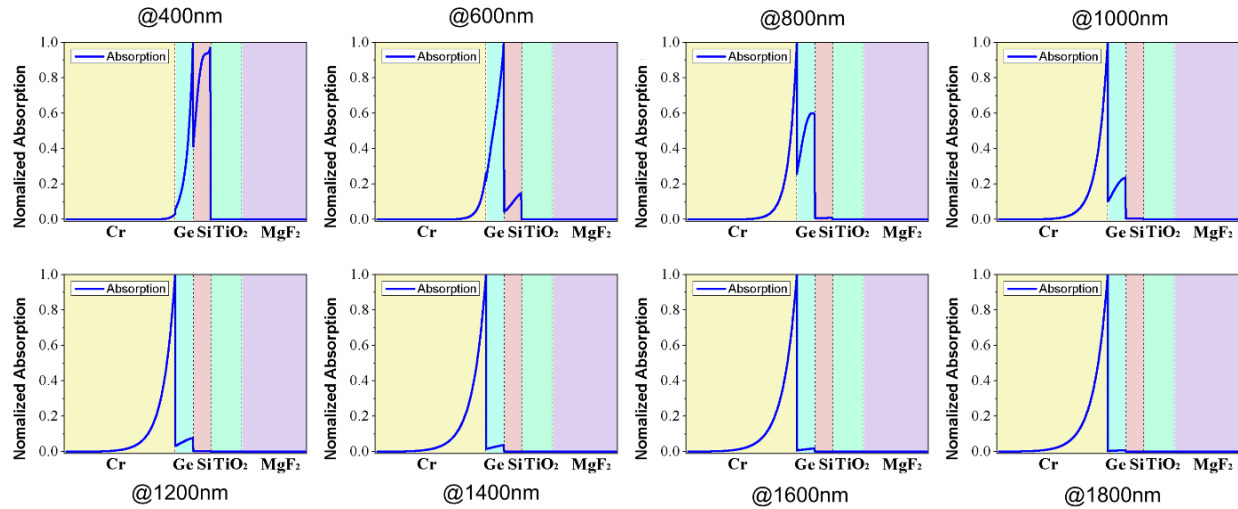
Figure 6.3.8 The layer absorption distribution profile of the ultrabroadband absorber for 5-layer structure at different wavelengths, showing the shift of absorption layer from Si to Cr with increasing wavelength.
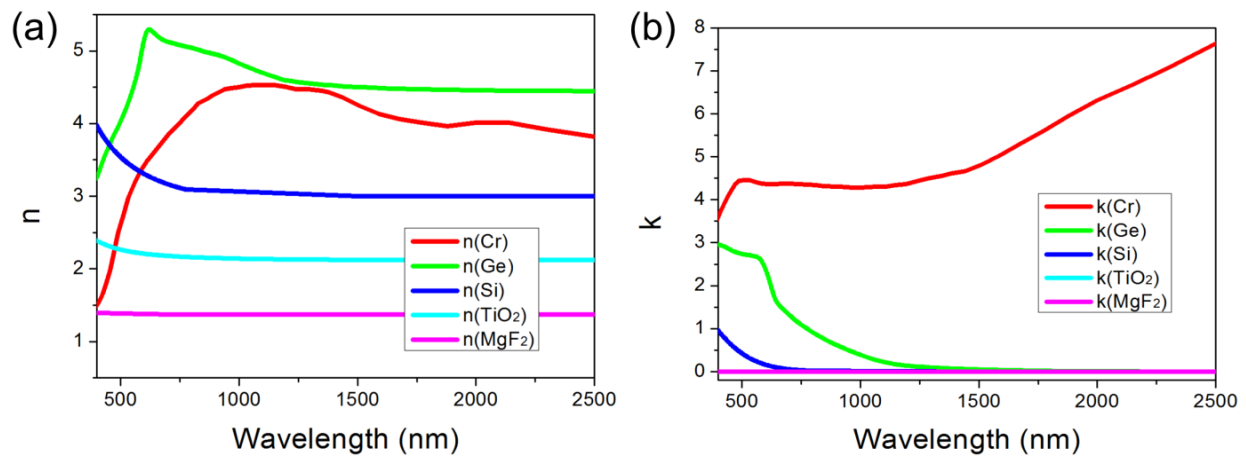
Figure 6.3.9 The optical constants of the material used in the simulation. The data of Cr comes from Palik while other materials were obtained by spectrometry method or ellipsometry method.

On the basis of the explanations including the antireflection effect in Figure 6.3.7 and the tandem absorptive materials aimed for a specific wavelength region in Figure 6.3.8, the physical origin of the ultrabroadband absorption of our design is further elaborated here. A simplified film stack composed of the thick chromium layer and the ARCs is described in Figure 6.3.10 (a), where the extinction coefficients of Ge and Si are assumed to be zero, while the optical constants of TiO_2 and MgF_2 remain invariant, as shown in Figure 6.3.9. By adding the ARC, the reflectance of the

97

device is significantly reduced compared with that of the single thick chromium layer, as shown by the red dotted line. For the wavelengths beyond 1200 nm, the reflection remains the same whether Si and Ge are assumed absorptive or not, which means that the reflection valley at 1710 nm is caused only by the antireflection effects on the absorptive Cr layer. Besides, the reflectance for the 600-900 nm region and the 400-600 nm region can be greatly suppressed when the non-absorptive hypothetic material is substituted by the actual Ge and Si with absorption, as seen by the blue and green dotted lines, respectively, verifying the tandem absorption property in Figure 6.3.8. Moreover, we investigate net phase shifts to explore the absorption resonances induced by Ge and Si layers, shown in Figure 6.3.10 (b). As can be seen from the figure, the resonances in each cavity layer, where the net phase shift is equal to a multiple of 2π, correspond to the absorption peaks in Figure 6.3.1 (b). Note that although the ultrathin highly absorbing media are much thinner than the quarter wavelength of incident light ($h << \lambda/4n$, where h denotes the thickness of the spacer, λ is the resonant wavelength and n represents the refractive index of the spacer), the nontrivial phase shift associated with the reflections from the interface between semiconductor (air) and non-ideal metals (*i.e.*, finite conductivity) makes up the difference [148]. The positions of the resonances are indicated as the intersection of the dashed and solid lines, all of which correspond exactly to the valley in the reflection spectrum (red scatter line). It is obvious that creating the resonances in different semiconductor materials at different wavelengths (*i.e.*, overlapped resonance behavior) leads to a very strong absorption that corresponds to the reflection dip. For example, the reflection valleys near 434 and 580 nm, which are represented by (1) and (2), respectively, result from the strong resonance absorption of the Si layer. At the long-wavelength region near 1710 nm (4), where all semi-conductive and dielectric layers turn transparent, the resonances within the Ge and Si layers indicating the strong absorption of the

single Cr substrate are achieved by the enhanced transmission resulting from those resonances within transparent layers, *i.e.*, antireflection effects. Similarly, the reflectance dip at 839 nm (3) resulted from the antireflection effects induced by the $Si/TiO_2/MgF_2$ stack and the correspondingly enhanced absorption within the Ge layer, which can be seen in Figure 6.3.10 (a). So the resonances of the tandem structure comprising diverse absorptive materials and the antireflection property arising from the graded index profile structure both contribute to the ultrabroadband absorption with high efficiency of this structure.
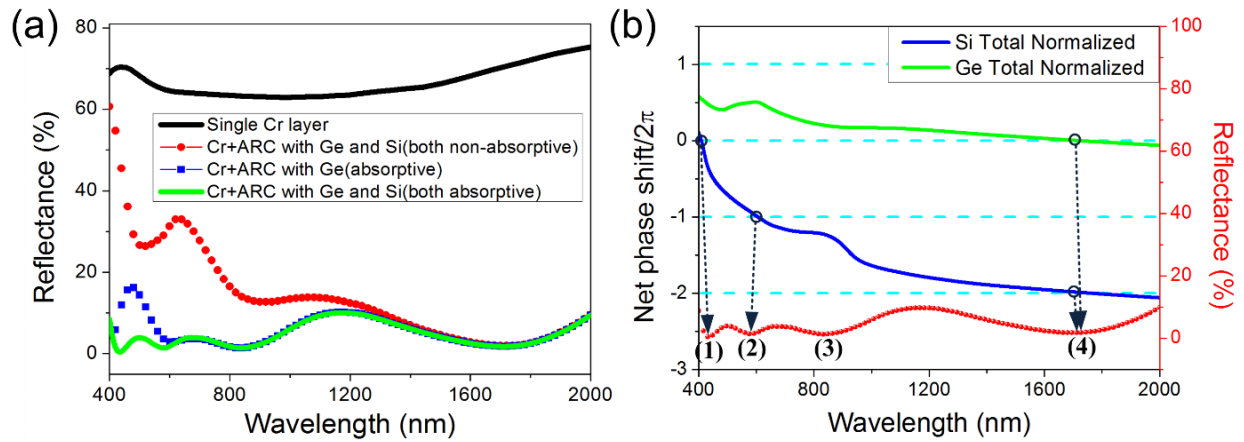
Figure 6.3.10 (a) The reflectance of the proposed structure with different materials: practical absorptive materials or non-absorptive hypothetic materials. ARC: $Ge/Si/TiO_2/MgF_2$ where the extinction coefficients of Ge and Si is set artificially while the optical constants of TiO_2 and MgF_2 remain invariant as shown in Figure 6.3.9. (b) The net phase shift in each absorptive layer of Film stack 1 and the corresponding reflectance curve. The resonances indicated by the phase shift curves (the net phase shifts are equal to the multiple of 2π) are in great consistency with the reflection dips.

For the solar-harvesting energy applications, it is highly desired for the solar absorbers to fully cover the solar spectrum up to 2500 nm, which can be accomplished by inserting additional semiconductor-metal stacks. Figure 6.3.11 (a) presents a schematic representation of the device, which has an additional cavity (Ge) whose resonance appears at 2200 nm, showing a much-improved absorption bandwidth (2.1 μm). The required dimensions of the film stack 2, [Cr(200 nm)/Ge(52 nm)/ Cr(21 nm)/Ge(33 nm)/Si(34 nm)/TiO$_2$(57 nm)/MgF$_2$(111 nm)], is optimized to achieve the broadest bandwidth with highly efficient absorptions. By placing additional Ge-Cr

layers in the five-layer stack, a new resonance is created at longer wavelengths, leading to an even broader bandwidth. The calculated and measured absorption spectra are plotted in Figure 6.3.11 (b), showing the efficient absorption across the entire band of 400-2500 nm with the measured average absorption of 96.82%, which agrees well with the simulated value of 96.71%, implying a great improvement over the state-of-the-art solar thermal absorber, especially that in ref. [200], showing ~85% absorption. The efficient absorption bandwidth is dramatically expanded with a new reflection dip appearing, as shown in Figure 6.3.11 (c), which arises from the additional semiconductor-metal stack. Figure 6.3.11 (d) shows the calculated absorption bandwidth and the average absorption efficiency as a function of the number of Ge-Cr pairs. We should note that the band edges correspond to the wavelength positions where the absorption efficiency is no lower than 90% and the minimal band edge is kept at 400 nm, which means the results shown in the figure are the maximal band edges. It is clear that increasing the number of Ge-Cr pairs enables the absorption property to be further broadened, while still preserving the high absorption efficiency (>93%). It is thus expected that a much broader absorption characteristic up to 3.5 μm or even more can be achieved by inserting more stacks of semiconductor−metal layers, thereby opening the door to a multitude of new applications.
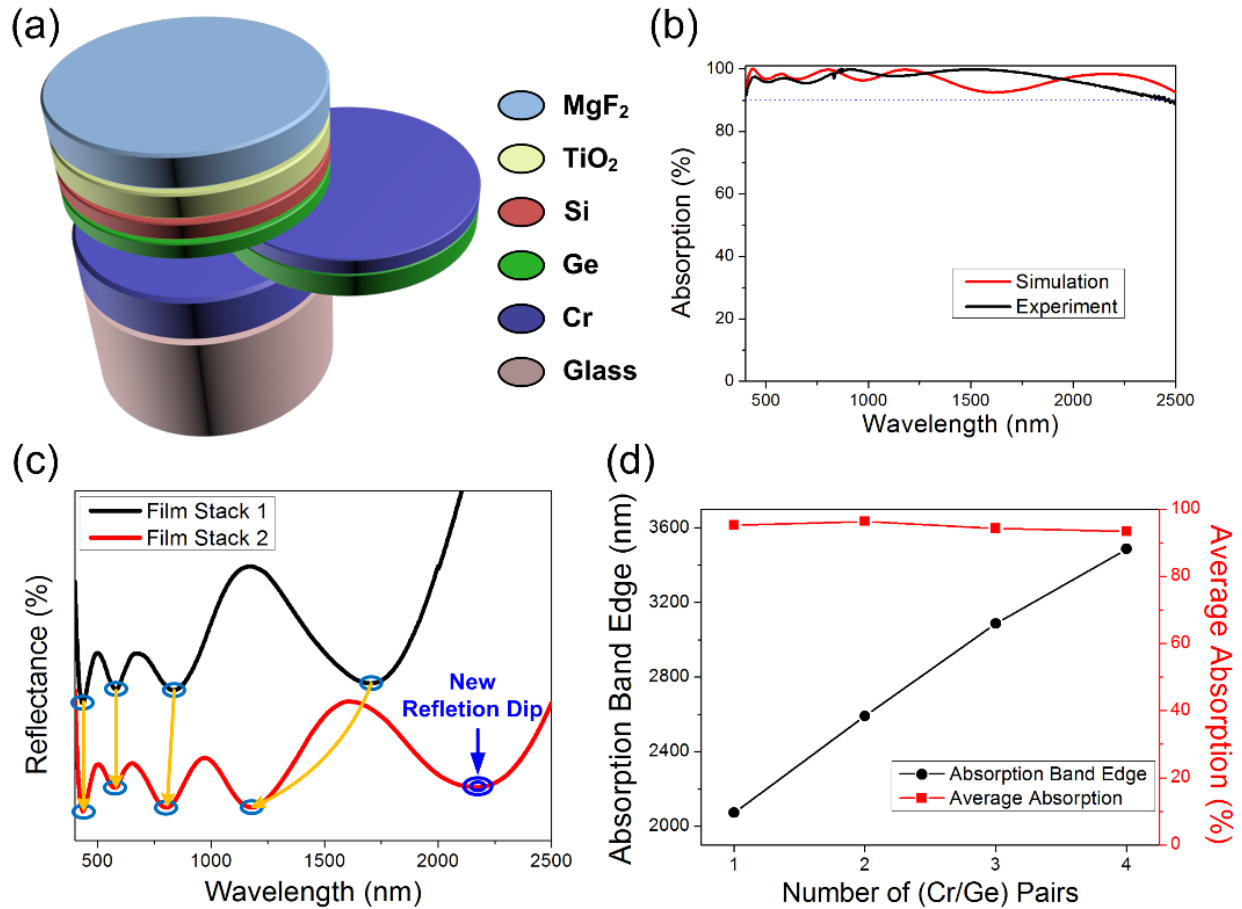
Figure 6.3.11 (a) The schematic diagram of the improved ultrabroadband absorber with 7 layers by inserting Ge/Cr layers. (b) The simulated and measured absorption of the improved 7-layer absorber. (c) The calculated reflectance spectra of the 7 layers film stack. One additional reflection dip is created by the inserted Ge/Cr pair as compared to 5-layer structure as shown with the circled valley reflectance. (d) The relationship between the absorption characteristic and the number of Cr/Ge pairs, and it indicates that the absorption band can be broadened by 500 nm after inserting every additional Cr/Ge pair.

6.4 Conclusion

In summary, we have shown wide-angle, polarization-independent ultrathin broadband absorber utilizing the multi-cavity resonance effects based on two different configurations. Both designed structures are simply composed of very few layers and any complex fabrication process (*e.g.*, lithography and etching) is not required to fabricate the device. All these advantages are highly desired in various applications including, such as on-chip multichannel filters, solar-thermal harvesting, light detecting, and imaging. In addition, considering both designs already involve

semiconductor media, they can be potentially applied to PV cells by inserting efficient hole and

electron transporting layers, and using a transparent electrode, such as ITO, on the top.

Chapter 7

Lenticular-Lens-Based Colored Antiglare Dashboard Surfaces

7.1 Introduction

In recent years, vehicles with colored interior decorations, which are appealing to consumers, have taken a considerable market share [212, 213]. Various materials, such as fabric, leather, and vinyl, are commonly used for the colored interiors [212]. Although the vehicle interior decorations improve steadily in the past, the dashboard under the windshield is always black to avoid the issue of veiling glare. The veiling glare is a ghost image of the vehicle dashboard created by reflection from the windshield and projected into the drivers' eyes (Figure 7.1.1). This projected image disturbs the driver's visual field and thus creates potential safety issues due to the reduced visibility of objects ahead [214-219].
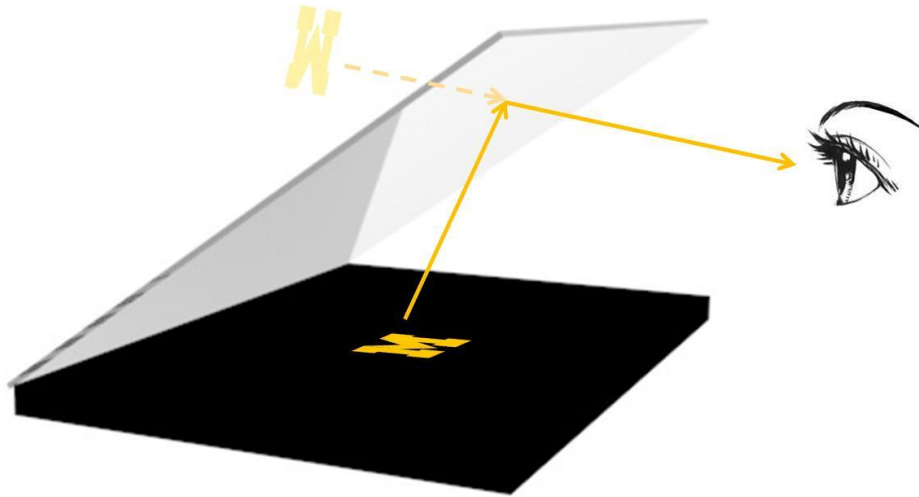
Figure 7.1.1 The definition of the veiling glare effects.

There have been past efforts to design dashboard surfaces that can produce desired colors, and at the same time, avoid veiling glare. For example, a veiling reduction system which integrates absorption-type polarizers and reflective color filters beneath has been proposed [220, 221]. However, the brightness of the dashboard is limited by the absorption nature of the polarizer. This issue can be mitigated by replacing the absorption-type polarizers with reflection type wire grid polarizers, which both increases the reflection brightness from dashboards and eases the requirement for the lamination of reflective color filters and polarizers [222].

In this chapter, we report a design based on lenticular lens arrays that can enable colored dashboard, which shows desirable colors and at the same time, avoids veiling glare [43]. This is achieved by laminating an alternating absorber/colored stripes underneath a lenticular lens array with specific dimensions, where the light in the veiling glare range is absorbed by the black strips leaving light from colored stripes reaching driver's eye. As an experimental demonstration, a 3.5 cm × 3.5 cm size sample with the lens pitch of 50 μm is fabricated by using thermal imprinting, which represents

a low-cost manufacturing method [223-225]. Due to the small period of the fabricated lenses, the lens array can be potentially extended to a display system with high resolution if replacing the stripes with active light emitting devices.

7.2 Design Principle and Results

A simplified windshield-dashboard system is depicted in Figure 7.2.1 (a). The rake angle θ of the dashboard system, which is defined as the angle between the windshield and the dashboard, ranges from 25° to 35° for different vehicle models. The rake angle plays an important role affecting the veiling glare as the reflectivity increases with the incident angles of light onto the windshield glass according to the Fresnel equations as plotted in Figure 7.2.2. Light reflected from the windshield into drivers' eyes cause the veiling glare. In practice, the driver usually has a viewing angle φ of ±15° with respect to the horizontal direction (Figure 7.2.1 (a)). It is the reflected light falling into drivers' viewing angle that produces the veiling glare. Here, the positive value φ (designated as φ_1 in the plot) corresponds to the light coming from above the horizontal direction, while the negative φ (*i.e.*, φ_2) from below. Veiling glare becomes a serious issue if the dashboard is not covered with black absorbing material, as one experience when placing a piece of white paper on the dashboard, which causes strong reflected light into the driver's eyes.
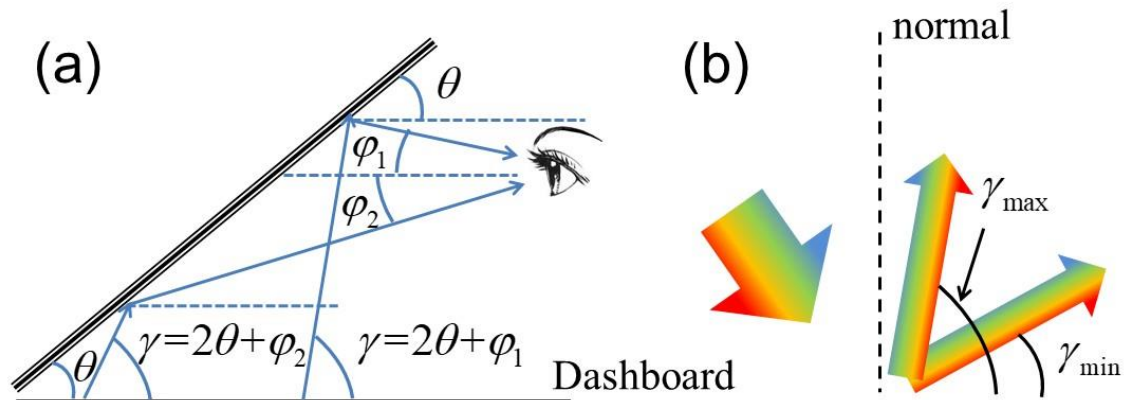
Figure 7.2.1 Veiling glare angular range calculation with rake angle θ and the direction of light rays from windshield φ. (a) A schematic diagram draws a relation between reflection angle from dashboard γ and θ, φ as $\gamma = 2\theta + \varphi$. (b) Veiling glare range for vehicles with different rake angles varies between $\gamma_{min} = 2\theta - 15°$ and $\gamma_{max} = 2\theta + 15°$ with θ ranging from 25° to 35°. The whole veiling glare range lies in the right half plane with respect to the normal of the incident plane.

The veiling glare angle γ is the angle where the reflected light from dashboard will enter the view field of drivers, leading to a veiling glare. It is related to the rake angle θ and the viewing angle φ as $\gamma = 2\theta + \varphi$. Considering drivers' viewing angle φ of $\pm 15°$, the veiling glare angular range is calculated to be $\gamma_{min} = 2\theta - 15°$ to $\gamma_{max} = 2\theta + 15°$. Considering the value of θ (from 25° to 35°), γ lies in the right half plane as shown in Figure 7.2.1 (b). For an anti-glare dashboard, the reflection needs to be suppressed in the angular range between γ_{min} and γ_{max}.
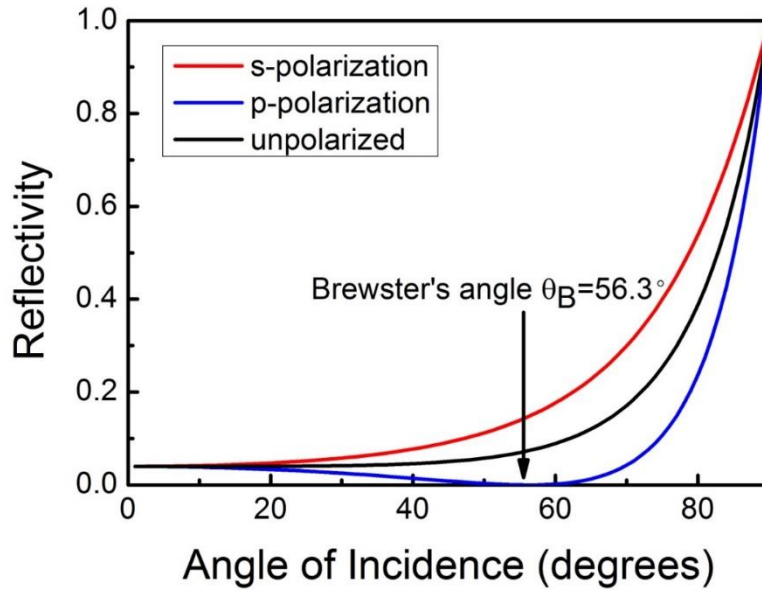
Figure 7.2.2 Reflectance of the air and windshield glass interface dependence on incident angles. The ambient light of daily driving environment can be regarded as unpolarized. The Brewster's angle for the p-polarization corresponds to an angle where reflectivity is zero. The refractive index of glass here is selected as 1.5 without dispersion.

Lenticular lenses are cylindrical periodic lens arrays that provide different magnified images at different angles. They are commonly integrated in 3D printing and electronic displays to create special visual effects (*e.g.*, animation and depth of illusion) by controlling light propagation with curved shapes [226-231]. By using lenticular lenses, different images are observed with different viewing positions. As illustrated in Figure 7.2.3 (a), if lenticular lens array is placed on top of alternating colored stripes, the bright colored (yellow) stripe can be viewed on the left side with respect to the normal, while the dark color can be observed from the right half.
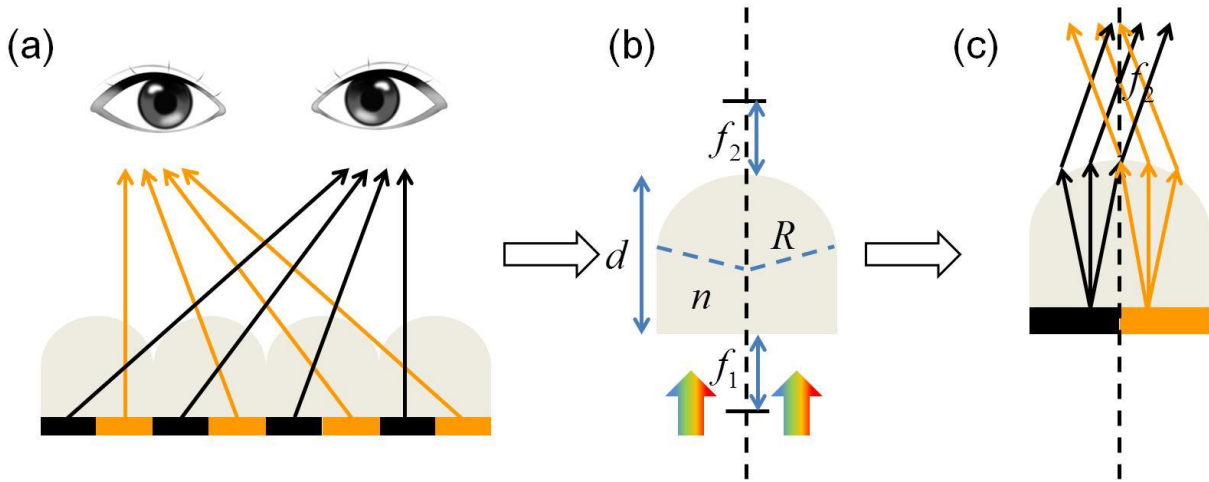
Figure 7.2.3 Physical explanation of the light guidance property of the lenticular lenses. (a) Different images can be observed when viewed from different angles and this contributes to the various visual effects created with the lenticular lens array. (b) Analysis of the dimension of a single lenticular lens. The thickness of the lens d can be expressed with the refractive index n and the radius R as $d = nR / (1 - n)$. (c) Schematic of refraction of light rays coming from the bottom side. The Light from the colored area will be directed to the left half, and the light from the dark area is refracted to the right.

The property of the lenticular lenses can be simply explained using the ABCD transfer matrix method. The transfer function $\overleftrightarrow{M}$ of a single lenticular lens is [117]:

$$\overleftrightarrow{M} = \begin{pmatrix} 1 & 0 \\ -\dfrac{1-n}{R} & n \end{pmatrix} \begin{pmatrix} 1 & d \\ 0 & 1 \end{pmatrix} \begin{pmatrix} 1 & 0 \\ 0 & \dfrac{1}{n} \end{pmatrix} = \begin{pmatrix} 1 & \dfrac{d}{n} \\ \dfrac{n-1}{R} & 1 - d\dfrac{1-n}{nR} \end{pmatrix}, \tag{7.2.1}$$

where d is the thickness of the lens, n is the refractive index of the lens constituent material, R is the radius of the curved dome. R is a negative value when light coming from the bottom side (Figure 7.2.3 (b)). The three matrices in the calculation of $\overleftrightarrow{M}$, from right to left, correspond to the light refraction at the interface between the air and the flat bottom plane of the lens, light propagation within the lens, and the refraction between the top dome and the air, respectively. It should be noted that Equation 7.2.1 is valid in cases where the curvature of top surface is relative small compared to the thickness of the lens. More accurate analysis can be performed with ray-tracing method, which will be discussed later. Based on Equation 7.2.1, the bottom and top focal lengths f_1 and f_2 can be obtained as

$$f_1 = \frac{R}{1-n} - \frac{d}{n}, f_2 = \frac{R}{1-n}. \tag{7.2.2}$$

For a typical lenticular lens, the bottom focal plane overlaps with the flat bottom plane of the lens, i.e., $f_1 = 0$. Based on this condition, the thickness d is related to the radius R and the refractive index n as

$$d = \frac{nR}{1-n}. \tag{7.2.3}$$

Since the bottom plane is a focal plane, light coming from the same point on this plane will exit the lens in parallel. Moreover, as depicted in Figure 7.2.3 (c), the light rays from a random point in the colored area will be refracted into the left half space, and light from any position within the dark area will go into the right plane. This illustrates the control function of the light propagation with lenticular lenses shown in Figure 7.2.3 (a).

As analyzed above, when colored stripes are correctly placed underneath the lenticular lens array, light rays from different areas are directed into different angular range (Figure 7.2.3 (c)). If the black area in Figure 7.2.3 (c) is coated with light absorbing materials, while the yellow colored area is coated with any colored reflective materials, the out-coming light from the bottom of a single lens itself is always refracted in the left half plane, which is out of the veiling glare range defined in Figure 7.2.1 (b). This satisfies the aforementioned anti-glare design criteria.

Additional considerations need to be taken into account when using an array of lenses to cover the dashboard. As illustrated in Figure 7.2.4 (a), light from the colored stripes can also be refracted into the right half plane by the adjacent lenses. By ray-tracing the left- and right-edge positions of the colored stripes, the conditions to avoid veiling glare are $\alpha > \gamma_{max}$ and $\beta < \gamma_{min}$, where α is the minimal refracted angle by the single lens itself for light rays coming from the colored stripe (corresponding to the light coming from the left-edge point of the colored area), β is the maximal

angle of refraction by the adjacent lens for colored light rays (corresponding to the light coming from the right-edge position of the colored stripe), and γ_{min}, γ_{max} define the veiling glare range as shown in Figure 7.2.1 (b). By adjusting the position and width of the area of the substrate underneath the lenses, the anti-glare condition is

$$\alpha = \arctan\left(\frac{f_2}{a_2 - w/2}\right) \geq \gamma_{max} \tag{7.2.4}$$

$$\beta = \arctan\left(\frac{f_2}{a_1 + w/2}\right) \leq \gamma_{min} \tag{7.2.5}$$

where f_2 is the focal length, w the period of the lenticular lens array, a_1 and a_2 the distances from the right and left-edge points of the colored stripe to the right edge of a single lenticular lens, respectively.
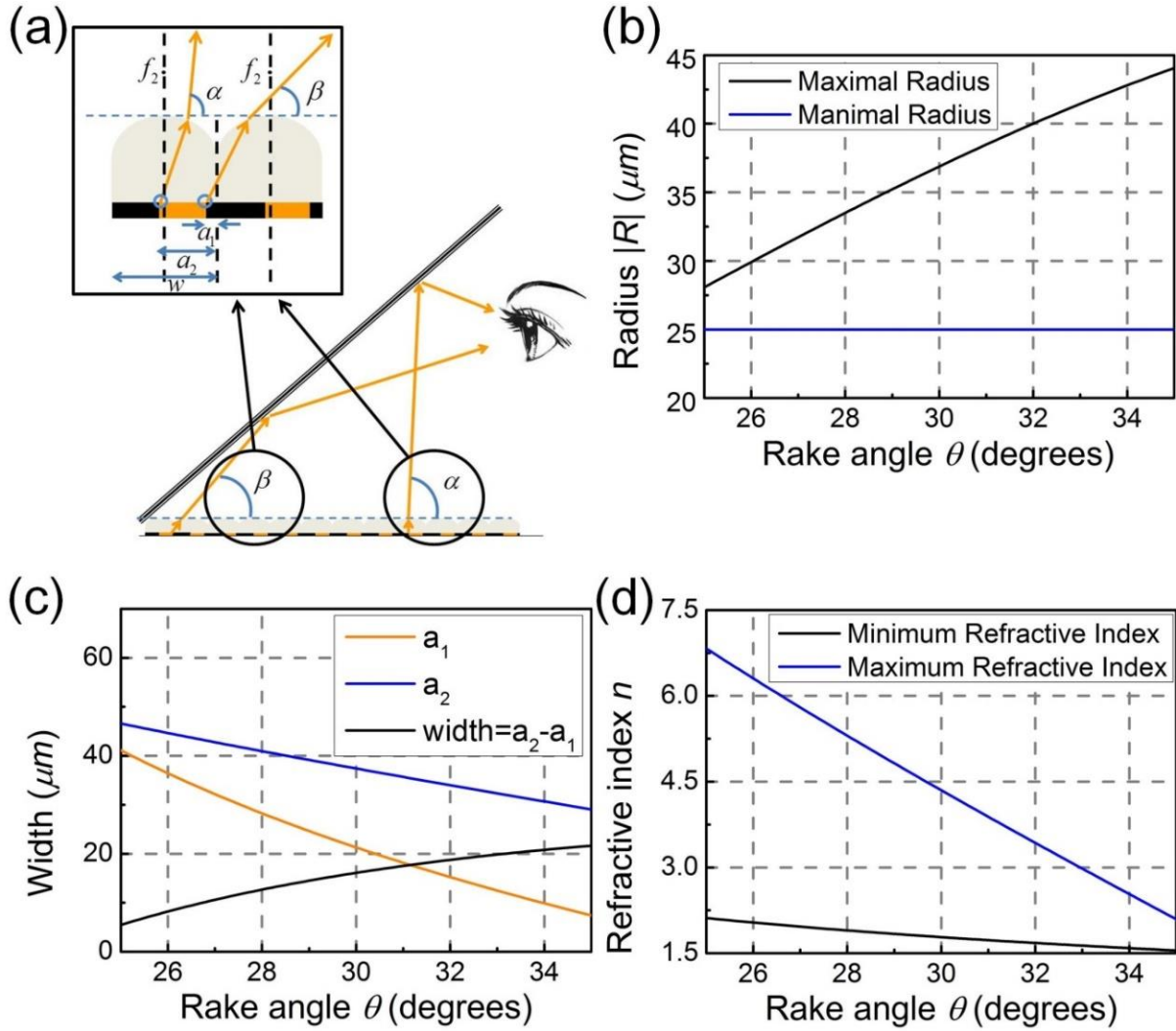
Figure 7.2.4 Design criteria for lenticular lens array. (a) Analysis of anti-glare conditions for lenticular lens array. Two extreme positions on the dashboard are used to analyze the veiling glare range. α is the minimal refracted angle by the single lens itself for light coming from the colored stripe (corresponding to the light coming from the left-most point of the colored area within one period), β is the maximal angle of refraction by the adjacent lens for colored light rays (corresponding to the light coming from the right-most position of the colored stripe within one period). (b) Maximal and minimal radius $|R|$ of the curved dome dependence on rake angle θ. The minimal value is determined by the lens geometry $|R| \geq w / 2$, and the maximal value of $|R|$ is fixed according to Equation 7.2.6 with $a_2 > a_1$. (c) Position and width of the colored stripes when $|R| = w / 2 = 25$ μm. (d) The relation between the refractive index of material n and the rake angle θ. The position and width of the colored area are fixed as $a_1 = 7$ μm and $a_2 = 27$ μm.

An additional consideration is to make the width of the single lens beyond the resolution capability of human eyes and the lens curves cannot be perceived by our eyes. According to the Rayleigh criterion [117], the finest feature which naked eyes can resolve at viewing distance of $L = 25$ cm is $L\sin\theta = 1.22L\lambda / D \approx 56$ μm, considering the wavelength of visible light ($\lambda \sim 550$ nm) and the

111

pupil diameter ($D \sim 3$ mm). Assuming $\alpha = \gamma_{max}$ and $\beta = \gamma_{min}$, the largest width of the colored stripe can be obtained from Equation 7.2.4 and 7.2.5 as

$$a_2 - a_1 = w + \frac{|R|}{n-1}\left(\frac{1}{\tan(\gamma_{max})} - \frac{1}{\tan(\gamma_{min})}\right) \tag{7.2.6}$$

$$= 50 + \frac{|R|}{0.54}\left(\frac{1}{\tan(\gamma_{min} + 30°)} - \frac{1}{\tan(\gamma_{min})}\right),$$

where $f_2 = |R| / (n-1)$, $w = 50$ μm, refractive index n is set as 1.54 considering that cyclic olefin copolymer (COC) is used for lenticular lens fabrication, and $\gamma_{max} = \gamma_{min} + 30°$ as $\gamma = 2\theta + \varphi$ with φ of $\pm15°$. As depicted in Figure 7.2.4 (b), Equation 7.2.6 sets the upper limit of the radius from the condition that $a_2 > a_1$, while the smallest radius is $|R| = w/2$. When the radius is set as the minimal value, *i.e.*, $|R| = w/2$, the colored strip has the largest width $a_2 - a_1$, which will provide correspondingly highest brightness, according to Equation 7.2.6. Figure 7.2.4 (c) plots the dependence of the largest width of the colored stripe on the rake angle θ varying from 25° to 35° with Equation 7.2.4 – 7.2.6. It should be noticed that other values within the range calculated in Figure 7.2.4 (b) can be selected for $|R|$, and the satisfactory values of a_1 and a_2 can be obtained based on Equation 7.2.4 and 7.2.5. Finally, the lens material is not restricted to COC, but can be other polymeric films. Figure 7.2.4 (d) shows the dependence of the refractive index on the rake angle if we assume $a_1 = 7$ μm and $a_2 - a_1 = 20$ μm, which is the calculated result at $\theta = 35°$ in Figure 7.2.4 (c) and will also be used for the simulations. All the variations of $|R|$, the colored stripe width $a_2 - a_1$, and n provide more freedom for further designs.

As a specific example, the following parameters are used for detailed discussions: the radius $|R|$ and the period w are set as $|R| = w/2 = 25$ μm so that the curved top surface is exactly a semi-cylindrical one and the thickness of the lens is determined as $d = 71$ μm with Equation 7.2.3. The refractive index of the lens material COC is 1.54. Besides, the position of the colored area is fixed

with $a_1 = 7$ μm and $a_2 = 27$ μm, which means the colored area is 20 μm wide and satisfies the conditions of Equation 7.2.4 – 7.2.6, and the rake angle is assumed as $\theta = 35°$ corresponding to $\gamma_{min} = 55°$ and $\gamma_{max} = 85°$, respectively.
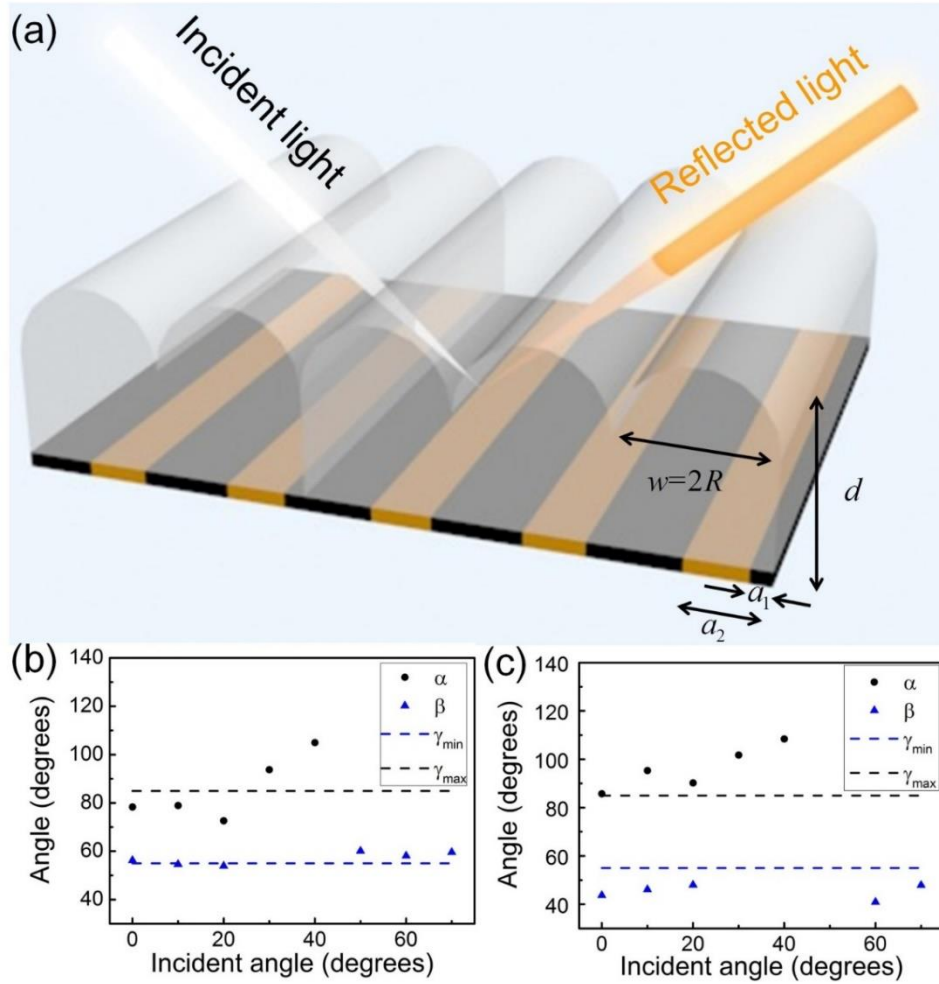
Figure 7.2.5 Reflection investigation of the designed lens. (a) Designed lenticular lens for the simulation. The reflective area is simulated with the 'Mirror' boundary conditions, which will reflect all light rays incident on it. (b) Dependence of α (the minimal refraction angle by the single lens itself, black solid circles) and β (the maximal refracted angle by the adjacent lens, blue triangles) on incident angles. Some portion of light will go into the veiling glare range, which is the range between black and blue dashed lines in the plot with $\gamma_{min} = 55°$ and $\gamma_{max} = 85°$, due to the aberration of the lenses. (c) Dependence of α (the minimal refraction angle by the single lens itself, black solid circles) and β (the maximal refracted angle by the adjacent lens, blue triangles) on incident angles of the optimized lens. All light rays are controlled out of the veiling glare range and the veiling glare is further reduced.

We use the design summarized above for further simulations using ray-tracing software (Zemax, Zemax LLC). All the parameters are shown in Figure 7.2.5 (a) and the 'mirror' boundary condition, which reflects light with ~95% efficiency, is used to simulate the reflective colored area. The unit

cell with a 50 μm pitch consists of a semi-cylinder with the radius of 25 μm atop and a cuboid beneath. The length along the lens lines can be randomly selected as we assume it is infinite. The lens is made of COC material with a refractive index around 1.54. Multiple incident light sources are set above the lens array to cover the unit cell for collecting the reflection angle data at different incident angles (from 0° to 70° with an increase step of 10°). Figure 7.2.6 shows the light propagation paths after incident on the designed periodic structure from different angles. The minimal refraction angle by the single lens itself α and the maximal refracted angle by the adjacent lens β are highlighted in selected angles, and they are summarized in Figure 7.2.5 (b). Since the simulated structure is based on the theoretical predictions, which assumes the top curvature is very thin, aberrations will occur for light ray incident on the very edge part of the lens. As a result, some light reflected from the reflective area will fall into the veiling glare range ($\gamma_{min} = 55°$ and $\gamma_{max} = 85°$), which can be seen by the dots inside the dashed line range in Figure 7.2.5 (b). At some incident angles, the data for α and β are missed because those light rays get absorbed by the absorber beneath as shown in Figure 7.2.6 (4) – (8).
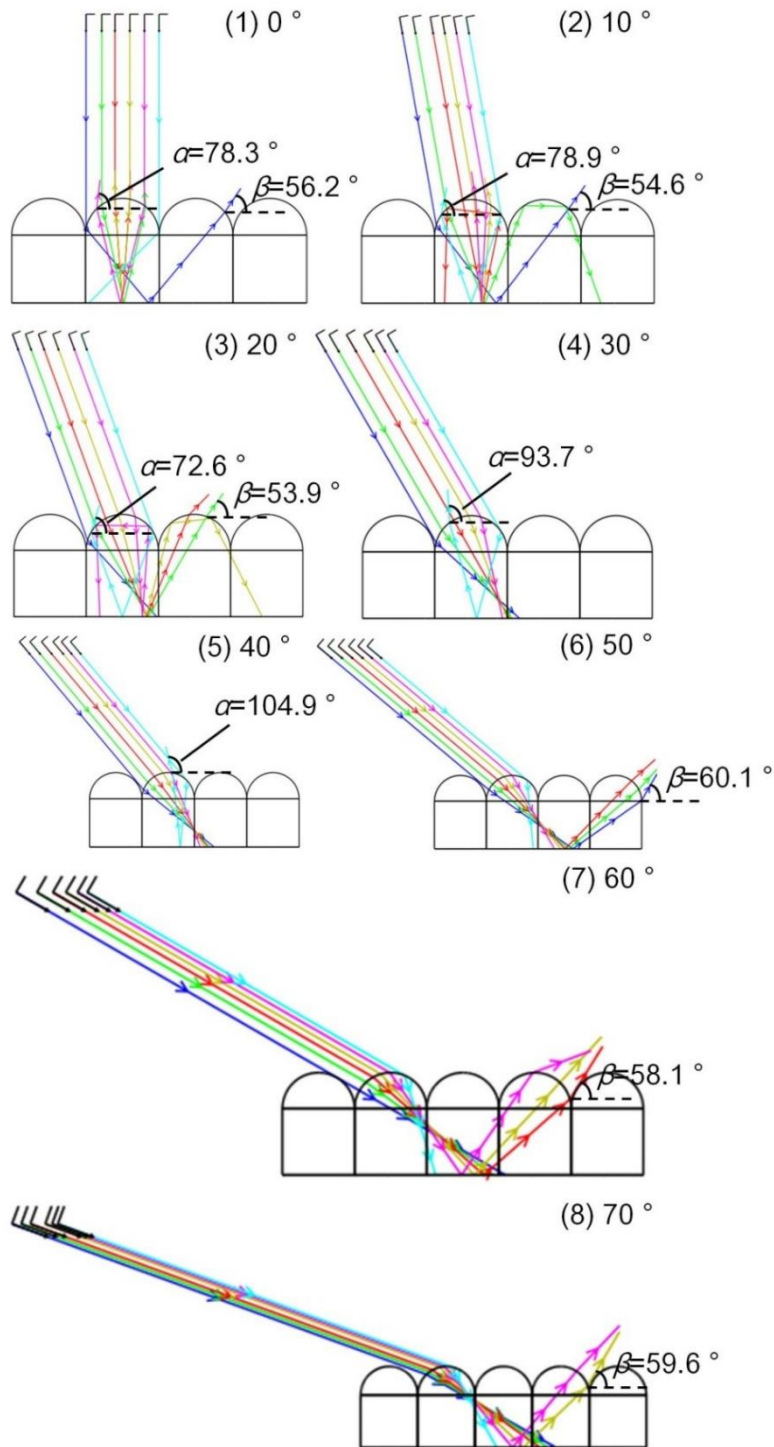
Figure 7.2.6 Trace of light rays from different incident angles of the initial designed lenticular lens (thickness $d = 71$ μm). (1) – (8) correspond to incident angles from 0° to 70°, respectively. As analyzed above, the out-coming light is refracted by both the single lens itself and the adjacent lens. Due to the aberrations from the cylindrical shape of the lens, the refracted light will fall into the veiling glare range at some incident angles.

Practically, the aberrations can be relieved efficiently by slightly reducing the lens thickness. When the lens thickness d is decreased from 71 μm to 61 μm, all light coming back from the reflective area beneath are well controlled out of the veiling glare range as illustrated in Figure 7.2.7 and 7.2.5 (c), which efficiently reduces the potential veiling glare after the lens sample being installed in the vehicles. Similarly, those missed data (*e.g.*, from 30° to 70° incident angles) are due to the absorption of the absorber areas. Here, we only consider the case where the drivers are viewing from the middle of vehicles. The definition of veiling glare angular range can also be extended for situations where light rays come from the side with the effective rake angle θ in the incident plane as shown in Figure 7.2.8. Then following the design criterion for removing the veiling glare $\alpha > \gamma_{max}$ and $\beta < \gamma_{min}$, satisfactory lens parameters can be obtained with Equation 7.2.4 – 7.2.6 and veiling glare can be removed by orientating the lens array on the dashboard with the lens length perpendicular to the incident light direction.
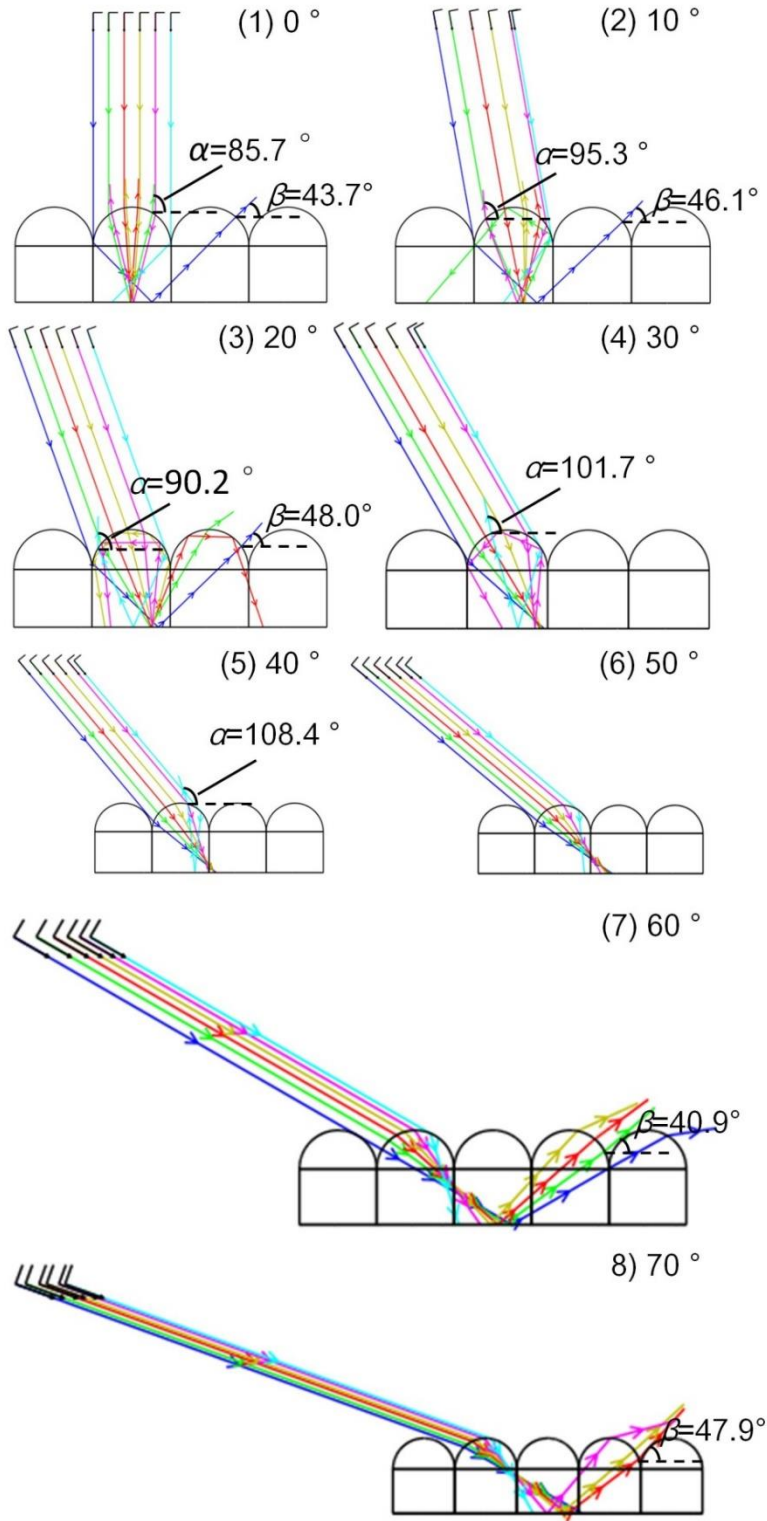
Figure 7.2.7 Trace of light rays from different incident angles of the optimized lenticular lens (thickness $d = 61$ μm). (1) – (8) correspond to incident angles from 0° to 70°, respectively. By reducing the thickness of the lens to $d = 61$ μm, the aberrations are greatly reduced, and all refracted light at various incident angles are controlled out of the veiling glare range.
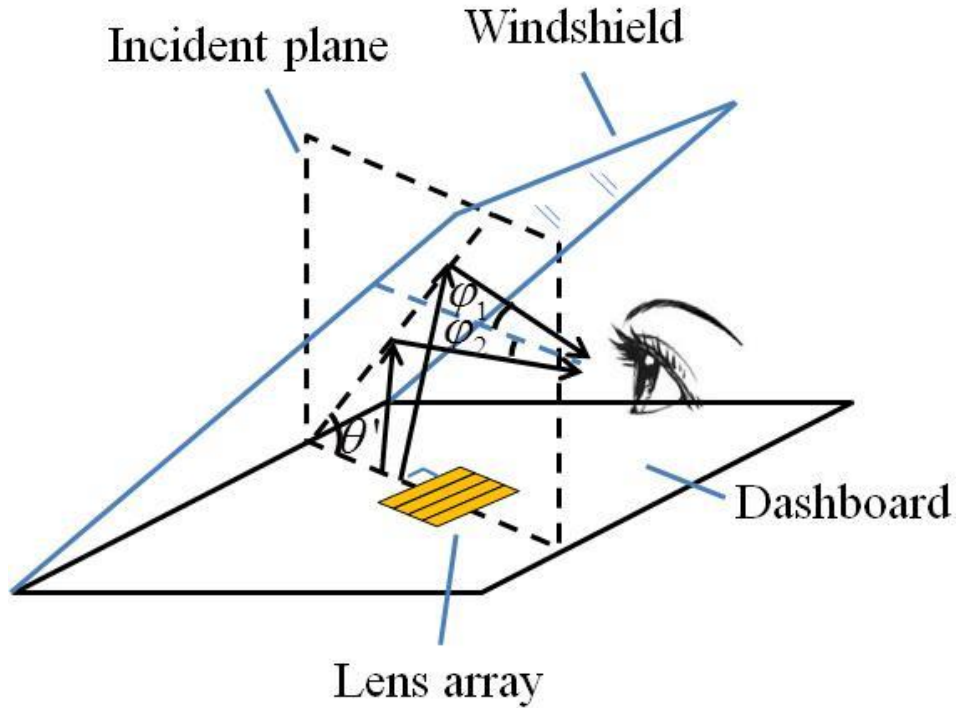
Figure 7.2.8 The schematic diagram for removing the veiling glare of light coming from the vehicle side. The drivers' viewing angle φ remains as $\pm15°$ and the lenses are well orientated so that the lens length is perpendicular to the incident light direction. Veiling glare due to light rays coming from the vehicle side can also be removed by orientating suitable lenticular lens array with the lens length perpendicular to the incident light direction. Here, effective rake angle θ' refers to the angle between the windshield and dashboard in the incident plane and the satisfactory lens parameters can be obtained with Equation 7.2.4 – 7.2.6 based on the corresponding veiling glare angular range (defined by $\gamma_{min} = 2\theta' + \varphi_2$ and $\gamma_{max} = 2\theta' + \varphi_1$).

Traditionally lenticular lenses can be manufactured via hot melt extrusion using extrusion drums, and such drums are typically made by diamond ruling method [226, 227]. However, the typical commercial lenticular lens has period of 250 μm, which cannot satisfy the design criteria described above. We used thermal imprinting method to fabricate the lens array, where the imprinting mold was made by diamond ruling by using an ultra-precision five-axis machining.

A 5 cm × 5 cm size Ni hard mold is fabricated for the thermal imprinting of the cylindrical lens array. Two 5 mm wide and 29 μm deep steps are created at both edges of the mold in order to control the final thickness of printed polymer lenses (see the illustration in Figure 7.2.9).
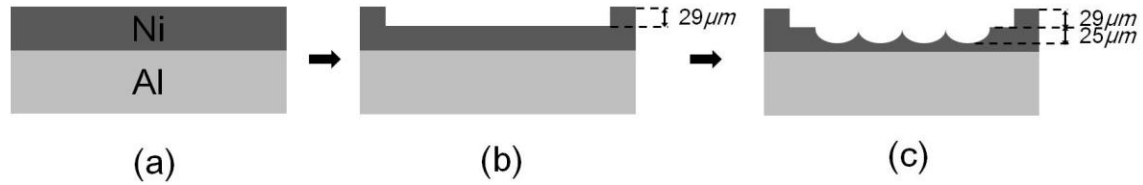
Figure 7.2.9 Preparation of the Ni mold with the precision five-axis planing machine. The diamond tool has an arc tip with the arc of 170° and a radius of 25 μm from Contour Fine Tooling Ltd. 200 μm thick Ni is electroplated onto the thick Al plate as the mold material since Ni is much softer when compared to Al and Cu considering the sharp diamond tip. Using an ultra-precision five-axis machining system (Nanotech 350FG, Moore Nanotechnology Systems LLC), two 29 μm steps are firstly planed out onto the Ni layer. Then the semi-cylindrical patterns inversed to the final lenses are created with the semi-circle shaped diamond tool.

COC resin is selected as the imprinting material due to its high tensile strength (~63 MPa) and modulus (~2.6 GPa), which facilitates handling in the subsequent thin film peeling off and transfer procedures. 9 Cyclic olefin copolymer (COC 8007, TOPAS Advanced Polymers Inc., Florence, Kentucky, USA) pellets are positioned on the untreated Si substrate as a 3×3 array of a 2 cm space and then pressed into a 70 μm thick film at 140°C for 8 minutes with 1 ton pressure covered with a Si superstrate. The superstrate is pre-treated with fluoro-containing monolayers to facilitate the subsequent de-molding process [232]. After separating the substrate and superstrate, the COC film stays on the untreated Si substrate due to its higher surface energy. To further reduce the defects, the film after heat pressing is put into a vacuum chamber at 140°C for 20 minutes. After coating a silicone releasing layer (OS-20, Dow Corning Corp.) onto the Ni mold, the thermal imprinting is operated at 140°C for 10 minutes with gradually increasing the pressure to 1 ton using the manual hydraulic press (Specac Ltd.), which leaves a residue layer around 7 μm on the very bottom. So, the overall thickness is around 61 μm (curved semi-circle 25 μm + spacer 29 μm + residue layer 7 μm), which satisfies the simulation design. The microscopic image in Figure 7.2.10 (e) shows that the imprinted lens array has a period of 50 μm.
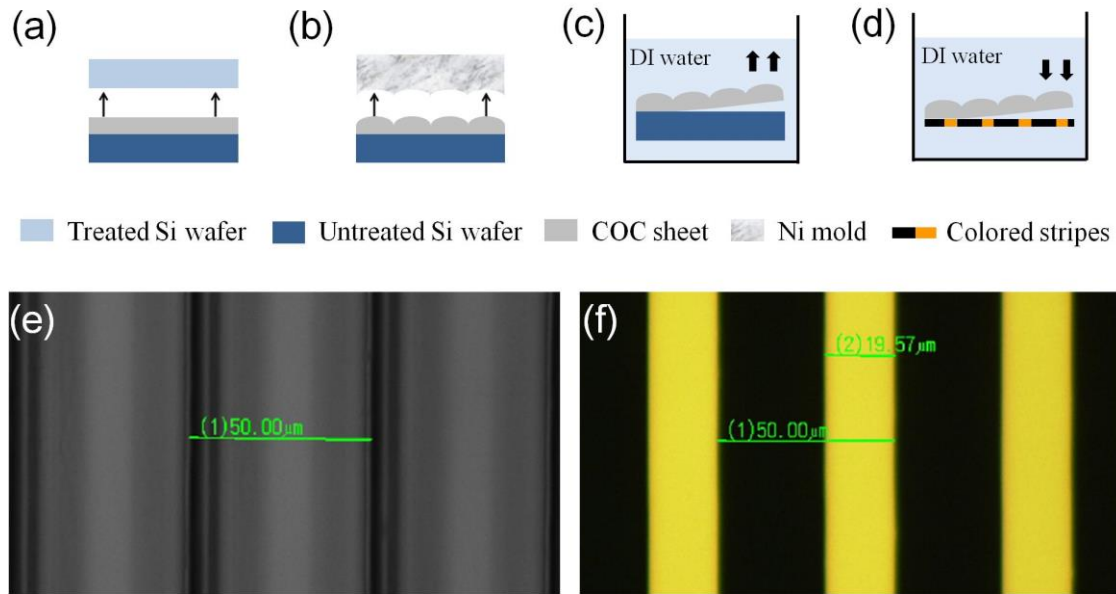
Figure 7.2.10 The fabrication process of the lenticular lens array and the alignment with the colored substrate. Due to the hydrophobic property of the COC, the peeling off and the alignment are done in the water, which guarantees lens sheet to be smooth and flat. (e) and (f) are the microscopic images of the imprinted lenses and the colored alternating stripe substrate, respectively.

For demonstration, a Si substrate is used to make the alternating absorptive/reflective stripe patterns using standard micro-fabrication facility. A Si wafer is firstly coated with absorbing materials consisting of multi-layer structures with chromium/germanium/silicon/titanium dioxide/magnesium fluoride which provide an averaged absorption >95% across the visible wavelength range [41, 42]. Subsequently, the colored stripes are fabricated by photolithography followed by Au deposition. Other colored materials can also be used. Figure 7.2.10 (f) is the microscopic image of the alternating stripe substrate with a pitch of 50 μm and the colored stripe width of 20 μm. Considering the water-repellent property of COC, the peeling-off of the thin lens is done in the water (Figure 7.2.10 (c)), which keeps the lens sheet flat and smooth. The alignment of the lens sheet and the absorber/colored stripe substrate is achieved with the help of the morié fringe. The 7 μm offset between the lens and the stripes (*i.e.*, $a_1 = 7$ μm) is aligned under the microscope as shown in Figure 7.2.11 (c). It is worth noting that even 100nm pitch mismatch

120

between the lens and absorber/yellow stripe substrate will create the morié fringe which is described in Figure 7.2.11 (d).
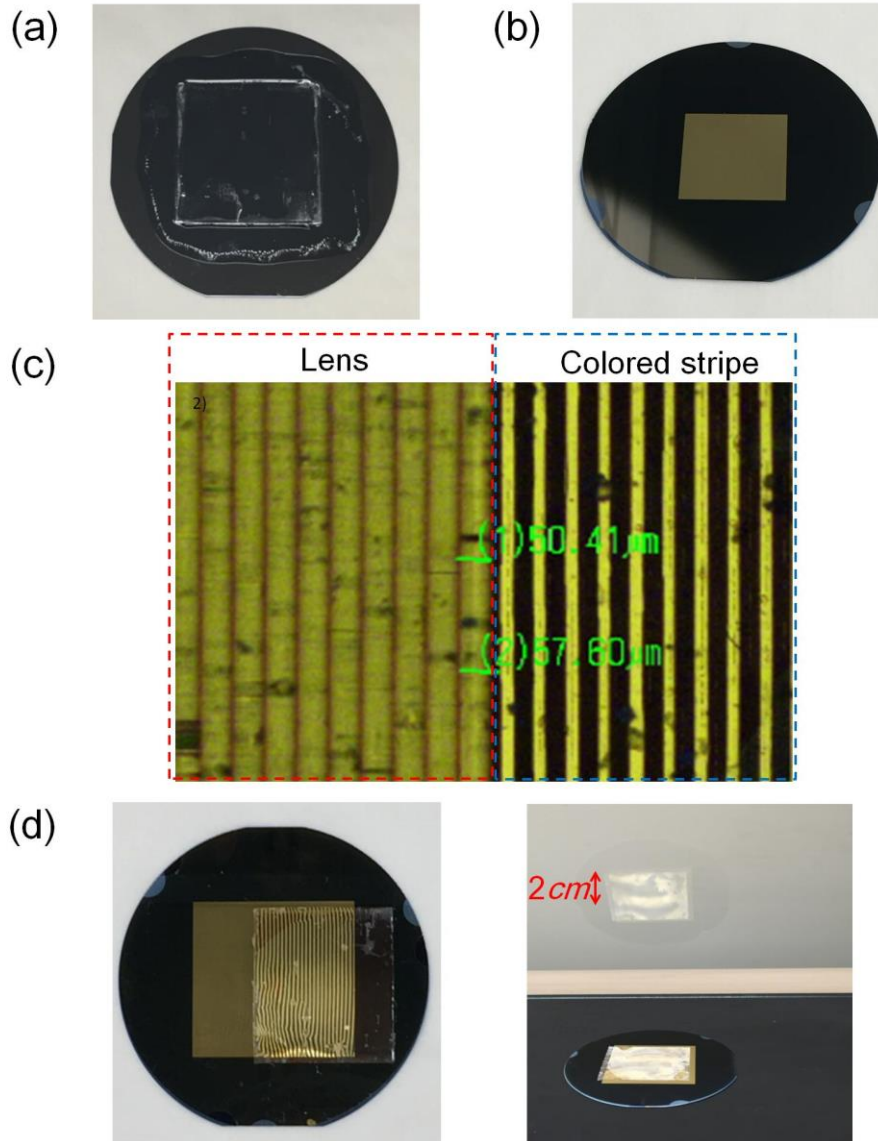
Figure 7.2.11 Alignment of the lenses and colored substrate. (a) – (b) Photos of the imprinted lenses and the alternating colored stripes, respectively. Both periods are 50 μm. The yellow stripes (Au) has a width of 20 μm and the width of the absorber stripe is 30 μm. (c) 7 μm offset between a lens unit and an absorber/Au stripe unit is achieved under the microscope. (d) The pitch mismatch between the lens and the substrate will cause the morié fringe. The left image shows the morié fringe of a period ~1.25 mm corresponding to a 2 μm pitch mismatch between the lens and the colored stripes. The right image shows the interference fringe with a period ~2 cm corresponding to a 120 nm pitch mismatch between the lens and the substrate.

As can be seen from Figure 7.2.12 (a), there is no reflection when the sample is viewed from within the veiling glare range, *i.e.*, the sample renders black, and therefore will not create veiling glare if

installed onto the dashboard. A small defected area is circled out in the figure due to the local misalignment which mainly comes from the defects of the lenses during the imprinting/separation process. On the other hand, when the observing angle is out of the veiling glare range, the sample turns bright yellow due to reflection from the Au stripes as shown in Figure 7.2.12 (b). Finally, Figure 7.2.12 (d) shows how the sample functions when it is put on a setup that mimics the windshield-dashboard in a vehicle (as shown in Figure 7.2.12 (c), the rake angle $\theta = 35°$). Clearly, the area covered by the sample appears bright yellow on the black dashboard, however there is no visible veiling glare from the windshield glass (except the small defected area mentioned in Figure 7.2.12 (a)) and we can see through the windshield easily. By comparison, when rotating the sample on the dashboard by 180°, the yellow image from windshield is reflected into our eyes (Figure 7.2.12 (e)), which further validates the design of the sample orientation as illustrated in Figure 7.2.4 (a). Due to the small period (~50 μm) of the lens array, the surface appears very smooth and no lens feature is visible to our eyes (Figure 7.2.12 (a) and (b)). Compared to traditional lenticular lenses, which typically have ~100 lenses per inch corresponding to ~250 μm period [226-228], our fabricated lenses can even be potentially applied for higher resolution displays when integrated with active devices such as LEDs.
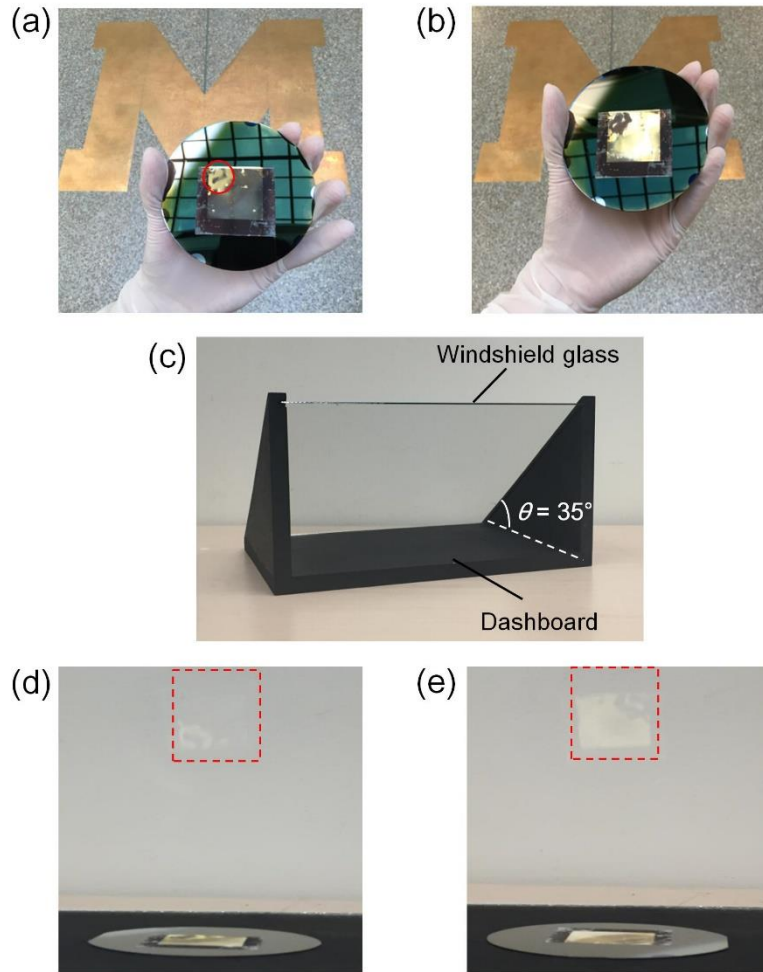
Figure 7.2.12 Demonstrations of samples on the windshield-dashboard setup. (a) and (b) show the final aligned sample when viewed in and out of the veiling glare range, respectively. (c) presents the windshield-dashboard setup with the rake angle $\theta = 35°$ for demonstration. The sample renders no reflection into the veiling glare range which is consistent with the prediction by the simulations and doesn't cause the veiling glare when installed on the dashboard as shown in (d). By comparison, projected image of the sample on the windshield is clearly observed if rotating the sample by 180° as presented in (e).

7.3 Conclusion

In summary, we demonstrate a lenticular-lens based design of a colored dashboard which simultaneously offers anti-veiling glare applications. The dashboard surface consists of a 50 μm period lenticular lens array made of COC material covering a surface of alternating stripes of absorber and reflective colored materials. By accurate design of the lens dimensions, unwanted light reflection from the bottom stripes are well controlled out of the veiling glare range and

simultaneously create visual colors to the drivers' eyes. It is worth noting that the mass production can be easily achieved by R2R imprinting [233-235]. Moreover, the small pitch design can be potentially extended to display systems inside vehicle due to its high resolution in the near future.

Chapter 8

Invisibility Cloak with Image Projection Capability

8.1 Introduction

Since the pioneering work that led to the realization of electromagnetic metamaterials over a decade ago, invisibility cloaking of an object to incoming waves has been one of the most appealing possibilities in the metamaterial research community [236]. A scattering cancellation method has been presented for cloaking a subwavelength object [237]. Transformation optics and conformal mapping can theoretically hide large objects [236, 238-240]. Following these fundamental concepts, early works have demonstrated cloaking technologies, mostly in narrowband of microwave frequencies [241, 242]. By reducing to a two-dimensional coordinate transformation, a quasi-conformal mapping approach called 'carpet cloaking' has been realized in the microwave, the near infrared, and the visible regions [243-248]. For an ideal cloaking operation these rigorous theories predict the requirement of extreme material parameters and spatial anisotropy of cloaking media. More recently, an optical metasurface cloak to a laser illumination has been realized by manipulating the reflection phase distribution [249]. It is, in general, difficult to implement cloak structures, particularly in the full visible spectrum. Thus, hiding large 3D

objects in the full visible wavelength range for practical applications remains a decade-old challenge.

In recent years, it has been possible to fabricate broadband invisibility cloaks in the full visible region when the omnidirectionality requirement is abandoned. In these cases, very promising results have been obtained when the transformation optics was simplified by removing the design restriction of phase preservation. A polygonal cloak structure made of calcite, which is a natural anisotropic material, was shown to hide a cylindrical object with a diameter of a few millimeters, following the study of calcite carpet cloaks [250-252]. In ref. [253], a large object was concealed in normal incidence by using a cloak structure consisting of isotropic material lenses. A number of authors have reported various cloak structures consisting of conventional optical components in the visible region [254-258].

On the other hand, there is a tremendous amount of information such as texts, images, and movies in our daily lives owing to the significant achievements in the image projection technology [259-261]. Modern human vision systems such as 3D displays rely on several psychological cues where overlapping of images, shading, textured gradients are used to create various depth perceptions in the human brain. However, these image-based devices are often associated with ambiguities and errors because of the inability to correctly carry the depth profile information. It is suggested in ref. [259] that in order to achieve the perfect 3D display technology, some novel methods to generate physiological cues such as binocular display, convergence, and accommodation are necessary, which to be combined in the imaging system with existing psychological cues described earlier. To create physiological cues, modern displays often utilize optical elements such as lenticular lenses, parallax barriers, curved lens arrays, holography, and see-through display technologies. However, the aspect of optical invisibility cloaking in such imaging systems has

never been explored. For example, the combination of the cloaking with the imaging systems can allow an additional degree of freedom for the physiological cues such as used for the realization of see-through 3D displays and augmented reality technologies that could be beneficial to the thrust for transparent electronics in the future [262, 263].

In this chapter, we experimentally demonstrate an invisibility cloak where a large object can be concealed in the cloak structure and any images can be projected on it simultaneously [44]. This unique functionality can be obtained through the use of one polarization of light for the cloaking and the other orthogonal polarization for the image projection due to the insensitivity of human eyes to the polarization. Such approach has never been captured by any other reports in the past.

8.2 Design Principle and Results

Our cloak structure consists of commercially available optical components; polarizers for oblique incidence ($P_{o,1-4}$) and for normal incidence ($P_{n,1}$), and mirrors (M_{1-4}), as shown in Figure 8.2.1 (a). We regard our structure as a twelve-port device and each port is labeled by 1 to 12. In the description of the mechanism of our structure below, we consider that the scene behind the cloak structure is built at the observation point in front of the cloak structure, assuming ideal performance of each component. The regions of the scene are labeled by I to IV, and here we assume that regions I and IV (II and III) are observed via the horizontally (vertically) polarized light. Due to the symmetry of the cloak structure, we consider here the half of the structure for the explanation of the cloak mechanism. To illustrate the image projection capability, one lateral side (port 4) has the polarizer $P_{n,1}$ and the other lateral side (port 9) does not have a polarizer for comparison.
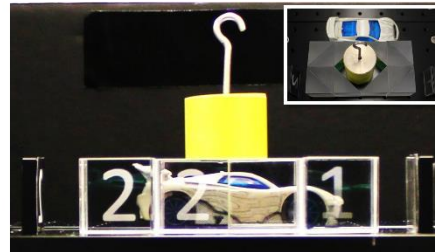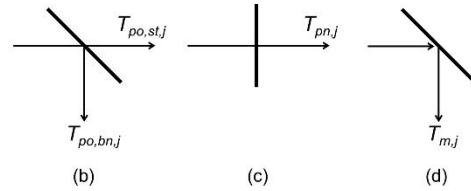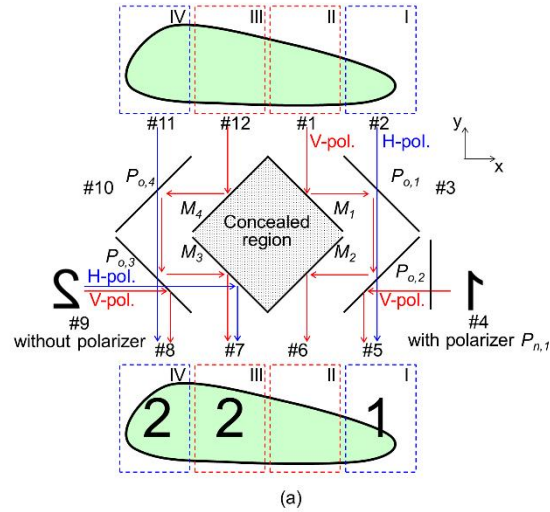
Figure 8.2.1 (a) Configuration of a cloak structure having the image projection capability. The structure consists of polarizers for oblique incidence ($P_{o,1}$-$P_{o,4}$), mirrors (M_1-M_4), and a polarizer for normal incidence ($P_{n,1}$), where port 4 has the polarizer $P_{n,1}$, and port 9 does not have a polarizer for comparison. Labels of transmission coefficients of (b) a polarizer for oblique incidence, (c) a polarizer for normal incidence, and (d) a mirror for the use in Table 8.2.1. (e) Experimental observation of the cloak structure. The inset shows the experimental setup. A toy car is placed behind the cloak structure and a cylindrical object is partly inserted in the cloak structure. The white number "1" or "2" printed on a black paper reversely in the left and right is attached on each lateral side, port 4 or port 9.

Consider first the unpolarized light traveling in the $-y$ direction from region II of the scene behind the cloak structure in Figure 8.2.1 (a). The light is reflected by mirror M_1 into the $+x$ direction. Here we assume that at ideal obliquely incident polarizers P_{o1-4}, the vertically polarized light is bent by 90° ($T_{po,bn,V} = 1$ and $T_{po,st,V} = 0$ in Figure 8.2.1 (b)) and the horizontally polarized light passes straight through ($T_{po,bn,H} = 0$ and $T_{po,st,H} = 1$ in Figure 8.2.1 (b)). Thus, the vertically

polarized light is bent twice at $P_{o,1}$ and $P_{o,2}$ and then comes out at port 6 via the reflection at mirror M_2. Likewise, for the unpolarized light coming from region I, the horizontally polarized light goes through the two polarizers $P_{o,1}$ and $P_{o,2}$ and comes out at port 5. Other orthogonal polarized lights coming from areas I and II go out at port 3 (light paths are not presented). In other words, the scene behind the cloak structure is built at the observation point through the use of 50% incidence.

Table 8.2.1 Transmission coefficients of the cloak structure of Figure 8.2.1 (a). The cloak structure is regarded as a twelve-port device and transmission coefficients for six ports are presented due to the mirror symmetry of the structure. Each coefficient in the table is defined in Figure 8.2.1 (b) – (d). Parentheses ($T_{j=V}$,$T_{j=H}$) represent transmittances for vertical polarization and horizontal polarization, assuming ideal performance of each component ($T_{m,j} = 1$, $T_{po,st,j} = 1$ or 0, $T_{po,bn,j} = 1$ or 0, and $T_{po,st,j}T_{po,bn,j} = 0$). 1/0 represents that the transmittance can be changed by polarized light.

| | | Input port | | | | | |
		1	2	3	4	5	6
Output port	1	-	0	$T_{po,st,j}T_{m,j}$ (0,1)	0	$T_{po,bn,j}T_{po,st,j}T_{m,j}$ (0,0)	$T_{po,bn,j}^2 T_{m,j}^2$ (1,0)
	2	0	-	$T_{po,bn,j}$ (1,0)	0	$T_{po,st,j}^2$ (0,1)	$T_{po,st,j}T_{po,bn,j}T_{m,j}$ (0,0)
	3	$T_{po,st,j}T_{m,j}$ (0,1)	$T_{po,bn,j}$ (1,0)	-	0	0	0
	4	0	0	0	-	$T_{po,bn,j}T_{pn,j}$ (1/0,0)	$T_{po,st,j}T_{pn,j}T_{m,j}$ (0,1/0)
	5	$T_{po,bn,j}T_{po,st,j}T_{m,j}$ (0,0)	$T_{po,st,j}^2$ (0,1)	0	$T_{po,bn,j}T_{pn,j}$ (1/0,0)	-	0
	6	$T_{po,bn,j}^2 T_{m,j}^2$ (1,0)	$T_{po,st,j}T_{po,bn,j}T_{m,j}$ (0,0)	0	$T_{po,st,j}T_{pn,j}T_{m,j}$ (0,1/0)	0	-

In our structure, the capacity for another 50% light is used for the image projection. The information sources "1" and "2" are placed at ports 4 and 9, respectively, which are reversed in the left and right due to the mirror reflection. Consider the light paths from port 9. The horizontal light goes through polarizer $P_{o,3}$ and is reflected by mirror M_3 and then goes out at port 7 while the vertical light comes out at port 8 by a 90° bent at the polarizer $P_{o,3}$. As a result, we observe "2" in both regions III and IV. On the other hand, from port 4, we observe "1" in only region I by inserting polarizer $P_{n,1}$ that allows the transmission of the vertically polarized light. Therefore, the

information can be projected in any region(s) as desired. Table 8.2.1 shows the summary of light paths with labels of ideal components defined in Figure 8.2.1 (b) − (d). We comprehend the mechanisms of the cloaking and the image projection presented above.

The experimental setup is shown in the inset of Figure 8.2.1 (e). Our cloak was implemented with four wire-grid polarizer cubes (89-604, Edmund Optics) and four right angle mirrors (45-595, Edmund Optics). White numbers "1" and "2" are printed on black papers reversely in the left and right, respectively, and these papers are placed at lateral sides. A wire-grid polarizer film (47-102, Edmund optics) is attached on the black paper having "1", where the vertically polarized light passes through. A cylindrical object is placed within the cloak structure, where the cylindrical object is partly in the concealed region while remaining upper part is exposed outside the cloak structure. There is a toy car behind the cloak structure and we capture screen shots through a camera in front of the cloak structure. Figure 8.2.1 (e) shows an experimental observation of the cloak structure from the camera. The cylindrical object becomes invisible in the cloaking area and the car behind the cloak structure is observed. We observe "1" in region I and "2" in regions III and IV, as we designed. Therefore, the mechanism of our invisibility cloak with the image projection capability has been experimentally verified for human eyes.

We further investigate the image projection ability, particularly, the placement of the image projection. We show that an image can be projected at the middle of neighboring regions as well as each region. As expected from the experimental demonstration of Figure 8.2.1 (e), the text "CLOAK" appears at region I (Figure 8.2.2 (b)) by selecting the vertical polarization (Figure 8.2.2 (a)), which is directly reflected by the side polarizer P_{o2}, and appears at region II (Figure 8.2.2 (e)) with the horizontally polarized light going through the polarizer P_{o2} and being reflected by the mirror M_2 instead (Figure 8.2.2 (d)). In this experimental demonstration, the wire-grid polarizer

film (47-102, Edmund optics) was rotated by 90° for the polarization change. The text "CLOAK" can be projected at the middle of regions I and II (Figure 8.2.2 (h)) via the horizontally polarized light for "CL" and the vertically polarized light for "OAK" (Figure 8.2.2 (g)). Therefore, proper use of polarizers for an image enables the projection in any places on the cloak structure while the invisibility cloak phenomenon is maintained (Figure 8.2.2 (c), (f), and (i)).
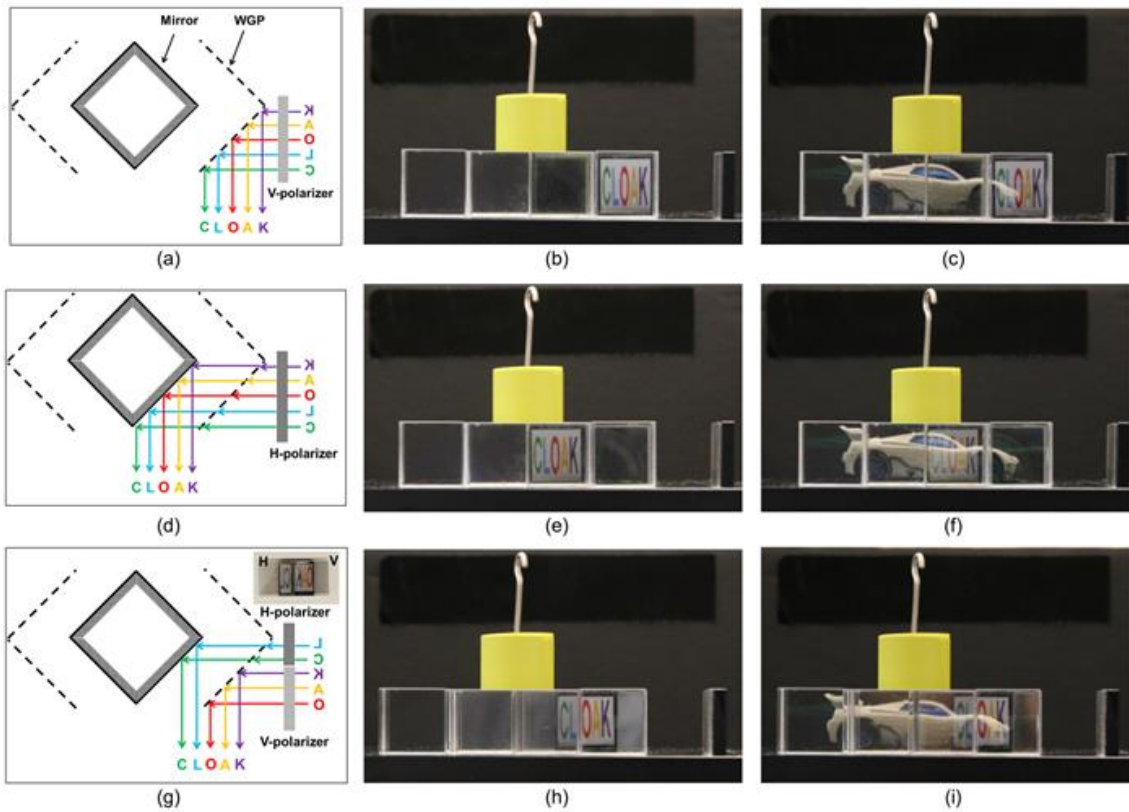
Figure 8.2.2 Image projection ability. The text "CLOAK" appears in region I for (a) − (c), in region II for (d) − (f), and in the middle of regions I and II for (g) − (i). Light paths (a), (d), (g), the image projection (b), (e), (h), and the cloaking (c), (f), (i) are presented.

The dependence of our structure on the view angle is experimentally and numerically investigated and shown in Figure 8.2.3. To illustrate the main reason for the degradation of the rebuilt scene with the increase of the view angle, the cloak structure now consists of polarizers and mirrors that are attached on glass plates (Figure 8.2.3 (a)), instead of glass blocks. This allows us to envision

what happens in the cloak structure by optical paths clearly without the effect of the refractive index of glass. The half of the structure is used for this investigation due to the symmetry of our cloak structure; the scene including a car has the same size as the summation of regions I and II. Optical paths from the original scene are calculated and the scene rebuilt at the observation plane is obtained (Figure 8.2.3 (b)) by using the commercial optical design software Zemax. The view angle has been set at 0°, 2°, and 4°, respectively. In the normal direction, the rebuilt scene is same as the original scene except for the half of the brightness (Figure 8.2.3 (d)) due to the use of 50% light (Figure 8.2.3 (e)). As the view angle increases, the rebuilt image is degraded manifesting as the lack of the information (black lines in Figure 8.2.3 (g), (j)) and the wrong position of the information (the middle part of the red car appears at the left edge in Figure 8.2.3 (g), (j)), respectively. These can be analyzed and well understood from optical paths tracing as shown in Figure 8.2.3 (e), (h), (k) for different incident angles. Taking the 4° incidence for example, light path *A-B* (yellow color ray) represents one source of image information lacking as the light ray is reflected to the neighboring wire-grid polarizer P_{o2} directly at the oblique incidence. On the other hand, the wrong position of the output image information is credited to the rays near *F-G-H* path (highlighted as the cyan color), where unpolarized light is directly incident onto the wire-grid polarizer at large angles of incidence and then split into two different paths with one path going to the correct position while the other to the left edge. It is worthwhile to mention that there is another source represented by and near *C-D-E* (red color) for both the two image degradation results. This portion of light is completely misled to the output edge leaving a black line at the center. Note that the lack and the wrong position of the information mentioned above are consistent with the cloak structure of Figure 8.2.1 (e).
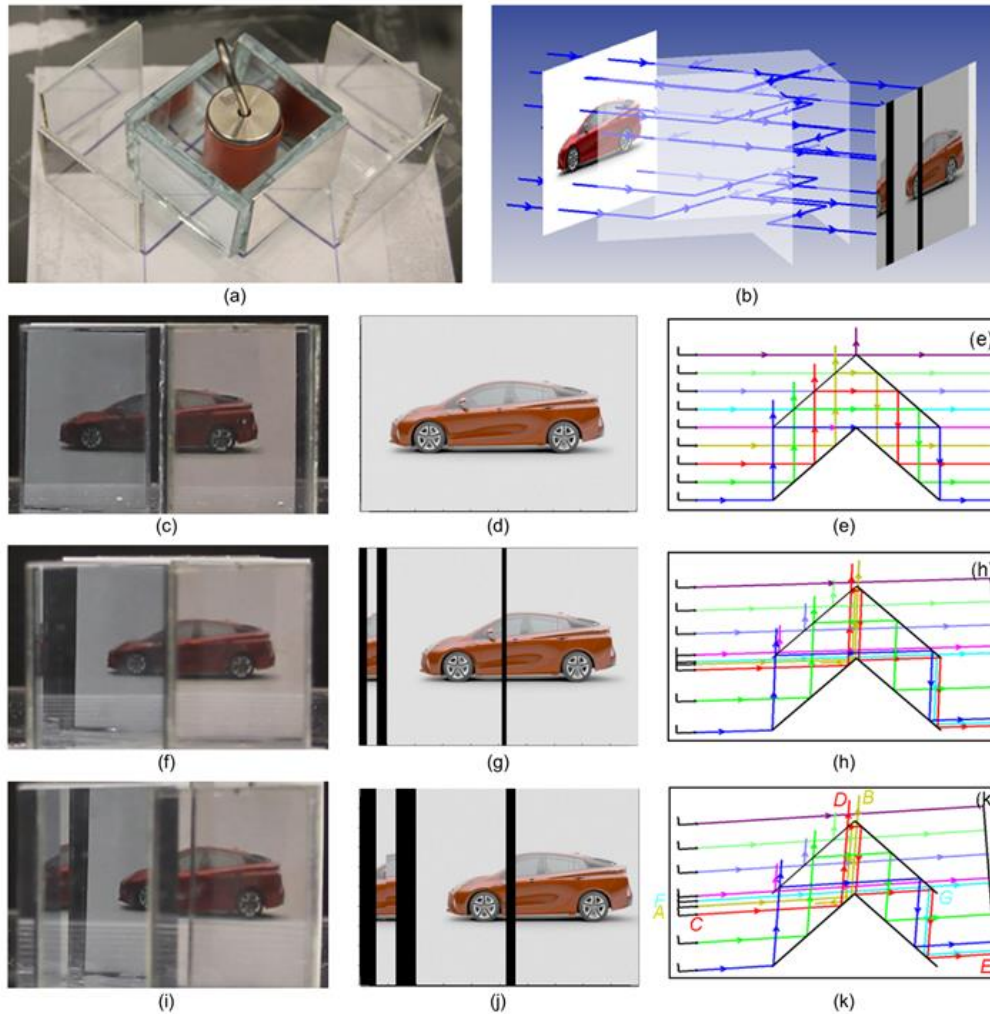
Figure 8.2.3 View angular dependence of the cloak structure. (a) Experimental setup. (b) Simulation setup. Experimental observations of the scene including a red car ((c), (f), (i)), the simulation results ((d), (g), (j)), and the corresponding light paths ((e), (h), (k)) are presented at view angles of $0°$ ((c) − (e)), (b) $2°$ ((f) − (h)), and (c) $4°$ ((i) − (k)), respectively.

8.3 Conclusion

In recent times, modern electronic devices such as cellphones, smart glasses, and computers are desired to be transparent [264]. The need for transparent objects with the display function is not limited to personal electronics. Tremendous applications have also been envisioned from the automotive industry, household appliances to healthcare sector. Typically, two approaches are adopted to realize transparent devices; firstly, a quest for materials with the unusual combination

of high electrical conductivity and high optical transparency such as ITO, and the composites of carbon nanotubes, graphene, and silver nanowires [265]. Despite the recent significant progress, mass application of these materials has remained challenging. On the other hand, driven by the desire to develop augmented reality experience, transparent or see-though displays are aimed to project virtual images of 2D or 3D objects utilizing optical components such as wedge-shaped prisms, spherical mirrors, array of lenses, etc [266]. Holography based optical elements have also been used [267]. However, as we discussed before, optical cloaking approaches combined with the imaging systems have not been explored in the past. In our experiment, we have used printed papers as information sources for the experimental demonstrations in order to verify the mechanism and architecture of the display aspect in combination with cloaking the central part of the device. In practical applications, one can implement two thin-type displays having electrically switchable polarizers at ports 4 and 9 and project text messages and movies at any locations of the cloak structure. We believe that combining the invisibility cloaking with the image projection capability promises an alternative route to realize next generation transparent devices.

In conclusion, we have explored a cloak structure that provides the image projection capability. Due to the insensitivity of polarization for human eyes, the cloaking and the image projection are simultaneously obtained via the use of orthogonal polarizations in our structure. The mechanism of our structure was experimentally verified for human eyes. Our cloak structure consists of commercially available optical components and provides a significant further step towards practical applications in see-through displays and electronics.

Chapter 9

Large-Scale and High-Performance Transparent Electrodes Based on Ultrathin Copper-Doped Silver

9.1 Introduction

Transparent electrodes have attracted considerable interest in a wide variety of applications including LEDs, PVs, EMI shielding, and smart windows [45-47, 55, 268, 269]. In addition to high conductivity and optical transparency, the recent advances of display technologies require both excellent flexibility and processability at room temperature of novel transparent conductors [54-56]. ITO is traditionally utilized as a transparent electrode due to its high visible transmission and good electrical conductivity. However, its applications in flexible devices are significantly hindered by both the poor mechanical flexibility and the required high annealing temperature. In recent years, DMD-based transparent electrodes have been noted as potential alternatives due to various advantages, including high conductivity and transparency, excellent flexibility, low-cost fabrication, great compatibility with different substrates, etc [269-272]. In order to meet the requirement for the real-world applications, both the structural stability and the transparency of the sandwiched metallic layer need to be improved.

In this chapter, we report on a highly-transparent and stable transparent electrode of excellent flexibility based on a new Cu-doped Ag [60]. This metallic film is ultrathin (<10 nm), ultra-smooth (roughness <1 nm), and of low loss, which can significantly enhance the electrode transparency. In addition, it maintains the high conductivity of Ag itself and only requires the room-temperature deposition method, thus providing new platforms for various applications that are impossible with traditional methods. Moreover, ultrathin doped silver is well protected from degradation under accelerated test under high temperature and humidity (85°C, 85% relative humidity) by selecting suitable dielectrics, which can simultaneously improve the broadband transmission of tri-layer stack by reducing the reflection. The novel transparent electrode exhibits ~89% absolute transmission across the whole visible wavelength range on PET polymeric substrates, which surpasses the transparency of the substrate itself. The EMI shielding capability of DMD structures is subsequently explored and evaluated to fully exploit the potential of the proposed highly-conductive ultrathin Ag alloy [61]. The present approach has resolved the problems faced by existing flexible transparent electrodes and may have the potential to replace traditional indium tin oxide counterparts for flexible optoelectronics, thus facilitating high-performance flexible displays and optoelectronic devices.

9.2 Dielectric-Metal-Dielectric Based Highly-Transparent Electrodes

A schematic diagram of the proposed highly-transparent flexible electrode employing a DMD configuration on a PET substrate is presented in Figure 9.2.1 (a). A ~6.5 nm Cu-doped Ag is sandwiched between two lossless dielectrics (40 nm zinc oxide (ZnO) and 60 nm Al_2O_3), which are used to enhance the visible transmission via exciting multiple transmission resonances due to their broadband perfect index match with the middle ultrathin metallic layer. The whole stack presents low sheet resistance (R_s) of ~18.6 Ω/sq due to

the high conductivity of the Cu-doped Ag layer. As depicted in Figure 9.2.1 (b), an average transmission

(from 400 to 700 nm wavelength) of ~88.70% is attained with well-suppressed reflection, which agrees

well with the calculation (~88.86%) and even surpasses the transparency of the PET itself (~88.01%). The

flat transmission spectrum corresponds to a relatively small b* value of only ~1.2 under D65 illumination,

clearly indicating the neutral color appearance of the fabricated device as shown in Figure 9.2.1 (c), which

is highly desired in various applications including touch panels and smart windows.
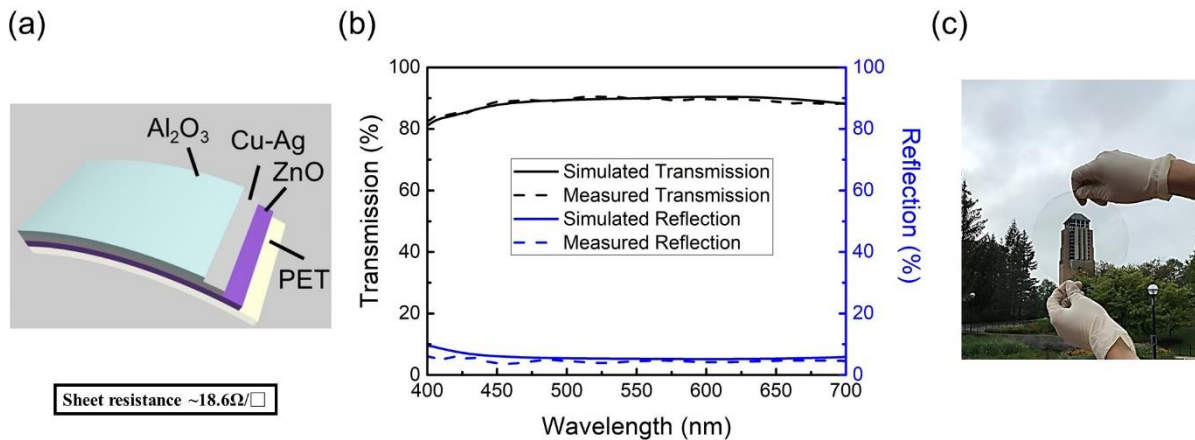
Figure 9.2.1 (a) A schematic diagram of the proposed flexible transparent electrode with great electric performance. (b) Calculated and measured optical transmission and reflection spectra, showing great agreement. (c) The optical image of the fabricated sample, showing great transparency.

Typically, Ag is selected as the middle metal due to its high conductivity and low optical loss and

the bottom and top dielectrics are used to induce the broadband transmission of the entire stack via

suppressing the reflection. It is well studied that the growth of Ag follows the Volmer-Weber mode.

Isolated islands are formed at the initial deposition stage of Ag atoms and these islands keep

growing and eventually connect to form a semi-continuous (conductive) film as the deposition

continues. The percolation threshold, which denotes the critical thickness leading to a conductive

film, of pure Ag is between 10~20 nm. Thus, the overall transparency of previous reported DMD

electrodes is limited due to the relatively thick Ag. As shown in Figure 9.2.2 (a), the Cu-doped Ag

alloy film is formed via a simple co-sputtering process, in which a small amount of Cu is

introduced into Ag. As a result, the percolation threshold of Cu-doped Ag is significantly reduced

from ~15 nm of pure Ag to ~6 nm, which is critical in further enhancing the transparency of the

DMD electrode. The SEM image provided in Figure 9.2.2 (b) clearly verifies the ultra-smooth

surface of the thin Cu-doped Ag featuring a RMS roughness of only ~0.42 nm (as shown by the

AFM image in Figure 9.2.2 (c)), which is in drastic contrast to the island morphology of 9 nm pure

Ag (Figure 9.2.2 (d)).
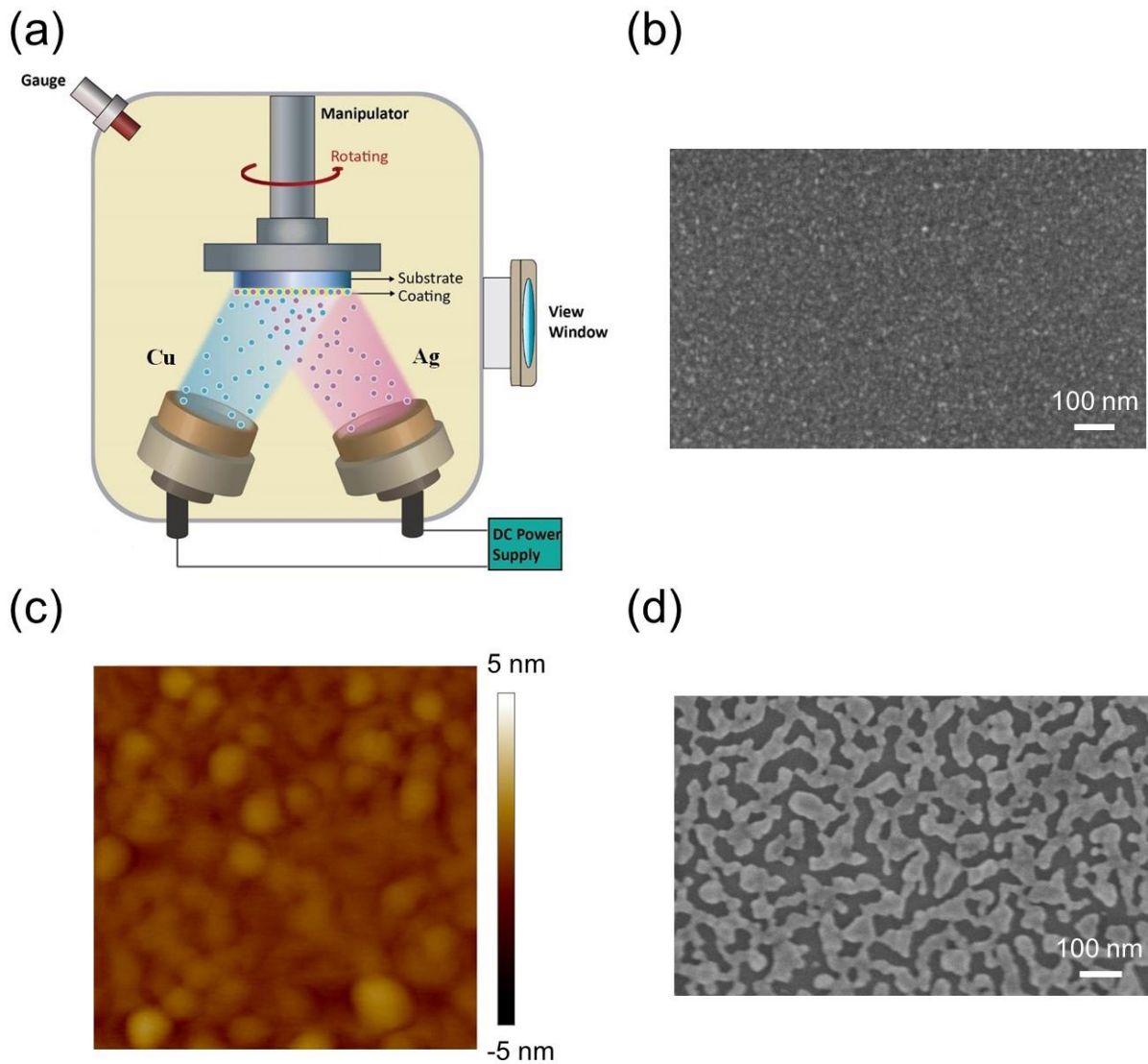
Figure 9.2.2 (a) The co-sputtering system for Cu-Ag deposition. SEM (b) and AFM (c) images of the ~6.5 nm Cu-Ag film. (d) SEM image of 9 nm pure Ag, showing discontinuous island morphology.

It is worthwhile noting that the DMD stack exhibit excellent flexibility due to the high reducibility of Cu-doped Ag. After 1,000 times bending cycles, the film shows no obvious conductivity change bending at a bending radius of 4mm and <20% change at a bending radius of 3mm (Figure 9.2.3 (a) and (b)). ZnO and Al_2O_3 are employed as the bottom and top dielectrics, respectively, due to the great performance in both improving the transmission and protecting the ultrathin metallic layer from moisture and thermal degradation. As presented in Figure 9.2.3 (c), the stack with the protection of two dielectrics has survived the accelerated test under high temperature and humidity (85°C, 85% relative humidity), showing <15% change of R_s after 120 hours test, while the R_s of the ultrathin Cu-doped Ag without any protects increases quickly to infinity under the same test condition within only 8 hours.
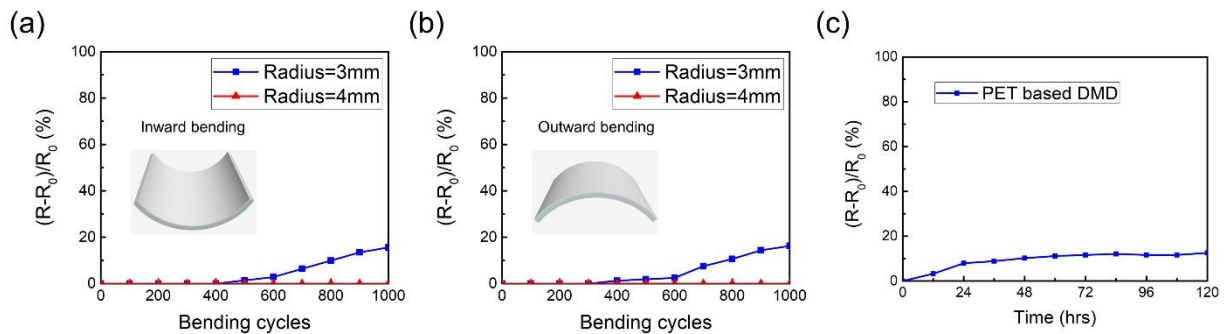
Figure 9.2.3 Dynamic inward (a) and outward (b) bending test results of DMD-based transparent electrodes as a function of bending cycles. (c) Accelerated humidity test results of DMD-based transparent electrodes as a function of test duration. The test condition is 85°C and 85% relative humidity.

9.3 Broadband Transparent Electromagnetic Interference Shielding by Ultrathin Doped Silver

The explosive advance of information technology, especially the rapid rising of modern electronics and highly integrated circuits, has created significant electromagnetic energy pollution, which is also known as electromagnetic interference (EMI) [273-277]. EMI

causes unacceptable malfunction of electronic systems used in a wide range of industrial, commercial, and scientific research applications, such as aerospace, aircraft, automobile, and satellite communication instruments [278-280]. In addition, it is reported that long-term exposure to the intensive electromagnetic radiations may cause several health hazards, including cancer and insomnia [281, 282]. Therefore, it is essential to eliminate the adverse electromagnetic waves to protect sensitive circuits and preserve a healthy living environment.

Great efforts have been made to develop transparent EMI shielding materials used for observation windows, LCDs, shielding cabinet, and mobile communication devices, which require both high optical transparency and strong electromagnetic wave attenuation. Especially, good mechanical flexibility is highly desired so that EMI shielding devices can be manufactured in a scalable and low-cost fashion [276, 280, 283, 284]. Recently, carbon-based nanomaterials, such as carbon nanotubes (CNTs) [285, 286], carbon nanofiber [287], carbon-based composites [288, 289], and graphite nanosheets (GNs), have been extensively investigated as effective EMI shielding materials because of their light weight [290, 291], chemical stability, and excellent mechanical properties. However, most of the carbon-based materials suffer from low transmittance in the visible range, which greatly limits their applications in relevant optical areas. Low transparency could be mitigated by using ultrathin graphene [292]. However, it is reported that the EMI shielding effectiveness (SE) of a monolayer chemical vapor deposition (CVD) grown graphene is only 2.27 dB [293], which is far from being able to satisfy the requirement in most applications. Although cascading graphene films provides a way to increase attenuation, the optical transparency is inevitably sacrificed [294]. Therefore, carbon-based materials are not a good choice for

simultaneous high transparency and shielding performance. Transparent conductors including ITO films and metallic patterns (*e.g.*, metal meshes and metallic nanowires) have attracted increasing attention as promising materials in transparent EMI area owing to their excellent conductivity and optical transparency [295, 296]. These transparent metal-based meshes could achieve great EMI shielding with high optical transmittance. Reported ring-shaped metallic mesh (17 dB @95%) and crackle-template-based metallic mesh (26.0 dB @91%) are among the best single-layer EMI shielding structures [297, 298]. However, the fabrication processes using photolithography or other patterning methods and additional steps of photoresist removal increase the cost and complexity. Hu et al. reported a poly(ethersulfone)/Ag Nanowires(AgNWs)/PET sandwiched structure (15 dB @85%), which shows good chemical stability [299]. Jung et al. reported AgNWs percolation network on poly(dimethylsiloxane) substrate (20 dB @93.8%) based on vacuum filtration and transfer method, showing great stretchable shielding performance [300]. Nevertheless, the large-scale production still remains a question considering sophisticated fabrication processes.

Thin metal films have been investigated as an alternative for transparent EMI shielding materials due to the required facile fabrications. Ag is the most widely used material for this application due to its highest conductivity and lowest optical loss among all metals [269, 301-303]. In order to improve the optical transparency, ultrathin Ag films are highly desired. However, a thinner Ag film with larger R_s will directly reduce the EMI SE as depicted in Figure 9.3.1 (a). The relationship between SE and R_s is predicted by the transmission-line theory as SE = $20\log_{10}(1 + \eta_0 / 2R_s)$, where $\eta_0 = 377$ Ω is the impedance of the free space. On the other hand, it is very difficult to achieve a continuous and smooth

Ag film at a thin thickness due to its special Volmer-Weber growth mode, which forms 3D islands during the film growth. This results in high R_s and additional absorption loss that further limits the EMI shielding performance.
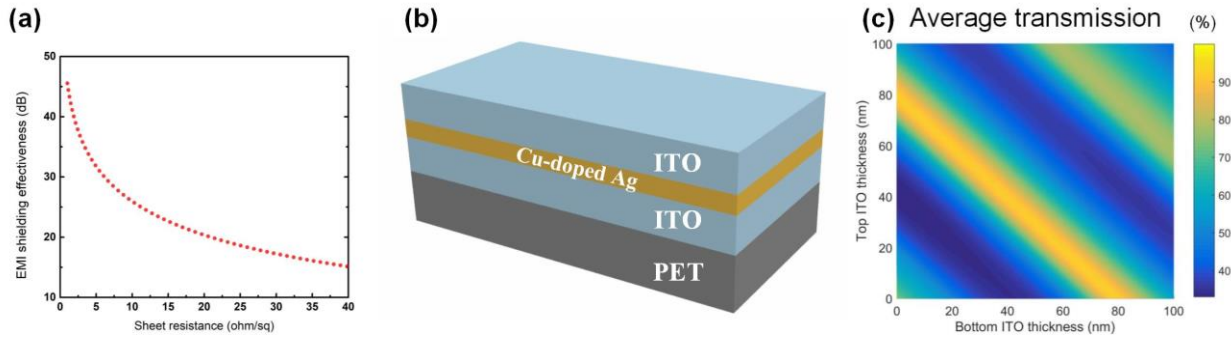
Figure 9.3.1 (a) Calculated EMI SE as a function of R_s for thin Ag films. (b) Schematic of the ITO and Cu-doped Ag layers in the DMD configuration on PET substrate. (c) Calculated average visible transmittance of EMAGS film for various thicknesses of the top and bottom ITO layers with 8 nm Cu-doped Ag.

In this section, we employ a DMD configuration base on the proposed ultrathin (8 nm) Cu-doped Ag to solve the trade-off issue between transparency and microwave shielding of traditional EMI shielding materials. Due to the high conductivity and low loss of the sandwiched ultrathin metallic film, high transparency and shielding capability can be achieved. Transparent conductive dielectrics functioning as effective AR layers are added at two sides of the metallic layer forming the DMD structure to further improve the visible transmission and EMI SE simultaneously, where the latter is due to the enhanced conductivity of the whole stack. Experimental results of this DMD-based electromagnetic Ag shield film (EMAGS) show an average EMI SE of 26 dB with average 96.5% visible transmittance (reference to PET substrate), which are among the best shielding results reported so far. It also exhibits significantly improved EMI shielding stability under mechanical deformation. We have further proved that a double-layer EMAGS (D-EMAGS) film that simply stacks two EMAGS films together exhibits an average EMI SE of over 30 dB, and SE can be improved to >50 dB in each band by

separating two layers with a quarter-wavelength space. In addition, large-area EMAGS films were demonstrated with R2R sputtering, which indicates that the proposed EMI shielding devices are advantageous for mass-production over traditional patterned metallic structures.

The conductive DMD configuration of the Cu-doped Ag layer sandwiched between two ITO layers on the PET substrate is shown in Figure 9.3.1(b). In order to get maximal light transmission, the thickness of the ITO as optical AR layers should be optimized to make reflected light beams cancel out as much as possible in the visible regime via destructive interference [304-306]. For this purpose, the average transmittance (400-700 nm) is calculated by varying thickness of the top and bottom ITO layers from 0 to 100 nm with the Cu-doped Ag layer fixed at 8 nm using transfer matrix method. It can be seen in the Figure 9.3.1(c) that the average transmittance is dependent on the thickness of dielectric layers. Maximum transmittance is achieved when both top and bottom ITO thicknesses are 40 nm, thus the proposed EMAGS film is optimized as ITO (40 nm)/Cu-doped Ag (8 nm)/ITO (40 nm). It should be noted that other transparent conductive dielectrics with similar refractive index such as ZnO and fluorine doped tin oxide (FTO) can also be used as the AR layers in the DMD structure. However, ITO is selected in this work due to its relatively high conductivity, which can boost the shielding performance of the EMAGS film.

The EMAGS film is subsequently sputtered on the PET substrate using a R2R sputtering system at room temperature, which shows great advantages over traditional metal patterned structures for mass-production. Figure 9.3.2 (a) and (b) present photographs of the fabricated sample. Figure 9.3.2 (a1) demonstrates the highly transparent 2 cm $\times$ 2 cm

EMAGS film, through which the logo could be observed clearly. Figure 9.3.2 (a2) is the bending state of the same EMAGS film, showing great flexibility. A large-area (200 cm × 50 cm) EMAGS film fabricated by the roll-to-roll method is shown in Figure 9.3.2 (b). The measured optical transmittance in the range of 300-1000 nm of the EMAGS film is presented in Figure 9.3.2 (c). For comparison, the transmission of the ITO (≈40 nm thick, the same as the ITO layers used in EMAGS films), PET substrate, and 8 nm Cu-doped Ag layer are plotted. It should be noted that the transmission of EMAGS, ITO, and Cu-doped Ag films are relative values with reference to the PET substrate, which has an average visible transmittance (400-700 nm) of 88.1%, as shown in Figure 9.3.2 (c). The average transmittance of the EMAGS film exceeds 96% (peak transmittance of 98.5% at 600 nm) in the visible range, which is much higher than both the pure Cu-doped Ag and ITO layers. This is due to the optimized DMD configuration and the suppressed reflection via AR dielectric layers as shown in Figure 9.3.2 (d). The optical reflection of the EMAGS film in the 400-700 nm wavelength range is much lower than that of the Cu-doped Ag film, and even lower than the PET substrate.
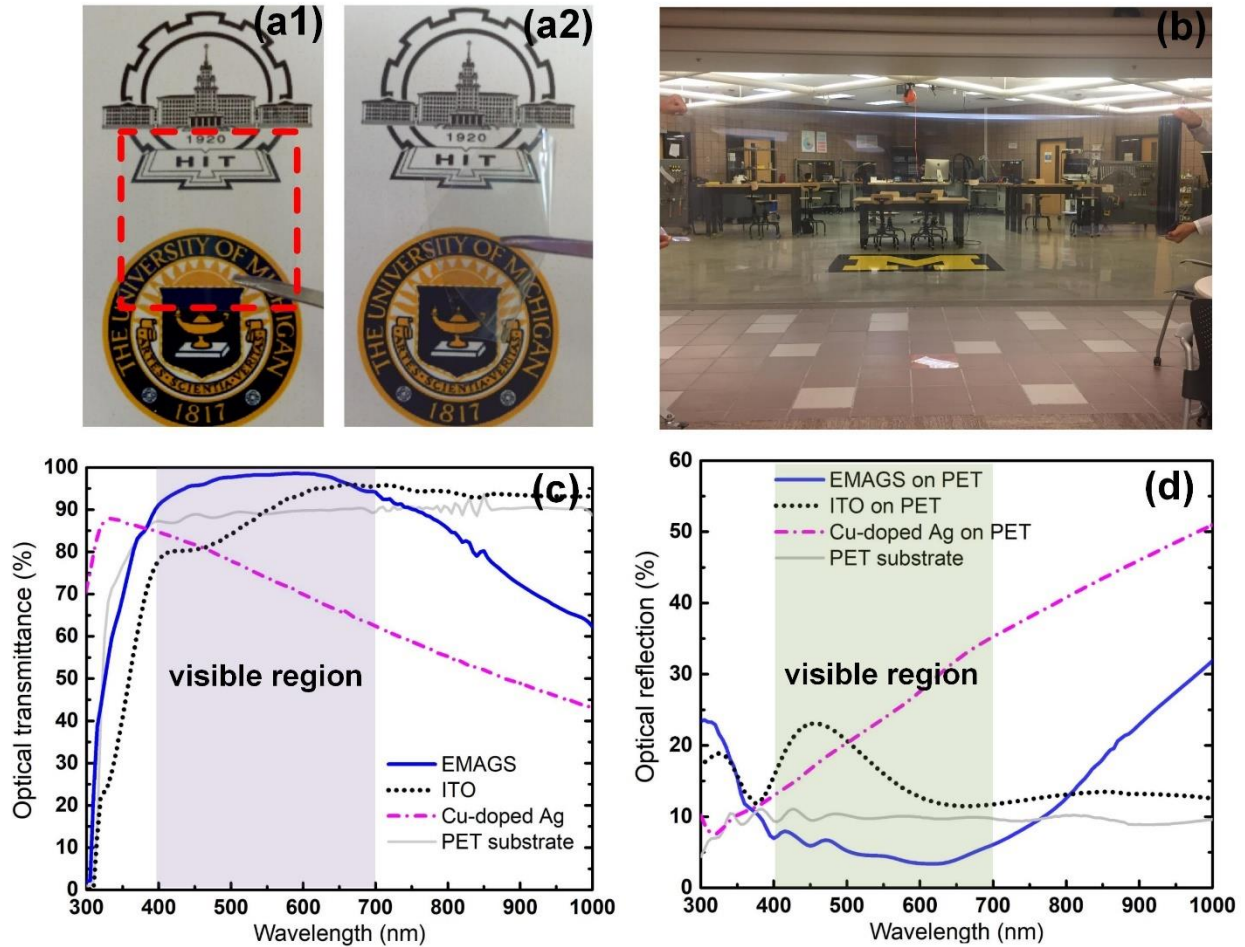
Figure 9.3.2 Photographs of (a1) EMAGS film with good transparency, (a2) EMAGS film under folding, showing outstanding flexibility, (b) A large-area (200 cm × 50 cm) transparent EMAGS film on PET fabricated by a roll-to-roll process. (c) Transmittance and (d) reflection spectra of the EMAGS, Cu-doped Ag (8 nm), ITO (40 nm), and PET substrate from 300-1000 nm.

The EMI SE of a material is defined as the logarithmic ratio of incident power to that of the transmitted power and is normally expressed in decibel unit. Higher EMI SE value means the stronger power attenuation and negligible electromagnetic wave could pass through the shielding materials. For commercial shielding applications, such as mobile phones and laptop computers, EMI SE of 20 dB is required, which corresponds to only 1% transmission of incoming electromagnetic wave [307]. To investigate the EMI shielding performance, the EMAGS films deposited on PET are measured using a waveguide

configuration. A schematic of measurement setup is shown in Figure 9.3.3. The measured RF bands are as broad as 32 GHz, which covers the bands of X (8-12 GHz), Ku (12-18 GHz), K (18-26.5 GHz), and Ka (26.5-40 GHz). For different microwave bands, we tailored the EMAGS samples to fit specific waveguides. Before measurements, the two port thru-reflect-line calibration is used to correct the system, which introduces a 12-term error correction at each frequency.
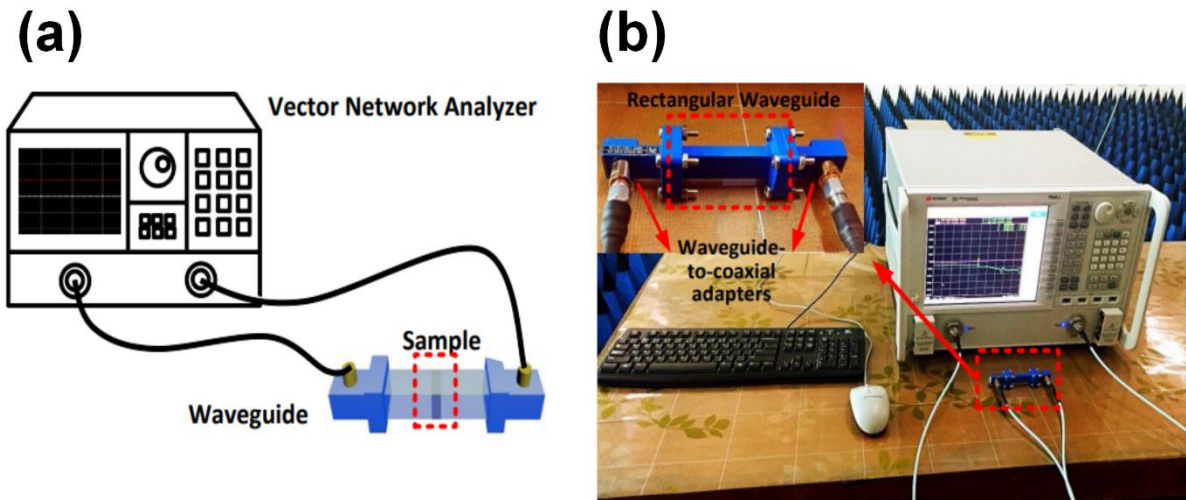
Figure 9.3.3 (a) Schematic illustration and (b) photograph of the measurement setup for the EMI shielding. Inset in (b) shows the rectangular waveguide of the Ka-band.

Figure 9.3.4 shows the EMI SE of the EMAGS films in different frequency bands across the 8-40 GHz range. As a comparison, the ITO film and the PET substrate are also measured. A pure PET film without EMAGS is completely transparent to electromagnetic waves, with the EMI SE of nearly 0 dB in the entire measured bands. The small peaks in the higher frequency band (Figure 9.3.4 (d)) are caused by the interferences between reflections from top and bottom interfaces of the PET. In the entire frequency range of 8-40 GHz, the EMAGS exhibits an excellent shielding performance, with average EMI SE of nearly 26 dB (Figure 9.3.4 (a) – (d)), which blocks ~99.7% power. More importantly, there

is no roll-off behaviour of the SE when the frequency increases, which results in the effective and indiscriminate shielding performance across a wide range. This broad (32 GHz bandwidth) and efficient (>20 dB) EMI SE of our proposed EMAGS film outperforms most previously-reported EMI shielding materials based on patterned metal structures. For instance, the EMI SE of square metal-mesh structure decreases rapidly in a narrow band, which shows a 5 dB decrease even within the Ku band. The same EMI shielding roll-off behaviour at high frequencies is also found in the ring-based and cracked-based metal-meshes due to the high transmission of electromagnetic waves at shorter wavelengths through the patterned opening [297, 298]. As a comparison, Figure 9.3.4 also provides the SE of the 8 nm Cu-doped Ag (~23 dB) and 40 nm ITO (~19 dB) films, both of which are lower than that of the EMAGS structure.

We further investigated the shielding performance of the double-layer EMAGS (D-EMAGS) by simply stacking two EMAGS films together. It presents the EMI SE above 30 dB from 8 to 40 GHz, with peak efficiency of 39 dB at 29 GHz. Fluctuations in the measured curves of the D-EMAGS film are attributed to the multiple reflections between the two EMAGS layers. The average transmittance of the D-EMAGS in the visible range is ~93%. To exploit the shielding potentials of the D-EMAGS, the two EMAGS layers are further separated by a space equal to a quarter of the centre wavelength in each band [308]. Ultrahigh SE is achieved by these configurations, with average SE of >50 dB.
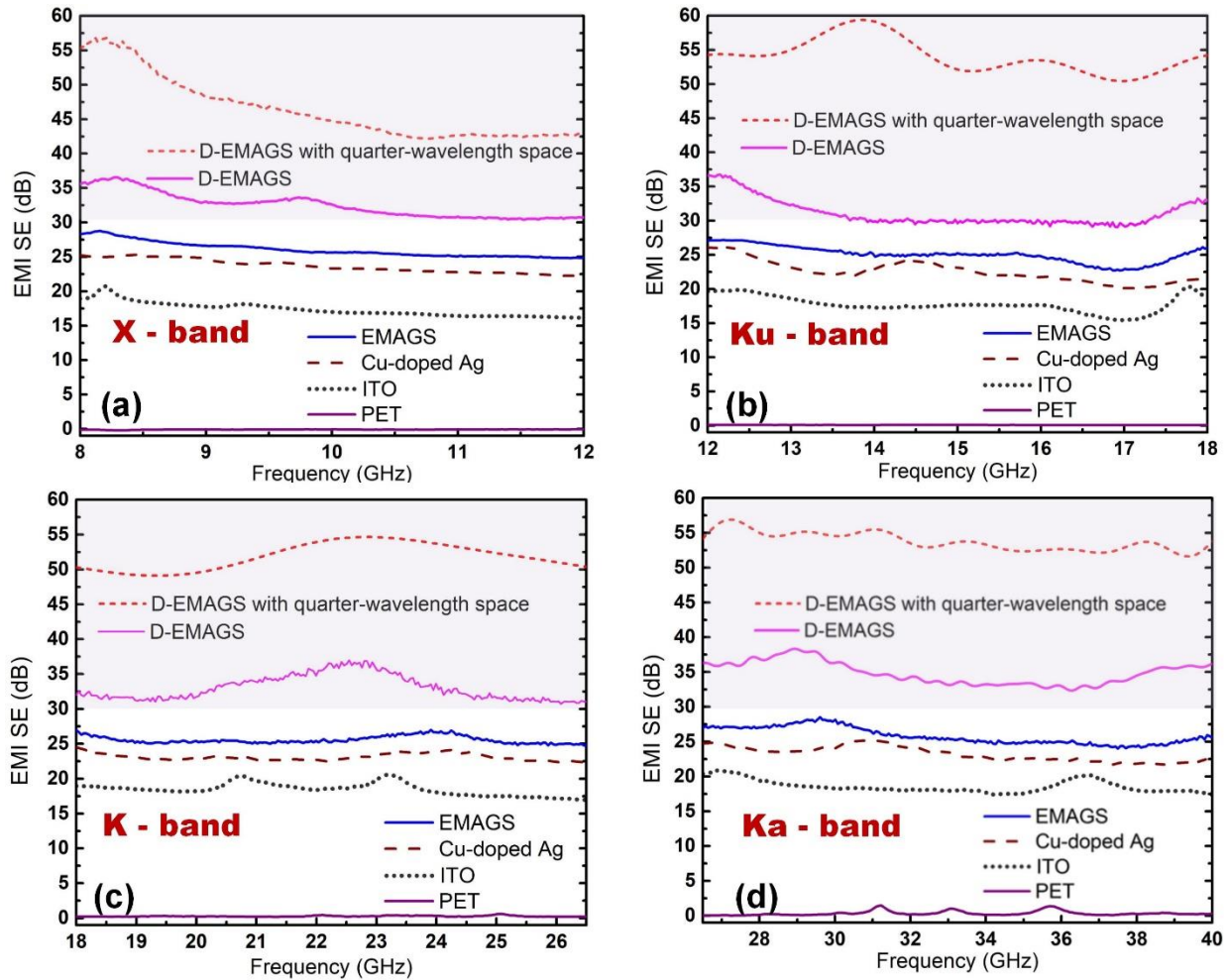
Figure 9.3.4 Measured EMI SE results of EMAGS, double-layer EMAGS, double-layer EMAGS separated by a quarter-wavelength space, Cu-doped Ag (8 nm), ITO (40 nm) and PET films at (a) X-band (8-12 GHz), (b) Ku-band (12-18 GHz), (c) K-band (18-26.5 GHz), (d) Ka-band (26.5-40 GHz).

When the electromagnetic wave is incident on the shielding materials, the incident power can be divided into reflected (R), absorbed (A), and transmitted power (T) with the relationship that A + R + T = 1. Using the scattering parameters (S_{11} and S_{21}) of the EMAGS film measured by the waveguide method, the microwave reflection and absorption in the range of 8–40 GHz can be correspondingly calculated.
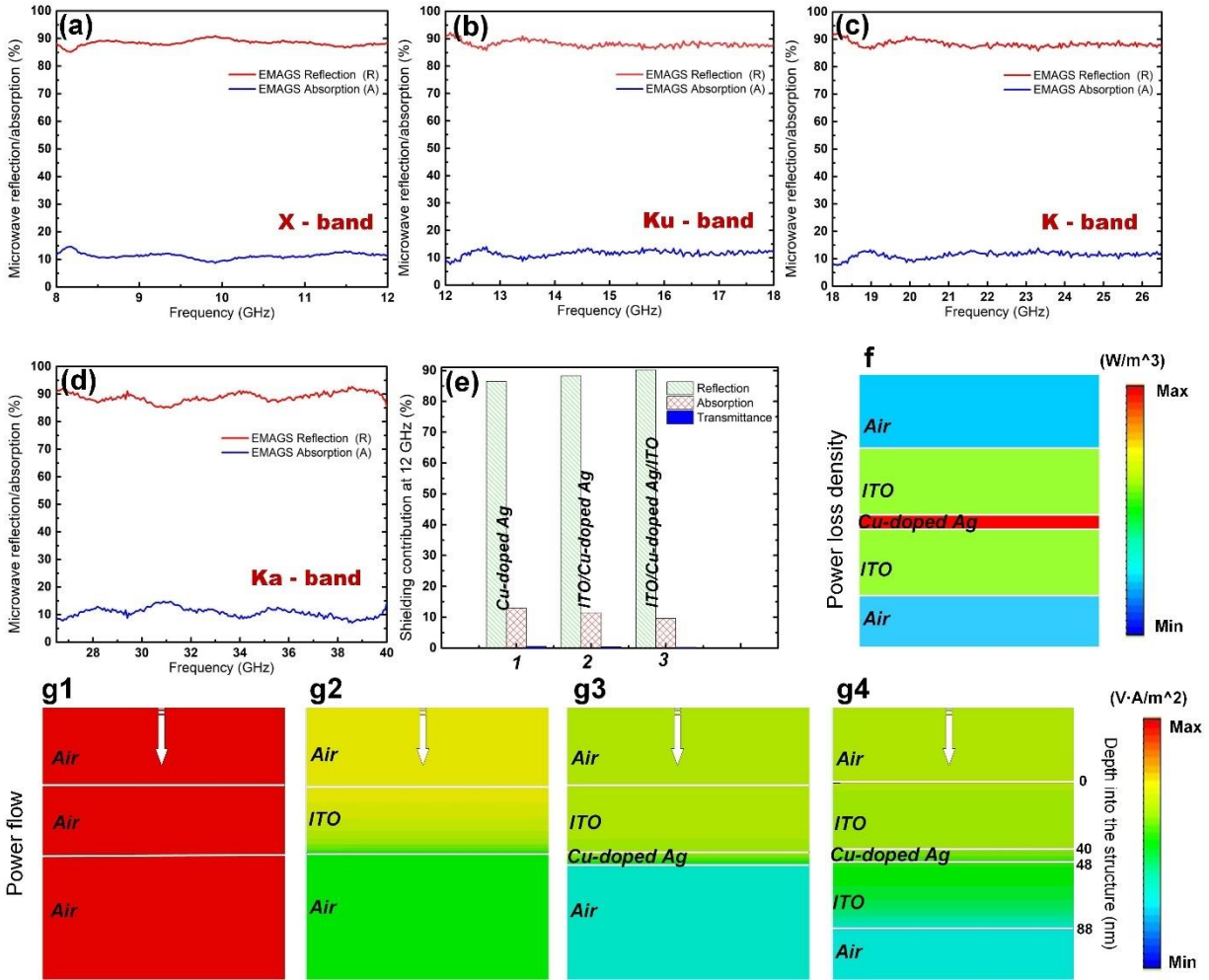
Figure 9.3.5 Measured microwave reflection (R) and absorption (A) of EMAGS film in the (a) X-band (8-12 GHz), (b) Ku-band (12-18 GHz), (c) K-band (18-26.5 GHz), (d) Ka-band (26.5-40 GHz). (e) Calculated power loss density within each layer of the ITO/Cu-doped Ag/ITO structure at 12 GHz using CST microwave studio. (f) Calculated shielding contribution from R and A of the 1) Cu-doped Ag, 2) ITO/Cu-doped Ag, and 3) ITO/Cu-doped Ag/ITO structures. Simulated power flow within the structure of the (g1) Air, (g2) ITO, (g3) ITO/Cu-doped Ag, (g4) ITO/Cu-doped Ag/ITO structures at 12 GHz using CST microwave studio. The white arrow in (g1) –(g4) denotes the incident electromagnetic wave direction.

Figure 9.3.5 (a) – (d) show the measured microwave reflection and absorption of EMAGS films as a function of incident frequencies. Overall, the average reflection and absorption are 88.5% and 11.2% of the incident power, respectively. We use 12 GHz frequency as an example to look into the shielding contribution from reflection and absorption of different structures: 1) Cu-doped Ag, 2) ITO/Cu-doped Ag, and 3) ITO/Cu-doped Ag/ITO and the results are summarized in Figure 9.3.5 (e). From the bar chart, it is obvious that the

149

shielding is mainly caused by the strong reflection for all the structures. Moreover, from 1) to 3), there is an upward trend for the reflection, rising from 86.2 % to 90.2%, while absorption experiences a decline, indicating that the shielding enhancement is originated from the increased reflection. At microwave frequencies, the real (n) and imaginary (k) parts of refractive index of the conductor (*e.g.*, Cu-doped Ag and ITO) are on the order of 10^4, so the reflection at the first air-conductor interface is close to the unity. The follow-up reflection from back conductor-air interface will reduce the total reflection to some extent by producing the destructive interference. However, less microwave can reach the back conductor-air interface when the thickness of the conductor increases (*e.g.*, adding more ITO layers in this case) and the influence of this secondary reflection on the total reflection intensity gets much weakened, which is consistent with the observation in Figure 9.3.5 (e). In addition to the dominant reflection, a certain portion of microwave also gets shielded through absorption inside the conductors. The microwave absorption contributed by the conductive dielectrics and metal layer, respectively, in the EMAGS structure are further examined. In Figure 9.3.5 (f), the contour plot of the simulated power loss density shows that the metal layer contributes more in the microwave absorption because of its larger attenuation coefficients (higher n and k). Essentially, the ITO and Cu-doped Ag layers behave like three parallel resistors under the same electrical potential when the electromagnetic wave is incident upon the EMAGS structure. Therefore, a conductive element featuring lower resistance (*i.e.*, Cu-doped Ag layer) will result in a relative stronger ohmic loss and higher microwave absorption. Figure 9.3.5 (g) illustrates the simulated power flow distribution within different structures at 12 GHz using CST microwave studio. By subsequently adding the 40 nm ITO and 8 nm Cu-doped Ag layers ((g2) – (g4)), the

entire incident EM field is blocked step by step due to both the reflection and absorption of these conductors and shows the minimal power transmission through the ITO/Cu-doped Ag/ITO structure.
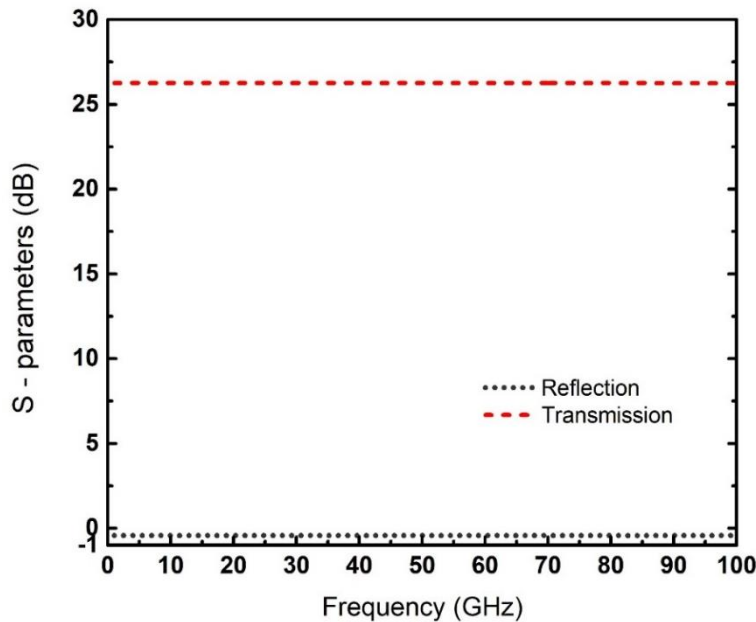
Figure 9.3.6 Simulated transmission and reflection of EMAGS film using commercial CST microwave package. The results show that the simulated EMI SE of the EMAGS film is around 26 dB up to 100 GHz, very close to the measured result. EMAGS film shows reflection of -0.4 dB in the entire band, which means nearly 90% reflection of incident power.

The reflection-dominant mechanism and broadband EMI shielding performance can be more intuitively explained by regarding the ITO/Cu-doped Ag/ITO stacks as an effective single layer of high electrical conductivity. Due to high-density carriers, the highly conductive layer has a much lower impedance across the wide microwave range compared with that of the free space (377 Ω). As a result, most of the incident electromagnetic waves get reflected back to the free space due to the large impedance mismatch at the air/EMAGS interface. In fact, the theoretical shielding bandwidth of the EMAGS film is much broader than our measurement range without any decrease in SE, which is verified by CST simulation in Figure 9.3.6.
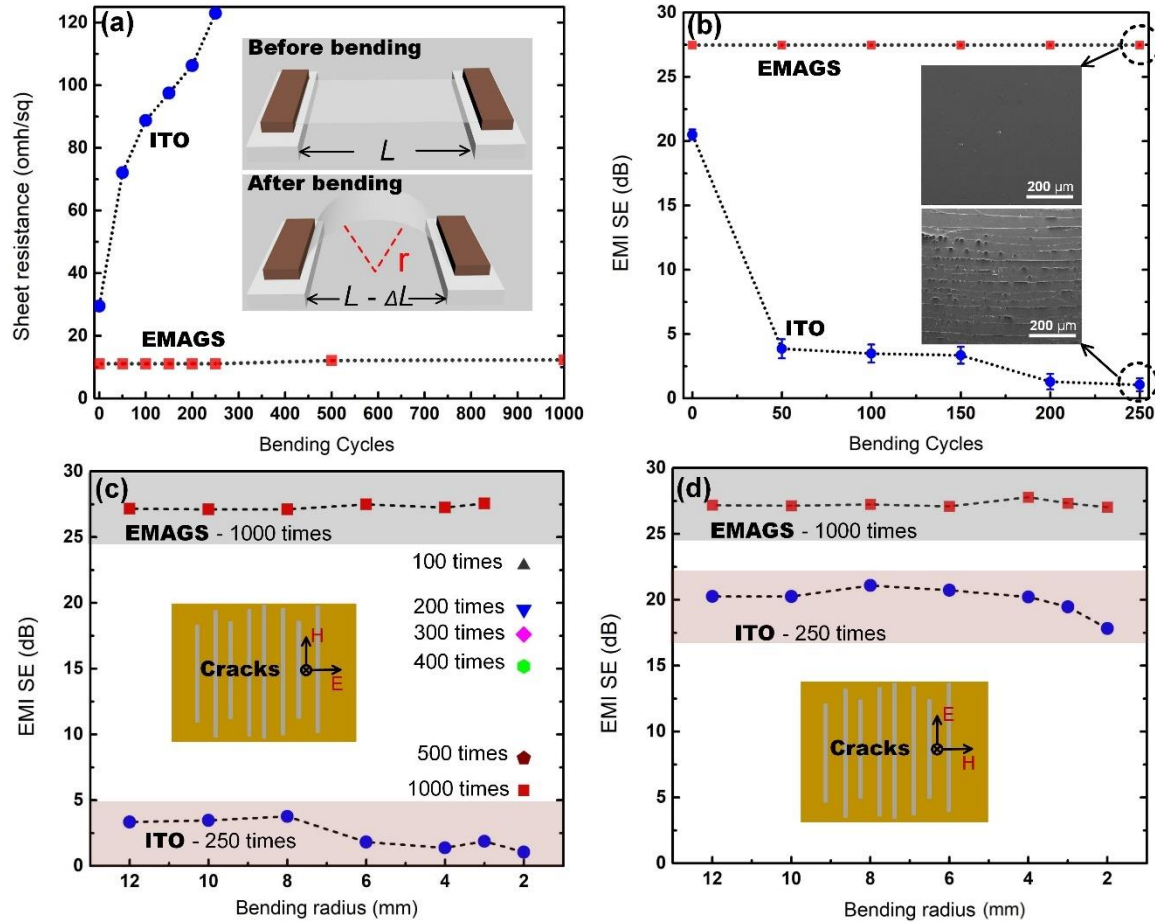
Figure 9.3.7 (a) Measured R_s of EMAGS and ITO (40 nm) on PET substrate as a function of bending cycles at the bending radius of 6 mm. Inset is a schematic illustration of the bending system. (b) EMI SE at 12 GHz of EMAGS and ITO films as a function of bending cycles at the same bending radius. Inset shows the SEM images of corresponding films after 250 times bending. EMI SE at 12 GHz of EMAGS and ITO films as a function of bending radius for (c) TM and (d) TE waves. Insets show the orientations of the electric and magnetic fields of two polarizations with respect to crack lines.

To evaluate mechanical flexibility of the EMAGS film, the change of the EMI SE of EMAGS films is measured as a function of the bending cycles and radius under repeated bending. The schematic of the bending setup is shown by the inset in Figure 9.3.7 (a). Different bending radius (*r*) could be controlled through adjusting the distance (*ΔL*) between the two ends from the initial state (*L*) [309]. As presented in Figure 9.3.7 (a), R_s of the EMAGS film remains almost unchanged after 250 bending cycles at a bending radius of 6 mm and slightly increases from 11.0 to 12.1 Ω/sq after 1000 bending cycles. In

contrast, R_s of the 40 nm ITO film drastically increases from 29.5 Ω/sq to 123.0 Ω/sq after only 250 times bending. Figure 9.3.7 (b) shows the change of the EMI SE at 12 GHz as a function of bending cycles at the bending radius of 6 mm. In comparison, the same bending tests are carried out with ITO films. It is interesting to note that after 250 bending cycles, the EMI SE of EMAGS film remains its initial high performance, while there is a significant drop on EMI shielding of ITO film after only 50 bending cycles due to the large cracks on the surface (as shown by the inset SEM image in the plot). With the bending cycles increasing from 50 to 250, the EMI SE of the ITO film continues to decline, showing almost no shielding effect (<1 dB) after 250 times repeated bending. The inset in Figure 9.3.7 (b) provides the SEM image of EMAGS film after bending test, which is free of any visible cracks. This is consistent with stable R_s and shielding performance of the proposed EMAGS film after extensive bending. Meanwhile, it is worth noting that measured R_s and EMI SE of both ITO and EMAGS films matches well with the predicted relationship presented in Figure 9.3.1 (a).

Then, we further investigated the change of the shielding performance for different polarizations with the bending radius varying from 12 to 2 mm as shown in Figure 9.3.7 (c) and (d). Remarkably, the EMI SE of EMAGS film shows no decrease after 1000 times bending when bending radius is larger than 3 mm. When r further goes down to 2 mm, SE for TM waves (*i.e.*, the electric field perpendicular to the crack lines as shown by inset in Figure 9.3.7 (c)) tends to decline with the increase of bending cycles. As illustrated in the plot at $r = 2$ mm, the EMI SE decreased to 23 dB and 6 dB after 100 and 1000 bending cycles, respectively. On the other hand, high SE remains after 1000 times bending for TE polarization (*i.e.*, the electric field parallel to the crack lines as shown by inset in Figure

9.3.7 (d)). The dependence of EMI SE on the polarizations is because that thin conductive films with crack lines after bending are essentially wire grid polarizers for RF waves considering the sub-wavelength distance between crack lines. Therefore, TM waves can easily go through, while TE polarization is effectively reflected. The same phenomena can be observed when bending ITO films. Regardless of the bending radius, EMI SE of ITO for TM waves drops significantly after 250 bending cycles (SE <5 dB), which contrasts the great flexibility of our EMAGS films. But for TE polarization shows only a small decrease after 250 times bending even at a radius of 2 mm, which is consistent with the wire grid polarizer model proposed for conductive thin films with bending crack lines.
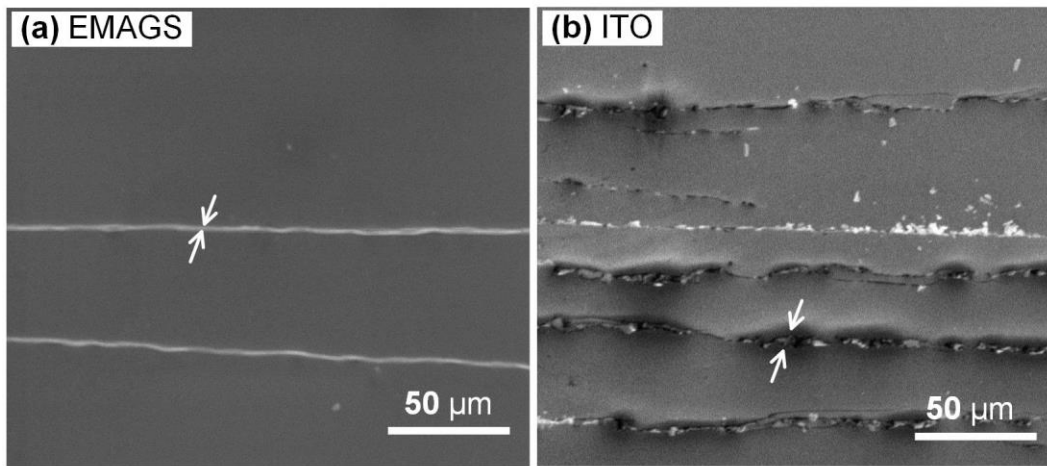
Figure 9.3.8 SEM images showing cracks of (a) EMAGS film and (b) ITO (40 nm) film after 250 bending cycles at the bending radius of 3mm. White arrows in the figures indicate the crack lines on the films.

SEM images in Figure 9.3.8 directly compare the surface morphologies of EMAGS and ITO films after bending tests at r = 3 mm. At the same bending cycles of 250, the crack lines on the ITO films are much more pronounced than those of EMAGS films. The shallow and narrow crack lines on the surface of the EMAGS films exhibits no influence on shielding as validated in Figure 9.3.7. The result indicates that the mechanical flexibility of the DMD structure gets significantly improved, which is due to both the high ductility

of the thin Cu-doped Ag sandwiched between and the enhanced cohesive strength of ITO after adding the metallic interlayer [310-312]. The flexible EMAGS film shows excellent EMI shielding stability under mechanical deformation, which enables their potential use as high-performance EMI shielding materials in flexible electronics. As summarized in Figure 9.3.9, when considering both optical transmittance and microwave shielding performance, the EMAGS film outperforms most previous transparent shielding structures and materials, including metal-meshes [297, 298, 313], graphene-based materials [293, 294, 314], graphene hybrid structure [315], silver nanowires [299, 300, 316], multilayer Ag/acrylate stack, and commercial transparent foils. Although EMI SE of Graphene/Metallic mesh structures could reach 29 dB at 12 GHz, however, it drops quickly to only 13 dB at 40 GHz [317].
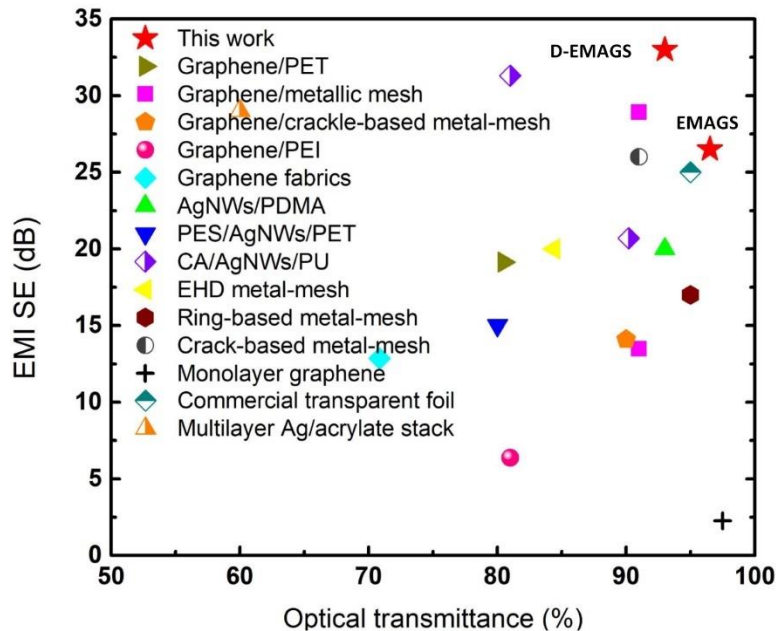
Figure 9.3.9 Comparison of EMI SE and average optical transmittance of our EMAGS and D-EMAGS films with previously-reported transparent shielding materials.

9.4 Conclusion

In conclusion, we have demonstrated a high-performance transparent conductor employing a DMD configuration featuring great transparency, conductivity, flexibility, and stability. It has the potential to replace traditional ITO-based transparent conductor and open up new possibilities for various applications including next-generation advanced display technologies and RF shielding materials.

Chapter 10

Extended Applications Using Ray-Tracing Methods

10.1 Introduction

LIDAR is a 3D laser scanning technology that is used to measure the distance to a target and visualize the surroundings with pulsed laser light. It is widely used in terrestrial, airborne, and mobile applications. It is also the key hardware component in autonomous cars, which functions as eyes and enables the car of 360° of visibility. The existence of a target is detected if LIDAR sensor receives the reflected laser light from the object. Due to the flat surface and low reflectance, little incident light can get back to the LIDAR sensors from transparent materials such as glasses and windows, especially when they are tilted. Different methods that mainly focus on optimizing the mapping algorithm for the LIDAR system have been proposed to solve this issue [64-66]. However, it is still not applicable to all circumstances. In this chapter, we propose a novel design of retroreflective micro particles that reflect light back to the original light source irrespective of incident angles, which offers a physical solution to this long-existing problem [62]. After embedding these retroflectors into transparent media, LIDAR sensors can easily detect windows and glasses at all circumstances with the help of the reflected light from these particles. As the

dimensions of the embedded micro-scale elements are beyond the resolution of human eyes, the visual appearance of transparent objects will not be affected.

On the other hand, we also discuss a new approach for planar solar concentrators (PSCs) employing curved micro-reflectors [63]. Solar concentrators are widely used in PV and photothermal conversion systems [67-69]. The planar geometry of a concentrator suggests numerous advantages of minimizing the use of reflecting materials, the device volume, and the installation cost, which open up new possibilities in various applications where the compactness of devices is highly pursued such as building-integrated solar systems and solar-energy-harvesting modules on satellites. The flat concentrator presented in this chapter is realized by collapsing a conventional concave cylindrical mirror into a planar configuration with a thickness of 15 μm, which corresponds to only 1/457 of the thickness of the original bulk device. Since each curved facet maintains the spherical shape, the proposed concentrator presents high focusing performance at all incident angles.

10.2 Retroreflective Particles for Transparent LIDAR Glasses

When light is incident on a reflective silica particle, light gets reflected into all directions as shown by the simulation results in Figure 10.2.1 (a). Here, half of the particle sphere is coated with reflective materials (*e.g.*, reflective metals) and the particle radius is selected as 3 μm. Based on the paraxial approximation, the transfer function $\overleftrightarrow{M}$ of a particle is [117]:

$$\overleftrightarrow{M} = \begin{pmatrix} 1 & 0 \\ -\dfrac{1-n}{R} & n \end{pmatrix} \begin{pmatrix} 1 & 2R \\ 0 & 1 \end{pmatrix} \begin{pmatrix} 1 & 0 \\ \dfrac{1-n}{nR} & \dfrac{1}{n} \end{pmatrix} = \begin{pmatrix} \dfrac{2}{n} - 1 & \dfrac{2R}{n} \\ \dfrac{-2(n-1)^2}{nR} & 3 - \dfrac{2}{n} \end{pmatrix},$$

where n is the refractive index of the constituent material and R is the radius. After coating the half

sphere, paraxial rays get retro-reflected only when the first term $(2 / n - 1)$ is equal to 0, *i.e.*, $n =$

2, which is validated in Figure 10.2.1 (b). However, it is easy to understand that non-paraxial rays

do not get perfectly reflected back due to the significant spherical aberrations [117] as shown in

Figure 10.2.1 (c). The very limited amount of retro-reflected light obviously cannot guarantee the

object being 'seen' by the sensor.
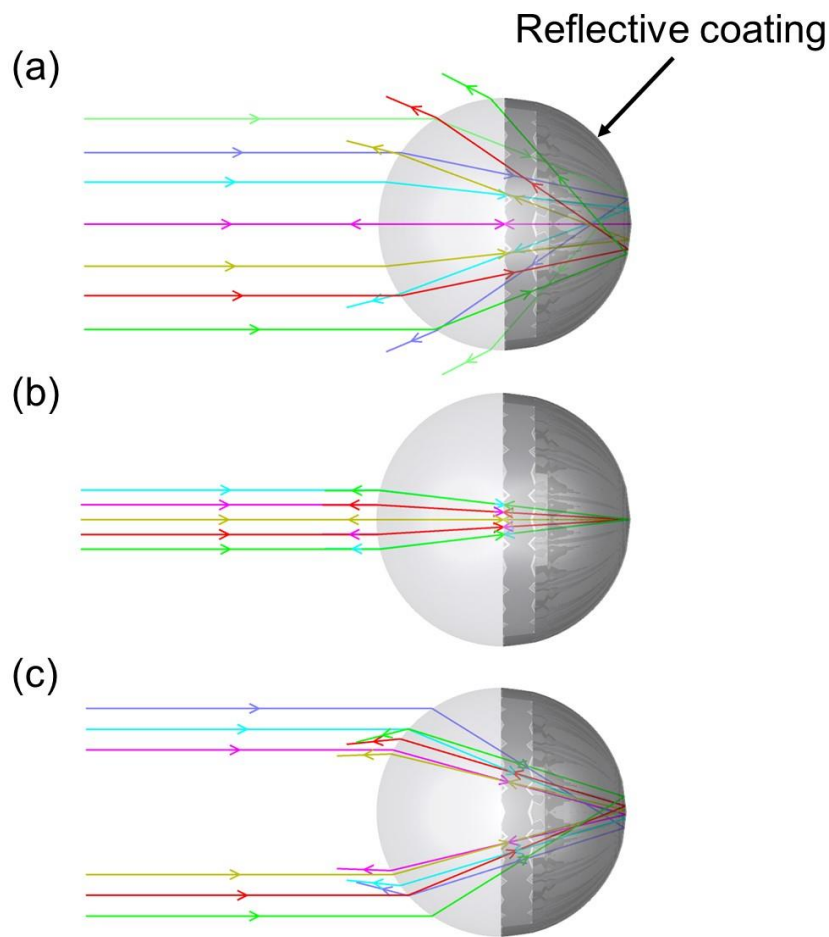
Figure 10.2.1 (a) Ray tracing of light incident on a reflective silica particle ($n = 1.45$). (b) Trace of paraxial rays incident on a reflective particle with refractive index of 2. (c) Trace of non-paraxial rays incident on the same particle in (b).

To relieve the aberrations for non-paraxial rays, a core-shell particle with the core and shell regions

consisting of materials of two different refractive indices is proposed (Figure 10.2.2 (a)). The

refractive indices of the core and shell materials are 1.81 and 1.77, respectively. It is clear that paraxial and non-paraxial rays get refracted to different extents, thereby focusing within a small spot simultaneously at the back reflective coating, which subsequently get retro-reflected. Due to the symmetry of the spherical geometry of the particle, incident light will be reflected to the source irrespective of the incident angles as shown in Figure 10.2.2 (b). Therefore, it can be expected that transparent glasses will be detected by LIDAR system with the inclusion of these micro-scale retro-reflective elements.
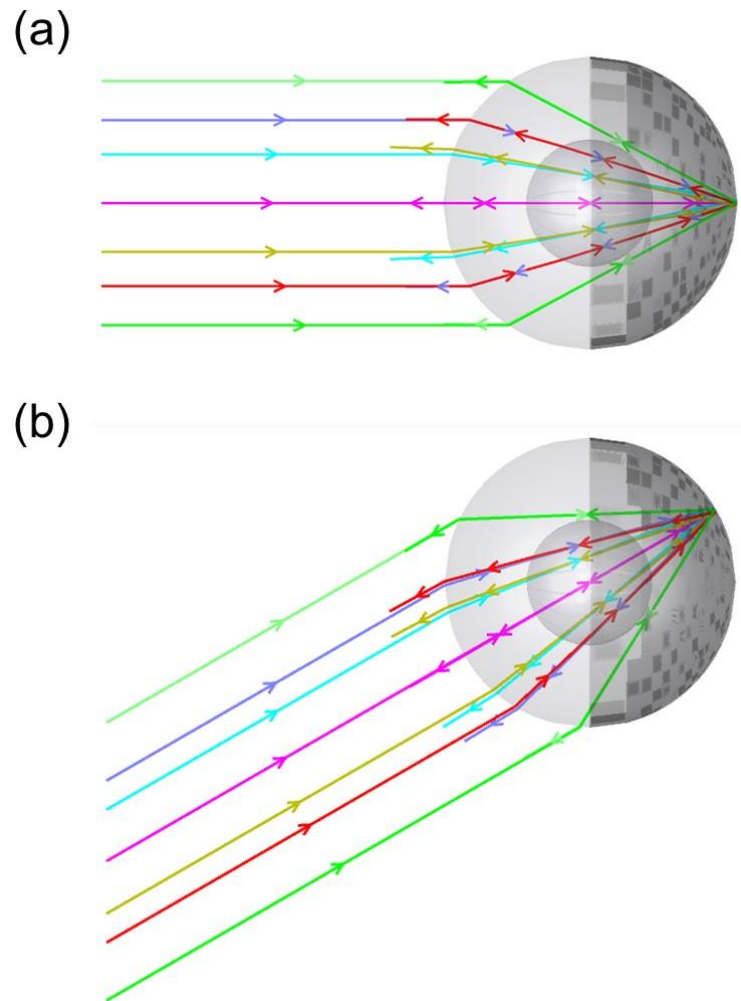
Figure 10.2.2 Ray tracing of light incident on the core-shell particle at (a) normal and (b) oblique incidence (30°). The refractive indices of the core and shell materials are 1.81 and 1.77, respectively.

10.3 Planar Solar Concentrator Based on Curved Micro-Reflectors

Figure 10.3.1 (a) shows a schematic diagram of a conventional focusing mirror with a concave cylindrical surface and bulk volume. In fact, only the curved surfaces contribute to the final focusing effects as shown in 10.3.1 (b) and most of the underneath blocks can be removed (Figure 10.3.1 (c)). Here, the height of each surface facet is designed to be the same and denoted as h, and the width of the concentrator is designated as w. The remaining surface materials can collapse into a planar concentrator as illustrated in 10.3.1 (d).
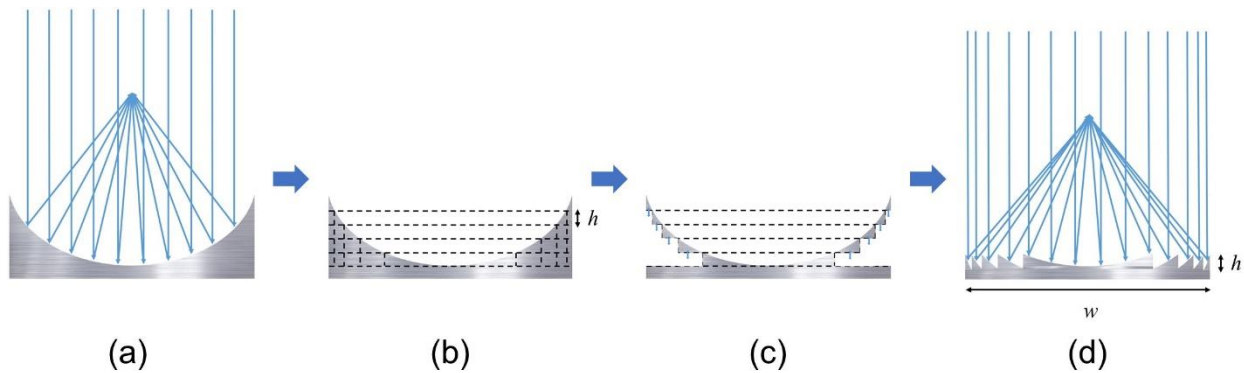
Figure 10.3.1 A method of collapsing a bulk focusing mirror into a planar concentrator.

Following the above design principle, a ~6.86mm deep focusing mirror with the radius (r) of the cylindrical surface of 120 mm and w of 80 mm is converted into a planar configuration with $h =$ 15 μm, which is subsequently fabricated on a 200 μm thick PET substrate by UV imprinting as shown in Figure 10.3.2 (a) – (c). The widths of the widest segment in the center and the narrowest facet at the edge are around ~3.79 mm and 25 μm, respectively. The Ni mold is prepared by diamond ruling using an ultra-precision five-axis machining. Figure 10.3.2 (d) provides a microscopic image of a part of device after the imprinting and the photograph in Figure 10.3.2 (e)

is the final sample (80 mm (w) × 50 mm) after the deposition of the reflective material (*e.g.*, reflective metals or multilayered broadband PCs).

(a) Thermal imprinting (b) Demolding (c) Reflector deposition

(d) (e)
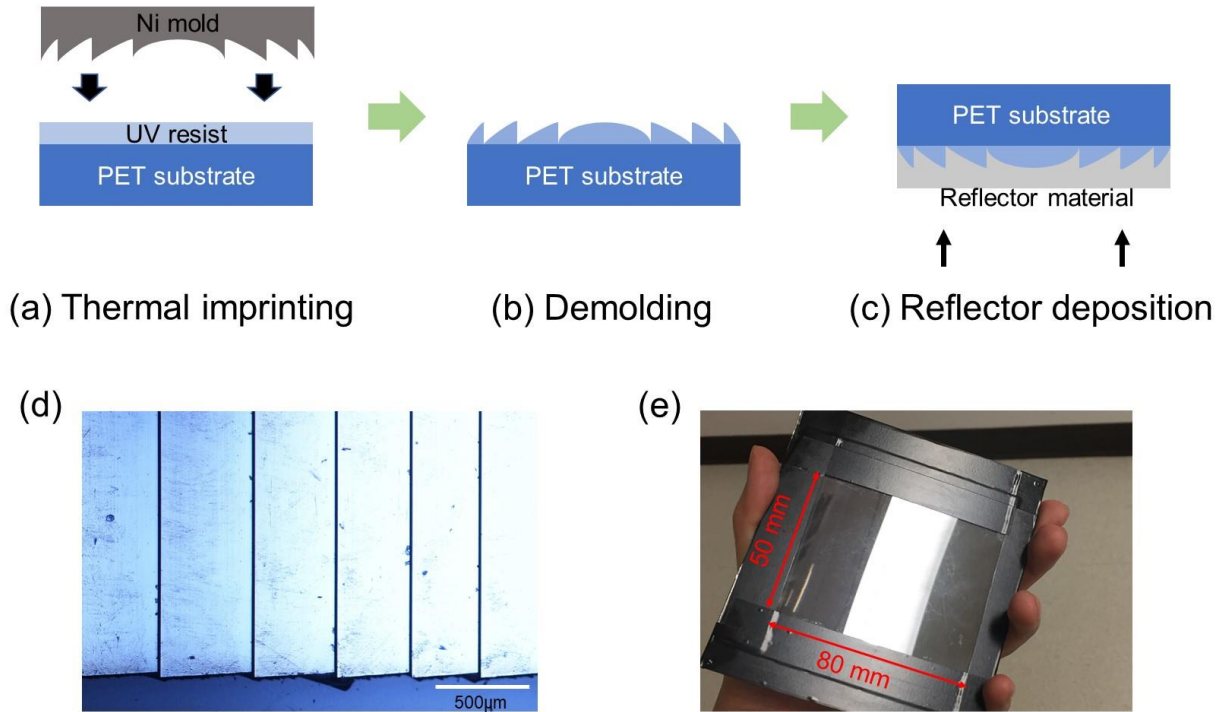
Figure 10.3.2 (a) – (c) Fabrication process of the planar concentrator on a PET substrate. (d) A microscopic image of a part of the imprinted device after step (b). (e) A photograph of the final planar concentrator.

Figure 10.3.3 presents the optical setup for characterizing the focusing capability of the planar concentrator. A solar simulator (Oriel Sol3A 94063A) is used as the light source and a reflective mirror is placed beneath to direct the light onto the sample. The focusing intensity and images are recorded by a CMOS camera (Mightex BCE-C050-U). Table 10.3.1 summarizes the performance of fabricated concentrator. The concentration ratio is defined as the ratio between the focusing linewidth and width of the sample, and the focusing efficiency is the amount of the focused light compared to the incident light intensity. It should be noted that the focal length (~40 mm) is slightly smaller than $r/2$ due to the refraction of the thick PET substrate. The summarized results in the

162

table clearly validates the high focusing performance of the designed flat concentrator at all incident angles.
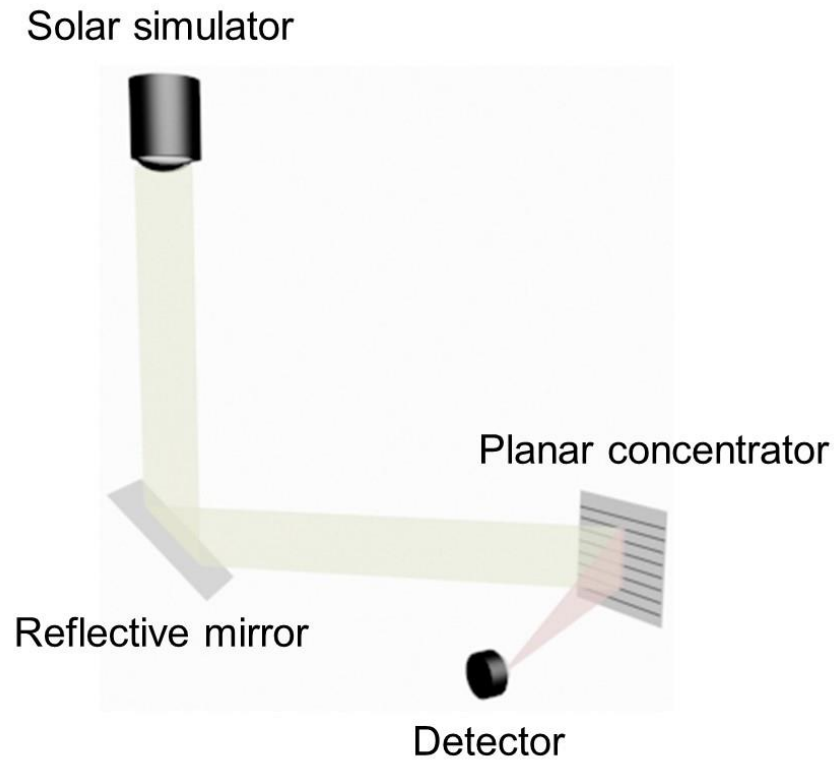
Figure 10.3.3 Optical setup for characterizing the focusing capability of the planar concentrator.

Table 10.3.1 A summary of the focusing performance of the planar solar concentrator.

Incident angle (°)	Focal length (mm)	Focusing linewidth (mm)	Concentration ratio	Depth of field (mm)	Focusing efficiency (%)
0	37	2.28	35:1	10.36	78.2
10	37	2.72	29:1	4.93	76.7
20	34	3.21	25:1	4.98	75.1
30	33	3.37	24:1	3.72	75.0

10.4 Conclusion

In summary, more optics-related applications including retroreflective particles for LIDAR systems and omnidirectional PSCs for efficient energy harvesting have been proposed employing ray-tracing methods. By adopting a core-shell structure, paraxial and non-paraxial incident rays can be simultaneously focused within a small spot on the back reflective coating of a particle and then get retro-reflected back to the light source. Therefore, embedding the micro-scale retroreflective elements into glasses and windows can potentially enable the detection of transparent objects without affecting their transparent optical appearance. In addition, a flat solar concentrator that can effectively collect solar radiation from all angles has been demonstrated via collapsing the concave cylindrical surface of a conventional focusing mirror into multiple micron facets. It significantly reduces the device thickness from ~6.86 mm to only 15 μm while maintains the high focusing performance, which holds the great promise for various applications where high compactness is highly desired.

Chapter 11

Summary and Future Directions

The thesis explores the possibility of bringing optical concepts and devices out of the lab and extending them into real-world applications.

New approaches for angle- and polarization-independent reflective-type structural colors based on simple multilayered configurations and their potential applications in vehicle paints are discussed in Chapter 2. To reduce the manufacturing cost and apply the technology to object surfaces of different shapes, all-solution-processed color filters achieved via electroplating methods are demonstrated in Chapter 3. Two additional applications of structural colors are proposed in Chapter 4 and 5. In Chapter 4, trans-reflective filters exhibiting a distinct colored reflection while transmitting the remaining broadband light spanning the solar spectrum are designed for highly-efficient colored solar cells by integrating them with c-Si solar panels. Considering that a high-index semiconductor layer (a-Si) is involved in the filter, the passive device is adapted into an active solar cell to further boost the efficiency performance of the whole colored solar panel. In Chapter 5, we present a decorative NIR-transmitting camouflage coating employing 1D PCs, which can hide the unappealing appearance of the NIR sensors that are widely used in nowadays cell phones and automobiles. As a special color, nanostructured 'perfect black' featuring

broadband absorption at the visible frequency is achieved by exciting multiple resonances in highly absorbing media, which can potentially improve the efficiency of solar energy harvesting and conversion as studied in Chapter 6.

In addition to the various applications related to structural colors, we also introduce different optical elements into vehicle interiors. In Chapter 7, a novel anti-glare colored dashboard surface is demonstrated by laminating a lenticular lens array with an alternating absorber/colored stripe substrate. Chapter 8 reports a multi-functional invisible cloaking device with the image display capabilities employing wire grid polarizers and mirrors for transparent vehicle pillars, which can improve both the driving experience and safety.

In Chapter 9, transparent conductors possessing outstanding flexibility, transparency, and conductivity are realized based on ultrathin and ultra-smooth Cu-doped Ag, which holds great promise to replace traditional ITO for future high-performance flexible optoelectronics. Other applications employing ray-tracing methods including retroreflective particles based on a core-shell configuration and omnidirectional planar solar concentrators achieved with collapsed multiple micro-reflectors are described in Chapter 10.

Some further works are critical to improve the market competitiveness of above devices or systems in the future.

1.   Structural colors: High-purity colors employing environmental-friendly materials and with even simpler designs and lower manufacturing cost are highly desired.

2.   Colored solar cells: Both the optical and electrical performance of the top colored solar cell need to be further enhanced by either utilizing more suitable active materials or optimizing the device configuration for even higher efficiency of the whole solar panel.

3.   Colored dashboards: Realizing the display functionality of the dashboard by replacing the colored stripes on the substrate with micron LED elements is a valuable direction for study.

4.   Optical cloaks: High compactness is highly desired for optical cloaking devices in real pillar applications. Therefore, we should investigate feasible solutions, such as reoptimizing the design configuration and involving other optical elements, to compact cloaking designs.

5.   Transparent electrodes: The stability of the ultrathin silver alloy under different harsh conditions need to be tested and guaranteed before being used in a real environment.

Bibliography

[1]   A. F. Koenderink, A. Alù, and A. Polman. "Nanophotonics: Shrinking light-based technology." *Science*, vol. 348, no. 6234, 2015, pp. 516-521.

[2]   J. A. Schuller, E. S. Barnard, W. Cai, Y. C. Jun, J. S. White, and M. L. Brongersma. "Plasmonics for extreme light concentration and manipulation." *Nat. Mater.*, vol. 9, no. 3, 2010, pp. 193-204.

[3]   H. A. Atwater and A. Polman. "Plasmonics for improved photovoltaic devices." *Nat. Mater.*, vol. 9, no. 3, 2010, pp. 205-213.

[4]   J. D. Caldwell, I. Vurgaftman, J. G. Tischler, O. J. Glembocki, J. C. Owrutsky, and T. L. Reinecke. "Atomic-scale photonic hybrids for mid-infrared and terahertz nanophotonics." *Nat. Nanotechnol.*, vol. 11, no. 1, 2016, pp. 9-15.

[5]   N. Meinzer, W. L. Barnes, and I. R. Hooper. "Plasmonic meta-atoms and metasurfaces." *Nat. Photon.*, vol. 8, no. 12, 2014, pp. 889-898.

[6]   F. Xia, H. Wang, D. Xiao, M. Dubey, and A. Ramasubramaniam. "Two-dimensional material nanophotonics." *Nat. Photon.*, vol. 8, no. 12, 2014, pp. 899-907.

[7]   D. K. Gramotnev and S. I. Bozhevolnyi. "Plasmonics beyond the diffraction limit." *Nat. Photon.*, vol. 4, no. 2, 2010, pp. 83-91.

[8]   Z. Fang and X. Zhu. "Plasmonics in Nanostructures." *Adv. Mater.*, vol. 25, no. 28, 2013, pp. 3840-3856.

[9]   P. Vukusic, J. R. Sambles, and C. R. Lawrence. "Structural colour: Colour mixing in wing scales of a butterfly." *Nature*, vol. 404, no. 6777, 2000, p. 457.

[10]   J. Zi, X. Yu, Y. Li, X. Hu, C. Xu, X. Wang, X. Liu, and R. Fu. "Coloration strategies in peacock feathers." *Proc. Natl. Acad. Sci.*, vol. 100, no. 22, 2003, pp. 12576-12578.

[11]   P. Vukusic and J. R. Sambles. "Photonic structures in biology." *Nature*, vol. 424, no. 6950, 2003, pp. 852-855.

[12]   S. Vignolini, P. J. Rudall, A. V. Rowland, A. Reed, E. Moyroud, R. B. Faden, J. J. Baumberg, B. J. Glover, and U. Steiner. "Pointillist structural color in Pollia fruit." *Proc. Natl. Acad. Sci.*, vol. 109, no. 39, 2012, pp. 15712-15715.

[13]   B. R. Wasik, S. F. Liew, D. A. Lilien, A. J. Dinwiddie, H. Noh, H. Cao, and A. Monteiro. "Artificial selection for structural color on butterfly wings and comparison with natural evolution." *Proc. Natl. Acad. Sci.*, vol. 111, no. 33, 2014, pp. 12109-12114.

[14]   Y. Zhang, B. Dong, A. Chen, X. Liu, L. Shi, and J. Zi. "Using Cuttlefish Ink as an Additive to Produce -Non-iridescent Structural Colors of High Color Visibility." *Adv. Mater.*, vol. 27, no. 32, 2015, pp. 4719-4724.

[15]   K.-T. Lee, C. Ji, D. Banerjee, and L. J. Guo. "Angular- and polarization-independent structural colors based on 1D photonic crystals." *Laser Photon. Rev.*, vol. 9, no. 3, 2015, pp. 354-362.

[16] C. Ji, K.-T. Lee, and L. J. Guo. "High-color-purity, angle-invariant, and bidirectional structural colors based on higher-order resonances." *Opt. Lett.*, vol. 44, no. 1, 2019, pp. 86-89.

[17] C. Ji, S. Acharya, K. Yamada, S. Maldonado, and L. J. Guo, in preparation.

[18] C. Ji, C. Yang, W. Shen, K.-T. Lee, Y. Zhang, X. Liu, and L. J. Guo. "Decorative near-infrared transmission filters featuring high-efficiency and angular-insensitivity employing 1D photonic crystals." *Nano Res.*, in press. DOI: 10.1007/s12274-018-2249-8.

[19] C. Ji, Z. Zhang, T. Masuda, Y. Kudo, and L. J. Guo. "Vivid-colored silicon solar panels with high efficiency and non-iridescent appearance." Under review.

[20] C. Ji, Q. Cui, T. Masuda, Y. Kudo, X. Chen, and L. J. Guo, in preparation.

[21] P. Spinelli, V. E. Ferry, J. v. d. Groep, M. v. Lare, M. A. Verschuuren, R. E. I. Schropp, H. A. Atwater, and A. Polman. "Plasmonic light trapping in thin-film Si solar cells." *J. Opt.*, vol. 14, no. 2, 2012, p. 024002.

[22] J. Zhu, Z. Yu, S. Fan, and Y. Cui. "Nanostructured photon management for high performance solar cells." *Mater. Sci. Eng. R-Rep.*, vol. 70, no. 3-6, 2010, pp. 330-340.

[23] V. E. Ferry, M. A. Verschuuren, M. C. v. Lare, R. E. I. Schropp, H. A. Atwater, and A. Polman. "Optimized Spatial Correlations for Broadband Light Trapping Nanopatterns in High Efficiency Ultrathin Film a-Si:H Solar Cells." *Nano. Lett.*, vol. 11, no. 10, 2011, pp. 4239-4245.

[24] V. E. Ferry, M. A. Verschuuren, H. B. T. Li, E. Verhagen, R. J. Walters, R. E. I. Schropp, H. A. Atwater, and A. Polman. "Light trapping in ultrathin plasmonic solar cells." *Opt. Express*, vol. 18, no. S2, 2010, pp. A237-A245.

[25] J. Zhu, C.-M. Hsu, Z. Yu, S. Fan, and Y. Cui. "Nanodome Solar Cells with Efficient Light Management and Self-Cleaning." *Nano. Lett.*, vol. 10, no. 6, 2010, pp. 1979-1984.

[26] K. X. Wang, Z. Yu, V. Liu, Y. Cui, and S. Fan. "Absorption Enhancement in Ultrathin Crystalline Silicon Solar Cells with Antireflection and Light-Trapping Nanocone Gratings." *Nano. Lett.*, vol. 12, no. 3, 2012, pp. 1616-1619.

[27] S. Wang, B. D. Weil, Y. Li, K. X. Wang, E. Garnett, S. Fan, and Y. Cui. "Large-Area Free-Standing Ultrathin Single-Crystal Silicon as Processable Materials." *Nano. Lett.*, vol. 13, no. 9, 2013, pp. 4393-4398.

[28] X. Chen, B. Jia, J. K. Saha, B. Cai, N. Stokes, Q. Qiao, Y. Wang, Z. Shi, and M. Gu. "Broadband Enhancement in Thin-Film Amorphous Silicon Solar Cells Enabled by Nucleated Silver Nanoparticles." *Nano. Lett.*, vol. 12, no. 5, 2012, pp. 2187-2192.

[29] P. Pathi, A. Peer, and R. Biswas. "Nano-Photonic Structures for Light Trapping in Ultra-Thin Crystalline Silicon Solar Cells." *Nanomaterials*, vol. 7, no. 1, 2017, p. 17.

[30] W. Chihhui, N. Burton, III, J. Jeremy, M. Andrew, Z. Byron, S. Steve, and S. Gennady. "Metamaterial-based integrated plasmonic absorber/emitter for solar thermo-photovoltaic systems." *J. Opt.*, vol. 14, no. 2, 2012, p. 024005.

[31] L. Zhou, Y. Tan, D. Ji, B. Zhu, P. Zhang, J. Xu, Q. Gan, Z. Yu, and J. Zhu. "Self-assembly of highly efficient, broadband plasmonic absorbers for solar steam generation." *Sci. Adv.*, vol. 2, no. 4, 2016, p. e1501227.

[32] N. T. Panagiotopoulos, E. K. Diamanti, L. E. Koutsokeras, M. Baikousi, E. Kordatos, T. E. Matikas, D. Gournis, and P. Patsalas. "Nanocomposite Catalysts Producing Durable, Super-Black Carbon Nanotube Systems: Applications in Solar Thermal Harvesting." *ACS Nano*, vol. 6, no. 12, 2012, pp. 10475-10485.

[33] X. Hu, W. Xu, L. Zhou, Y. Tan, Y. Wang, S. Zhu, and J. Zhu. "Tailoring Graphene Oxide-Based Aerogels for Efficient Solar Steam Generation under One Sun." *Adv. Mater.*, vol. 29, no. 5, 2017, p. 1604031.

[34] X. Li, W. Xu, M. Tang, L. Zhou, B. Zhu, S. Zhu, and J. Zhu. "Graphene oxide-based efficient and scalable solar desalination under one sun with a confined 2D water path." *Proc. Natl. Acad. Sci.*, vol. 113, no. 49, 2016, pp. 13953-13958.

[35] X. Hu, X. Zhang, L. Liang, J. Bao, S. Li, W. Yang, and Y. Xie. "High-Performance Flexible Broadband Photodetector Based on Organolead Halide Perovskite." *Adv. Funct. Mater.*, vol. 24, no. 46, 2014, pp. 7373-7380.

[36] H. Yuan, X. Liu, F. Afshinmanesh, W. Li, G. Xu, J. Sun, B. Lian, A. G. Curto, G. Ye, Y. Hikita, Z. Shen, S.-C. Zhang, X. Chen, M. Brongersma, H. Y. Hwang, and Y. Cui. "Polarization-sensitive broadband photodetector using a black phosphorus vertical p–n junction." *Nat. Nanotechnol.*, vol. 10, no. 8, 2015, pp. 707-713.

[37] K. K. Manga, J. Wang, M. Lin, J. Zhang, M. Nesladek, V. Nalla, W. Ji, and K. P. Loh. "High-Performance Broadband Photodetector Using Solution-Processible PbSe–TiO2–Graphene Hybrids." *Adv. Mater.*, vol. 24, no. 13, 2012, pp. 1697-1702.

[38] H. Wang, Q. Chen, L. Wen, S. Song, X. Hu, and G. Xu. "Titanium-nitride-based integrated plasmonic absorber/emitter for solar thermophotovoltaic application." *Photonics Res.*, vol. 3, no. 6, 2015, pp. 329-334.

[39] W.-X. Zhou, Y. Shen, E.-T. Hu, Y. Zhao, M.-Y. Sheng, Y.-X. Zheng, S.-Y. Wang, Y.-P. Lee, C.-Z. Wang, D. W. Lynch, and L.-Y. Chen. "Nano-Cr-film-based solar selective absorber with high photo-thermal conversion efficiency and good thermal stability." *Opt. Express*, vol. 20, no. 27, 2012, pp. 28953-28962.

[40] J. Yan, M. H. Kim, J. A. Elle, A. B. Sushkov, G. S. Jenkins, H. M. Milchberg, M. S. Fuhrer, and H. D. Drew. "Dual-gated bilayer graphene hot-electron bolometer." *Nat. Nanotechnol.*, vol. 7, no. 7, 2012, pp. 472-478.

[41] K.-T. Lee, C. Ji, and L. J. Guo. "Wide-angle, polarization-independent ultrathin broadband visible absorbers." *Appl. Phys. Lett.*, vol. 108, no. 3, 2016, p. 031107.

[42] C. Yang, C. Ji, W. Shen, K.-T. Lee, Y. Zhang, X. Liu, and L. J. Guo. "Compact Multilayer Film Structures for Ultrabroadband, Omnidirectional, and Efficient Absorption." *ACS Photonics*, vol. 3, no. 4, 2016, pp. 590-596.

[43] C. Ji, G. Zhu, C. Zhang, S. Nam, Q. Li, L. Xia, W. Zhang, D. Banerjee, and L. J. Guo. "Lenticular-Lens-Based Colored Antiglare Dashboard Surfaces." *Adv. Mater. Technol.*, vol. 2, no. 1, 2016, p. 1600177.

[44] D. Banerjee, C. Ji, and H. Iizuka. "Invisibility cloak with image projection capability." *Sci. Rep.*, vol. 6, 2016, p. 38965.

[45] M.-G. Kang, M.-S. Kim, J. Kim, and L. J. Guo. "Organic Solar Cells Using Nanoimprinted Transparent Metal Electrodes." *Adv. Mater.*, vol. 20, no. 23, 2008, pp. 4408-4413.

[46] M. G. Kang and L. J. Guo. "Nanoimprinted Semitransparent Metal Electrodes and Their Application in Organic Light-Emitting Diodes." *Adv. Mater.*, vol. 19, no. 10, 2007, pp. 1391-1396.

[47] C. Zhang, D. Zhao, D. Gu, H. Kim, T. Ling, Y.-K. R. Wu, and L. J. Guo. "An Ultrathin, Smooth, and Low-Loss Al-Doped Ag Film and Its Application as a Transparent Electrode in Organic Photovoltaics." *Adv. Mater.*, vol. 26, no. 32, 2014, pp. 5696-5701.

[48] C. Zhang, N. Kinsey, L. Chen, C. Ji, M. Xu, M. Ferrera, X. Pan, V. M. Shalaev, A. Boltasseva, and L. J. Guo. "High-Performance Doped Silver Films: Overcoming

Fundamental Material Limits for Nanophotonic Applications." *Adv. Mater.*, vol. 29, no. 19, 2017, p. 1605177.

[49] C. Zhang, N. Hong, C. Ji, W. Zhu, X. Chen, A. Agrawal, Z. Zhang, T. E. Tiwald, S. Schoeche, J. N. Hilfiker, L. J. Guo, and H. J. Lezec. "Robust Extraction of Hyperbolic Metamaterial Permittivity Using Total Internal Reflection Ellipsometry." *ACS Photonics*, vol. 5, no. 6, 2018, pp. 2234-2242.

[50] J. Wu, M. Agrawal, H. A. Becerril, Z. Bao, Z. Liu, Y. Chen, and P. Peumans. "Organic Light-Emitting Diodes on Solution-Processed Graphene Transparent Electrodes." *ACS Nano*, vol. 4, no. 1, 2010, pp. 43-48.

[51] S. K. Deb, S.-H. Lee, C. Edwin Tracy, J. Roland Pitts, B. A. Gregg, and H. M. Branz. "Stand-alone photovoltaic-powered electrochromic smart window." *Electrochim. Acta*, vol. 46, no. 13-14, 2001, pp. 2125-2130.

[52] D. R. Cairns, R. P. Witte, D. K. Sparacin, S. M. Sachsman, D. C. Paine, G. P. Crawford, and R. R. Newton. "Strain-dependent electrical resistance of tin-doped indium oxide on polymer substrates." *Appl. Phys. Lett.*, vol. 76, no. 11, 2000, pp. 1425-1427.

[53] A. Kumar and C. Zhou. "The Race To Replace Tin-Doped Indium Oxide: Which Material Will Win?" *ACS Nano*, vol. 4, no. 1, 2010, pp. 11-14.

[54] A. Khan, S. Lee, T. Jang, Z. Xiong, C. Zhang, J. Tang, L. J. Guo, and W.-D. Li. "High-Performance Flexible Transparent Electrode with an Embedded Metal Mesh Fabricated by Cost-Effective Solution Process." *Small*, vol. 12, no. 22, 2016, pp. 3021-3030.

[55] D. S. Hecht, L. Hu, and G. Irvin. "Emerging Transparent Electrodes Based on Thin Films of Carbon Nanotubes, Graphene, and Metallic Nanostructures." *Adv. Mater.*, vol. 23, no. 13, 2011, pp. 1482-1513.

[56] K. Ellmer. "Past achievements and future challenges in the development of optically transparent electrodes." *Nat. Photon.*, vol. 6, no. 12, 2012, pp. 809-817.

[57] F. Bonaccorso, Z. Sun, T. Hasan, and A. C. Ferrari. "Graphene photonics and optoelectronics." *Nat. Photon.*, vol. 4, no. 9, 2010, pp. 611-622.

[58] M. Zhang, S. Fang, A. A. Zakhidov, S. B. Lee, A. E. Aliev, C. D. Williams, K. R. Atkinson, and R. H. Baughman. "Strong, Transparent, Multifunctional, Carbon Nanotube Sheets." *Science*, vol. 309, no. 5738, 2005, p. 1215.

[59] M. Vosgueritchian, D. J. Lipomi, and Z. Bao. "Highly Conductive and Transparent PEDOT:PSS Films with a Fluorosurfactant for Stretchable and Flexible Transparent Electrodes." *Adv. Funct. Mater.*, vol. 22, no. 2, 2011, pp. 421-428.

[60] C. Ji, C. Zhang, Z. Zhang, Q. Cui, H. Wang, D. Liu, and L. J. Guo, in preparation.

[61] H. Wang, C. Ji, C. Zhang, Y. Zhang, Z. Zhang, Z. Lu, J. Tan, and L. J. Guo. "Unlocking the Full Potential of Broadband Transparent Electromagnetic Interference Shielding by Ultrathin Doped Silver." Under review.

[62] C. Ji and L. J. Guo, in preparation.

[63] C. Ji, J. Chen, and L. J. Guo, in preparation.

[64] A. Diosi and L. Kleeman. "Advanced sonar and laser range finder fusion for simultaneous localization and mapping." *Proceedings of 2004 IEEE/RSJ International Conference on Intelligent Robots and Systems (IROS)*, *Sendai, Japan*, *28 Sept.-2 Oct. 2004*. Edited by H. Inooka et al., IEEE, 2004, pp. 1854-1859.

[65] S.-W. Yang and C.-C. Wang. "Dealing with laser scanner failure: Mirrors and windows." *Proceedings of 2008 IEEE International Conference on Robotics and Automation*,

Pasadena, CA, USA, 19-23 May 2008. Edited by S. Hutchinson et al., IEEE, 2008, pp. 3009-3015.

[66]   S. Pu and G. Vosselman. "Knowledge based reconstruction of building models from terrestrial laser scanning data." *ISPRS J. Photogramm. Remote Sens.*, vol. 64, no. 6, 2009, pp. 575-584.

[67]   T. Tao, H. Zheng, K. He, and A. Mayere. "A new trough solar concentrator and its performance analysis." *Sol. Energy*, vol. 85, no. 1, 2011, pp. 198-207.

[68]   G. D. Sootha and B. S. Negi. "A comparative study of optical designs and solar flux concentrating characteristics of a linear fresnel reflector solar concentrator with tubular absorber." *Sol. Energy Mater. Sol. Cells*, vol. 32, no. 2, 1994, pp. 169-186.

[69]   K. Lovegrove, G. Burgess, and J. Pye. "A new 500 m^2 paraboloidal dish solar concentrator." *Sol. Energy*, vol. 85, no. 4, 2011, pp. 620-626.

[70]   K. Kumar, H. Duan, R. S. Hegde, S. C. W. Koh, J. N. Wei, and J. K. W. Yang. "Printing colour at the optical diffraction limit." *Nat. Nanotechnol.*, vol. 7, no. 9, 2012, pp. 557-561.

[71]   J. Hong, E. Chan, T. Chang, T.-C. Fung, B. Hong, C. Kim, J. Ma, Y. Pan, R. V. Lier, S.-g. Wang, B. Wen, and L. Zhou. "Continuous color reflective displays using interferometric absorption." *Optica*, vol. 2, no. 7, 2015, pp. 589-597.

[72]   S. Yokogawa, S. P. Burgos, and H. A. Atwater. "Plasmonic Color Filters for CMOS Image Sensor Applications." *Nano. Lett.*, vol. 12, no. 8, 2012, pp. 4349-4354.

[73]   S. Kim, H.-J. Kwon, S. Lee, H. Shim, Y. Chun, W. Choi, J. Kwack, D. Han, M. Song, S. Kim, S. Mohammadi, I. Kee, and Y. Lee Sang. "Low-Power Flexible Organic Light-Emitting Diode Display Device." *Adv. Mater.*, vol. 23, no. 31, 2011, pp. 3511-3516.

[74]   R. D. Jansen-van Vuuren, A. Armin, A. K. Pandey, P. L. Burn, and P. Meredith. "Organic Photodiodes: The Future of Full Color Detection and Image Sensing." *Adv. Mater.*, vol. 28, no. 24, 2016, pp. 4766-4802.

[75]   F.-J. Ko and H.-P. D. Shieh. "High-efficiency micro-optical color filter for liquid-crystal projection system applications." *Appl. Opt.*, vol. 39, no. 7, 2000, pp. 1159-1163.

[76]   P. B. Catrysse, W. Suh, S. Fan, and M. Peeters. "One-mode model for patterned metal layers inside integrated color pixels." *Opt. Lett.*, vol. 29, no. 9, 2004, pp. 974-976.

[77]   K. Chung, S. Yu, C.-J. Heo, J. W. Shim, S.-M. Yang, M. G. Han, H.-S. Lee, Y. Jin, S. Y. Lee, N. Park, and J. H. Shin. "Flexible, Angle-Independent, Structural Color Reflectors Inspired by Morpho Butterfly Wings." *Adv. Mater.*, vol. 24, no. 18, 2012, pp. 2375-2379.

[78]   K. Chung and J. H. Shin. "Range and stability of structural colors generated by Morpho-inspired color reflectors." *J. Opt. Soc. Am. A*, vol. 30, no. 5, 2013, pp. 962-968.

[79]   J.-G. Park, S.-H. Kim, S. Magkiriadou, T. M. Choi, Y.-S. Kim, and V. N. Manoharan. "Full-Spectrum Photonic Pigments with Non-iridescent Structural Colors through Colloidal Assembly." *Angew. Chem. Int. Ed.*, vol. 53, no. 11, 2014, pp. 2899-2903.

[80]   R. W. Sabnis. "Color filter technology for liquid crystal displays." *Displays*, vol. 20, no. 3, 1999, pp. 119-129.

[81]   A. Kristensen, J. K. W. Yang, S. I. Bozhevolnyi, S. Link, P. Nordlander, N. J. Halas, and N. A. Mortensen. "Plasmonic colour generation." *Nat. Rev. Mater.*, vol. 2, no. 1, 2016, p. 16088.

[82]   T. Xu, Y.-K. Wu, X. Luo, and L. J. Guo. "Plasmonic nanoresonators for high-resolution colour filtering and spectral imaging." *Nat. Commun.*, vol. 1, 2010, p. 59.

[83] J. Olson, A. Manjavacas, T. Basu, D. Huang, A. E. Schlather, B. Zheng, N. J. Halas, P. Nordlander, and S. Link. "High Chromaticity Aluminum Plasmonic Pixels for Active Liquid Crystal Displays." *ACS Nano*, vol. 10, no. 1, 2016, pp. 1108-1117.

[84] D. Franklin, Y. Chen, A. Vazquez-Guardado, S. Modak, J. Boroumand, D. Xu, S.-T. Wu, and D. Chanda. "Polarization-independent actively tunable colour generation on imprinted plasmonic surfaces." *Nat. Commun.*, vol. 6, 2015, p. 7337.

[85] J. Wang, Q. Fan, S. Zhang, Z. Zhang, H. Zhang, Y. Liang, X. Cao, and T. Xu. "Ultra-thin plasmonic color filters incorporating free-standing resonant membrane waveguides with high transmission efficiency." *Appl. Phys. Lett.*, vol. 110, no. 3, 2017, p. 031110.

[86] M. J. Uddin and R. Magnusson. "Efficient Guided-Mode-Resonant Tunable Color Filters." *IEEE Photonics Technol. Lett.*, vol. 24, no. 17, 2012, pp. 1552-1554.

[87] C.-H. Park, Y.-T. Yoon, V. R. Shrestha, C.-S. Park, S.-S. Lee, and E.-S. Kim. "Electrically tunable color filter based on a polarization-tailored nano-photonic dichroic resonator featuring an asymmetric subwavelength grating." *Opt. Express*, vol. 21, no. 23, 2013, pp. 28783-28793.

[88] G. Si, Y. Zhao, J. Lv, M. Lu, F. Wang, H. Liu, N. Xiang, T. J. Huang, A. J. Danner, J. Teng, and Y. J. Liu. "Reflective plasmonic color filters based on lithographically patterned silver nanorod arrays." *Nanoscale*, vol. 5, no. 14, 2013, pp. 6243-6248.

[89] K. Seo, M. Wober, P. Steinvurzel, E. Schonbrun, Y. Dan, T. Ellenbogen, and K. B. Crozier. "Multicolored Vertical Silicon Nanowires." *Nano. Lett.*, vol. 11, no. 4, 2011, pp. 1851-1856.

[90] T. Xu, H. Shi, Y.-K. Wu, A. F. Kaplan, J. G. Ok, and L. J. Guo. "Structural Colors: From Plasmonic to Carbon Nanostructures." *Small*, vol. 7, no. 22, 2011, pp. 3128-3136.

[91] D. Inoue, A. Miura, T. Nomura, H. Fujikawa, K. Sato, N. Ikeda, D. Tsuya, Y. Sugimoto, and Y. Koide. "Polarization independent visible color filter comprising an aluminum film with surface-plasmon enhanced transmission through a subwavelength array of holes." *Appl. Phys. Lett.*, vol. 98, no. 9, 2011, p. 093113.

[92] M. A. Vincenti, M. Grande, D. de Ceglia, T. Stomeo, V. Petruzzelli, M. De Vittorio, M. Scalora, and A. D'Orazio. "Color control through plasmonic metal gratings." *Appl. Phys. Lett.*, vol. 100, no. 20, 2012, p. 201107.

[93] Y. S. Do, J. H. Park, B. Y. Hwang, S.-M. Lee, B.-K. Ju, and K. C. Choi. "Plasmonic Color Filter and its Fabrication for Large-Area Applications." *Adv. Opt. Mater.*, vol. 1, no. 2, 2013, pp. 133-138.

[94] B. Ai, Y. Yu, H. Möhwald, and G. Zhang. "Responsive Monochromatic Color Display Based on Nanovolcano Arrays." *Adv. Opt. Mater.*, vol. 1, no. 10, 2013, pp. 724-731.

[95] H. J. Park, T. Xu, J. Y. Lee, A. Ledbetter, and L. J. Guo. "Photonic Color Filters Integrated with Organic Solar Cells for Energy Harvesting." *ACS Nano*, vol. 5, no. 9, 2011, pp. 7055-7060.

[96] H.-S. Lee, Y.-T. Yoon, S.-S. Lee, S.-H. Kim, and K.-D. Lee. "Color filter based on a subwavelength patterned metal grating." *Opt. Express*, vol. 15, no. 23, 2007, pp. 15457-15463.

[97] Y.-T. Yoon, H.-S. Lee, S.-S. Lee, S. H. Kim, J.-D. Park, and K.-D. Lee. "Color filter incorporating a subwavelength patterned grating in poly silicon." *Opt. Express*, vol. 16, no. 4, 2008, pp. 2374-2380.

[98] A. F. Kaplan, T. Xu, and L. J. Guo. "High efficiency resonance-based spectrum filters with tunable transmission bandwidth fabricated using nanoimprint lithography." *Appl. Phys. Lett.*, vol. 99, no. 14, 2011, p. 143111.

[99] C.-H. Park, Y.-T. Yoon, and S.-S. Lee. "Polarization-independent visible wavelength filter incorporating a symmetric metal-dielectric resonant structure." *Opt. Express*, vol. 20, no. 21, 2012, pp. 23769-23777.

[100] M. G. Han, C.-J. Heo, H. Shim, C. G. Shin, S.-J. Lim, J. W. Kim, Y. W. Jin, and S. Lee. "Structural Color Manipulation Using Tunable Photonic Crystals with Enhanced Switching Reliability." *Adv. Opt. Mater.*, vol. 2, no. 6, 2014, pp. 535-541.

[101] J. Zhou, A. Panday, Y. Xu, X. Chen, L. Chen, C. Ji, and L. J. Guo. "Visualizing Mie Resonances in Low-Index Dielectric Nanoparticles." *Phys. Rev. Lett.*, vol. 120, no. 25, 2018, p. 253902.

[102] Y.-K. R. Wu, A. E. Hollowell, C. Zhang, and L. J. Guo. "Angle-Insensitive Structural Colours based on Metallic Nanocavities and Coloured Pixels beyond the Diffraction Limit." *Sci. Rep.*, vol. 3, 2013, p. 1194.

[103] C. Yang, W. Shen, J. Zhou, X. Fang, D. Zhao, X. Zhang, C. Ji, B. Fang, Y. Zhang, X. Liu, and L. J. Guo. "Angle Robust Reflection/Transmission Plasmonic Filters Using Ultrathin Metal Patch Array." *Adv. Opt. Mater.*, vol. 4, no. 12, 2016, pp. 1981-1986.

[104] C.-S. Park, V. R. Shrestha, S.-S. Lee, E.-S. Kim, and D.-Y. Choi. "Omnidirectional color filters capitalizing on a nano-resonator of Ag-TiO$_2$-Ag integrated with a phase compensating dielectric overlay." *Sci. Rep.*, vol. 5, 2015, p. 8467.

[105] D. Banerjee and M. Zhang. "Quarter-wave design criteria for omnidirectional structural colors." *J. Mod. Opt.*, vol. 57, no. 13, 2010, pp. 1180-1188.

[106] K.-T. Lee, J.-Y. Jang, S. J. Park, C. Ji, S.-M. Yang, L. J. Guo, and H. J. Park. "Angle-Insensitive and CMOS-Compatible Subwavelength Color Printing." *Adv. Opt. Mater.*, vol. 4, no. 11, 2016, pp. 1696-1702.

[107] K.-T. Lee, J.-Y. Jang, S. J. Park, U. K. Thakur, C. Ji, L. J. Guo, and H. J. Park. "Subwavelength nanocavity for flexible structural transmissive color generation with a wide viewing angle." *Optica*, vol. 3, no. 12, 2016, pp. 1489-1495.

[108] K.-T. Lee, S. Seo, J. Y. Lee, and L. J. Guo. "Strong Resonance Effect in a Lossy Medium-Based Optical Cavity for Angle Robust Spectrum Filters." *Adv. Mater.*, vol. 26, no. 36, 2014, pp. 6324-6328.

[109] K.-T. Lee, J. Y. Lee, S. Seo, and L. J. Guo. "Colored ultrathin hybrid photovoltaics with high quantum efficiency." *Light: Sci. Appl.*, vol. 3, 2014, p. e215.

[110] A. S. Roberts, A. Pors, O. Albrektsen, and S. I. Bozhevolnyi. "Subwavelength Plasmonic Color Printing Protected for Ambient Use." *Nano. Lett.*, vol. 14, no. 2, 2014, pp. 783-787.

[111] C. Yang, W. Shen, Y. Zhang, H. Peng, X. Zhang, and X. Liu. "Design and simulation of omnidirectional reflective color filters based on metal-dielectric-metal structure." *Opt. Express*, vol. 22, no. 9, 2014, pp. 11384-11391.

[112] G. B. Smith, A. Gentle, P. D. Swift, A. Earp, and N. Mronga. "Coloured paints based on iron oxide and silicon oxide coated flakes of aluminium as the pigment, for energy efficient paint: optical and thermal experiments." *Sol. Energy Mater. Sol. Cells*, vol. 79, no. 2, 2003, pp. 179-197.

[113] S. Magkiriadou, J.-G. Park, Y.-S. Kim, and V. N. Manoharan. "Absence of red structural color in photonic glasses, bird feathers, and certain beetles." *Phys. Rev. E*, vol. 90, no. 6, 2014, p. 062302.

[114] C.-C. Lee, S.-H. Chen, and C.-c. Jaing. "Optical monitoring of silver-based transparent heat mirrors." *Appl. Opt.*, vol. 35, no. 28, 1996, pp. 5698-5703.

[115] H. Köstlin and G. Frank. "Optimization of transparent heat mirrors based on a thin silver film between antireflection films." *Thin Solid Films*, vol. 89, no. 3, 1982, pp. 287-293.

[116] H. A. Macleod. *Thin-film optical filters*. 3rd ed., Boca Raton, FL: CRC Press, 2001.

[117] M. Born and E. Wolf. *Principles of Optics*. 7th ed., New York, NY: Cambridge University Press, 1999.

[118] https://www.youtube.com/watch?v=nYu1ruSakRg&t=128s.

[119] P. Prod'homme, F. Maroun, R. Cortès, and P. Allongue. "Electrochemical growth of ultraflat Au (111) epitaxial buffer layers on H–Si (111)." *Appl. Phys. Lett.*, vol. 93, no. 17, 2008, p. 171901.

[120] P. Prodhomme, S. Warren, R. Cortès, H. F. Jurca, F. Maroun, and P. Allongue. "Epitaxial Growth of Gold on H–Si (111): The Determining Role of Hydrogen Evolution." *Chemphyschem*, vol. 11, no. 13, 2010, pp. 2992-3001.

[121] J. A. Switzer, J. C. Hill, N. K. Mahenderkar, and Y.-C. Liu. "Nanometer-Thick Gold on Silicon as a Proxy for Single-Crystal Gold for the Electrodeposition of Epitaxial Cuprous Oxide Thin Films." *ACS Appl. Mater. Interfaces*, vol. 8, no. 24, 2016, pp. 15828-15837.

[122] N. K. Mahenderkar, Q. Chen, Y.-C. Liu, A. R. Duchild, S. Hofheins, E. Chason, and J. A. Switzer. "Epitaxial lift-off of electrodeposited single-crystal gold foils for flexible electronics." *Science*, vol. 355, no. 6330, 2017, pp. 1203-1206.

[123] J. Eskhult and L. Nyholm. "Pulsed Galvanostatic and Potentiostatic Electrodeposition of Cu and Cu2O Nanolayers from Alkaline Cu (II)-Citrate Solutions." *J. Electrochem. Soc.*, vol. 155, no. 2, 2008, pp. D115-D122.

[124] J. Eskhult, M. Herranen, and L. Nyholm. "On the origin of the spontaneous potential oscillations observed during galvanostatic deposition of layers of Cu and Cu_2O in alkaline citrate solutions." *J. Electroanal. Chem.*, vol. 594, no. 1, 2006, pp. 35-49.

[125] H. Presting and U. König. "Future nanotechnology developments for automotive applications." *Mater. Sci. Eng. C.*, vol. 23, no. 6, 2003, pp. 737-741.

[126] A. Henemann. "BIPV: Built-in solar energy." *Renewable Energy Focus*, vol. 9, no. 6, Supplement, 2008, pp. 14-19.

[127] C.-M. Lai and Y.-P. Lin. "Energy Saving Evaluation of the Ventilated BIPV Walls." *Energies*, vol. 4, no. 6, 2011, pp. 948-959.

[128] T. Masuda, S. Hirai, M. Inoue, J. Chantana, Y. Kudo, and T. Minemoto. "Colorful, Flexible, and Lightweight $Cu(In,Ga)Se_2$ Solar Cell by Lift-Off Process With Automotive Painting." *IEEE J. Photovolt.*, vol. 8, no. 5, 2018, pp. 1326-1330.

[129] T. Masuda, Y. Kudo, and D. Banerjee. "Visually Attractive and High-Power-Retention Solar Modules by Coloring with Automotive Paints." *Coatings*, vol. 8, no. 8, 2018, p. 282.

[130] T. Masuda, K. Araki, K. Okumura, S. Urabe, Y. Kudo, K. Kimura, T. Nakado, A. Sato, and M. Yamaguchi. "Static concentrator photovoltaics for automotive applications." *Sol. Energy*, vol. 146, no., 2017, pp. 523-531.

[131] K. Araki, L. Ji, G. Kelly, and M. Yamaguchi. "To Do List for Research and Development and International Standardization to Achieve the Goal of Running a Majority of Electric Vehicles on Solar Energy." *Coatings*, vol. 8, no. 7, 2018, p. 251.

[132] A. Hinsch, W. Veurman, H. Brandt, K. Flarup Jensen, and S. Mastroianni. "Status of Dye Solar Cell Technology as a Guideline for Further Research." *Chemphyschem*, vol. 15, no. 6, 2014, pp. 1076-1087.

[133] L. M. Gonçalves, V. de Zea Bermudez, H. A. Ribeiro, and A. M. Mendes. "Dye-sensitized solar cells: A safe bet for the future." *Energy Environ. Sci.*, vol. 1, no. 6, 2008, pp. 655-667.

[134] X. Wang, L. Zhi, and K. Müllen. "Transparent, Conductive Graphene Electrodes for Dye-Sensitized Solar Cells." *Nano. Lett.*, vol. 8, no. 1, 2008, pp. 323-327.

[135] Z. He, C. Zhong, S. Su, M. Xu, H. Wu, and Y. Cao. "Enhanced power-conversion efficiency in polymer solar cells using an inverted device structure." *Nat. Photon.*, vol. 6, no. 9, 2012, pp. 591-595.

[136] G. Xu, L. Shen, C. Cui, S. Wen, R. Xue, W. Chen, H. Chen, J. Zhang, H. Li, Y. Li, and Y. Li. "High-Performance Colorful Semitransparent Polymer Solar Cells with Ultrathin Hybrid-Metal Electrodes and Fine-Tuned Dielectric Mirrors." *Adv. Funct. Mater.*, vol. 27, no. 15, 2017, p. 1605908.

[137] J.-H. Lu, Y.-H. Lin, B.-H. Jiang, C.-H. Yeh, J.-C. Kao, and C.-P. Chen. "Microcavity Structure Provides High-Performance (>8.1%) Semitransparent and Colorful Organic Photovoltaics." *Adv. Funct. Mater.*, vol. 28, no. 7, 2017, p. 1703398.

[138] J. H. Noh, S. H. Im, J. H. Heo, T. N. Mandal, and S. I. Seok. "Chemical Management for Colorful, Efficient, and Stable Inorganic–Organic Hybrid Nanostructured Solar Cells." *Nano. Lett.*, vol. 13, no. 4, 2013, pp. 1764-1769.

[139] Y. Li, J.-D. Lin, X. Che, Y. Qu, F. Liu, L.-S. Liao, and S. R. Forrest. "High Efficiency Near-Infrared and Semitransparent Non-Fullerene Acceptor Organic Photovoltaic Cells." *J. Am. Chem. Soc.*, vol. 139, no. 47, 2017, pp. 17114-17119.

[140] A. Colsmann, A. Puetz, A. Bauer, J. Hanisch, E. Ahlswede, and U. Lemmer. "Efficient Semi-Transparent Organic Solar Cells with Good Transparency Color Perception and Rendering Properties." *Adv. Energy Mater.*, vol. 1, no. 4, 2011, pp. 599-603.

[141] G. E. Eperon, V. M. Burlakov, A. Goriely, and H. J. Snaith. "Neutral Color Semitransparent Microstructured Perovskite Solar Cells." *ACS Nano*, vol. 8, no. 1, 2014, pp. 591-598.

[142] W. Zhang, M. Anaya, G. Lozano, M. E. Calvo, M. B. Johnston, H. Míguez, and H. J. Snaith. "Highly Efficient Perovskite Solar Cells with Tunable Structural Color." *Nano. Lett.*, vol. 15, no. 3, 2015, pp. 1698-1702.

[143] Y.-H. Chen, C.-W. Chen, Z.-Y. Huang, W.-C. Lin, L.-Y. Lin, F. Lin, K.-T. Wong, and H.-W. Lin. "Microcavity-Embedded, Colour-Tuneable, Transparent Organic Solar Cells." *Adv. Mater.*, vol. 26, no. 7, 2013, pp. 1129-1134.

[144] K.-T. Lee, J.-Y. Jang, J. Zhang, S.-M. Yang, S. Park, and H. J. Park. "Highly Efficient Colored Perovskite Solar Cells Integrated with Ultrathin Subwavelength Plasmonic Nanoresonators." *Sci. Rep.*, vol. 7, 2017, p. 10640.

[145] K. Diest, J. A. Dionne, M. Spain, and H. A. Atwater. "Tunable Color Filters Based on Metal−Insulator−Metal Resonators." *Nano. Lett.*, vol. 9, no. 7, 2009, pp. 2579-2583.

[146] J. Y. Lee, K.-T. Lee, S. Seo, and L. J. Guo. "Decorative power generating panels creating angle insensitive transmissive colors." *Sci. Rep.*, vol. 4, 2014, p. 4192.

[147] C. Ji, K.-T. Lee, T. Xu, J. Zhou, H. J. Park, and L. J. Guo. "Engineering Light at the Nanoscale: Structural Color Filters and Broadband Perfect Absorbers." *Adv. Opt. Mater.*, vol. 5, no. 20, 2017, p. 1700368.

[148] M. A. Kats, R. Blanchard, P. Genevet, and F. Capasso. "Nanometre optical coatings based on strong interference effects in highly absorbing media." *Nat. Mater.*, vol. 12, no. 1, 2013, pp. 20-24.

[149] M. A. Kats and F. Capasso. "Optical absorbers based on strong interference in ultra-thin films." *Laser Photon. Rev.*, vol. 10, no. 5, 2016, pp. 735-749.

[150] E.-H. Cho, H.-S. Kim, J.-S. Sohn, C.-Y. Moon, N.-C. Park, and Y.-P. Park. "Nanoimprinted photonic crystal color filters for solar-powered reflective displays." *Opt. Express*, vol. 18, no. 26, 2010, pp. 27712-27722.

[151] M. J. Uddin and R. Magnusson. "Highly efficient color filter array using resonant Si3N4 gratings." *Opt. Express*, vol. 21, no. 10, 2013, pp. 12495-12506.

[152] L. A. A. Petterson, L. S. Roman, and O. Inganäs. "Modeling photocurrent action spectra of photovoltaic devices based on organic thin films." *J. Appl. Phys.*, vol. 86, no. 1, 1999, pp. 487-496.

[153] D. M. Shcherbakova and V. V. Verkhusha. "Near-infrared fluorescent proteins for multicolor in vivo imaging." *Nat. Methods*, vol. 10, no. 8, 2013, pp. 751-754.

[154] S. Kim, Y. T. Lim, E. G. Soltesz, A. M. De Grand, J. Lee, A. Nakayama, J. A. Parker, T. Mihaljevic, R. G. Laurence, D. M. Dor, L. H. Cohn, M. G. Bawendi, and J. V. Frangioni. "Near-infrared fluorescent type II quantum dots for sentinel lymph node mapping." *Nat. Biotechnol.*, vol. 22, no. 1, 2003, pp. 93-97.

[155] J. V. Frangioni. "In vivo near-infrared fluorescence imaging." *Curr. Opin. Chem. Biol.*, vol. 7, no. 5, 2003, pp. 626-634.

[156] H. Park and K. B. Crozier. "Multispectral imaging with vertical silicon nanowires." *Sci. Rep.*, vol. 3, 2013, p. 2460.

[157] S. Koyama, Y. Inaba, M. Kasano, and T. Murata. "A Day and Night Vision MOS Imager With Robust Photonic-Crystal-Based RGB-and-IR." *IEEE Trans. Electron Devices*, vol. 55, no. 3, 2008, pp. 754-759.

[158] P. W. Barone, S. Baik, D. A. Heller, and M. S. Strano. "Near-infrared optical sensors based on single-walled carbon nanotubes." *Nat. Mater.*, vol. 4, no. 1, 2004, pp. 86-92.

[159] L. Yuan, W. Lin, S. Zhao, W. Gao, B. Chen, L. He, and S. Zhu. "A Unique Approach to Development of Near-Infrared Fluorescent Sensors for in Vivo Imaging." *J. Am. Chem. Soc.*, vol. 134, no. 32, 2012, pp. 13510-13523.

[160] P. Werle, F. Slemr, K. Maurer, R. Kormann, R. Mücke, and B. Jänker. "Near- and mid-infrared laser-optical sensors for gas analysis." *Opt. Lasers Eng.*, vol. 37, no. 2, 2002, pp. 101-114.

[161] S. Ghosh, S. Cherumukkil, C. H. Suresh, and A. Ajayaghosh. "A Supramolecular Nanocomposite as a Near-Infrared-Transmitting Optical Filter for Security and Forensic Applications." *Adv. Mater.*, vol. 29, no. 46, 2017, p. 1703783.

[162] R. J. Tucker. "Visibly opaque infrared transmitting optical filter containing a combination of copper and vanadyl phthalocyanine sulfonamides." U.S. Patent 4,039,467A. Aug. 2, 1977.

[163] M. Momose and A. Todokoro. "Infrared transmissive thermoplastic composition, and articles formed therefrom." U.S. Patent 7,727,418B2. June 1, 2010.

[164] M. D. Morgan, W. E. Horne, V. Sundaram, J. C. Wolfe, S. V. Pendharkar, and R. Tiberio. "Application of optical filters fabricated by masked ion beam lithography." *J. Vac. Sci. Technol. B*, vol. 14, no. 6, 1996, pp. 3903-3906.

[165] A. Heinzel, V. Boerner, A. Gombert, B. Bläsi, V. Wittwer, and J. Luther. "Radiation filters and emitters for the NIR based on periodically structured metal surfaces." *J. Mod. Opt.*, vol. 47, no. 13, 2000, pp. 2399-2419.

[166] J. Zhang, S. Xiao, C. Jeppesen, A. Kristensen, and N. A. Mortensen. "Electromagnetically induced transparency in metamaterials at near-infrared frequency." *Opt. Express*, vol. 18, no. 16, 2010, pp. 17187-17192.

[167] S. Zhang, W. Fan, K. J. Malloy, S. R. J. Brueck, N. C. Panoiu, and R. M. Osgood. "Near-infrared double negative metamaterials." *Opt. Express*, vol. 13, no. 13, 2005, pp. 4922-4930.

[168] A. A. Z. Sokar, F. X. Hutter, and J. N. Burghartz. "Generation of red color and near infrared bandpass filters using nano-scale plasmonic structures." *Proceedings of SPIE Optics + Optoelectronics*, *Prague, Czech Republic*, *13-16 April 2015*. Edited by V. Kuzmiak et al., SPIE, 2015, p. 95020U.

[169] Z. Yang, Y. Zhou, Y. Chen, Y. Wang, P. Dai, Z. Zhang, and H. Duan. "Reflective Color Filters and Monolithic Color Printing Based on Asymmetric Fabry–Perot Cavities Using Nickel as a Broadband Absorber." *Adv. Opt. Mater.*, vol. 4, no. 8, 2016, pp. 1196-1202.

[170] Z. Yang, Y. Chen, Y. Zhou, Y. Wang, P. Dai, X. Zhu, and H. Duan. "Microscopic Interference Full-Color Printing Using Grayscale-Patterned Fabry–Perot Resonance Cavities." *Adv. Opt. Mater.*, vol. 5, no. 10, 2017, p. 1700029.

[171] G. J. Hawkins, R. E. Sherwood, B. M. Barrett, M. Wallace, H. J. B. Orr, K. Matthews, and S. Bisht. "High-performance infrared narrow-bandpass filters for the Indian National Satellite System meteorological instrument (INSAT-3D)." *Appl. Opt.*, vol. 47, no. 13, 2008, pp. 2346-2356.

[172] H. J. B. Orr, M. Wallace, and G. B. Dalton. "Near-infrared bandpass filters with improved transparency for 1000nm spectral region using sputtered silicon compound films." *Proceedings of SPIE Astronomical Telescopes + Instrumentation*, *Marseille, France*, *23-28 June 2008*. Edited by E. Atad-Ettedgui et al., SPIE, 2008, p. 701830.

[173] A. Piegari, A. K. Sytchkova, I. Di Sarcina, and J. Bulir. "Visible and near-infrared filters for miniaturized spectrometers." *Proceedings of SPIE Astronomical Telescopes + Instrumentation*, *Marseille, France*, *23-28 June 2008*. Edited by E. Atad-Ettedgui et al., SPIE, 2008, p. 701855.

[174] S. A. Kumar, C. L. Nagendra, H. G. Shanbhogue, and G. K. M. Thutupalli. "Near-infrared bandpass filters from Si/SiO2 multilayer coatings." *Opt. Eng.*, vol. 38, no. 2, 1999, pp. 368-381.

[175] Y. Ohtera, T. Onuki, Y. Inoue, and S. Kawakami. "Multichannel Photonic Crystal Wavelength Filter Array for Near-Infrared Wavelengths." *J. Lightwave Technol.*, vol. 25, no. 2, 2007, pp. 499-503.

[176] C. Ufford and P. Baumeister. "Graphical aids in the use of equivalent index in multilayer-filter design." *J. Opt. Soc. Am.*, vol. 64, no. 3, 1974, pp. 329-334.

[177] S. K. Awasthi and S. P. Ojha. "Design of a tunable optical filter by using a one-dimensional ternary photonic band gap material." *Prog. Electromagn. Res. M*, vol. 4, 2008, pp. 117-132.

[178] J. N. Winn, Y. Fink, S. Fan, and J. D. Joannopoulos. "Omnidirectional reflection from a one-dimensional photonic crystal." *Opt. Lett.*, vol. 23, no. 20, 1998, pp. 1573-1575.

[179] Y. Fink, J. N. Winn, S. Fan, C. Chen, J. Michel, J. D. Joannopoulos, and E. L. Thomas. "A dielectric omnidirectional reflector." *Science*, vol. 282, no. 5394, 1998, pp. 1679-1682.

[180] H. Song, L. Guo, Z. Liu, K. Liu, X. Zeng, D. Ji, N. Zhang, H. Hu, S. Jiang, and Q. Gan. "Nanocavity Enhancement for Ultra-Thin Film Optical Absorber." *Adv. Mater.*, vol. 26, no. 17, 2014, pp. 2737-2743.

[181] D. Liu and Q. Li. "Sub-nanometer planar solar absorber." *Nano Energy*, vol. 34, 2017, pp. 172-180.

[182] K. L. Tsakmakidis, A. D. Boardman, and O. Hess. "'Trapped rainbow' storage of light in metamaterials." *Nature*, vol. 450, no. 7168, 2007, pp. 397-401.

[183] N. I. Landy, S. Sajuyigbe, J. J. Mock, D. R. Smith, and W. J. Padilla. "Perfect Metamaterial Absorber." *Phys. Rev. Lett.*, vol. 100, no. 20, 2008, p. 207402.

[184] Z.-P. Yang, L. Ci, J. A. Bur, S.-Y. Lin, and P. M. Ajayan. "Experimental Observation of an Extremely Dark Material Made By a Low-Density Nanotube Array." *Nano. Lett.*, vol. 8, no. 2, 2008, pp. 446-451.

[185] J. Hao, J. Wang, X. Liu, W. J. Padilla, L. Zhou, and M. Qiu. "High performance optical absorber based on a plasmonic metamaterial." *Appl. Phys. Lett.*, vol. 96, no. 25, 2010, p. 251104.

[186] J. Le Perchec, P. Quémerais, A. Barbara, and T. López-Ríos. "Why Metallic Surfaces with Grooves a Few Nanometers Deep and Wide May Strongly Absorb Visible Light." *Phys. Rev. Lett.*, vol. 100, no. 6, 2008, p. 066408.

[187] J. Wang, C. Fan, P. Ding, J. He, Y. Cheng, W. Hu, G. Cai, E. Liang, and Q. Xue. "Tunable broad-band perfect absorber by exciting of multiple plasmon resonances at optical frequency." *Opt. Express*, vol. 20, no. 14, 2012, pp. 14871-14878.

[188] A. Biswas, H. Eilers, F. Hidden, O. C. Aktas, and C. V. S. Kiran. "Large broadband visible to infrared plasmonic absorption from Ag nanoparticles with a fractal structure embedded in a Teflon AF® matrix." *Appl. Phys. Lett.*, vol. 88, no. 1, 2006, p. 013103.

[189] B. Zhang, Y. Zhao, Q. Hao, B. Kiraly, I.-C. Khoo, S. Chen, and T. J. Huang. "Polarization-independent dual-band infrared perfect absorber based on a metal-dielectric-metal elliptical nanodisk array." *Opt. Express*, vol. 19, no. 16, 2011, pp. 15221-15228.

[190] K. Aydin, V. E. Ferry, R. M. Briggs, and H. A. Atwater. "Broadband polarization-independent resonant light absorption using ultrathin plasmonic super absorbers." *Nat. Commun.*, vol. 2, 2011, p. 517.

[191] T. V. Teperik, F. J. García de Abajo, A. G. Borisov, M. Abdelsalam, P. N. Bartlett, Y. Sugawara, and J. J. Baumberg. "Omnidirectional absorption in nanostructured metal surfaces." *Nat. Photon.*, vol. 2, no. 5, 2008, pp. 299-301.

[192] Q. Gan, F. J. Bartoli, and Z. H. Kafafi. "Plasmonic-Enhanced Organic Photovoltaics: Breaking the 10% Efficiency Barrier." *Adv. Mater.*, vol. 25, no. 17, 2013, pp. 2385-2396.

[193] P. Zhu and L. J. Guo. "High performance broadband absorber in the visible band by engineered dispersion and geometry of a metal-dielectric-metal stack." *Appl. Phys. Lett.*, vol. 101, no. 24, 2012, p. 241116.

[194] C.-W. Cheng, M. N. Abbas, C.-W. Chiu, K.-T. Lai, M.-H. Shih, and Y.-C. Chang. "Wide-angle polarization independent infrared broadband absorbers based on metallic multi-sized disk arrays." *Opt. Express*, vol. 20, no. 9, 2012, pp. 10376-10381.

[195] Y. Cui, J. Xu, K. H. Fung, Y. Jin, A. Kumar, S. He, and N. X. Fang. "A thin film broadband absorber based on multi-sized nanoantennas." *Appl. Phys. Lett.*, vol. 99, no. 25, 2011, p. 253101.

[196] J. Hendrickson, J. Guo, B. Zhang, W. Buchwald, and R. Soref. "Wideband perfect light absorber at midwave infrared using multiplexed metal structures." *Opt. Lett.*, vol. 37, no. 3, 2012, pp. 371-373.

[197] D. Ji, H. Song, X. Zeng, H. Hu, K. Liu, N. Zhang, and Q. Gan. "Broadband absorption engineering of hyperbolic metafilm patterns." *Sci. Rep.*, vol. 4, 2014, p. 4498.

[198] J. Zhou, A. F. Kaplan, L. Chen, and L. J. Guo. "Experiment and Theory of the Broadband Absorption by a Tapered Hyperbolic Metamaterial Array." *ACS Photonics*, vol. 1, no. 7, 2014, pp. 618-624.

[199] Q. Liang, T. Wang, Z. Lu, Q. Sun, Y. Fu, and W. Yu. "Metamaterial-Based Two Dimensional Plasmonic Subwavelength Structures Offer the Broadest Waveband Light Harvesting." *Adv. Opt. Mater.*, vol. 1, no. 1, 2013, pp. 43-49.

[200] H. Deng, Z. Li, L. Stan, D. Rosenmann, D. Czaplewski, J. Gao, and X. Yang. "Broadband perfect absorber based on one ultrathin layer of refractory metal." *Opt. Lett.*, vol. 40, no. 11, 2015, pp. 2592-2595.

[201] P. Li, B. Liu, Y. Ni, K. K. Liew, J. Sze, S. Chen, and S. Shen. "Large-Scale Nanophotonic Solar Selective Absorbers for High-Efficiency Solar Thermal Energy Conversion." *Adv. Mater.*, vol. 27, no. 31, 2015, pp. 4585-4591.

[202] X. Chen, H. Gong, S. Dai, D. Zhao, Y. Yang, Q. Li, and M. Qiu. "Near-infrared broadband absorber with film-coupled multilayer nanorods." *Opt. Lett.*, vol. 38, no. 13, 2013, pp. 2247-2249.

[203] P. Bouchon, C. Koechlin, F. Pardo, R. Haïdar, and J.-L. Pelouard. "Wideband omnidirectional infrared absorber with a patchwork of plasmonic nanoantennas." *Opt. Lett.*, vol. 37, no. 6, 2012, pp. 1038-1040.

[204] G.-q. Du, L.-w. Zhang, and H.-t. Jiang. "Broadband and omnidirectional absorption in heterostructures with a highly absorptive metallic film and a dielectric Bragg reflector." *J. Appl. Phys.*, vol. 109, no. 6, 2011, p. 063525.

[205] X.-F. Li, Y.-R. Chen, J. Miao, P. Zhou, Y.-X. Zheng, L.-Y. Chen, and Y.-P. Lee. "High solar absorption of a multilayered thin film structure." *Opt. Express*, vol. 15, no. 4, 2007, pp. 1907-1912.

[206] J. Zhu, Z. Yu, G. F. Burkhard, C.-M. Hsu, S. T. Connor, Y. Xu, Q. Wang, M. McGehee, S. Fan, and Y. Cui. "Optical Absorption Enhancement in Amorphous Silicon Nanowire and Nanocone Arrays." *Nano. Lett.*, vol. 9, no. 1, 2009, pp. 279-282.

[207] J. Park, J.-H. Kang, A. P. Vasudev, D. T. Schoen, H. Kim, E. Hasman, and M. L. Brongersma. "Omnidirectional Near-Unity Absorption in an Ultrathin Planar Semiconductor Layer on a Metal Substrate." *ACS Photonics*, vol. 1, no. 9, 2014, pp. 812-821.

[208] J. Park, S. J. Kim, and M. L. Brongersma. "Condition for unity absorption in an ultrathin and highly lossy film in a Gires-Tournois interferometer configuration." *Opt. Lett.*, vol. 40, no. 9, 2015, pp. 1960-1963.

[209] S. S. Mirshafieyan and J. Guo. "Silicon colors: spectral selective perfect light absorption in single layer silicon films on aluminum surface and its thermal tunability." *Opt. Express*, vol. 22, no. 25, 2014, pp. 31545-31554.

[210] E. D. Palik. *Handbook of Optical Constants of Solids*. 1st ed., Orlando, FL: Academic Press, 1998.

[211] C. Yang, W. Shen, Y. Zhang, K. Li, X. Fang, X. Zhang, and X. Liu. "Compact Multilayer Film Structure for Angle Insensitive Color Filtering." *Sci. Rep.*, vol. 5, 2015, p. 9285.

[212] H. You, T. Ryu, K. Oh, M.-H. Yun, and K.-J. Kim. "Development of customer satisfaction models for automotive interior materials." *Int. J. Ind. Ergon.*, vol. 36, no. 4, 2006, pp. 323-330.

[213] T. Jindo and K. Hirasago. "Application studies to car interior of Kansei engineering." *Int. J. Ind. Ergon.*, vol. 19, no. 2, 1997, pp. 105-114.

[214] E. Bertilsson and E. Svensson. *Veiling glare in car windshields*. MA thesis, Luleå University of Technology, 2009.

[215] M. L. Mefford, J. F. Michael, and G. Adachi. *Daytime veiling luminance from windshields: Effects of scattering and reflection*. Ann Arbor, MI: The University of Michigan, 2003. UMTRI-2003-36.

[216] A. Dunsäter and M. Andersson. *Daytime veiling glare in automobiles caused by dashboard reflectance*. MA thesis, Linköping University, 2008.

[217] J. Schumann, M. J. Flannagan, M. Sivak, and E. C. Traube. "Daytime veiling glare and driver visual performance: Influence of windshield rake angle and dashboard reflectance." *J. Saf. Res.*, vol. 28, no. 3, 1997, pp. 133-146.

[218] J. L. Sauter, N. Bow, M. L. LaDriere, and S. C. Parman. *The Effects of Instrument Panel Top Color and Windshield Angle on Veiling Glare*. Detroit, MI: SAE International, 1992. No. 920105.

[219] C. D. Storms. *Instrument Panel Coatings to Reduce Veiling Glare and for Decorative Effects*. Detroit, MI: SAE International, 1994. No. 940646.

[220] C. H. Munro. "Veiling glare reduction system and method of controlling reflection from a vehicle windshield." U.S. Patent 8,467,129. June 18, 2013.

[221] K. M. Reitz. "Veiling glare reduction system." U.S. Patent 6,299,231. Oct. 9, 2001.

[222] D. Banerjee, L. J. Guo, and K.-T. Lee. "Panel with reduced glare." U.S. Patent 10,088,616B2. Oct. 2, 2018.

[223] S. Ahn, J. Cha, H. Myung, S.-m. Kim, and S. Kang. "Continuous ultraviolet roll nanoimprinting process for replicating large-scale nano- and micropatterns." *Appl. Phys. Lett.*, vol. 89, no. 21, 2006, p. 213101.

[224] L. J. Guo. "Nanoimprint Lithography: Methods and Material Requirements." *Adv. Mater.*, vol. 19, no. 4, 2007, pp. 495-513.

[225] C. Zhang, H. Subbaraman, Q. Li, Z. Pan, J. G. Ok, T. Ling, C.-J. Chung, X. Zhang, X. Lin, R. T. Chen, and L. J. Guo. "Printed photonic elements: nanoimprinting and beyond." *J. Mater. Chem. C*, vol. 4, no. 23, 2016, pp. 5133-5153.

[226] R. B. Johnson and G. A. Jacobsen. "Advances in lenticular lens arrays for visual display." *Proceedings of Optics and Photonics 2005*, *San Diego, CA, United States*, *31 July - 4 Aug. 2005*. Edited by P. Z. Mouroulis et al., SPIE, 2005, p. 587406.

[227] R. B. Johnson. "Improvements in lenticular lens arrays design and fabrication." *Proceedings of International Optical Design Conference 2006*, *Vancouver, BC, Canada*, *4-8 June 2006*. Edited by G. G. Gregory et al., SPIE, 2006, p. 634227.

[228] H. Kim, J. Kim, J. Kim, B. Lee, and S.-D. Lee. "Liquid crystal-based lenticular lens array with laterally shifting capability of the focusing effect for autostereoscopic displays." *Opt. Commun.*, vol. 357, 2015, pp. 52-57.

[229] Y. Takaki and N. Nago. "Multi-projection of lenticular displays to construct a 256-view super multi-view display." *Opt. Express*, vol. 18, no. 9, 2010, pp. 8824-8835.

[230] S. Pastoor and M. Wöpking. "3-D displays: A review of current technologies." *Displays*, vol. 17, no. 2, 1997, pp. 100-110.

[231] C. v. Berkel, D. W. Parker, and A. R. Franklin. "Multiview 3D LCD." *Proceedings of Electronic Imaging: Science and Technology*, *San Jose, CA, United States*, *28 Jan. - 2 Feb. 1996*. Edited by M. T. Bolas et al., SPIE, 1996, pp. 32-39.

[232] M. Beck, M. Graczyk, I. Maximov, E. L. Sarwe, T. G. I. Ling, M. Keil, and L. Montelius. "Improving stamps for 10 nm level wafer scale nanoimprint lithography." *Microelectron. Eng.*, vol. 61-62, 2002, pp. 441-448.

[233] S. H. Ahn and L. J. Guo. "High-Speed Roll-to-Roll Nanoimprint Lithography on Flexible Plastic Substrates." *Adv. Mater.*, vol. 20, no. 11, 2008, pp. 2044-2049.

[234] S. H. Ahn and L. J. Guo. "Large-Area Roll-to-Roll and Roll-to-Plate Nanoimprint Lithography: A Step toward High-Throughput Application of Continuous Nanoimprinting." *ACS Nano*, vol. 3, no. 8, 2009, pp. 2304-2310.

[235] C. Stuart and Y. Chen. "Roll in and Roll out: A Path to High-Throughput Nanoimprint Lithography." *ACS Nano*, vol. 3, no. 8, 2009, pp. 2062-2064.

[236] J. B. Pendry, D. Schurig, and D. R. Smith. "Controlling Electromagnetic Fields." *Science*, vol. 312, no. 5781, 2006, pp. 1780-1782.

[237] A. Alù and N. Engheta. "Achieving transparency with plasmonic and metamaterial coatings." *Phys. Rev. E*, vol. 72, no. 1, 2005, p. 016623.

[238] U. Leonhardt. "Optical Conformal Mapping." *Science*, vol. 312, no. 5781, 2006, pp. 1777-1780.

[239] L. Xu and H. Chen. "Conformal transformation optics." *Nat. Photon.*, vol. 9, no. 1, 2015, pp. 15-23.

[240] B. Zhang. "Electrodynamics of transformation-based invisibility cloaking." *Light: Sci. Appl.*, vol. 1, 2012, p. e32.

[241] R. Fleury and A. Alù. "Cloaking and invisibility: A review." *Prog. Electromagn. Res.*, vol. 147, pp. 171–202.

[242] D. Schurig, J. J. Mock, B. J. Justice, S. A. Cummer, J. B. Pendry, A. F. Starr, and D. R. Smith. "Metamaterial Electromagnetic Cloak at Microwave Frequencies." *Science*, vol. 314, no. 5801, 2006, pp. 977-980.

[243] J. Li and J. B. Pendry. "Hiding under the Carpet: A New Strategy for Cloaking." *Phys. Rev. Lett.*, vol. 101, no. 20, 2008, p. 203901.

[244] R. Liu, C. Ji, J. J. Mock, J. Y. Chin, T. J. Cui, and D. R. Smith. "Broadband Ground-Plane Cloak." *Science*, vol. 323, no. 5912, 2009, pp. 366-369.

[245] L. H. Gabrielli, J. Cardenas, C. B. Poitras, and M. Lipson. "Silicon nanostructure cloak operating at optical frequencies." *Nat. Photon.*, vol. 3, no. 8, 2009, pp. 461-463.

[246] J. Valentine, J. Li, T. Zentgraf, G. Bartal, and X. Zhang. "An optical cloak made of dielectrics." *Nat. Mater.*, vol. 8, no. 7, 2009, pp. 568-571.

[247] T. Ergin, N. Stenger, P. Brenner, J. B. Pendry, and M. Wegener. "Three-Dimensional Invisibility Cloak at Optical Wavelengths." *Science*, vol. 328, no. 5976, 2010, pp. 337-339.

[248] M. Gharghi, C. Gladden, T. Zentgraf, Y. Liu, X. Yin, J. Valentine, and X. Zhang. "A Carpet Cloak for Visible Light." *Nano. Lett.*, vol. 11, no. 7, 2011, pp. 2825-2828.

[249] X. Ni, Z. J. Wong, M. Mrejen, Y. Wang, and X. Zhang. "An ultrathin invisibility skin cloak for visible light." *Science*, vol. 349, no. 6254, 2015, pp. 1310-1314.

[250] H. Chen and B. Zheng. "Broadband polygonal invisibility cloak for visible light." *Sci. Rep.*, vol. 2, 2012, p. 255.

[251] B. Zhang, Y. Luo, X. Liu, and G. Barbastathis. "Macroscopic Invisibility Cloak for Visible Light." *Phys. Rev. Lett.*, vol. 106, no. 3, 2011, p. 033901.

[252] X. Chen, Y. Luo, J. Zhang, K. Jiang, J. B. Pendry, and S. Zhang. "Macroscopic invisibility cloaking of visible light." *Nat. Commun.*, vol. 2, 2011, p. 176.

[253] H. Chen, B. Zheng, L. Shen, H. Wang, X. Zhang, N. I. Zheludev, and B. Zhang. "Ray-optics cloaking devices for large objects in incoherent natural light." *Nat. Commun.*, vol. 4, 2013, p. 2652.

[254] Y. Yang, B. Zhang, E. Li, and H. Chen. "Towards omnidirectional, large scale, full polarization, and broadband practical invisibility cloaks: challenges and progress." *EPJ Appl. Metamat.*, vol. 1, 2014, p. 7.

[255] J. C. Howell, J. B. Howell, and J. S. Choi. "Amplitude-only, passive, broadband, optical spatial cloaking of very large objects." *Appl. Opt.*, vol. 53, no. 9, 2014, pp. 1958-1963.

[256] J. S. Choi and J. C. Howell. "Paraxial ray optics cloaking." *Opt. Express*, vol. 22, no. 24, 2014, pp. 29465-29478.

[257] J. Sun, J. Zeng, X. Wang, A. N. Cartwright, and N. M. Litchinitser. "Concealing with Structured Light." *Sci. Rep.*, vol. 4, 2014, p. 4093.

[258] Q. Cheng, K. Wu, Y. Shi, H. Wang, and G. P. Wang. "Directionally hiding objects and creating illusions above a carpet-like device by reflection holography." *Sci. Rep.*, vol. 5, 2015, p. 8581.

[259] J. Hong, Y. Kim, H.-J. Choi, J. Hahn, J.-H. Park, H. Kim, S.-W. Min, N. Chen, and B. Lee. "Three-dimensional display technologies of recent interest: principles, status, and issues [Invited]." *Appl. Opt.*, vol. 50, no. 34, 2011, pp. H87-H115.

[260] J. Geng. "Three-dimensional display technologies." *Adv. Opt. Photon.*, vol. 5, no. 4, 2013, pp. 456-535.

[261] E. Cuche, F. Bevilacqua, and C. Depeursinge. "Digital holography for quantitative phase-contrast imaging." *Opt. Lett.*, vol. 24, no. 5, 1999, pp. 291-293.

[262] F. Zhou, H. B.-L. Duh, and M. Billinghurst. "Trends in augmented reality tracking, interaction and display: A review of ten years of ISMAR." *Proceedings of the 7th IEEE/ACM International Symposium on Mixed and Augmented Reality*, *Cambridge, UK*, *15-18 Sept. 2008*. Edited by M. A. Livingston et al., IEEE, 2008, pp. 193-202.

[263] D. W. F. Van Krevelen, and R. Poelman. "A survey of augmented reality technologies, applications and limitations." *Int. J. Virtual Reality*, vol. 9, no. 2, 2010, pp. 1-20.

[264] D. McCoul, W. Hu, M. Gao, V. Mehta, and Q. Pei. "Recent Advances in Stretchable and Transparent Electronic Materials." *Adv. Electron. Mater.*, vol. 2, no. 5, 2016, p. 1500407.

[265] L. Daniel, G. Gaël, M. Céline, C. Caroline, B. Daniel, and S. Jean-Pierre. "Flexible transparent conductive materials based on silver nanowire networks: a review." *Nanotechnology*, vol. 24, no. 45, 2013, p. 452001.

[266] O. Cakmakci and J. Rolland. "Head-worn displays: a review." *J. Disp. Technol.*, vol. 2, no. 3, 2006, pp. 199-216.

[267] I. Kasai, Y. Tanijiri, T. Endo, and H. Ueda. "A Practical See-Through Head Mounted Display Using a Holographic Optical Element." *Opt. Rev.*, vol. 8, no. 4, 2001, pp. 241-244.

[268] D. Zhao, C. Zhang, H. Kim, and L. J. Guo. "High-Performance Ta_2O_5/Al-Doped Ag Electrode for Resonant Light Harvesting in Efficient Organic Solar Cells." *Adv. Energy Mater.*, vol. 5, no. 17, 2015, p. 1500768.

[269] R. A. Maniyara, V. K. Mkhitaryan, T. L. Chen, D. S. Ghosh, and V. Pruneri. "An antireflection transparent conductor with ultralow optical loss (<2 %) and electrical resistance (<6 $\Omega\,sq^{-1}$)." *Nat. Commun.*, vol. 7, 2016, p. 13771.

[270] X. Guo, X. Liu, F. Lin, H. Li, Y. Fan, and N. Zhang. "Highly Conductive Transparent Organic Electrodes with Multilayer Structures for Rigid and Flexible Optoelectronics." *Sci. Rep.*, vol. 5, 2015, p. 10569.

[271] X. Yang, P. Gao, Z. Yang, J. Zhu, F. Huang, and J. Ye. "Optimizing ultrathin Ag films for high performance oxide-metal-oxide flexible transparent electrodes through surface energy modulation and template-stripping procedures." *Sci. Rep.*, vol. 7, 2017, p. 44576.

[272] T.-H. Kim, S.-H. Park, D.-H. Kim, Y.-C. Nah, and H.-K. Kim. "Roll-to-roll sputtered ITO/Ag/ITO multilayers for highly transparent and flexible electrochromic applications." *Sol. Energy Mater. Sol. Cells*, vol. 160, 2017, pp. 203-210.

[273] F. Shahzad, M. Alhabeb, C. B. Hatter, B. Anasori, S. Man Hong, C. M. Koo, and Y. Gogotsi. "Electromagnetic interference shielding with 2D transition metal carbides (MXenes)." *Science*, vol. 353, no. 6304, 2016, pp. 1137-1140.

[274] J. Liu, H.-B. Zhang, R. Sun, Y. Liu, Z. Liu, A. Zhou, and Z.-Z. Yu. "Hydrophobic, Flexible, and Lightweight MXene Foams for High-Performance Electromagnetic-Interference Shielding." *Adv. Mater.*, vol. 29, no. 38, 2017, p. 1702367.

[275] K. R. Vinod, P. Saravanan, T. R. Suresh Kumar, R. Radha, M. Balasubramaniam, and S. Balakumar. "Enhanced shielding effectiveness in nanohybrids of graphene derivatives with Fe_3O_4 and ε-Fe_3N in the X-band microwave region." *Nanoscale*, vol. 10, no. 25, 2018, pp. 12018-12034.

[276] B. Shen, W. Zhai, and W. Zheng. "Ultrathin Flexible Graphene Film: An Excellent Thermal Conducting Material with Efficient EMI Shielding." *Adv. Funct. Mater.*, vol. 24, no. 28, 2014, pp. 4542-4548.

[277] B. Wen, M. Cao, M. Lu, W. Cao, H. Shi, J. Liu, X. Wang, H. Jin, X. Fang, W. Wang, and J. Yuan. "Reduced Graphene Oxides: Light-Weight and High-Efficiency Electromagnetic Interference Shielding at Elevated Temperatures." *Adv. Mater.*, vol. 26, no. 21, 2014, pp. 3484-3489.

[278] Z. Zeng, H. Jin, M. Chen, W. Li, L. Zhou, and Z. Zhang. "Lightweight and Anisotropic Porous MWCNT/WPU Composites for Ultrahigh Performance Electromagnetic Interference Shielding." *Adv. Funct. Mater.*, vol. 26, no. 2, 2015, pp. 303-310.

[279] D. D. L. Chung. "Electromagnetic interference shielding effectiveness of carbon materials." *Carbon*, vol. 39, no. 2, 2001, pp. 279-285.

[280] S. Geetha, K. K. Satheesh Kumar, C. R. K. Rao, M. Vijayan, and D. C. Trivedi. "EMI shielding: Methods and materials—A review." *J. Appl. Polym. Sci.*, vol. 112, no. 4, 2009, pp. 2073-2086.

[281] L. Kheifets, A. A. Afifi, and R. Shimkhada. "Public Health Impact of Extremely Low-Frequency Electromagnetic Fields." *Environ. Health Perspect.*, vol. 114, no. 10, 2006, pp. 1532-1537.

[282] S. Szmigielski. "Cancer morbidity in subjects occupationally exposed to high frequency (radiofrequency and microwave) electromagnetic radiation." *Sci. Total Environ.*, vol. 180, no. 1, 1996, pp. 9-17.

[283] Z. Chen, C. Xu, C. Ma, W. Ren, and H.-M. Cheng. "Lightweight and Flexible Graphene Foam Composites for High-Performance Electromagnetic Interference Shielding." *Adv. Mater.*, vol. 25, no. 9, 2013, pp. 1296-1300.

[284] H. Xu, S. M. Anlage, L. Hu, and G. Gruner. "Microwave shielding of transparent and conducting single-walled carbon nanotube films." *Appl. Phys. Lett.*, vol. 90, no. 18, 2007, p. 183119.

[285] Y. Chen, H.-B. Zhang, Y. Yang, M. Wang, A. Cao, and Z.-Z. Yu. "High-Performance Epoxy Nanocomposites Reinforced with Three-Dimensional Carbon Nanotube Sponge for Electromagnetic Interference Shielding." *Adv. Funct. Mater.*, vol. 26, no. 3, 2015, pp. 447-455.

[286] N. Li, Y. Huang, F. Du, X. He, X. Lin, H. Gao, Y. Ma, F. Li, Y. Chen, and P. C. Eklund. "Electromagnetic Interference (EMI) Shielding of Single-Walled Carbon Nanotube Epoxy Composites." *Nano. Lett.*, vol. 6, no. 6, 2006, pp. 1141-1145.

[287] M.-S. Cao, W.-L. Song, Z.-L. Hou, B. Wen, and J. Yuan. "The effects of temperature and frequency on the dielectric properties, electromagnetic interference shielding and microwave-absorption of short carbon fiber/silica composites." *Carbon*, vol. 48, no. 3, 2010, pp. 788-796.

[288] G. Wang, Z. Gao, S. Tang, C. Chen, F. Duan, S. Zhao, S. Lin, Y. Feng, L. Zhou, and Y. Qin. "Microwave Absorption Properties of Carbon Nanocoils Coated with Highly Controlled Magnetic Materials by Atomic Layer Deposition." *ACS Nano*, vol. 6, no. 12, 2012, pp. 11009-11017.

[289] M. H. Al-Saleh, W. H. Saadeh, and U. Sundararaj. "EMI shielding effectiveness of carbon based nanostructured polymeric materials: A comparative study." *Carbon*, vol. 60, 2013, pp. 146-156.

[290] M.-S. Cao, X.-X. Wang, W.-Q. Cao, and J. Yuan. "Ultrathin graphene: electrical properties and highly efficient electromagnetic interference shielding." *J. Mater. Chem. C*, vol. 3, no. 26, 2015, pp. 6589-6599.

[291] H.-B. Zhang, Q. Yan, W.-G. Zheng, Z. He, and Z.-Z. Yu. "Tough Graphene−Polymer Microcellular Foams for Electromagnetic Interference Shielding." *ACS Appl. Mater. Interfaces*, vol. 3, no. 3, 2011, pp. 918-924.

[292] R. R. Nair, P. Blake, A. N. Grigorenko, K. S. Novoselov, T. J. Booth, T. Stauber, N. M. R. Peres, and A. K. Geim. "Fine Structure Constant Defines Visual Transparency of Graphene." *Science*, vol. 320, no. 5881, 2008, p. 1308.

[293] S. K. Hong, K. Y. Kim, T. Y. Kim, J. H. Kim, S. W. Park, J. H. Kim, and B. J. Cho. "Electromagnetic interference shielding effectiveness of monolayer graphene." *Nanotechnology*, vol. 23, no. 45, 2012, p. 455704.

[294] S. Kim, J.-S. Oh, M.-G. Kim, W. Jang, M. Wang, Y. Kim, H. W. Seo, Y. C. Kim, J.-H. Lee, Y. Lee, and J.-D. Nam. "Electromagnetic Interference (EMI) Transparent Shielding of Reduced Graphene Oxide (RGO) Interleaved Structure Fabricated by Electrophoretic Deposition." *ACS Appl. Mater. Interfaces*, vol. 6, no. 20, 2014, pp. 17647-17653.

[295] W. Wang, B. Bai, Q. Zhou, K. Ni, and H. Lin. "Petal-shaped metallic mesh with high electromagnetic shielding efficiency and smoothed uniform diffraction." *Opt Mater Express*, vol. 8, no. 11, 2018, pp. 3485-3493.

[296] J. van de Groep, P. Spinelli, and A. Polman. "Transparent Conducting Silver Nanowire Networks." *Nano. Lett.*, vol. 12, no. 6, 2012, pp. 3138-3144.

[297] H. Wang, Z. Lu, and J. Tan. "Generation of uniform diffraction pattern and high EMI shielding performance by metallic mesh composed of ring and rotated sub-ring arrays." *Opt. Express*, vol. 24, no. 20, 2016, pp. 22989-23000.

[298] Y. Han, J. Lin, Y. Liu, H. Fu, Y. Ma, P. Jin, and J. Tan. "Crackle template based metallic mesh with highly homogeneous light transmission for high-performance transparent EMI shielding." *Sci. Rep.*, vol. 6, 2016, p. 25601.

[299] M. Hu, J. Gao, Y. Dong, K. Li, G. Shan, S. Yang, and R. K.-Y. Li. "Flexible Transparent PES/Silver Nanowires/PET Sandwich-Structured Film for High-Efficiency Electromagnetic Interference Shielding." *Langmuir*, vol. 28, no. 18, 2012, pp. 7101-7106.

[300] J. Jung, H. Lee, I. Ha, H. Cho, K. K. Kim, J. Kwon, P. Won, S. Hong, and S. H. Ko. "Highly Stretchable and Transparent Electromagnetic Interference Shielding Film Based on Silver

Nanowire Percolation Network for Wearable Electronics Applications." *ACS Appl. Mater. Interfaces*, vol. 9, no. 51, 2017, pp. 44609-44616.

[301] D. S. Ghosh, L. Martinez, S. Giurgola, P. Vergani, and V. Pruneri. "Widely transparent electrodes based on ultrathin metals." *Opt. Lett.*, vol. 34, no. 3, 2009, pp. 325-327.

[302] D. S. Ghosh, Q. Liu, P. Mantilla-Perez, T. L. Chen, V. Mkhitaryan, M. Huang, S. Garner, J. Martorell, and V. Pruneri. "Highly Flexible Transparent Electrodes Containing Ultrathin Silver for Efficient Polymer Solar Cells." *Adv. Funct. Mater.*, vol. 25, no. 47, 2015, pp. 7309-7316.

[303] W. Wang, M. Song, T.-S. Bae, Y. H. Park, Y.-C. Kang, S.-G. Lee, S.-Y. Kim, D. H. Kim, S. Lee, G. Min, G.-H. Lee, J.-W. Kang, and J. Yun. "Transparent Ultrathin Oxygen-Doped Silver Electrodes for Flexible Organic Solar Cells." *Adv. Funct. Mater.*, vol. 24, no. 11, 2013, pp. 1551-1561.

[304] K. X. Wang, Z. Yu, S. Sandhu, V. Liu, and S. Fan. "Condition for perfect antireflection by optical resonance at material interface." *Optica*, vol. 1, no. 6, 2014, pp. 388-395.

[305] R. Maas, S. A. Mann, D. L. Sounas, A. Alù, E. C. Garnett, and A. Polman. "Generalized antireflection coatings for complex bulk metamaterials." *Phys. Rev. B*, vol. 93, no. 19, 2016, p. 195433.

[306] J. Q. Xi, M. F. Schubert, J. K. Kim, E. F. Schubert, M. Chen, S.-Y. Lin, W. Liu, and J. A. Smart. "Optical thin-film materials with low refractive index for broadband elimination of Fresnel reflection." *Nat. Photon.*, vol. 1, no. 3, 2007, pp. 176-179.

[307] D.-X. Yan, H. Pang, B. Li, R. Vajtai, L. Xu, P.-G. Ren, J.-H. Wang, and Z.-M. Li. "Structured Reduced Graphene Oxide/Polymer Composites for Ultra-Efficient Electromagnetic Interference Shielding." *Adv. Funct. Mater.*, vol. 25, no. 4, 2014, pp. 559-566.

[308] Z. Lu, H. Wang, J. Tan, and S. Lin. "Microwave shielding enhancement of high-transparency, double-layer, submillimeter-period metallic mesh." *Appl. Phys. Lett.*, vol. 105, no. 24, 2014, p. 241904.

[309] J. Park, K. Lee, H.-D. Um, K.-H. Kim, and K. Seo. "Direct Fabrication of Flexible Ni Microgrid Transparent Conducting Electrodes via Electroplated Metal Transfer." *Adv. Mater. Technol.*, vol. 3, no. 1, 2017, p. 1700213.

[310] C.-W. Yang and J.-W. Park. "The cohesive crack and buckle delamination resistances of indium tin oxide (ITO) films on polymeric substrates with ductile metal interlayers." *Surf. Coat. Technol.*, vol. 204, no. 16, 2010, pp. 2761-2766.

[311] H. K. Lin, S. M. Chiu, T. P. Cho, and J. C. Huang. "Improved bending fatigue behavior of flexible PET/ITO film with thin metallic glass interlayer." *Mater. Lett.*, vol. 113, 2013, pp. 182-185.

[312] B. Sim, E.-H. Kim, J. Park, and M. Lee. "Highly enhanced mechanical stability of indium tin oxide film with a thin Al buffer layer deposited on plastic substrate." *Surf. Coat. Technol.*, vol. 204, no. 3, 2009, pp. 309-312.

[313] Z. Lu, L. Ma, J. Tan, H. Wang, and X. Ding. "Transparent multi-layer graphene/polyethylene terephthalate structures with excellent microwave absorption and electromagnetic interference shielding performance." *Nanoscale*, vol. 8, no. 37, 2016, pp. 16684-16693.

[314] J. Han, X. Wang, Y. Qiu, J. Zhu, and P. Hu. "Infrared-transparent films based on conductive graphene network fabrics for electromagnetic shielding." *Carbon*, vol. 87, 2015, pp. 206-214.

[315] Y. Han, Y. Liu, L. Han, J. Lin, and P. Jin. "High-performance hierarchical graphene/metal-mesh film for optically transparent electromagnetic interference shielding." *Carbon*, vol. 115, 2017, pp. 34-42.

[316] L.-C. Jia, D.-X. Yan, X. Liu, R. Ma, H.-Y. Wu, and Z.-M. Li. "Highly Efficient and Reliable Transparent Electromagnetic Interference Shielding Film." *ACS Appl. Mater. Interfaces*, vol. 10, no. 14, 2018, pp. 11941-11949.

[317] L. Ma, Z. Lu, J. Tan, J. Liu, X. Ding, N. Black, T. Li, J. Gallop, and L. Hao. "Transparent Conducting Graphene Hybrid Films To Improve Electromagnetic Interference (EMI) Shielding Performance of Graphene." *ACS Appl. Mater. Interfaces*, vol. 9, no. 39, 2017, pp. 34221-34229.